

Next Generation Optical Analysis for Agrochemical Research & Development



Submitted by

Nicholas Philip Gaunt

*to the University of Exeter as a thesis for the
degree of Doctor of Philosophy in Physics.*

This thesis is available for Library use on the understanding that it is copyright material and that no quotation from the thesis may be published without proper acknowledgement.

I certify that all material in this thesis which is not my own work has been identified and that no material has previously been submitted and approved for the award of a degree by this or any other University.

Nicholas P. Gaunt
September 2019

Abstract

The world's population is increasing rapidly and higher calorific diets are becoming more common; as a consequence the demand for grain is predicted to increase by more than 50% by 2050 without a significant increase in the available agricultural land. Maximising the productivity of the existing agricultural land is key to maintaining food security and agrochemicals continue to be a key enabler for the efficiency gains required. However, agrochemicals can be susceptible to significant losses and thus often require further chemical to be applied to compensate. Sources of such losses include spray drift, poor spray retention/capture by the target and poor penetration through the plant cuticle. The effectiveness of a crop protection agent depends not only on the intrinsic activity of the active ingredient (AI) but also on the physicochemical properties of the formulation. These properties can be modified by using formulation components, known as adjuvants, which can be used to help mitigate such losses. Adjuvants exert their effects by, for example, controlling droplet size and distribution through their effect on surface tension which can also improve penetration into leaves through the cuticle wax which coats the epidermis of leaves and acts as a protective barrier. However, characterising how they alter the movement of the AIs can be challenging.

Optical techniques have shown promise in a multitude of scientifically related areas, such as *in vivo* tissue imaging, but none have yet been applied to aiding the agrochemical industry. By probing the interactions between leaf surface and agrochemical agent, with light, one is able to obtain a large amount of diagnostic information, non-invasively. Whereas techniques like Raman

spectroscopy are limited by long acquisition times, coherent Raman techniques such as coherent anti-Stokes Raman scattering (CARS) and stimulated Raman scattering (SRS) are coherently driven and provide an enhanced signal, and also allow for video-rate imaging.

In this thesis, I have applied this cutting-edge laser imaging technique as a novel analytical technique that allows the *in situ* analysis of agrochemicals in living plant tissues at a cellular level. In Chapters 4 through 7, multiple factors essential for a functional and efficient agrochemical were considered and experimented. In Chapter 4, a typical industry study highlights the need for innovative and rapid technologies in the agrochemical industry. The resulting chapters (5, 6, and 7) outline several ways in which Coherent Raman Scattering (CRS) techniques can improve the current capabilities of agrochemical testing. By utilising a model system, paraffin wax, a cheap and rapid protocol can provide accurate diffusion information and repeatable results. Chapters 6 and 7 use both this protocol to gain comparative data on several adjuvants and active ingredients in paraffin wax and *in vivo*, in a variety of plants.

The ability to visualise agrochemical products on a leaf surface to reveal interactions between the materials of the product and with the leaf surface will enable a step change in the agrochemical design process, through determination of the spatial distribution of the materials and their roles within the applied products. It is hoped that the technology developed in this thesis could play a big role in the development of future agrochemical products that are tailored to maximise efficacy and minimise environmental impact.

Acknowledgements

Firstly, I would like to express my sincere gratitude to my supervisor Prof. Julian Moger for the continuous support for the duration of my PhD. His motivation and immense knowledge in a multitude of areas has proven invaluable. I could not have imagined having a better advisor to mentor me through this study.

Alongside Prof. Moger, I would like to thank my Syngenta supervisors: Niall Thomson and Faheem Padia, for their insightful comments and encouragement, always giving me the kick needed in the right direction and really helping me shape this project to the needs of industry, which was of paramount importance.

My sincere thanks go to Mark Seymour, Morag Woods, Melissa Brazier-Hicks and Ryan Ramsey who also provided me with areas to study and helpful advice along the way. Without Morag's support in particular, it would not have been possible to conduct the typical industry study shown in Chapter 4.

I thank several people at the University of Exeter including members of my group, both past and present; Saleh Alghamdi, Chun-Chin Wang, Natalie Garrett, Kelly Curtis and Sarah Saint-Jalm, all of whom have contributed to my project in stages and without their kind words and stimulating discussions, the last four years may not have been so much fun. The Biophysics group has been both an excellent academic resource and a fantastic social group.

I've made lots of new friends since moving down south, a long way from home. I'd like to express my appreciation to everyone who has made this adventure an

incredibly enjoyable one. From my rugby team, who taught me about south-western cider at great length, to my Friday football team, who have tried to teach me to accurately kick a ball, and given me a great outlet after a long day of writing this thesis!

I definitely owe a lot to music, especially for the last 6 months of late night sessions, writing until the sun comes up. Specifically, I would say the drum and bass works from the likes of Pendulum, Metrik, Sub Focus and Shock Culture (especially the UKF live set featuring the latter three) in an attempt to stay pumped up and awake enough to put words on paper, proved a massive help.

Last but definitely not the least, I would like to thank my nearest and dearest – my parents and my wonderful partner, April. April has put up with my late nights in the office and keyboards clacking at 3am, all without argument. She's been my absolute rock and I am truly grateful. My parents have been at the end of a phone every day, giving me tremendous amounts of support and taking an interest in this project, so much so they know what CARS and SRS stand for without the acronym section in this thesis.

From the bottom of my heart, thank you all so much!

Contents

.....	2
abstract	3
Acknowledgements	5
Contents.....	7
List of Figures.....	10
List of Tables.....	23
List of Acronyms.....	24
Chapter 1: Introduction.....	25
1.1 Thesis Aims	25
1.2 Organisation of Thesis	26
1.3 Food Security	27
1.4 Agrochemicals and Interactions	28
1.4.1 Agrochemicals.....	28
1.4.2 Agrochemical Industry.....	33
1.4.3 Plant Uptake	33
1.5 Plant Biology.....	34
1.5.1 Plant Anatomy	34
1.3.2 Plant Pathogens.....	39
Chapter 2: A Review of the Background Theory and Current Literature	42
2.1 Introduction.....	42
2.2 Mass Spectrometry.....	43
2.3 Autoradiography	45
2.4 Scanning Electron Microscopy.....	46
2.5 Optical Microscopy.....	47
2.5.1 Fluorescence Microscopy.....	47
2.5.2 Raman Spectroscopy.....	49
2.5.4 Coherent Raman Spectroscopy	53
2.5.4.1 Coherent anti-Stokes Raman scattering (CARS)	55
2.5.4.2 Stimulated Raman Scattering (SRS)	58
2.5.4.3 A Comparison between CARS and SRS	60
2.6 Diffusion.....	63
2.7 Fickian Diffusion.....	64
2.8 Non-Fickian Diffusion.....	65
2.9 Summary.....	66
Chapter 3: Instrumentation	67
3.1 Introduction.....	67
3.2 Spontaneous Raman Spectroscopy.....	67
3.3 Coherent Raman Spectroscopy (CRS)	68
3.4 LCMS.....	72
3.4.1 LC.....	72
3.4.2 MS.....	73
Chapter 4: Measuring agrochemical uptake using a conventional technique	76
4.1 Introduction.....	76
4.2 Leaf Wash.....	79
4.3 Hexane Partition.....	80

4.4 Treated Leaf Extracts	81
4.5 Total Recovery	83
4.6 Summary.....	84
Chapter 5: Development of an Analytical Model System for Cuticle Wax....	86
5.1 Introduction.....	86
5.2 Raman on wax	87
5.2.1 Cuticle wax.....	87
5.2.1.1 <i>Sedum Morganianum</i>	87
5.2.1.2 <i>Vitis Vinifera</i> (common grape).....	90
5.2.3 Paraffin wax.....	91
5.3 Paraffin vs. Cuticle wax.....	95
5.3.1 Raman Spectroscopy.....	95
5.3.2 CRS.....	97
5.4 Paraffin wax: A cuticle wax model diffusion system.....	101
5.5 Summary.....	103
Chapter 6: Development of a Diffusion Protocol for Agrochemical agents.	104
6.1 Diffusion Cell.....	106
6.2 Paraffin vs Cuticle waxes Diffusion.....	108
6.3 Active Ingredients	112
6.3.1 Azoxystrobin.....	112
6.3.2 Fludioxonil.....	113
6.3.3 Comparison and Discussion	114
6.4 Adjuvants.....	114
6.4.1 Acetophenone	115
6.4.2 Aerosol OT-B.....	116
6.4.3 Brij O10	117
6.4.4 Emulsogen EL360	118
6.4.5 Finsolv TN	119
6.4.6 Genagen (DMLA)	120
6.4.7 Hexamoll Dinch	121
6.4.8 Methyl Oleate	122
6.4.9 Nansa EVM.....	123
6.4.10 Pluronic PE 10400	124
6.4.11 Silwet L77.....	125
6.4.12 Soprophor BSU	126
6.4.13 Tween 20	127
6.5 Comparison and Discussion	128
6.6 Agrochemical Formulation Solutions into Paraffin Wax.....	129
6.6.1 Azoxystrobin.....	129
6.6.2 Fludioxonil.....	134
6.6.3 Finsolv TN	138
6.6.4 Tween 20.....	143
6.7 Comparison and Discussion	147
6.8 Active Ingredients with Adjuvants into Paraffin Wax.....	148
6.8.1 AZ with adjuvants	148
6.8.2 FDL with adjuvants	154
6.7 Comparison and Discussion	160
6.8 Summary.....	161
Chapter 7: Exploration of agrochemical diffusion <i>in planta</i>	163
7.1 Introduction.....	163
7.2 Cabbage	163
7.3 Ivy	169
7.4 Summary.....	176
8.1 Discussion.....	178

8.2 Conclusion	179
8.3 Future Directions	181
References	183
Appendix A	189
Appendix B	192

List of Figures

- Figure 1.1: Cartoon representation of the layers towards the surface of a corn leaf, an angiosperm that absorbs sprayed agrochemical through its cuticle.
- Figure 1.2: Chemical structure of 2,4-D
- Figure 1.3: Example of leaf images with various diseases (1) Apple Scab, *Venturia inaequalis* (2) Apple Black Rot, *Botryosphaeria obtusa* (3) Apple Cedar Rust, *Gymnosporangium juniperi-virginianae* (4) Apple healthy (5) Blueberry healthy (6) Cherry healthy (7) Cherry Powdery Mildew, *Podosphaera clandestina* (8) Corn Gray Leaf Spot, *Cercospora zeae-maydis* (9) Corn Common Rust, *Puccinia sorghi* (10) Corn healthy (11) Corn Northern Leaf Blight, *Exserohilum turcicum* (12) Grape Black Rot, *Guignardia bidwellii*, (13) Grape Black Measles (Esca), *Phaeomoniella aleophilum*, *Phaeomoniella chlamydospora* (14) Grape Healthy (15) Grape Leaf Blight, *Pseudocercospora vitis* (16) Orange Huanglongbing (Citrus Greening), *Candidatus Liberibacter spp.* (17) Peach Bacterial Spot, *Xanthomonas campestris* (18) Peach healthy (19) Bell Pepper Bacterial Spot, *Xanthomonas campestris* (20) Bell Pepper healthy (21) Potato Early Blight, *Alternaria solani*. Reprinted from Moharty *et al*¹
- Figure 2.1: Autoradiographs of corn and black nightshade (*Solanum nigrum*) plants, which were foliar and root treated. Reprinted from Grossmann *et al.* 2011

- Figure 2.2: Localisation of dyes in apples and peppers. Cu, cuticle; Ep, epidermal cells. Scale bars = 20 μ m. Reprinted from Liu, 2004
- Figure 2.3: Two fungicides azoxystrobin (az) and chlorothalonil (chl) imaged on maize leaves. (A) SRL and spontaneous Raman at C \equiv N bond (B) SRL image of a mixture of AZ and chl (C) chl distribution on maize (D) AZ distribution on maize leaf. Reprinted from Mansfield *et al.* (2013)
- Figure 3.1: Six types of vibrational modes
- Figure 3.2 Energy diagrams for the CARS process: (a) Schematic of the pump and probe beam interacting together: the envelope of the interferences beating at the frequency $1/\Omega$, (b) Schematic of the phase matching conditions for the momentum, k_p is used for pump and probe as it is usually the same beam used for both, (c) i. ii. and iii. are Jablonski diagrams contributing to the CARS signal: (i) Resonant CARS, (ii) and (ii) non-resonant CARS due to electronic contribution and other molecule respectively.
- Figure 3.3: Schematic of the SRS process. (a) Energy level diagram for the SRS process. (b) The difference in wavelengths of the input laser beams match that of a Raman vibration, the output is a loss in the pump beam and a gain in the Stokes beam. (c) The Stokes beam is modulated, a small loss in the pump beam is detected, using highly sensitive lock-in detection.
- Figure 4.1: i. Renishaw InVia system for spontaneous Raman measurements, and ii. Schematic showing the various components that make up the spectrometer and the beam paths for the 785/830 nm lasers

and resulting Raman signal [DG: diffraction grating, NF: notch filter, SL: streamline lens]. Schematic adapted from Sands *et al*²

- Figure 4.2: (i) The optical setup of fiber laser-based stimulated Raman scattering for AIs and wax. AOM: acousto-optic modulator, DM: dichroic mirror, OBJ: objective, FL: filter, PMT: photomultiplier tube, PD: photodiode, LIA: lock-in amplifier. (ii) Photograph of the coherent Raman experimental set-up, showing mirrors, dichroic mirror and telescope guiding beams to the scan unit.
- Figure 4.3: (A) Simple schematic for LC-MS and (B) Photograph of the set-up, showing Thermo Xcalibur software and automated injection port.
- Figure 5.1: Diagram outlining the different measurements in a foliar uptake study using LCMS.
- Figure 5.2: Amount recovered from three treatments of agrochemical solution onto cabbage leaf after leaf washes with water. AZ (blue), AZ with Tween 20 (red) and AZ with Finsolv TN (green)
- Figure 5.3: Amount recovered from three treatments of agrochemical solution onto cabbage leaf after hexane washes to remove cuticle wax. AZ (blue), AZ with Tween 20 (red) and AZ with Finsolv TN (green)
- Figure 5.4: Amount recovered from three treatments of agrochemical solution onto cabbage leaf after extraction process. AZ (blue), AZ with Tween 20 (red) and AZ with Finsolv TN (green)
- Figure 5.5: The sum of the amounts recovered from three treatments of agrochemical solution onto cabbage leaf after water washing, extraction

process, and the hexane washes of the cuticle wax. AZ (blue), AZ with Tween 20 (red) and AZ with Finsolv TN (green)

- Figure 6.1: Mean Raman spectrum of wax extracted from *Sedum Morganianum*, in the fingerprint region. The spectrum was measured using the 785nm laser with 300 l/mm grating.
- Figure 6.2: Mean Raman spectrum of wax extracted from *Sedum Morganianum*, in the high wavenumber region. The spectrum was measured using the 785nm laser with 300 l/mm grating.
- Figure 6.3: Mean Raman spectrum of wax extracted from *vitis vinifera*, in the fingerprint region. The spectrum was measured using the 785nm laser with 300 l/mm grating.
- Figure 6.4: Mean Raman spectrum of wax extracted from *vitis vinifera*, in the high wavenumber region. The spectrum was measured using the 785nm laser with 300 l/mm grating.
- Figure 6.5: i) Generalised structure of Paraffin Wax, with some common plant wax constituents; ii), iii) and iv) showing different position or amounts of alkanol groups, with v) aldehyde and vi) ketone groups
- Figure 6.6: Mean Raman spectrum of paraffin wax, in the fingerprint region. The spectrum was measured using the 785nm laser with 300 l/mm grating.
- Figure 6.7: Mean Raman spectrum of paraffin wax, in the high wavenumber region. The spectrum was measured using the 785nm laser with 300 l/mm grating.

- Figure 6.8: Mean Raman spectra comparing the wax extracted from *vitis vinifera* (red), *sedum morganianum* (blue) and paraffin wax (green) in the high wave number region.
- Figure 6.9: Mean Raman spectra comparing the wax extracted from *vitis vinifera* (red), *sedum morganianum* (blue) and paraffin wax (green) in the fingerprint region.
- Figure 6.10: CARS image and 3D representation of a) Paraffin wax block b) extracted *sedum morganianum* wax block and c) extracted grape wax block at the CH₂ peak (2845cm⁻¹). Scale bar represents 10μm
- Figure 6.11: SRS images to investigate laser damage on a paraffin wax sample using 180mW average power. (A) First scan, (B) Difference between (A) and (C), with (C) Last (80th) scan, (D) composite image. Laser damage minimal throughout rapid scan, with some highlighted regions with change circled in (B) and (D).
- Figure 6.12: The diffusion curves for uptake of AZ into (A) Grape and (B) SM
- Figure 6.13: Diffusion coefficients for the uptake of AZ into SM (green), Grape (red) and paraffin (blue)
- Figure 7.1: Internal structure of a typical leaf. The surface of a leaf contains waxy cuticle, epidermal cells as cover for the upper and lower surface, and palisade mesophyll to aid the absorption of light.

- Figure 7.2: (A) Schematic of diffusion cell, made 130 μ m height. (B). WE showing the edge of the wax, with the background shown in black. Scale bar represents 2 μ m

- Figure 7.3: The diffusion curves for uptake of AZ into (A) Grape and (B) SM

- Figure 7.4: Diffusion coefficients for the uptake of AZ into SM (green), Grape (red) and paraffin (blue)

- Figure 7.5: Mean Raman spectra for AI Azoxystrobin, with chemical structure and tentatively assigned peak of interest, which appears in paraffin wax's silent region.

- Figure 7.6: Mean Raman spectra for AI Fludioxonil, with chemical structure and tentatively assigned peak of interest, which appears in paraffin wax's silent region.

- Figure 7.7: Mean Raman spectra for adjuvant Acetophenone, with chemical structure and tentatively assigned peaks of interest, which appear in paraffin wax's silent region.

- Figure 7.8: Mean Raman spectra for adjuvant Aerosol OT-B, with chemical structure and tentatively assigned peak of interest, which appears in paraffin wax's silent region.

- Figure 7.9: Mean Raman spectra for adjuvant Brij O10, with chemical structure and no tentatively assigned peaks of interest, as no recognised unique vibrations appear in paraffin wax's silent region.

- Figure 7.10: Mean Raman spectra for adjuvant Emulsogen, with chemical structure and tentatively assigned peak of interest, which appears in paraffin wax's silent region.
- Figure 7.11: Mean Raman spectra for adjuvant Finsolv TN, with chemical structure and tentatively assigned peaks of interest, which appear in paraffin wax's silent region.
- Figure 7.12: Mean Raman spectra for adjuvant Gengagen DMLA, with chemical structure and tentatively assigned peak of interest, which appears in paraffin wax's silent region.
- Figure 7.13: Mean Raman spectra for adjuvant Hexamoll Dinch, with chemical structure and tentatively assigned peak of interest, which appears in paraffin wax's silent region.
- Figure 7.14: Mean Raman spectra for adjuvant Methyl Oleate, with chemical structure and tentatively assigned peaks of interest, which appear in paraffin wax's silent region.
- Figure 7.15: Mean Raman spectra for adjuvant Nansa EVM, with chemical structure and tentatively assigned peak of interest, which appears in paraffin wax's silent region.
- Figure 7.16: Mean Raman spectra for adjuvant Pluronic PE10400, with chemical structure and no tentatively assigned peaks of interest, as no recognised unique vibrations appear in paraffin wax's silent region.

- Figure 7.17: Mean Raman spectra for adjuvant Silwet L77, with chemical structure and no tentatively assigned peaks of interest, as no recognised unique vibrations appear in paraffin wax's silent region.
- Figure 7.18: Mean Raman spectra for adjuvant Soprophor BSU, with chemical structure and tentatively assigned peak of interest, which appears in paraffin wax's silent region.
- Figure 7.19: Mean Raman spectra for adjuvant Tween 20, with chemical structure and tentatively assigned peak of interest, which appears in paraffin wax's silent region.
- Figure 7.20: Hyperspectral data for a droplet of AZ in water imaged by SRS at its signal at the spontaneous Raman peak at 2220cm^{-1} , corresponding with the $\text{C}\equiv\text{N}$ vibration. (A) Shows the off-resonance image with (B) showing intense resonance from the peak.
- Figure 7.21: (A) SRS x-y images of the penetration depth into three wax samples as a function of time. The spectrum indicates the signal from $\text{C}\equiv\text{N}$ recorded every 60 seconds for a total of 720 seconds, from the initial contact. The colour spectra labelled 1-3 show various repeats. The untreated wax is shown on the far left (labelled wax) and the off resonance is to its immediate right (labelled OR). Scale bar, $2\mu\text{m}$. (B) Shows the diffusion of AZ into wax, over 720 seconds, imaged with Coherent Raman scattering images of paraffin wax's CH_2 (CARS, green) and AZ's chemically specific $\text{C}\equiv\text{N}$ (SRS, magenta). Field of view $129.3\mu\text{m}^2$.

- Figure 7.22: Diffusion depth profile for AZ, as a function of time, into paraffin wax.
- Figure 7.23: The area under the curve divided by the square root of time provides us with diffusion coefficients over time, for Tween 20 into paraffin wax
- Figure 7.24: Hyperspectral data for a droplet of FDL in water imaged by SRS at its signal at the spontaneous Raman peak at 2221cm^{-1} , corresponding with the $\text{C}\equiv\text{N}$ vibration. (A) Shows the off-resonance image with (B) showing intense resonation from the peak.
- Figure 7.25: SRS x-y images of the penetration depth of FDL into three wax samples as a function of time. The spectrum indicates the signal from $\text{C}\equiv\text{N}$ recorded every 60 seconds for a total of 720 seconds, from the initial contact. The three colour spectra show repeats. The untreated wax is shown on the far left (labelled wax) and the off resonance is to its immediate right (labelled OR). Scale bar, $2\mu\text{m}$.
- Figure 7.26: Diffusion depth profile for FDL, as a function of time, into paraffin wax.
- Figure 7.27: The area under the curve divided by the square root of time provides us with diffusion coefficients over time, for Tween 20 into paraffin wax
- Figure 7.28: Hyperspectral data for a droplet of Finsolv TN in water imaged by SRS at its signal at the spontaneous Raman peak between $1702\text{-}1735\text{cm}^{-1}$ showing the peak at 1723cm^{-1} , corresponding with the

C=O vibration. (A) Shows the off-resonance image with (B) showing intense resonance from the intense peak.

- Figure 7.29: Finsolv TN uptake into paraffin wax, shown as a pseudo-coloured time series, with magenta representing Finsolv TN and green representing the paraffin wax. Images were acquired every minute for 30 minutes, with 6 of these time-points compiled here between initial contact at $t=0$ seconds, and 720 seconds. Scale bar = 10 microns
- Figure 7.30: Diffusion depth profile for Finsolv TN, as a function of time, into paraffin wax.
- Figure 7.31: The area under the curve divided by the square root of time provides us with diffusion coefficients over time, for Finsolv TN into paraffin wax.
- Figure 7.32: Hyperspectral data for a droplet of Tween 20 in water imaged by SRS at its signal at the spontaneous Raman peak at 1737cm^{-1} , corresponding with the C=O vibration. (A) Shows the off-resonance image with (B) showing intense resonance from the peak.
- Figure 7.33: Tween 20 uptake into paraffin wax, shown as a pseudo-coloured time series, with magenta representing Tween 20 and green representing the paraffin wax. Images were acquired every minute for 30 minutes, with 6 of these time-points compiled here between initial contact at $t=0$ seconds, and 720 seconds. Scale bar = 10 microns
- Figure 7.34: Diffusion depth profile for Tween 20, as a function of time, into paraffin wax.

- Figure 7.35: The area under the curve divided by the square root of time provides us with diffusion coefficients over time, for Tween 20 into paraffin wax
- Figure 7.36: Diffusion coefficients for Finsolv TN and Tween 20, from 7.31 and 7.35 respectively, plotted on the same axis to reveal Finsolv TN's increased diffusivity over 720 seconds.
- Figure 7.37: SRS x-y images of the penetration depth of AZ into three paraffin wax samples as a function of time. The spectrum indicates the signal from CEN recorded every 60 seconds for a total of 720 seconds, from the initial contact. The three colour spectra show AZ, AZ with Finsolv TN and AZ with Tween 20 respectively. The untreated wax is shown on the far left (labelled wax) and the off resonance is to its immediate right (labelled OR).
- Figure 7.38: Six different time-points, showing the uptake of AZ into wax, with and without the addition of adjuvants Tween 20 (green) and Finsolv TN (blue). AZ unaided is shown in red. Time points 0-720 showing AZ with and without adjuvant.
- Figure 7.39: Diffusion coefficients of (A) AZ with Tween 20 and (B) AZ with Finsolv TN.
- Figure 7.40: SRS x-y images of the penetration depth of FDL into three wax samples as a function of time. The spectrum indicates the signal from CEN recorded every 60 seconds for a total of 720 seconds, from the initial contact. The three colour spectra show FDL, FDL with Tween 20 and FDL with Finsolv TN respectively. The untreated wax is shown on

the far left (labelled wax) and the off resonance is to its immediate right (labelled OR). Scale bar, 2 μ m.

- Figure 7.41: Six different time-points, showing the uptake of FDL into wax, with and without the addition of adjuvants Tween 20 (green) and Finsolv TN (blue). AZ unaided is shown in red. Time points 0-720 showing AI with and without adjuvant.
- Figure 7.42: Diffusion coefficients of (A) FDL with Tween 20 and (B) FDL with Finsolv TN
- Figure 8.1: CRS image of wax surface on a cabbage leaf. 2 photon-fluorescence (2PF) and SRS, as well as the Brightfield image, can be simultaneously gathered, and merged. Pump beam, set to 838.6nm had average power of 80mW, with Stokes beam, also averaging 80mW, is fixed at 1032nm. Scale bar = 10 μ m
- Figure 8.2: SRS x-y images of the penetration depth of FDL into cabbage leaf section samples as a function of time. The spectrum indicates the signal from CEN recorded every 60 seconds for a total of 720 seconds, from the initial contact. The two colour spectra show FDL and FDL with Finsolv TN respectively. The untreated leaf is shown on the far left (labelled Cabbage Leaf) and the off resonance is to its immediate right (labelled OR).
- Figure 8.3: Diffusion depth profile for FDL, as a function of time, into a cabbage leaf section
- Figure 8.4: Diffusion coefficients calculated from Figure 8.3 for FDL with and without Finsolv TN, into a cabbage leaf section. The data set

coloured green shows FDL alone, whereas FDL with Finsolv TN is shown in red.

- Figure 8.5: CRS image of wax surface on an ivy leaf. 2 photon-fluorescence (2PF) and SRS, as well as the Brightfield image, can be simultaneously gathered, and merged. Pump beam, set to 838.6nm had average power of 80mW, with Stokes beam, also averaging 80mW, is fixed at 1032nm. Scale bar = 10um
- Figure 8.6: SRS x-y images of the penetration depth of FDL into ivy leaf section samples as a function of time. The spectrum indicates the signal from CEN recorded every 60 seconds for a total of 720 seconds, from the initial contact. The two colour spectra show FDL and FDL with Finsolv TN respectively. The untreated leaf is shown on the far left (labelled Ivy Leaf) and the off resonance is to its immediate right (labelled OR).
- Figure 8.7: Diffusion depth profile for FDL, as a function of time, into a ivy leaf section, with the green line representing FDL unaided, and the red showing the uptake improvement, with aid from adjuvant Finsolv TN.
- Figure 8.8: Diffusion coefficients calculated from Figure 8.3 for FDL with and without Finsolv TN, into a cabbage leaf section. The data set coloured green shows FDL alone, whereas FDL with Finsolv TN is shown in red.
- Figure 9.1: Three stages showing the uptake of agrochemical agent Dicamba-d₃ in corn cells.

List of Tables

- Table 1: Historical account of pesticide use. Adapted from Mahmood *et al.*³
- Table 2: Comparative table of the advantages and disadvantages of *in planta* characterisation techniques used in the agrochemical industry
- Table 3: Peak assignments of the most prominent peaks in the Raman spectrum for Paraffin wax in both fingerprint and high wave number regions.
- Table 4: Peak assignments, from Socrates (2004), of the most prominent peaks in the Raman spectra for extracted waxes in fingerprint region.⁶⁶
- Table 5: Scalable differences between the extracted wax samples, and our model system of Paraffin wax.
- Table 6: Active Ingredient and adjuvant chemical properties.

List of Acronyms

2,4-D	2,4-Dichlorophenoxyacetic acid
AI	Active Ingredient
AOM	Acousto-optic Modulator
AZ	Azoxystrobin
BHC	β -Benzene Hexachloride
CARS	Coherent anti-Stokes Raman spectroscopy
CHL	Chlorothalonil
CRS	Coherent Raman spectroscopy
Cu	Cuticle
DDT	Dichlorodiphenyltrichloroethane
DG	Diffraction Grating
DM	Dichroic Mirror
EDX	Energy dispersive X-ray microanalysis
EI	Electron Impact
Ep	Epidermal
ESI	Electrospray Ionisation
FDL	Fludioxonil
FL	Filter
FOV	Field of view
GCMS	Gas Chromatography Mass Spectroscopy
LCMS	Liquid Chromatography Mass Spectroscopy
LIA	Lock-in Amplifier
MALDI	Matrix-assisted laser desorption/ionisation
NF	Notch Filter
OBJ	Objective
OPO	Optical Parametric Oscillator
PD	Photodiode
PMT	Photomultiplier Tube
R&D	Research and Development
SEM	Scanning Electron Microscopy
SERS	Surface-Enhanced Raman Spectroscopy
SL	Streamline Lens
SRG	Stimulate Raman Gain
SRL	Stimulated Raman Loss
SRS	Stimulated Raman scattering
ToF-SIMS	Time of Flight Secondary Ion Mass Spectroscopy
2PF	Two Photon Fluorescence

Chapter 1: Introduction

With world population increasing towards 10 billion, it is becoming evident that current food production cannot keep up with demand. UN demographers are now projecting a population of up to 12.3 billion people at the end of the century.⁴ With more mouths, all demanding a higher calorie diet, the push to promote non-petroleum energy sources and limits on available farmland, improving agricultural productivity is essential. The problems are further exacerbated by land erosion and climate change.

A step change in agricultural productivity has occurred previously during the green revolution when higher-yielding seed varieties, mechanisation and then chemical inputs significantly increased productivity between 1940-70.⁵ While productivity has continued to increase since the 1970s another step change is required to feed the growing population.

Agrochemicals, such as herbicides, fungicides and insecticides, are a key factor in improving crop yields and without them around 40% of the world's food would not exist.⁶ The widespread use of newer and more effective products since the middle of the last century has increased food security and improved standards of living around the world.

1.1 Thesis Aims

The purpose of this research is to aid the agrochemical industry and the future of food security.

The aim of this thesis is to utilise laser imaging techniques such as Coherent Anti-Stokes Raman Scattering (CARS) and Stimulated Raman Scattering (SRS)

as novel analytical techniques that will give the agrochemical industry the tools for *in situ* analysis of agrochemicals in living plant tissues at a cellular level.

Furthermore, the project aims to eliminate the need for standard molecular labels, which are usually heavier than the agrochemical molecule itself. Such large labels can perturb the movement of agrochemicals and skew any data. An aim of this thesis therefore is to reveal interactions between the materials of the product and with the leaf surface in real time and label-free.

Thus the final aim will be to assess the differences of multiple agrochemical agents, allowing a deeper look into their efficacy.

These processes will be the stepping stones to future of next generation agrochemistry, and ensure to aid the fight against global hunger.

1.2 Organisation of Thesis

This thesis is organised into eight chapters. Following this introduction, Chapter 2 presents the previous research in this area, along with relevant theory,, utilising the current state of the art techniques such as Liquid Chromatography Mass Spectrometry (LCMS), Gas Chromatography Mass Spectrometry (GCMS), autoradiography and Scanning Electron Microscopy (SEM), before talking about the relatively new techniques in CARS and SRS to aid the problems at hand. Chapter 2 outlines the background theories of the methods used with Chapter 3, which then explains the experimental setup, instrumentation and methods used throughout the thesis. Chapter 4 will then start the results chapters, explaining the current state of research, utilising LCMS to perform typical experiments on the uptake of agrochemicals into plants. Chapter 5 will then compare to this, exploring the work on plant cuticle

wax diffusion, and the model system of paraffin wax we have utilised for identical samples. Chapter 6 will take a larger step, presenting detailed findings into work on *in situ* measurements, on full leaf experiments. Finally, Chapter 7 will zoom in and show the preliminary results on active ingredient uptake into individual plant cells, as well as summarising and discussing the outcomes and future of this area.

1.3 Food Security

The definition of food security, which can be traced back to the 1943 Conference of Food and Agriculture, was stated as the availability of “secure, adequate and suitable supply of food for everyone”. This concept subsequently evolved to an international level, with donor countries giving their agricultural surpluses to overseas countries in need.⁷

Stages of food insecurity range from food secure situations to full-scale famine. Food insecurity exists when people do not have adequate physical, social or economic access to food, a problem that faces around 870 million people worldwide, according to Syngenta’s Good Growth Plan.⁸ With population increasing by around 200,000 per day, we could see an estimated 12.3 billion people by the end of the century. With that population increase in mind, we could be reaching the terrible milestone that is 1 billion suffering from hunger. Even more shocking is the staggering figure of 7 million hectares of farmland are being lost every year. In order to feed this growing population, the world will have to grow more food in the next 50 years, than it has in the past 10,000.⁸

From these statistics, it is obvious that some things need to change in our methods of food production. Possibly most importantly, making crops and land more efficient. The ability to do this would surely be the key factor in aiding the

rejuvenation of eco-systems and revitalising rural communities, increasing the amount of arable land.

Agrochemicals are always under scrutiny, but without them losses of yield could reach 75% in foods such as potatoes.^{9,10} As well as struggling to feed the population, the food vs. fuel debate is still an ongoing balance, and another reason why we may be unsuccessful in feeding the entire growing population. Eager to promote non-petroleum energy sources to reduce dependence on oil imports and slow global warming due to fossil fuel emissions, the United States, Brazil, and the European Union are promoting biofuels made from food crops.^{6,11} Ethanol production (mainly in the United States and Brazil) tripled up to almost 16 billion gallons between 2001 and 2007. Biofuel production has also been promoted by government initiatives such as subsidies and tax incentives. An analyst of global resources at the Earth Policy Institute, wrote “We are witnessing the beginning of one of the great tragedies of history. The United States, in a misguided effort to reduce its oil insecurity by converting grain into fuel for cars, is generating global food insecurity on a scale never seen before.”¹²

1.4 Agrochemicals and Interactions

1.4.1 Agrochemicals

Chemicals, such as a fertiliser, hormone, fungicide, insecticide, or soil treatment, are collectively known as agrochemicals, which improve the production of crops by controlling fungi and insect infestations in fields. Agrochemicals are under constant scrutiny for the damage they can do to nature if they are misused.^{13,14} Without agrochemicals, we would reportedly lose 40% of global crop yields annually.¹⁵ The valuable contribution of

agrochemicals has made their use common practice in agriculture. From the end of the 20th century to the present, the total global grain output increased by 200 million tonnes. Even now, China annually has reported loses of around 10% of their grain because of a variety of pests, whereas that percentage rises to 15%, or 37.5 million tonnes a year, in India from pests and other factors.¹⁶ The use of agrochemicals has significantly increased to combat these loses, with a reported 2.5 million pounds of pesticides being used worldwide per year.¹⁷

Despite the relatively recent Event breakthrough of agrochemistry, the use of pesticides dates back to the Roman era, where it was noted that burning sulphur on land would kill pests, and using salts, ash or bitters could help control weed growth. One Roman naturalist even supported the use of arsenic as an early insecticide.¹⁸ This idea was built upon in the 1600s where a mixture of arsenic and honey was used to control ant populations on farmland, and then again in 1867 where arsenic was used to fight

growing numbers of the potato beetle in the USA.³ Modern chemical crop protection is a relatively new idea, with many of the breakthroughs in development occurring after the middle of the 20th century. The major breakthrough coming after World War II, when the discovery and production of synthetic herbicides, insecticides and fungicides allowed significant contribution to the development of agriculture. This period is marked by the discovery of Aldrin, dichlorodiphenyltrichloroethane (DDT) in 1939, Dieldrin, β -Benzene Hexachloride (BHC), 2,4-Dichlorophenoxyacetic acid (2,4-D), Chlordane and Endrin.^{19,20} A historical account of agrochemical invention is compiled in Table 1. Year

1867	Paris Green (form of copper arsenite) used to control Colorado potato beetle
1885	Introduction of a copper mixture to control mildew
1892	Potassium dinitro-2-cresylate was produced in Germany
1939	DDT discovered by Paul Muller; organophosphate insecticides and phenoxyacetic herbicides were discovered
1950s	Captan and glyodin (fungicides) and malathion (insecticide) were discovered
1961-1971	'Agent Orange' introduced
1972	DDT banned
2001	The Stockholm Convention was held, in which an international treaty was signed for the elimination or restriction of persistent organic pollutant

Table 1: Historical account of pesticide use. Adapted from Mahmood *et al.*³

Although there are many minor classifications, which won't be covered in this study, agrochemicals can typically be classed as herbicides, insecticides and fungicides. Out of these, herbicides are the largest class of pesticides,

comprising around 50% of the world usage. These products aid the control or destruction of weeds and unwanted plants, and due to their ease of use, nearly all agricultural land in the United States is treated with herbicides.

Insecticides are the second largest category. Having being discovered during the 1950s, they found widespread use in agriculture due to their high toxicity to a wide variety of insects. However, this quality which made them so desirable, also led to several of them being banned due to their harmful effects on humans. Synthetic replacements for these compounds, like Pyrethroids, are an example of a more modern insecticide. These compounds are less toxic, and are based on natural chemicals, which can be found in plants like chrysanthemums.

Our final category consists of the fungicides, which commercially consist of, amongst other chemistry classes, halogenated compounds like carbamates, organophosphates and dithiocarbamates. These products are primarily used to protect crops and seeds from various fungi.

It is known that the penetration of an agrochemical into a leaf is related to its physicochemical properties, with the uptake rate being directly correlated with an Active Ingredient's (AI's) molecular size and lipophilicity²¹, which can prove a challenge for an agrochemical. The use of adjuvants can aid the diffusivity of agrochemicals, having being used to increase foliar uptake, and limit the amount of losses from spray drift and poor penetration.²² Adjuvants can increase the diffusivity of an agrochemical by impacting factors such as droplet size, distribution and adhesion.²³ However, quantifying the effects of an adjuvant on the AI has been a challenge that current analytical methods fail to meet all the demands, a problem we address in the upcoming chapters.

1.4.2 Agrochemical Industry

Agrochemical companies produce a range of different goods for growers to use. These companies produce pesticides, as well as commodity chemicals, fertilisers and preservatives. As will be discussed in Chapter 2, one of the current challenges of the industry is to analyse agrochemicals in an attempt to monitor how they interact with the plant, soil and pest utilising the current state of the art techniques such as LCMS and GCMS. However, these techniques give no spatial resolution, which is a key requirement for any instruments that can further this field.

1.4.3 Plant Uptake

Agrochemicals can enter a plant in numerous ways, however by absorption into the leaf is the most common practice, and is where I shall focus the efforts of this thesis. One of the most common forms of pesticide application, especially in conventional agriculture, is the use of sprays. Due to the ease of application and cost/time effectiveness, it is widely used to reduce risk of crop loss, through pest damage or plant pathogens. The sprays convert a formulation into size-controlled droplets, maximising the contact with the plant.²⁴ The drop size is a crucial balance; large droplets are less susceptible to spray drift, whereas small droplets maximise contact with the target organism.²⁵ However, in places of high wind, the small droplets will most likely be less effective and contaminate other areas.

Better analytical tools are required, and are crucial to ensure, in order to engineer the next generation of agrochemical formulations with enhanced uptake and reduced environmental impact. The current methods, which are

covered in Chapter 2, have some limitations. Overcoming these could have a positive impact on agrochemical performance.

1.5 Plant Biology

To analyse how agrochemicals interact with plants, we need to understand the cellular material a chemical needs to pass through. Plants can be broken down into two kingdoms, seed-bearing and non-seed-bearing, Angiosperms and Gymnosperms respectively,^{28,29} which are both susceptible to current pesticide treatments. However, Gymnosperms, which do not have flowers or fruit, are not considered to be relevant in this study, due to their infrequent use in human consumption.

1.5.1 Plant Anatomy

Before looking at plant anatomy in detail, it should be made clear this is only a study of Angiosperms, which make up 90% of all plant species, including the entirety of fruit and vegetables, as these are the main consumable plants grown in industry.³⁰ These differ from Gymnosperms, which consist of the coniferous plant groups like evergreens (pine and fir) and also deciduous trees like Ginkgo Biloba. Their seeds are not enclosed in organic “flesh” as with angiosperms - rather they are relatively naked, attached to the cone without an endosperm exterior around the seed, with the term Gymnosperm coming from the Greek meaning "naked seed".

Angiosperms, on the other hand, produce seeds that are covered.²⁹ They are flowering plants, this includes flowering trees but the category is much wider including regular flowers. Angiosperm seeds are not naked, but surrounded in organic material that protects them, providing nutrients when the environment is right for them to implant into the soil. For example, when it rains and when it is

warm enough to begin growth. Angiosperms also reproduce faster than gymnosperms due to their smaller reproductive parts, therefore can fertilise much faster, which is true of both the male and female genetic material.

While the early study of angiosperms attracted the attention of both chemists and botanists alike, it was not until the introduction of synthetic dyes in the latter part of the 19th century that any considerable amount of attention was directed towards pigment chemistry.³¹ Plant pigments, and their autofluorescence properties pose a major concern for optical analytical techniques, with image saturation a challenge to overcome, and will be a major aim of this thesis. Colour is imparted to a plant, from many of its different molecules. For example, the mixture of chlorophyll molecules found in spinach allows absorption of several wavelengths of visible light, with distinct absorbance peaks in the blue range (400–500 nm) and in the yellow-red range (600–700 nm), with the combination of visible light that is not absorbed appearing green to the human eye. Chlorophyll contains a porphyrin ring in its structure, with a magnesium ion in the centre.³² The porphyrin ring accounts for much of the molecule's light absorbance. Found in the thylakoid plate of a plant chloroplast, chlorophyll is a fluorescent substance, which absorbs light of one wavelength and then emit a new and longer wavelength of light. Chlorophyll absorbs light in the violet and blue regions of the visible spectra. If a violet or blue light is shined through a sample of spinach extract, the solution turns red, with the intensity of this colouring being an indication of how much chlorophyll is in the sample.³³ The use of fluorescence techniques is one way the agrochemical industry has analysed and monitored agrochemicals inside a plant, which will be discussed further in Chapter 2.

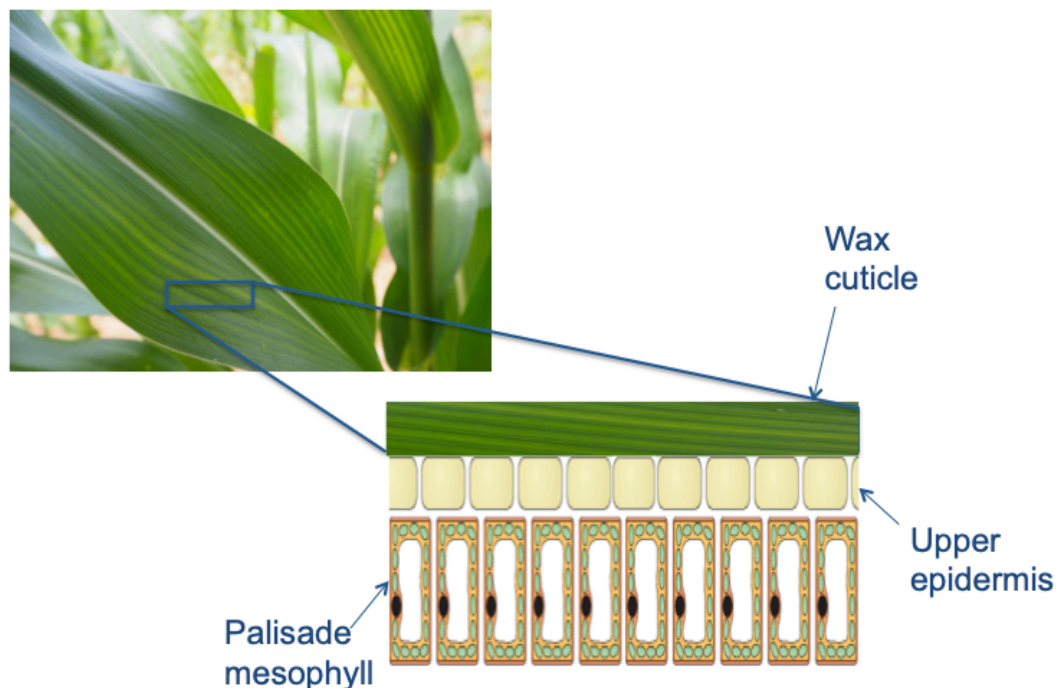


Figure 1.1: Cartoon representation of the layers towards the surface of a corn leaf, an angiosperm that absorbs sprayed agrochemical through its cuticle. The majority of current agrochemicals are designed to enter through the plant cuticle via a spray, or aerosol type method.²⁵ The cuticle is an extracellular hydrophobic layer that covers the aerial epidermis of all land plants, providing protection against desiccation and external environmental stresses.^{24,34} Plant cuticles compose of covalently linked macromolecular cutin scaffolds³⁵, and also contain a variety of organic solvent-soluble lipids (or waxes). Although the cuticle is usually considered independently from the underlying polysaccharide cell wall of the epidermis, the two structures are physically associated and have some overlapping functions.

The plant cuticle presents a physical barrier to pathogens, blocking them from entering the stomata, wounds, or vectors.^{34,35} However, fungal pathogens can

breach and rupture the cuticle using a combination of enzymatic degradation and mechanical breakup.³⁶ The latter is often accomplished by the formation of a swollen appressorium structure (a specialised cell typically in fungi that expands inside a leaf, rupturing it) that extends an infectious peg via turgor pressure.³⁷ While mechanical rupture may be sufficient for cuticle penetration, particularly of thinner cuticles, most fungal pathogens also secrete, a class of small, nonspecific esterases that hydrolyze the cutin polyester and release free cutin monomers, these are called cutinases³⁸. During polymeric cutin hydrolysis, the released cutin monomers can act as elicitors of plant defense responses and are classed as “damage-associated molecular patterns”. At micromolar concentrations, these compounds induce the production of hydrogen peroxide and other defense responses. However, as Boller and Felix published in 2009, the mechanism of plant perception of free cutin monomers is still unknown.³⁹

As mentioned previously, agrochemicals are mostly applied through absorption from a spray. Less likely, but more effectively, agrochemicals can also enter a plant by direct injection to the stem, this method will not be explored in the boundaries of this thesis. The method of diffusion through cuticle wax utilises the movement of chemicals from the surface to the interior of the leaf. To do this, a chemical must pass through the cuticle and continue through the upper epidermis and palisade mesophyll. An initial issue with current pesticides and agrochemicals are their high surface tensions, which provides poor contact with the leaf. This, due to waxy projections and hairs, results in poor efficiency, which will be explored in this chapter.

The use of surfactants and emulsifiers may improve the leaf contact of aqueous spray solutions, and oil-soluble pesticides are combined with a carrier with good leaf-contact properties.^{22,25} The compatibility of pesticide and leaf cuticle heavily relies on the interaction between respective chemical and physical properties. Ergo, the polarity of the cuticle and the pesticide are of considerable importance.

Cuticle polarity increases from the leaf surface toward pectins in cell walls and to the aqueous environment of the cell. Because of this, the outer layer of the cuticle favours non-polar pesticides like 1,1,1-trichloro-2,2-bis(p-chlorophenyl) ethane (DDT) or the long-chain alkyl esters of 2,4-dichloro-phenoxyacetic acid (2,4-D).^{15,40} The inner portion, however, allows passage more readily to polar compounds like 2,4-D, with structure shown in Figure 1.2, and restrict the passage of lipophilic compounds like DDT. Thus, DDT residues in plants are usually surface residues, which can be removed with solvents that remove the outer cuticle.^{15,24} This makes compounds like DDT highly effective agrochemicals. However, DDT began to show negative reactions that led to its eventual withdrawal.

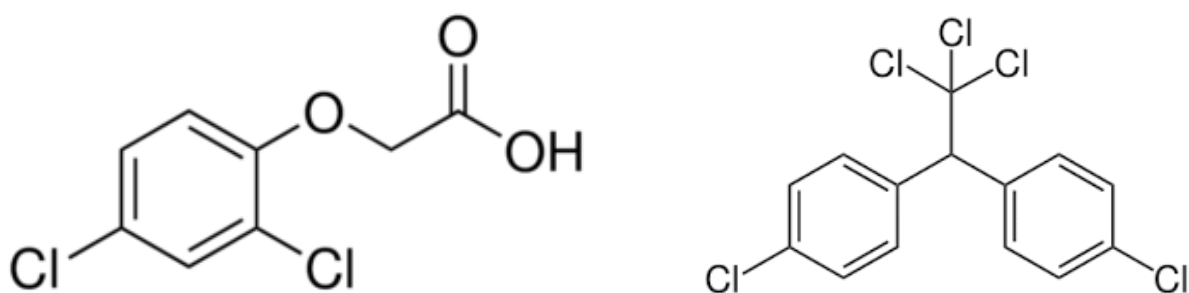


Figure 1.2: Chemical structures of 2,4-D and DDT, respectively.

In order for pesticides to work, they require a balance between absorption and movement through the plant, known as translocation.^{24,41} A major priority for any systemic pesticide is to only kill insects that are harmful to the plant. With

this it becomes essential that a pesticide is able to be translocated and absorbed, allowing it to be taken in by the leaves and roots and be present to kill any pest that consumes any part of the plant. Extensive absorption with no translocation gives ineffective vegetation control for a systemic pesticide.

1.3.2 Plant Pathogens

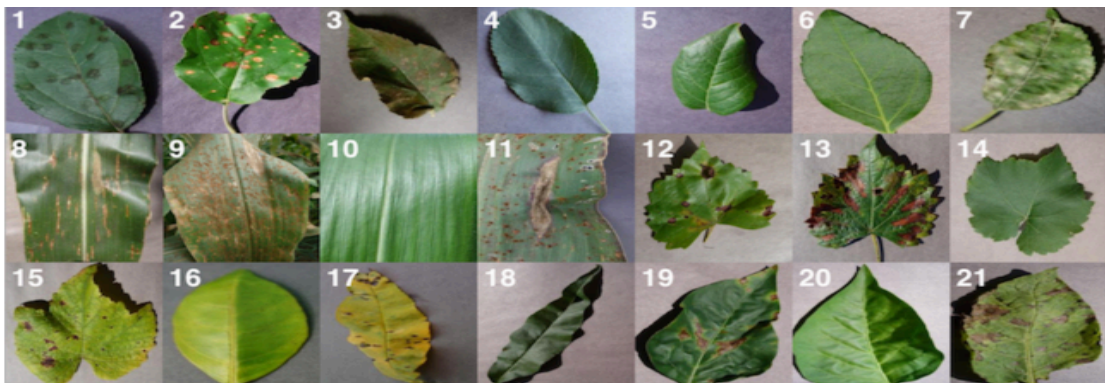
As well as pests contaminating/eating crops, there are many possible plant-killers that agrochemicals are needed for, the majority of which fall into the categories of either fungal or bacterial pathogens.³⁰

Fungal diseases constitute the largest number of plant pathogens and are responsible for a range of serious plant diseases and cause most vegetable and crop diseases.⁴² These diseases can damage a plant by killing or stressing cells and can source from infected seed, soil, crop debris, nearby crops and weeds.^{36,43} The diseases are the most serious cause of crop loss and are very infectious, as fungi can be very easily spread by wind and water splash, and also through the movement of contaminated soil, animals, workers, machinery, tools, seedlings and other plant material.⁴² They enter plants through natural openings such as stomata and through wounds, which are caused by pruning (either by human or animal), harvesting, hail (or other extreme weather), insects, other diseases, and mechanical damage.

Pathogenic bacteria can also cause many serious diseases in crops.⁴¹ They do not penetrate directly into plant tissue, like fungi, but need to enter through wounds or natural plant openings.⁴⁴ Wounds can result from damage by insects, other pathogens, and tools during operations such as pruning and picking.

Bacteria become an issue and multiply when factors are conducive for them to become active and reproduce. Factors such as humidity extremes, crop-overcrowding, poor air circulation, plant stress caused by over-watering, under-watering, or irregular watering, poor soil health, and deficient or excess nutrients all allow bacteria to ruin crop yields.^{43,44}

Bacterial organisms can survive and thrive in soil and crop debris, and in seeds and other plant parts. Weeds can act as reservoirs for bacterial diseases. Bacteria spread in infected seed, propagating material and crop residues, through water splash and wind-driven rain, and on contaminated equipment and workers' hands. Overhead irrigation favours the spread of bacterial diseases. A



visual dataset of different crop diseases can be seen in Figure 1.3, highlights many of the diseases commonly associated with poor plant health, and several avoidable symptoms with good agrochemistry.

Figure 1.3: Example of leaf images with various diseases (1) Apple Scab, *Venturia inaequalis* (2) Apple Black Rot, *Botryosphaeria obtusa* (3) Apple Cedar Rust, *Gymnosporangium juniperi-virginianae* (4) Apple healthy (5) Blueberry healthy (6) Cherry healthy (7) Cherry Powdery Mildew, *Podosphaera clandestine* (8) Corn Gray Leaf Spot, *Cercospora zae-maydis* (9) Corn Common Rust, *Puccinia sorghi* (10) Corn healthy (11) Corn Northern Leaf Blight, *Exserohilum*

turcicum (12) Grape Black Rot, Guignardia bidwellii, (13) Grape Black Measles (Esca), Phaeomoniella aleophilum, Phaeomoniella chlamydospora (14) Grape Healthy (15) Grape Leaf Blight, Pseudocercospora vitis (16) Orange Huanglongbing (Citrus Greening), Candidatus Liberibacter spp. (17) Peach Bacterial Spot, Xanthomonas campestris (18) Peach healthy (19) Bell Pepper Bacterial Spot, Xanthomonas campestris (20) Bell Pepper healthy (21) Potato Early Blight. Adapted and reprinted from Moharty *et al*¹

Chapter 2: A Review of the Background Theory and Current Literature

The literature review in this chapter was compiled into a review paper entitled Advances In Analytical Capability To Power Agrochemical Product Design, published by Outlooks on Pest Management in April 2018.⁴⁵ A copy of this, along with all other publications and presentations are attached in Appendix B.

2.1 Introduction

To put this work into context, one has to consider the theoretical and previous work in this field. As mentioned in Chapter 1, many techniques have been used extensively throughout the agrochemical industry, and as a result there is a large amount of literature available that is beyond the scope of this work. For this thesis, the focus will be on the literature that explores the use of these techniques for their characterisation ability. Table 2 compares the available methods and the following text discusses the pros and cons, referring to previous works.

Multiple techniques are already used in the agrochemical industry to monitor the interactions of agrochemicals with crops, however, none of the current techniques alone can meet the demands of sensitive, non-destructive, high spatial resolution imaging in real time. Results gathered from many countries by the Codex Committee on Pesticide Residues showed the majority of the methods referred to pesticides amenable to gas chromatography (GC) or liquid chromatography (LC).⁴⁶ These methods cover approximately 75% of the compounds in the Codex system and do not satisfy the *in planta* characterisation needs. Other techniques include Time-of-Flight Secondary Ion Mass Spectroscopy (ToF-SIMS), Matrix-assisted laser desorption/ionisation

(MALDI) and autoradiography, plus emerging methods such as spontaneous and coherent Raman scattering.

Technique	Non-invasive/Non-destructive (<i>in planta</i>)	Spatial Resolution	Chemical Label Free	Chemical Specificity	Low Detection Limit	Cost of Use	Real-time	Quantitative
GCMS	✗	Low	✓	High	✓	Moderate	✗	✓
LCMS	✗	Low	✓	High	✓	High	✗	✓
SEM (EDX)	✗	Very high	✓	Low	✓	High	✗	✓
Fluorescent Microscopy	✓	High	✗ *	High [§]	✓	Low	✓	✓
Imaging Mass Spectrometry	✗	Moderate	✓	High	✓	High	✓	✓
Autoradiography	✓	Low	✓	High [§]	✓	Moderate	✓	✓
Spontaneous Raman microscopy	✗ **	High	✓	High	✗	Low	✗	N/A
Coherent Raman Spectroscopy	✓	High	✓	High	✓	High	✓	✓

*Bar specialised cases

**Due to fluorescence of chlorophyll
§ If labelled

Table 2: Comparative table of the advantages and disadvantages of *in planta* characterisation techniques used in the agrochemical industry.

2.2 Mass Spectrometry

Mass spectrometry (MS) in combination with chromatography is the most widely used analytical technique for pesticide residue analysis. MS in combination with chromatography separates all of the components in a sample and provides a

compound-specific output and can provide you with quantitative high chemical specificity, without the use of labels, when measuring agrochemical uptake. However, MS provides only very limited spatio-temporal information, and cannot be used *in planta*. In 2006, Alder *et al* reported a comparative study on the capabilities of mass spectrometry in combination with chromatography for the determination of a multitude of pesticides.⁴⁷ GCMS with electron impact (EI) ionization and the combination of LC with tandem mass spectrometers (LCMS/MS) using electrospray ionization (ESI) are identified as the techniques most often applied in multi-residue methods for pesticides at present with LCMS currently being the most common technique. However, its inability to provide spatial resolution or the ability to monitor compounds *in planta* in a non-destructive manner are major limitations.

ToF-SIMS and MALDI-MS both suffer from similar disadvantages to MS techniques, being destructive and with very limited spatio-temporal information achievable. ToF-SIMS has been used to analyse polymers and biological materials since the late 1960s⁴⁸, whereas MALDI was first reported in 1994.⁴⁹ The predominant method used since then has been MALDI-ToF MS, which has been applied to visualise proteins and peptides, allowing identification of compounds directly on tissue surfaces⁴¹ and distinguishing between low molecular weight proteins in plant matter.⁴¹ The technique proved to be a rapid, accurate and cost effective method of microbial characterisation and identification. With its generated characteristic mass spectral fingerprints it was ideal for strain typing and identification. The conventional technique of MALDI-ToF MS requires the destruction of the specimen under study. However, with many advancements made to MALDI-ToF, the specimen may be partially preserved for further studies. In cases with small mass differences, say different

nucleotides, the technique may not be able to determine the mass accurately. MALDI-ToF is also mostly limited to two dimensions, which is a major limitation for *in planta* imaging.

2.3 Autoradiography

Autoradiography is widely used by the agrochemical industry to visualise the *in planta* distributions of radioisotopically-labelled substances. The technique utilises radioactive nuclei, such as tritium, radioactive phosphorus and carbon, to map the movement of molecules. This allows the systemic distribution of labelled organic molecules such as carbohydrates and proteins to be visualised *in planta*. For example, it has been used to monitor the spreading of the bacterium *Bacillus thuringiensis* within cotton plants, systemically map the translocation and translaminar bioavailability of neonicotinoid insecticides in cabbages⁵⁰ and visualise the uptake and distribution of insecticides, through radish roots⁵¹ and black nightshade⁵² shown in Figure 2.1.

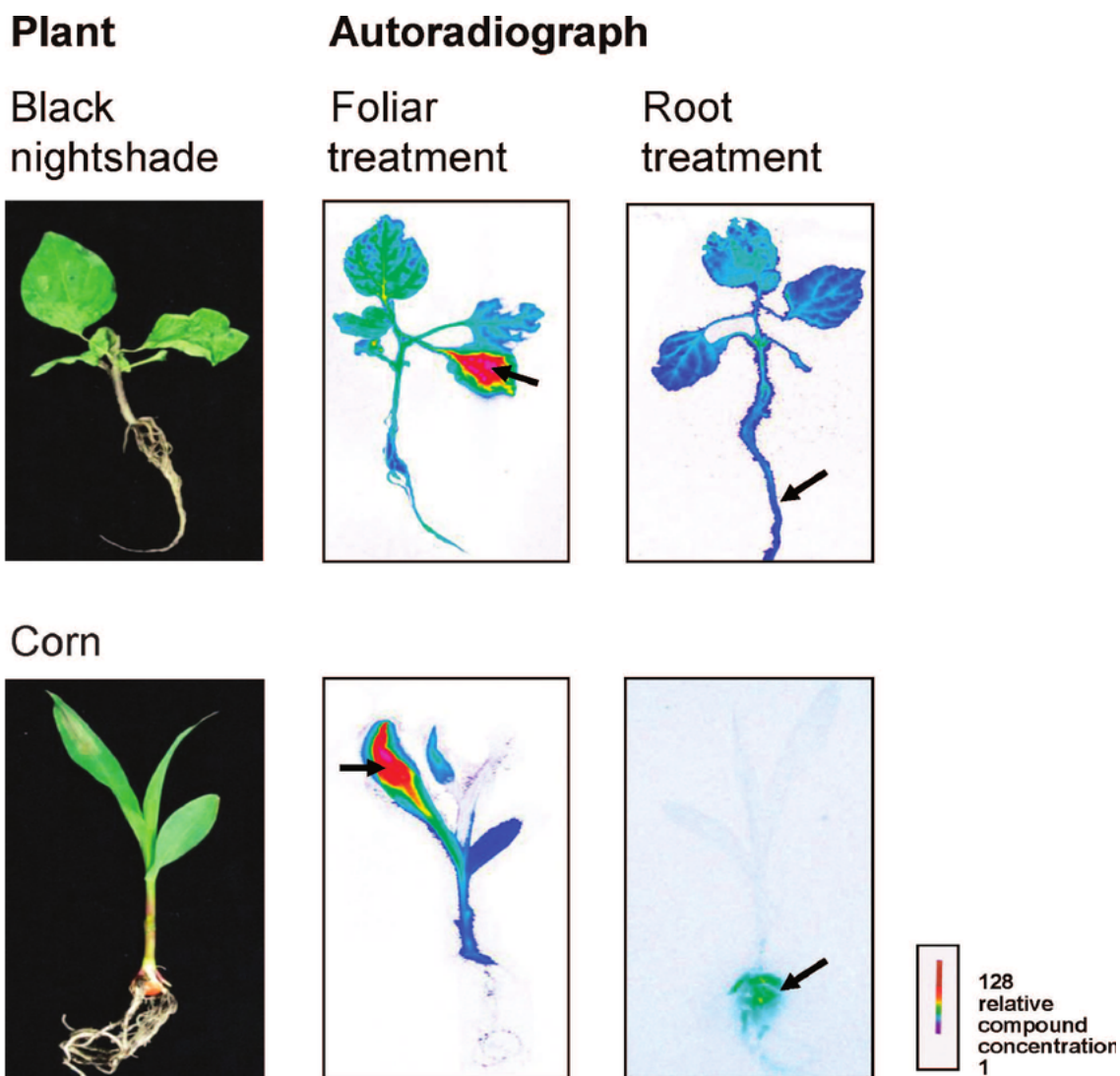


Figure 2.1: Autoradiographs of corn and black nightshade (*Solanum nigrum*) plants, which were foliar and root treated. Reprinted from Grossmann *et al.* 2011

Although autoradiographic imaging of radiolabelled compounds can provide non-destructive information about their systemic distribution, it lacks sufficient spatial resolution to determine their localisation at the cellular scale.

2.4 Scanning Electron Microscopy

Scanning electron microscopy (SEM), with Energy Dispersive X-ray microanalysis (EDX), is a well-known technique in the agrochemical industry. Commonly coupled together, the techniques can provide simultaneously both

topography and elemental composition of a sample with submicron spatial resolution. This technique has been used to detect specific elements in soils and plants and has been used to characterise the distribution pattern of active ingredients on plant surfaces.⁵³ Whilst being one of the most cost-effective methods, SEM-EDX provides low chemical specificity and usually requires a sample to be coated with gold and held under vacuum, meaning real-time *in planta* measurements are impossible, as are measurements of materials remaining on the surface. Another significant limitation is that the spatial localisation and quantification of molecules is only possible when the molecule has at least one distinctive element that does not occur naturally in or on the untreated sample.

2.5 Optical Microscopy

Optical techniques are preferable as they provide non-invasive imaging with a diffraction limited spatial resolution. However, the major challenge in optical imaging is deriving chemically specific contrast from the molecular species of interest. The following sections discuss the various optical techniques that can be used to provide optical contrast of agrochemical AIs.

2.5.1 Fluorescence Microscopy

Fluorescence microscopy has become ubiquitous within modern biology and with the advent of immunolabelling and genetically encoded fluorophores it can be used to provide the spatio-temporal distribution of biomolecules at the cellular scale with a high degree of chemical specificity. Today, fluorescence microscopy has become an essential tool in biology. The application of a diverse range of fluorophores has made it possible to identify cells and sub-microscopic cellular components with a high degree of specificity amid non-fluorescing material. Through the use of multiple fluorescent label, different

probes can identify several target molecules simultaneously. For example in 2004 Liu *et al* showed the transcuticular diffusion of three dyes and the effects of surfactants on the diffusion of these compounds (Figure 2.2).⁵⁴

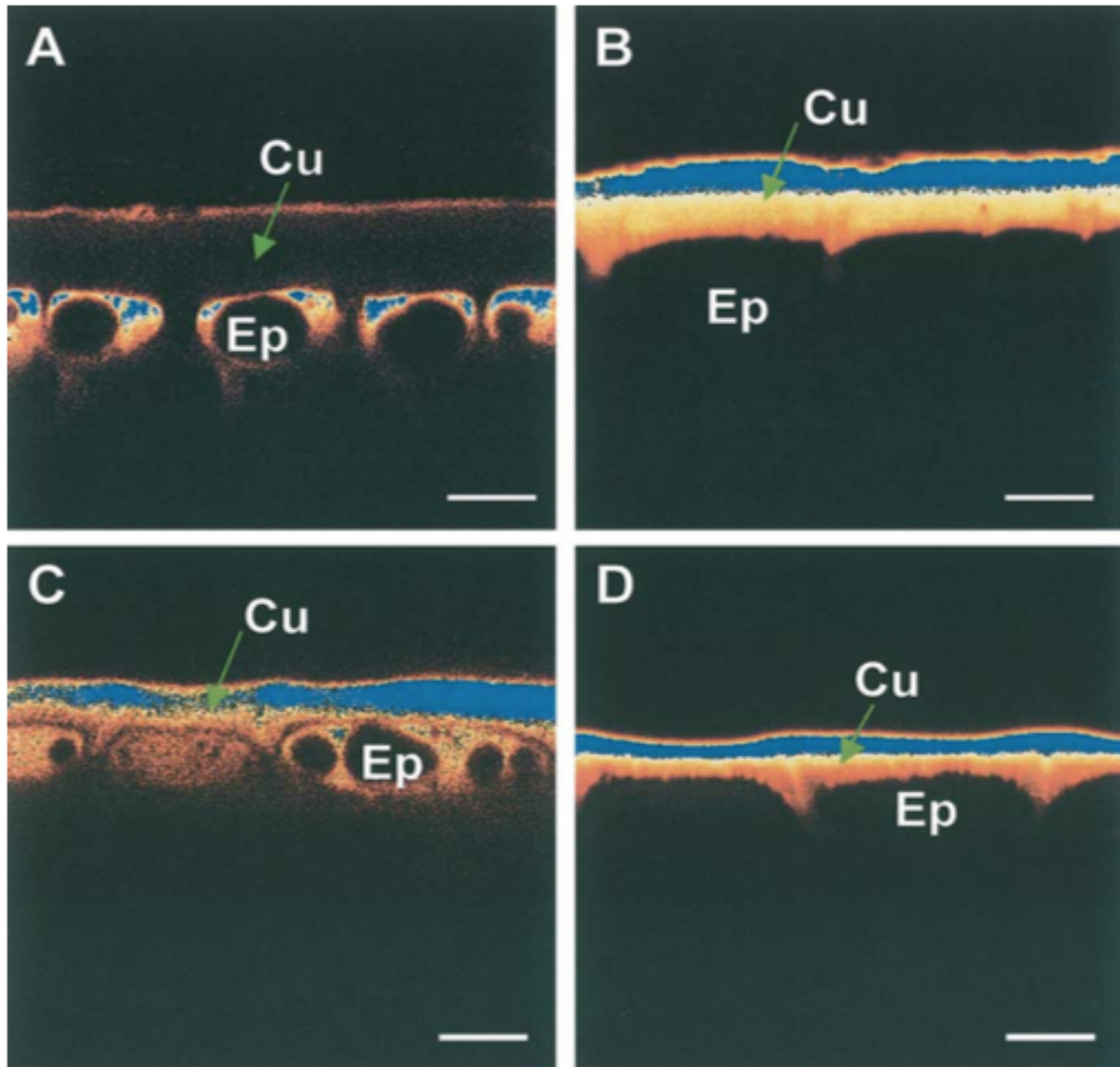


Figure 2.2: Localisation of dyes in apples and peppers. Cu, cuticle; Ep, epidermal cells. Scale bars = 20 μm . Reprinted from Liu, 2004

Despite having several advantages over non-optical techniques, confocal has several limitations such as depth-of-field and a reliance on fluorescent species. Unless a compound exhibits intrinsic fluorescence, it must be labelled with a fluorophore in order to provide contrast. The addition of fluorophores to

macromolecules such as proteins causes very little perturbation, as their molecular weights are typically 10-100-fold greater than that of fluorophores, which are usually of the order of a few hundred Da. However, these fluorophores are in most cases comparable in size of agrochemical active ingredients (AI) and hence drastically alter their transport kinetics. Moreover, the use of these large labels can perturb biological function and may be phytotoxic, which complicates their use for studying long-term biological dynamics.

2.5.2 Raman Spectroscopy

Optical techniques based on vibrational spectroscopy provide *in situ* chemical analysis derived from the vibrational frequencies of molecular bonds within a sample. However, due to water absorption and the intrinsically low spatial resolution associated with the long infrared wavelengths required to excite molecular vibrations directly, infrared absorption techniques have limited value for bio-imaging. However, Raman scattering, provides analysis of IR vibrational frequencies by examining the inelastic scattering of visible (or near IR) light. The Raman scattered light is frequency-shifted with respect to the incident light by discrete amounts which correspond to molecular vibrational frequencies. The spectrum of Raman scattered light excited by a single incident wavelength consists of a series of peaks that correspond to the molecular vibrational frequencies. This can be regarded as a chemical fingerprint of a sample and holds a wealth of information regarding chemical composition and conformation.

Modern Raman spectroscopy techniques are rapidly becoming recognised as valuable analytical tools for agrochemical R&D, being utilised to determine and identify various pesticides in crops. For example, both Liu and Liu and Zhang *et al* demonstrated the characteristic peaks of standard pesticide spectra could

be identified on the surface of fruits and vegetables.^{55,56} In addition, enhanced systems, such as Surface-Enhanced Raman spectroscopy (SERS) are even more sensitive and thus can be used to produce protocols for environmental particulates analysis with the goal to monitor exposure to organic pollutants and quickly identify health risks and environmental contaminants.⁵⁷

However, to understand further the theory behind Raman, it is important to first look at its beginnings and early work, The Raman Effect was discovered by C.V. Raman in 1921, to establish reason as to why the sea was blue. Seven years later, the effect was studied and finally documented in liquids, again by C.V. Raman and K.S. Krishnan, shortly followed by its establishment in crystals by G. Landsberg and L. Mandelstam. Raman scattering is described as the effect by which incident monochromatic light either gains or loses energy to the vibrations of molecules, causing a measurable shift in frequency of the scattered light relative to the incident light. Raman scattering is a two-photon event, in which an incident photon with a high enough energy for a vibrational transition, but lower than that required for an electronic transition, promotes a molecule to a virtual state. The molecule then returns either to the original state, emitting a photon with the same frequency as the incident photon, known as Rayleigh scattering, or, if there is a change in the polarity of the molecule, its energy changes and therefore its molecular vibrational state.

We can use Hooke's Law to describe this behaviour. Under Hooke's Law, the vibration of these individual bonds within diatomic molecules can be described as:

$$\omega_m = \frac{1}{2\pi} \sqrt{\frac{K}{\mu}} \quad \text{- Eq. 1}$$

Considering the atoms and bonds between them as springs with masses, where K refers to the spring constant of the bond, and μ is the reduced or inertial mass, which is inversely proportional to the bond strength, ω_m , the molecular vibration. μ can be described as:

$$\mu = \frac{m_1 m_2}{m_1 + m_2} \quad \text{- Eq. 2}$$

Where m_1 and m_2 are the masses of the atoms, which shows that both the atoms and bonds provide characteristic molecular vibrations. Raman active molecules show symmetric vibrations, which cause the largest distortion to the electron cloud. Whereas polar bonds and asymmetric vibrations allow IR absorptions, caused by a dipole change, Raman peaks appear proportional to the polarity of the molecule. For example, the IR spectra for CO_2 would show a peak from asymmetric stretching, with one oxygen atom moving away from the carbon atom, and generating a net change in dipole moment. However, we would not see a peak for the symmetric stretching, as both oxygen atoms are moving away from the carbon, cancelling the net dipole moment. Raman scattering, on the other hand, does provide us with information about molecular symmetry. In order to be Raman active there must be a change in the size, shape or orientation of the electron cloud that surrounds the molecule. This change occurs in symmetric vibrations alone, which are outlined in Figure 3.1,

along with other typical bond vibrations in molecules, including symmetric stretching, in-plane rocking and out-of-plane twisting and wagging.

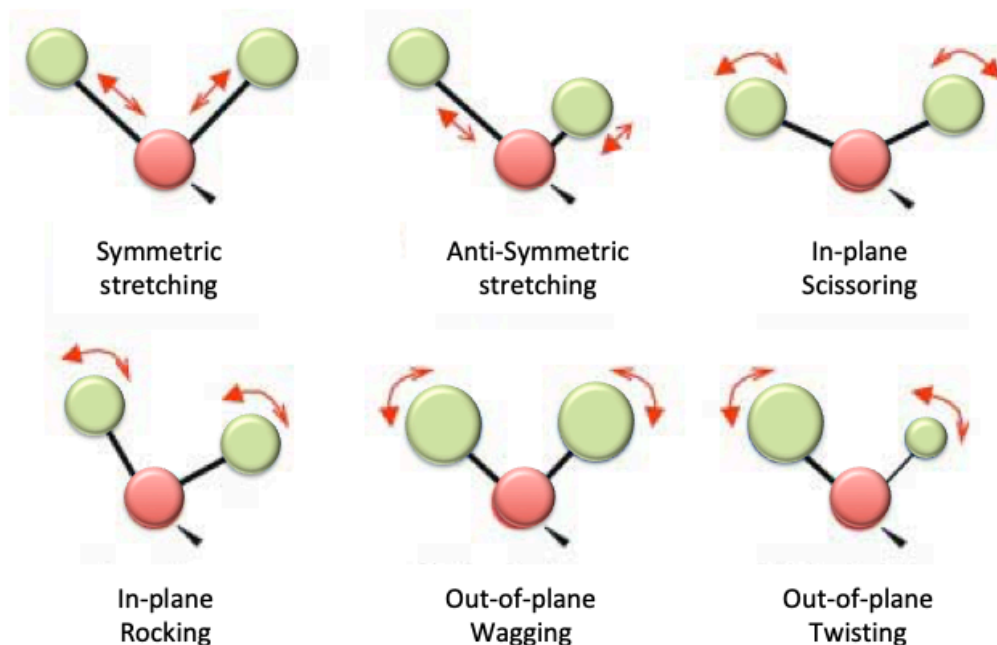


Figure 2.3: Six types of vibrational modes

Unfortunately, Raman scattering is an extremely weak effect and typical photon conversion efficiencies in biological materials are of the order of 1 in 10^{58} . This severely limits the application of Raman for studying living systems since long acquisition times (100 ms to 1 s per pixel) at relatively high excitation powers (several hundred mW) are required to image most biomolecules with sufficient sensitivity. This lack of sensitivity is compounded by its susceptibility to interference from autofluorescence. The Stokes-shifted Raman scattered light is overwhelmed by fluorescent emissions, which virtually prohibits its application in all but a few applications in living plant tissues.

When interacting with a molecule, monochromatic light is either absorbed or scattered depending on the energy of the light. If the light has a dissimilar

energy to the difference between the ground and excited states of the molecule it's interacting with, it will scatter. Raman techniques are an example of this, being an inelastic scattering process. This effect, known as the Raman effect, is a result of a variation in the polarity of a molecule due to molecular vibrations, transferring energy either from incident photon to molecule, or the molecule to the photon.

Broadly, Raman techniques can be categorised as either linear or non-linear. In spontaneous Raman scattering, the signal intensity is directly proportional to the intensity of the incident beam, making it a linear technique. Coherent Raman scattering techniques, however, are non-linear processes due to their higher order dependence on the incident light intensity. This, amongst many other factors, are responsible for Raman signal enhancement of $\times 10^6$ over spontaneous Raman, allowing rapid imaging. This chapter outlines and explains the background theory further behind the techniques used in this thesis.

2.5.4 Coherent Raman Spectroscopy

Fortunately, far stronger Raman signals can be obtained using an emerging Raman based imaging technique known as Coherent Raman scattering (CRS).⁵⁹ CRS achieves signal enhancement by focusing the excitation energy onto a specific Raman mode of the biomolecules of interest. A pump and Stokes beam, with frequencies ω_p and ω_s respectively, are incident upon the sample with the frequency difference $\omega_p - \omega_s$ chosen to match the molecular vibrational frequency of interest. Under this resonant condition, bonds are coherently driven by the excitation fields and a strong nonlinear coherent Raman signal is produced. Due to the nonlinear dependence of the signal on excitation intensity, further enhancement can be achieved by excitation with ultra-short light pulses, which deliver extremely high peak intensities with

modest average powers that are comparable with those routinely used in confocal microscopy. Optimal conditions for CRS require pulses of a few picoseconds in duration that have sufficient intensity to excite CRS without having bandwidths that extend beyond the line width of typical Raman bands.

When applied in microscopy format, CRS benefits from the nonlinear nature of the process which confines the signal to a sub-micron focus that can be scanned in space, allowing three-dimensional mapping of biomolecules with sub-micron resolution. CRS microscopy has particular advantages for bio-imaging: chemically specific contrast is derived from the vibrational signature of endogenous biomolecules within the sample, negating the need for extraneous labels/stains; low energy near-IR excitation wavelengths can be employed which reduce photodamage and increase depth penetration into scattering tissues; since the CRS process does not leave sample molecules in an excited state it does not suffer from photobleaching and can be used for long term time series studies.

Coherent Raman scattering microscopy may be achieved by detecting either coherent anti-Stokes Raman scattering (CARS) or stimulated Raman scattering (SRS).

2.5.4.1 Coherent anti-Stokes Raman scattering (CARS)

CARS is the first coherent Raman technique to be discussed. A nonlinear process that typically produces signal intensities more than 10^6 of that of spontaneous Raman.⁶⁶ This technique was first demonstrated by Maker and Terhune (1965), when they showed the anti-Stokes signal resonantly enhances when the beat frequency, $\omega_p - \omega_s$ (where ω_p is the pump photon frequency, and ω_s is the Stokes photon frequency), matches a Raman active vibration.⁶⁷

CARS is a Four-Wave Mixing (FWM) process, which has three electromagnetic fields: a pump field, the Stokes field and a Probe field. All of these interact on a sample to produce a fourth, the anti-Stokes field. The CARS principles are described in Figure 3.2, showing a pump photon excited an electron to a virtual state and a Stokes photon is stimulated emitted from this state, simultaneously with a probe photon (of frequency ω_{pr}) is absorbed to another virtual state. This whole interaction therefore emits a photon of frequency

$$\omega_{as} = \omega_p - \omega_s + \omega_{pr} \quad \text{-Eq3}$$

and is the resulting signal we are interested in. The pump and probe fields are provided by the same laser source, for the experiments described in this thesis.

When comparing the process to spontaneous Raman spectroscopy, one can note the similarities between the two, but for CARS, the Stokes process originates from the applied laser field, rather than being spontaneous. The several order magnitude enhancement for CARS comes from the actively driven nuclear vibrations, provided by two incident electric fields. In spontaneous Raman, the incident field induces a dipole moment that oscillates with identical frequency to that of the electric field. However, when two electric fields interact with a molecule, they actively oscillate the molecule at the beat frequency of the

two fields, providing time-varied force, and in turn oscillates the nuclear mode. For CARS signal to occur, both pump and Stokes beams must be overlapping in time, in order to get coherent interferences.

CARS has a non-linear background, which is the main disadvantage of this microscopy. However, CARS provides many advantages, since CARS induces signal from vibrational signal there is no photobleaching effect possible, there is no need for pinholes, and finally, since we record the Anti-Stoke signal, the light is blue-shifted which prevents single-photon fluorescence pollution. These benefits have made CARS become an increasingly used microscopy tool over the last decade, with the improvement of illumination collimation with the use of infrared picosecond lasers.

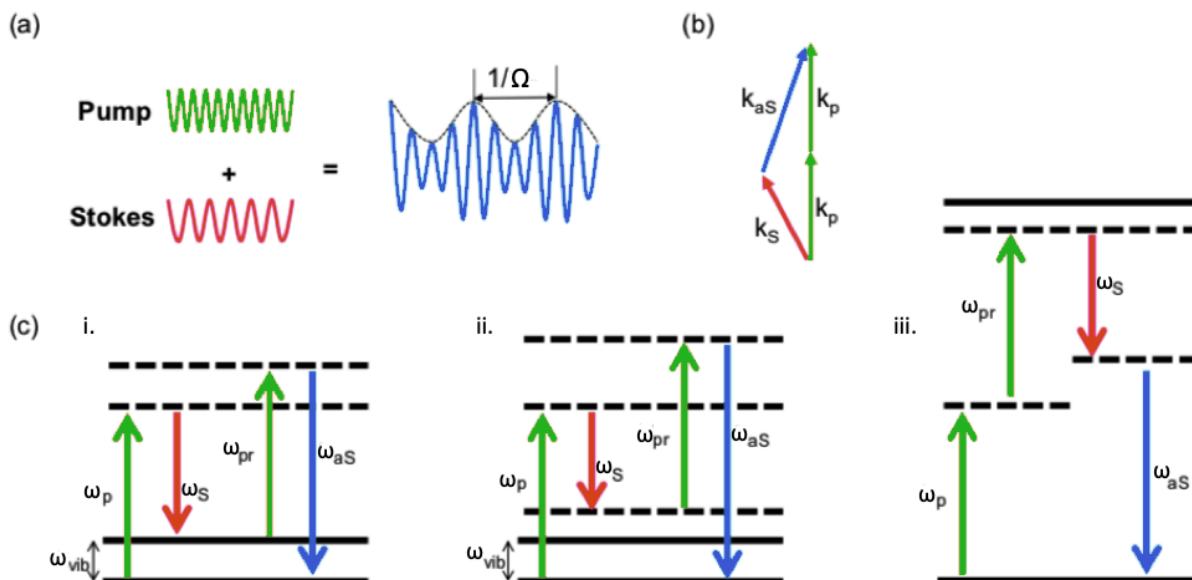


Figure 2.4: Energy diagrams for the CARS process: (a) Schematic of the pump and probe beam interacting together: the envelope of the interferences beating at the frequency $1/\Omega$, (b) Schematic of the phase matching conditions for the momentum, k_p is used for pump and probe as it is usually the same beam used for both, (c) i. ii. and iii. are Jablonski diagrams contributing to the CARS signal: (i) Resonant CARS, (ii) and (iii) non-resonant CARS due to electronic contribution and other molecule respectively.

In Figure 2.4, we show the CARS signal generation energy diagram, with c) i), ii) and iii) showing the resonant, non-resonant and two-photon contributions respectively. This thesis works specifically with plant materials, which contain a large amount of chlorophyll, which limit current analytical methods due to a large contribution from two-photon, and thus saturating images.

However, this can be limited. The CARS signal generated consists of three different frequencies (non-resonant, resonant and combined) which can either destructively or constructively interfere depending on the relative phase between the paths, which is dictated by the phase differences between both the Stokes frequencies and the probe frequencies. By using epi-CARS over forward

CARS, we can use this to destructively interfere with the non-resonant background, allowing a strong resonance signal.

2.5.4.2 Stimulated Raman Scattering (SRS)

SRS can be simply described as a two-photon process, with a series of schematics that can summarise it shown below, in Figure 2.5.

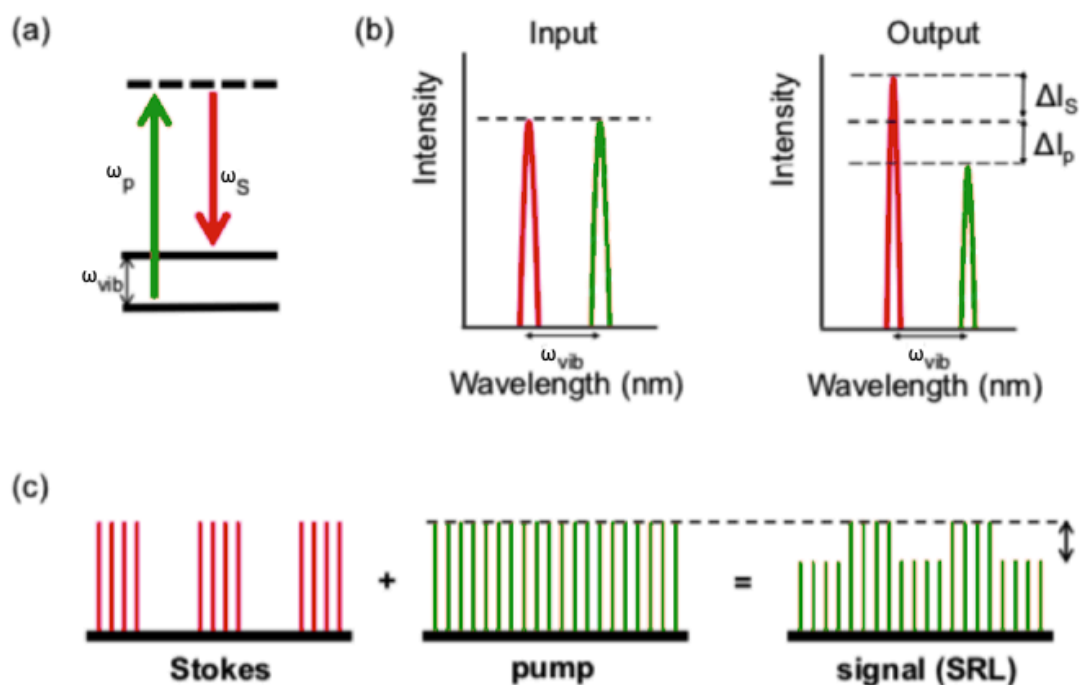


Figure 2.5: Schematic of the SRS process. (a) Energy level diagram for the SRS process. (b) The difference in wavelengths of the input laser beams match that of a Raman vibration, the output is a loss in the pump beam and a gain in the Stokes beam. (c) The Stokes beam is modulated, a small loss in the pump beam is detected, using highly sensitive lock-in detection.

It shows an absorbed pump photon, ω_p , exciting the molecule to a new virtual energy level, allowing the emission of a new photon, ω_s , returning to the lower

level, with the difference between these states of the molecule matching the molecules Raman vibrational mode. This process is almost identical to that of spontaneous Raman, however, differs due to this emission being stimulated, rather than spontaneous.

Again, SRS requires the pump and Stokes beams to be overlapped in time on the sample and the SRS signal arising as previously described for CARS, allowing these two processes to occur simultaneously. SRS, albeit similar to the CARS process, is detected differently. SRS is detected by measuring a minute energy transfer, which causes a measurable change in amplitude of both pump and Stokes beams. As can be seen in the figure, the pump photon is absorbed by the molecules as the Stokes photon is emitted, resulting in a negative energy transfer of the pump beam, known as stimulated Raman loss (SRL) and a positive energy transfer for the Stokes beam, stimulated Raman gain (SRG).

To detect the pump beam, the SRS signal is modulated at a known frequency as SRS can only occur when both beams overlap in time and space. The loss in this beam occurs at the same frequency as the modulated Stokes beam. This intensity change in the pump beam is what we measure, as our SRS signal. In order to measure this after a sample, a long-pass filter blocks the Stokes beam, allowing the small signal to enter a highly sensitive lock-in amplifier, which extracts the SRS signal from the background signal and allows amplification of our signal.

SRS, unlike CARS, has a resonant background, as the signal is produced only when the difference between pump and Stokes beams match that of a specific

Raman vibrational mode. However, it is worth pointing out that SRS is not completely background free, as it can be affected by two-photon absorption and other nonlinear interactions.

2.5.4.3 A Comparison between CARS and SRS

CARS uses the anti-Stokes signal generated at frequency $\omega_{as} = 2\omega_p - \omega_s$, which, by using filters, is spectrally isolated from the pump and Stokes beams, and its intensity used to map the location of biomolecules of interest. The anti-Stokes (blue) shift of the emission with respect to the excitation wavelengths makes CARS more resistant to interference from sample autofluorescence than spontaneous Raman. However, for highly fluorescent samples such as plant tissues, the usually weak two-photon fluorescence (also blue-shifted with respect to the excitation wavelengths) overlaps and overwhelms the CARS signal. SRS relies on detecting subtle changes in the intensities of the excitation fields that occur by virtue of stimulated excitation.⁶⁰ When the difference frequency, $\omega_p - \omega_s$, matches a molecular vibrational frequency the intensity of the Stokes beam, I_s , experiences a gain, ΔI_s , while the intensity of the pump beam, I_p , experiences a loss, ΔI_p . The intensity transfer from the pump to the Stokes beam only occurs when both beams are incident upon the sample and can be detected with high sensitivity using modulation transfer detection. Modulating the intensity of the Stokes beam modulates the SRS process and hence transfers an intensity modulation onto the pump beam. The amplitude of the transferred intensity modulation is directly proportional to the concentration of target molecules and by modulating at frequencies above laser noise (>1 MHz) can be detected with a lock-in amplifier with great sensitivity (1 in 10⁶ photons).

CRS's high spatio-temporal resolution has had a huge impact in biomedical research and has already been demonstrated to have adequate sensitivity to allow the visualisation of various tissues like skin⁵⁸ and made significant advances in the field of cancer diagnosis.⁶¹ In addition, CRS has been used to image the diffusion of low molecular weight drug molecules into human skin and nails.^{62,63} These measurements have similarities to that of an AI diffusing across a cuticle boundary and hence indicate that CRS has potential to overcome the limitations of fluorescence. However, strong two-photon absorption in heavily pigmented leaves have prevented *in planta* applications of CRS.

More recently, Mansfield *et al.* developed an SRS detection technique that overcomes the effect of two-photon absorption, combining structural imaging with *in situ* chemical analysis of plant materials, providing real-time subcellular spatial resolution *in planta*, shown in Figure 2.6.⁶⁴ Following this, Littlejohn *et al.*, showed that SRS can be used to acquire in-vivo, 3D images of cuticles, thanks to SRS's low autofluorescence compared to CARS.⁶⁵

Both CARS and SRS show a lot of promise in the agrochemical area, enabling real-time high spatial resolution imaging technique with high chemical specificity. CRS techniques have been shown to provide quantitative information, whilst remain non-destructive *in planta*. These advances could lead to CRS being more heavily utilised as next generation techniques for agrochemical development and research, particularly in the modelling and measurement of *in situ* diffusion pathways.

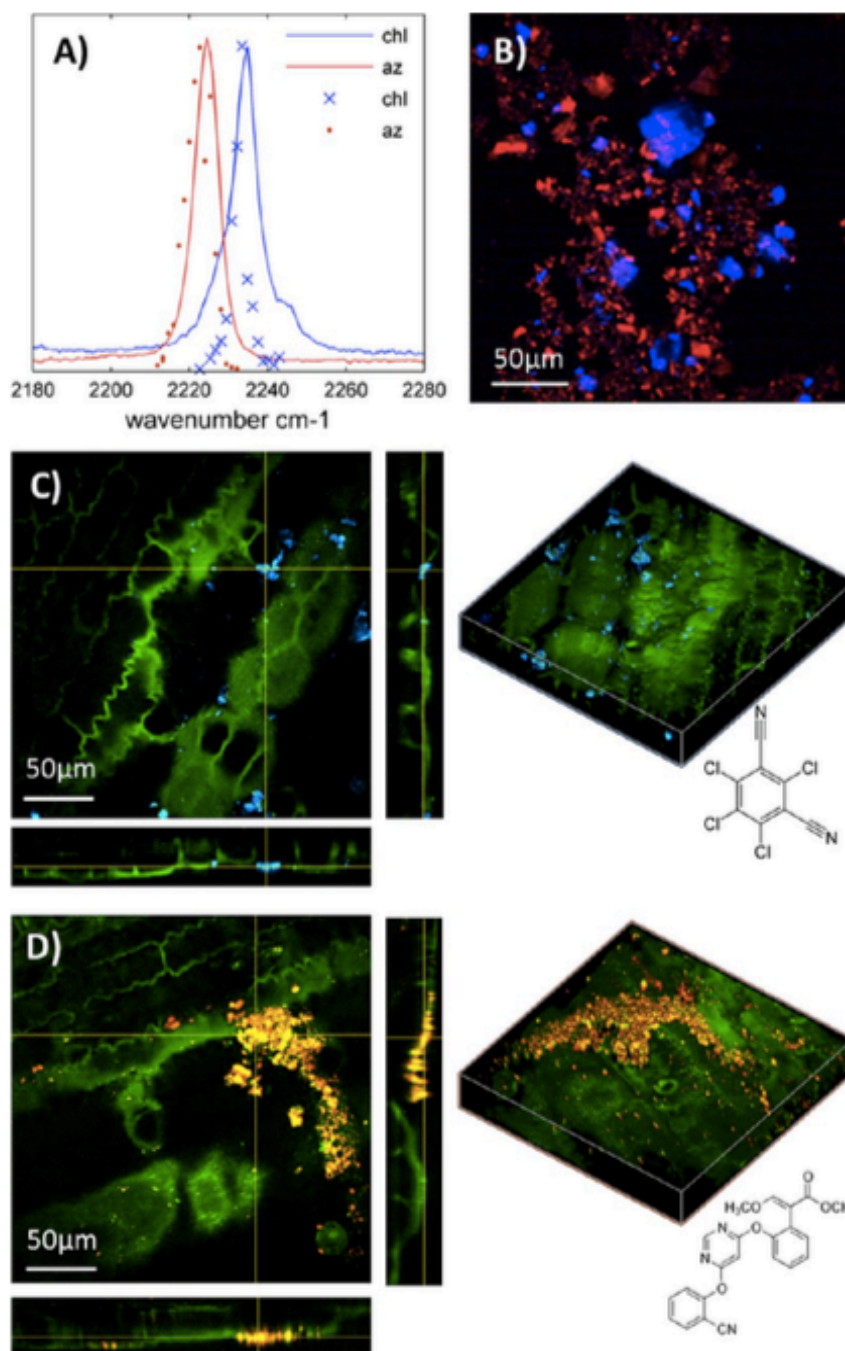


Figure 2.6: Two fungicides azoxystrobin (az) and chlorothalonil (chl) imaged on maize leaves. (A) SRL and spontaneous Raman at C≡N bond (B) SRL image of a mixture of AZ and chl (C) chl distribution on maize (D) az distribution on maize leaf. Reprinted from Mansfield *et al.* (2013)

2.6 Diffusion

While spray application of agrochemicals is known to be effective, inefficiencies arise during a sprays' deposition, and its' subsequent retention on a leaf surface. Also, challenges arise for a systemic pesticides' penetration and translocation, mentioned in the previous chapter. To this order, enhancing the efficacy of agrochemicals has many benefits. Discovering attributes that increase the penetration of agrochemicals can enhance efficacy and reduce the amount of active ingredient required lower the spray volume required, lead to a much more cost-effective process. With the plant cuticle being a rate-limiting barrier in foliar penetration, it is essential to ensure extensive research has been performed to investigate the factors involved in the mass transport of chemical compounds across the plant cuticle. As such, many of these mechanisms, that influence penetration, are still unknown and the differ greatly between species.

Diffusion, derived from the Latin word *diffundere* meaning to spread out, is a mass transport phenomenon, which plays a major part in many processes. Brownian motion, the well-known never-ending movement of particles in suspension in a fluid describes a random walk of microscopic particles within a fluid. Interestingly, this motion has allowed the rationalization of countless natural facts such as disease spread, dissemination of pollutants, as well as a deep insight into the workings of NMR spectroscopy. Inside this thesis, I use it to rationalise the transport of agrochemicals into a plant. It is essential to understand diffusion theories we can apply to study the mathematics of diffusion and the influences of varying microstructure has.

2.7 Fickian Diffusion

Fickian diffusion is commonly used to describe most molecular transport, for simplicity assumed in one singular direction. This occurs in a series of local and random steps, however the existence of a gradient imposes an overall directional trend.

Fick's first law can be defined as steady state diffusion, meaning the diffusion flux does not change over time, and thus the concentration profile will be linear, when plotted as a function of position in sample. The concentration gradient, therefore, will correspond graphically following the equation:

$$\frac{dC}{dx} = \frac{C_A - C_B}{x_A - x_B} \quad \text{-Eq. 4}$$

With C being the concentration of the diffusing species, and x being the position within the sample.

Fick's first law states that the diffusion flux along a given direction is proportional to this gradient, which is often referred to as the driving force in diffusion.

Most commonly, Fick's first law is shown as follows:

$$J = -D \frac{dC}{dx} \quad \text{-Eq. 5}$$

Where J is the diffusion flux, which is the amount of substance in a given area at a given time, D representing the diffusivity, C being the concentration of the diffusing species and x being the position within the sample.

In many situations, however, the concentration gradient changes with time. Fick's second law describes diffusion with a concentration change with respect

to time. It can be derived from Fick's first law and the law of mass conservation and can be described as the following differential equation:

$$\frac{\partial C}{\partial t} = \frac{\partial}{\partial x} \left(D \frac{\partial C}{\partial x} \right) = D \frac{\partial^2 C}{\partial x^2} \quad \text{-Eq. 6}$$

Where C is the concentration, dependent on location (x) and time (t), and D is the diffusion coefficient.

As a fingerprint for Fickian diffusion, the following observations and assumptions can be made towards the diffusion of agrochemical agents within wax:

- During the experiment, there is a constant source of agrochemical agent on the wax surface.
- Furthermore, initially, there is no agrochemical agent in the wax.
- And, lastly, the wax can be considered infinitely thick such that no chemical diffuses all the way through during the observation period.

Therefore, an analytical solution to Fick's 2nd law can then predict SRS profiles to evolve as a function of time and position according to the following expression:

$$\frac{S}{S_{z=0}} = 1 - \operatorname{erf} \left(\frac{z}{2(D_i t)^{0.5}} \right) \quad \text{-Eq. 7}$$

In which D_i shows constant diffusivity, z is the distance diffused, and S is the output signal.

2.8 Non-Fickian Diffusion

However, on the contrary to Fickian law, if the rate of penetrant diffusion is of the same order, or that of concentration independence, Fick's law does not represent an accurate description for the phenomenon. This can be explained since the diffusing penetrant has caused a deformation, which induces a stress

that interacts with the Brownian motion of the fluid molecules. With this explanation in mind, there are many studies proposing diffusion models based on a modified flux resulting from the sum of a Fickian flux and a non Fickian flux:

$$\frac{\partial \sigma}{\partial t} = -\nabla (J_{NF}(C) + J_{NF}(\sigma)) \quad \text{-Eq. 8}$$

Where C stands for the concentration of the penetrant and σ represents the stress.

2.9 Summary

The agrochemical industry would benefit from a non-destructive, real-time characterisation technique with high chemical selectivity and high spatial resolution. Although many techniques meet some of these requirements, currently only CRS enables all to be met by a single measurement. The use of CRS techniques such as CARS and SRS enables the monitoring and imaging of active ingredients *in planta*, at video-rate speed without the use of potentially interfering labels and could help guide the development of improved agrochemical formulations.

In this chapter I further highlighted many disadvantages of current techniques used in the agrochemical industry. Since the work undertaken herein is concerned with enhancing the application of Raman techniques in agrochemistry, it was also pertinent to consider the theory of diffusion and the Raman Effect. Alongside this, the chapter explored diffusion theories relevant to this work, and the modelling which will aid the future of the agrochemical industry.

Chapter 3: Instrumentation

3.1 Introduction

As the previous chapter outlined the theory and the origins of the techniques used in this thesis, this chapter will provide description and experimental protocol used throughout to measure signals. The more heavily used systems, Raman and CRS, include detailed descriptions of the detection methods used for each varying experiment.

3.2 Spontaneous Raman Spectroscopy

The Raman Spectroscopy in this thesis was performed using a Renishaw RM1000 Raman micro-spectrometer, that utilised both 785 nm and 830 nm continuous laser sources. The 785 nm laser source, with 1200 line/mm grating provides spectral resolution of 1 cm^{-1} . For approximately the same spectral resolution when using the 830 nm laser source, a doubled grating of 2400 cm^{-1} is required. The Renishaw v1.2 WiRE software controls all spectral acquisition parameters including the illumination power, scan speed and number of acquisitions. The micro-spectrometer also has a variety of objectives equipped: 5x/0.12NA, 20x/0.40NA, 40x/0.55NA and 50x/0.75NA. Prior to each experiment, the system was calibrated with a silicon sample. This is well known for showing a singular strong peak at 521 cm^{-1} and is commonly used as a reference.

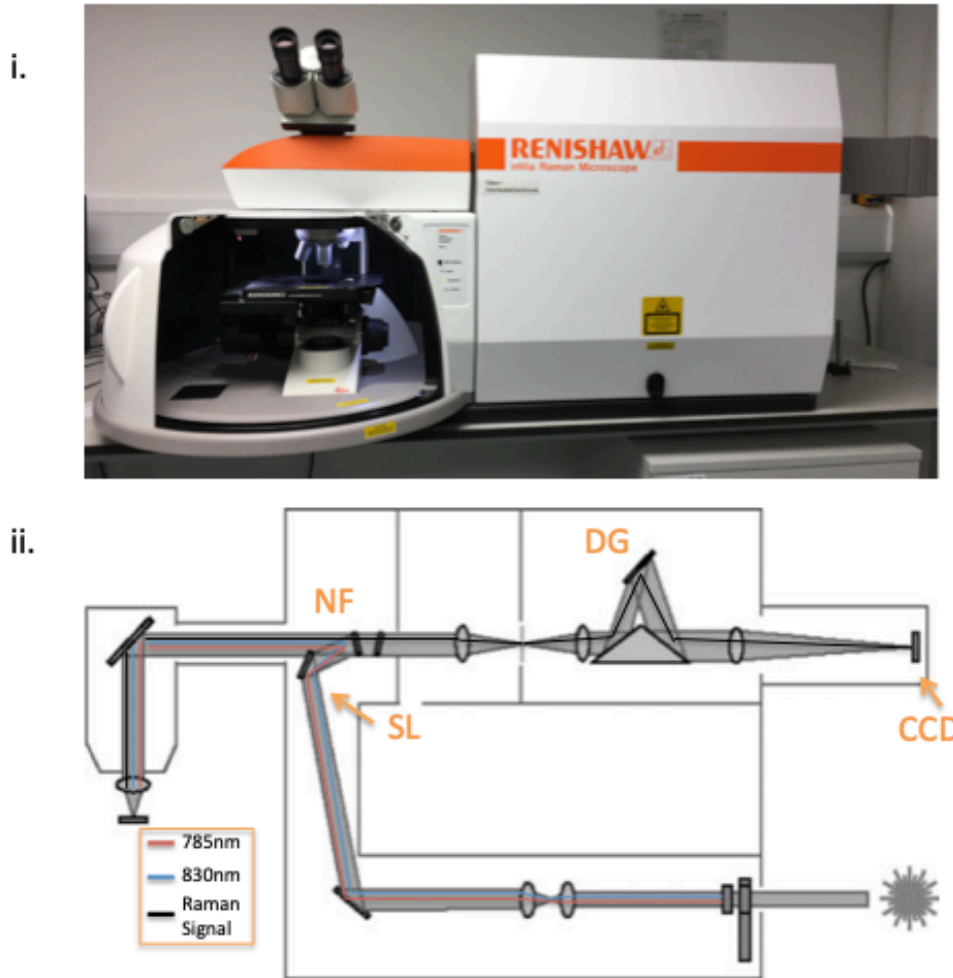


Figure 3.1: i. Renishaw InVia system for spontaneous Raman measurements, and ii. Schematic showing the various components that make up the spectrometer and the beam paths for the 785/830 nm lasers and resulting Raman signal [DG: diffraction grating, NF: notch filter, SL: streamline lens].

Schematic adapted from Sands *et al*²

3.3 Coherent Raman Spectroscopy (CRS)

SRS microscopy was performed using a custom-built imaging system based on a commercial laser scanning microscope and a picosecond laser. The laser source consisted of a picosecond mode-locked fiber laser (aeroPULSE, NKT Photonics) providing 2 ps pulses at 1032 nm which were frequency-doubled to pump an optical parametric oscillator (OPO) which provide a tuneable signal

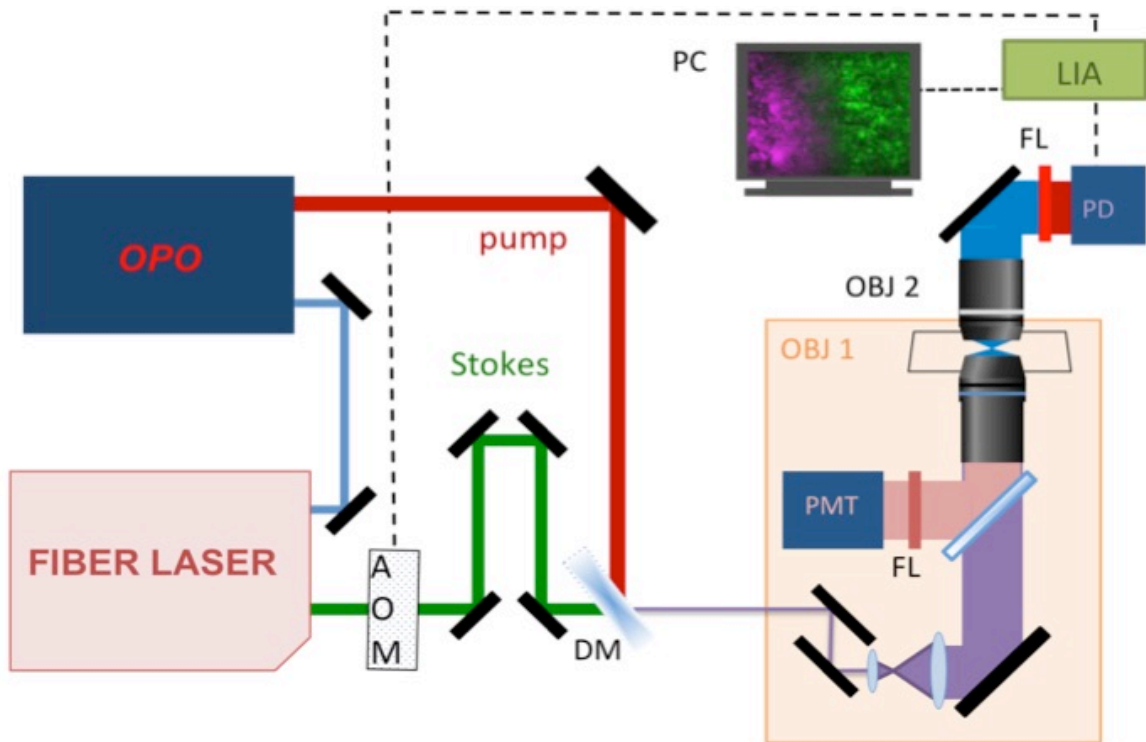
beam tuneable from 690 to 990 nm which served as the Stokes beam. In the optical setup shown in Figure 3.2 (i), pump and Stokes beams with frequencies ω_p and ω_s , respectively, are incident upon the sample with the frequency difference $\omega_p - \omega_s$ chosen to match the molecular vibrational frequency (Ω) of interest as illustrated in the energy diagram.

The Stokes beam was modulated at 8.25 MHz by using an acoustic optical modulator (AOMO 3080-122, Crystal Technology) and 80 MHz driver (AODR 1080AF-A1F0-1.0, Crystal Technology). All imaging was carried out on a modified confocal laser scan unit (Fluoview 300, Olympus) and an inverted microscope (IX71, Olympus). The light was focused onto the sample using a 60 \times NA1.2 water immersion microscope objective (UPlanSApo, Olympus). The pump and Stokes laser powers on the sample were controlled by a variable alternator for 6-12 mW. The forward propagated light was collected using a 100 \times NA1.4 oil immersion microscope objective (UPlanSApo, Olympus), and SRS was detected in the forward direction using a Si photodiode (FDS 1010, Thorlabs) with a 70 V reverse bias.

For stimulated Raman loss (SRL) imaging, the Stokes beam was blocked with a band-pass filter (CARS 890/220 nm, Chroma Technologies) and the pump beam was detected. To suppress the strong signal due to the laser pulsing at 76 MHz, the output voltage was filtered by a low pass filter (BLP-21.4+, Mini-Circuits) and then terminated by a 50 Ω resistor. The photodiode was connected to a radio frequency lock-in amplifier (SR844, Stanford Research Systems) referenced to the AOM driver. A 20 μ s integration time was chosen and images generated by recording the X output on the lock-in amplifier, and

this resulted in a 12 second frame rate of 512×512 pixels images. Image acquisition and processing were performed using ScanImage (Vidrio Technologies) and Fiji (National Institute of Health, NIH, open source software), respectively. For the SRS, spectral acquisition regions of interest were acquired as the OPO was sequentially tuned to provide pump wavelengths, giving values of $\omega_p - \omega_s$ over the spectral range $2200 - 2250 \text{ cm}^{-1}$. Intensity variations of the OPO signal were corrected by normalising each data point against the OPO signal intensity, which was recorded with a PIN photodiode. The linear power dependence of SRS signal on pump beam intensity allows compensation by straightforward linear normalisation.

(i)



(ii)

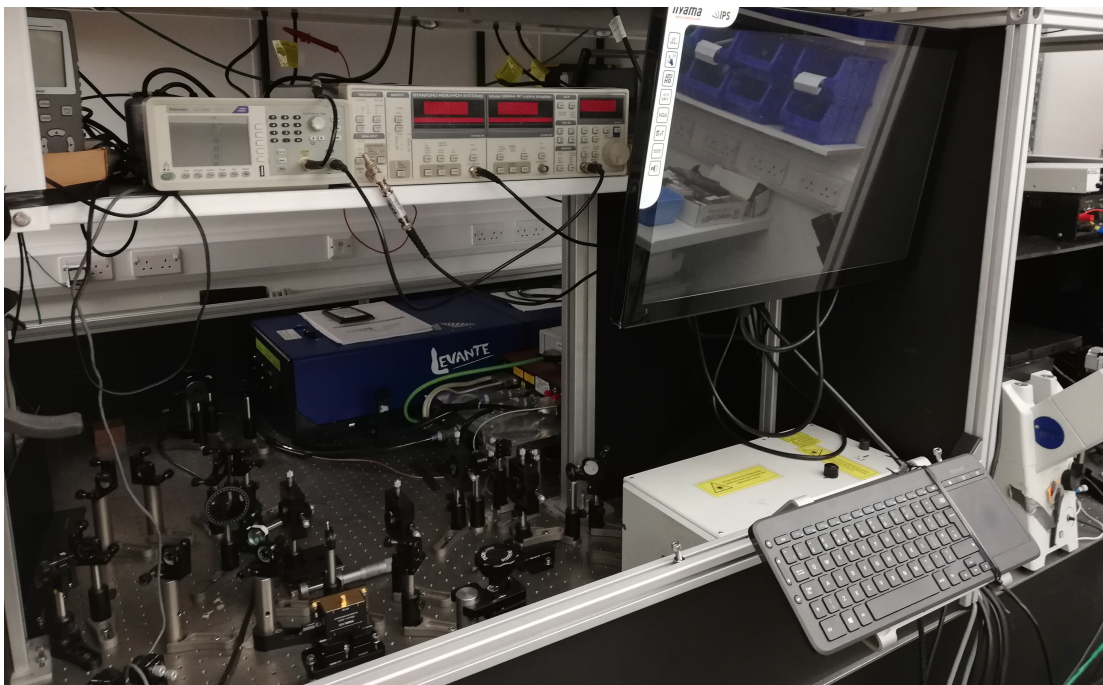


Figure 3.2: (i) The optical setup of fiber laser-based stimulated Raman scattering for AIs and wax. AOM: acousto-optic modulator, DM: dichroic mirror, OBJ: objective, FL: filter, PMT: photomultiplier tube, PD: photodiode, LIA: lock-

in amplifier. (ii) Photograph of the coherent Raman experimental set-up, showing mirrors, dichroic mirror and telescope guiding beams to the scan unit.

3.4 LCMS

3.4.1 LC

LC is used to separate analytes of interest from components involved in biological matrices and complex mixtures. The system consists of the mobile phase (which is contained in solvent reservoirs), pumps that keep the constant flow of the mobile phase through the system, sample injector, protection from contamination in the form of a guard column, another column for separation, and finally a detector with data processing ability.

LC can have a multitude of modes, including; reverse- or normal-phase chromatographies and hydrophilic interaction chromatography, and many others, which all experience advantages and disadvantages over their suitability for separation techniques when coupled to MS.

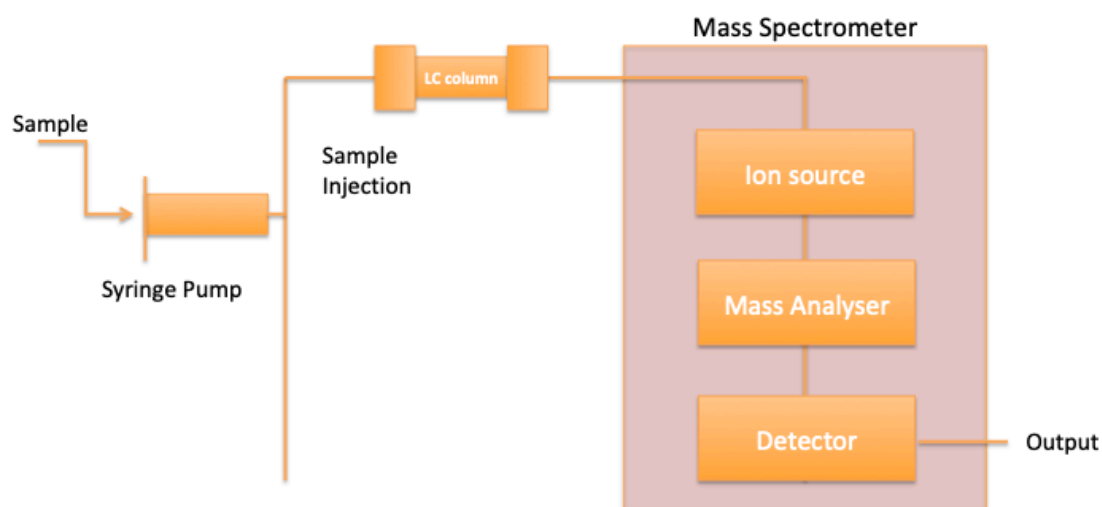
Out of these, RPC or its liquid counterpart – Reverse phase liquid chromatography (RPLC) are the most commonly utilised, working by partitioning between the analyte between a polar mobile phase and a hydrophobic stationary phase in the column. The mobile phase in this study is a mixture of aqueous (water) and organic solvent (acetonitrile), with the stationary phase of non-polar hydrocarbons bonded to an inert support inside the analytical column. RPLC has proven vital in industry, as has become widely used as a method of separation, thanks to its ability to analyse both non-polar and polar analytes.

3.4.2 MS

Mass spectrometry is highly selective, and therefore provides a wealth of structural information for the analysis of small molecules, with the main components shown in Figure 3.13, including: a route into the MS (here done by LC), an ion source, mass analyser and detector.. A sample in solution can be evaporated in the ion source, forming gas phase ions. These ions enter the mass analyser where an electromagnetic field separates the ions based on their m/z ratio, which is the ratio between mass and charge. Finally, this can be amplified on the detector, which generates a spectrum, visualised by software on the computer.

The system used for all LCMS measurements during this thesis is described here. Figure 3.3 (i) and (ii) show a simplistic schematic for the internal workings of the instrument, whilst (ii) shows an image of the setup

(A)



(B)



Figure 3.3: (A) Simple schematic for LC-MS and (B) Photograph of the set-up, showing Thermo Xcalibur software and automated injection port.

Agrochemical agents were detected using Thermo Vantage triple quadrupole mass spectrometer (Thermo Scientific) coupled with Acquity Liquid Chromatography system (Waters). The mass spectrometer system was

operated in negative ion mode using selected reaction monitoring mode. The voltage of the source was adjusted to 2200 V. The capillary temperature was 270°C. Nitrogen was used as a sheath and auxiliary gas, whilst argon gas at a pressure of 1.5 mTorr was used for collision. This was coupled with an LC system, which, for quantification, used the Thermo Xcalibur software package.

Chapter 4: Measuring agrochemical uptake using a conventional technique

4.1 Introduction

As mentioned in Chapter 2, around 75% of pesticide research in industry utilises LC and GCMS. To see the current state of the art method, and compare to the abilities of CRS, which will be explored in Chapters 5 and 6, typical industry experiments have been performed. These will show the uptake of various AIs and adjuvants into plants, and the biokinetic analysis industry is currently able to perform. The results are split into four individual parts outlined in Figure 4.1, starting with the leaf wash. This wash allows us to calculate the percentage of recovered material that had been micropipetted onto the leaf surface over time. Inverting this, we can therefore calculate the percentage that has lost from the leaf surface in this time frame. However, without the hexane partition and leaf extract steps that follow this, one could only conclude this amount is in the leaf, providing very little information about which layer of the section it has diffused to or indeed if it has broken down. By stripping the wax layer using hexane, and separately extracting from the leaf section that remains, one can successfully map if, at a certain point in time, the desired analyte is present inside the leaf itself or simply in the wax. Following this, there is a total recovery graph, to ensure the full amount of sample has been re-obtained over each section of the experiment. After, there will be a discussion of the limitations of this technique, which can be overcome or improved by using SRS. Chapters 5 and 6 will then explore experiments using SRS, and compare to the work in this chapter.

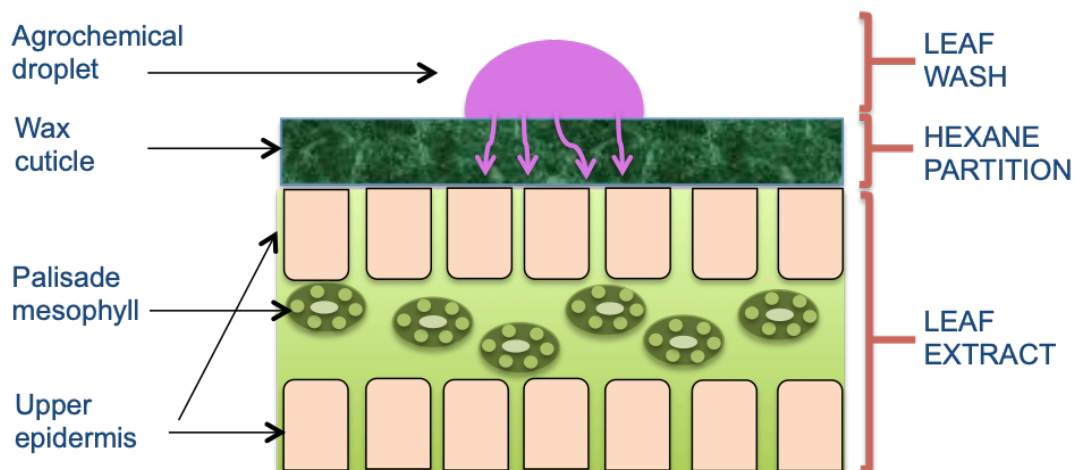


Figure 4.1: Diagram outlining the different measurements in a foliar uptake study using LCMS.

In industry, LC is used to separate the analyte(s) of interest in complex mixtures of hundreds of residues and matrix components. MS then involves the ionisation of the species or analyte in solution, for analysis. Whilst it is important MS is specific and sensitive to a certain species, LC separation is of paramount importance, in order to ensure high quality data.

For direct comparison to later chapters, I have measured the uptake of Azoxystrobin (AZ) into cabbage leaf sections, separately, and then with the addition of two adjuvants, 15-hydroxypentadecyl benzoate (known hereafter by its commercial name Finsolv TN) and Polyoxyethylene (20) sorbitan monolaurate (known hereafter as Tween 20), to measure the uptake difference.

For this foliar uptake study, including the partition into wax, diluted compounds (diluted to 1000 ppm) are applied at a rate of 10 x 0.4 μ l droplets into plant material, for a full equivalence of roughly 4 μ g of compound per treatment

allowing diffusion of the solution for time points; t=0, 10 20, 30, 60, 360 and 1440 minutes, with 4 replicates acquired per time point.

For samples taken immediately after application (t=0), plant material is sectioned to roughly 1.5 cm² areas and placed in 4ml acetonitrile and shaken for 20 seconds. Then the sections are removed and dried before being transferred into a prep tube containing 1 ml of 80:20 Acetonitrile:Water. From the washes and extracts, 1 ml samples are then transferred to LCMS for analysis. For all subsequent sample times, the plant material is placed in 4ml of water, before again being shaken for 20 seconds and then removed, dried and then hexane washed. Hexane washing in this set of experiments involves adding 10 ml of hexane, gently swirling into the solvent-containing jar, before removing the leaf segment which is then blot-dried and transferred into 1ml of 90:10 Acetonitrile:Water, for extraction using fast prep maceration, and centrifuged. Again, from the washes and extracts, 1ml samples are then transferred to LCMS for analysis.

Typical industry tests also show the hexane partition, which highlights the percentage of an agrochemical agent uptaken into a sample's wax layer, for all time-points after the initial measurement. To acquire this information, 5ml of 90:10 Acetonitrile:Water is added to each of the hexane wash samples. Again, the tubes are shaken for 20 seconds, before being allowed to settle and 1 ml of the lower acetonitrile layer being removed for LCMS analysis.

Therefore, for each experiment we will see information for the leaf wash and treated leaf extract at all time points, and the hexane partition for all time points after t=0, which will be discussed in separate sections.

4.2 Leaf Wash

The first part of this method, mentioned in the introduction, details that the sections of leaf are washed after allowing diffusion for the aforementioned time points. The collected samples hereafter show the percentage of agrochemical recovered in this leaf wash, and thus showing the percentage that has penetrated into the wax at each time point.

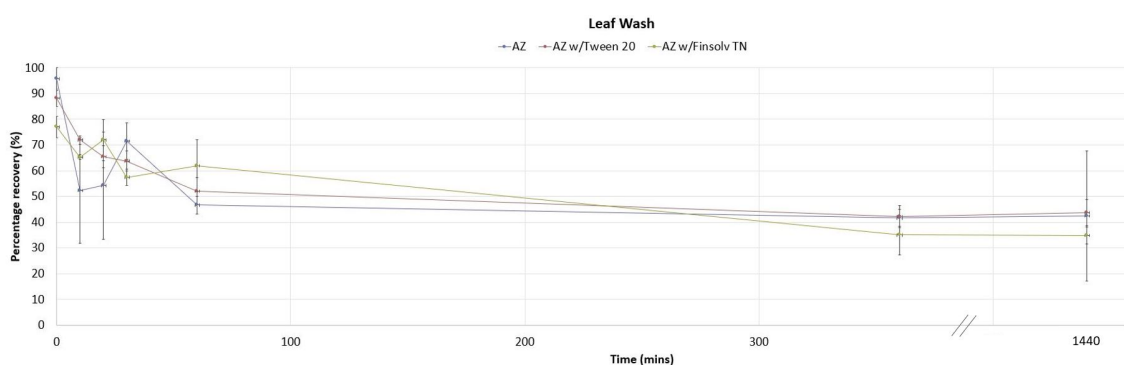


Figure 4.2: Percentage recovered from three treatments of agrochemical solution onto cabbage leaf after leaf washes with water. AZ (blue), AZ with Tween 20 (red) and AZ with Finsolv TN (green)

Figure 4.2 shows the percentage of AI recovered, and inversely the percentage that has penetrated into the wax of the cabbage sections. Here we can see, during the early time points, the difficulties AIs face with penetration through the wax surface. All three treatments show high percentages of recovered material over the first 30 minutes of the study. It is only after 60 minutes we see a larger spread of data points on average. After 60 minutes, Finsolv TN and Tween 20

both show no statistically significant effects on diffusivity into the cabbage section, with all treatments still recovering around 50% of the added material.

By time point 360 minutes we can see a steady decline in percentage of recovered material for all three leaf wash samples, with the addition of adjuvants proving insignificant over long periods of time, over samples without aid. All samples look to have plateaued at this point, with the final time point remaining near unchanged.

4.3 Hexane Partition

The second stage of this study shows the percentage of compound, which can be found in the cuticle wax at each time point. After the water washing, hexane is used to strip the wax from the leaf surface and the percentage of agrochemical agent can be calculated.

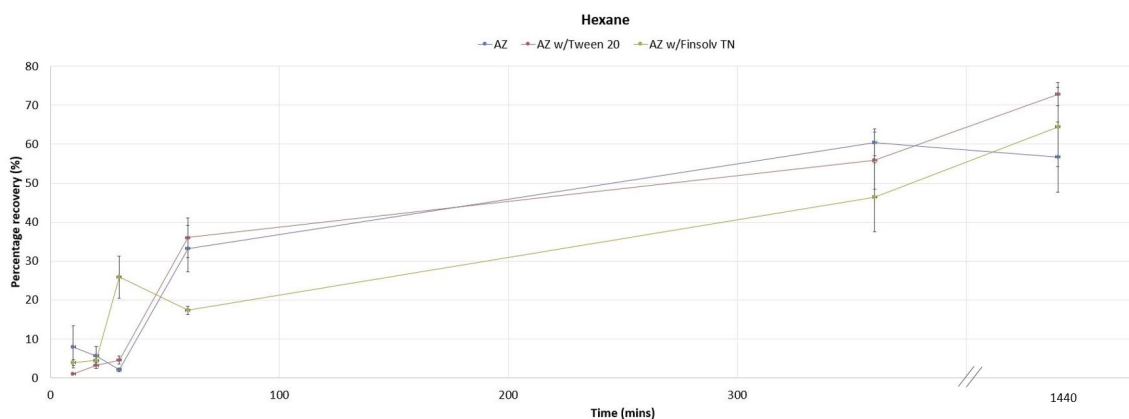


Figure 4.3: Percentage recovered from three treatments of agrochemical solution onto cabbage leaf after hexane washes to remove cuticle wax. AZ (blue), AZ with Tween 20 (red) and AZ with Finsolv TN (green)

Figure 4.3 shows the percentage of AZ and AZ with adjuvant recovered from the wax after hexane washes are used to strip the cuticle wax from the leaf surface. Among the initial time points we see a large positive spike in the percentage recovered from AZ with Finsolv TN, showing an initial boost to the diffusivity of the compound thanks to the addition of Finsolv TN. When you compare this to the other mixtures, AZ and AZ with Tween 20, you can see an uptake difference in recovered material between 20 and 30%. The next time point (t=60), however, complements the data shown in the leaf wash graph, with the AZ with Finsolv TN recovered material being lower than that of AZ alone and with the aid of Tween 20. This shows unequivocally how Finsolv TN manipulates the wax surface in such a way as to speed up the uptake of the AI into the wax, with the other mixtures, AZ and AZ with Tween 20 both proving to need double the percentage of time to diffuse through the wax to the same extent.

In the latter time points we do see AZ with Finsolv TN rising again, with gradient between the final two time points providing argument that diffusion is still occurring after the 1440-minute point. All, however, show no significant separation between the AI alone or with the use of adjuvants.

4.4 Treated Leaf Extracts

The next stage of a foliar uptake study sees the analysis of the leaf extracts which have been treated. Leaf samples are macerated using Fast Prep system. Sample tubes contain a ceramic bead, which aids maceration of the plant material and then centrifugation of the leaf section at 4000rpm for 15 minutes, and removing 1 mL of the sample for analysis. This will highlight the percentage

of agrochemical agent that has passed through the cuticle wax layer and is in the plant itself.

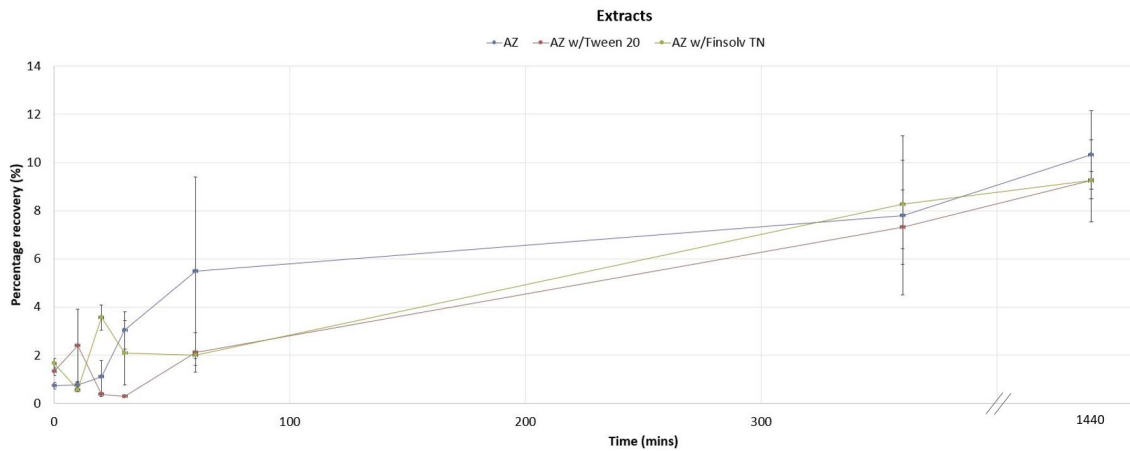


Figure 4.4: Percentage recovered from three treatments of agrochemical solution onto cabbage leaf after extraction process. AZ (blue), AZ with Tween 20 (red) and AZ with Finsolv TN (green)

Here, in Figure 4.4, you can see the progression of the agrochemical mixtures into the plant material itself, and shows us the percentage of agrochemical recovered from the leaf, after the centrifuge extraction process. As expected, these percentages are far smaller than that of the previous samples, with the majority of the early time points remaining under 4% recovered until $t=60$. At this point however, we do see a gap emerge between the unaided AI and with the use of adjuvants, with what one could say provides arguments that AZ diffuses greater individually once inside the plant, than when it is mixed with adjuvants. Furthermore, after 360 minutes, AZ with Finsolv TN shows a steeper uptake gradient, over that of AZ and AZ with Tween 20. This graph also shows all agrochemical compound mixtures overlapping at the end of this experiment, with an average 9.7% recovered over 24 hours, and no true difference to overall uptake of the AI, with or without the use of adjuvants.

The data, however, with extremely large error margins between samples, this data gives more reason to explore different, innovative technologies for the rapid and accurate quantification of diffusion.

4.5 Total Recovery

Finally, the total recovery shows the combined percentages of sample recovered from the cuticle wax, washes and leaf extracts, to show an overall percentage recovered over the course of the 24-hour experiment, which will show the total percentage of agrochemical agent added.

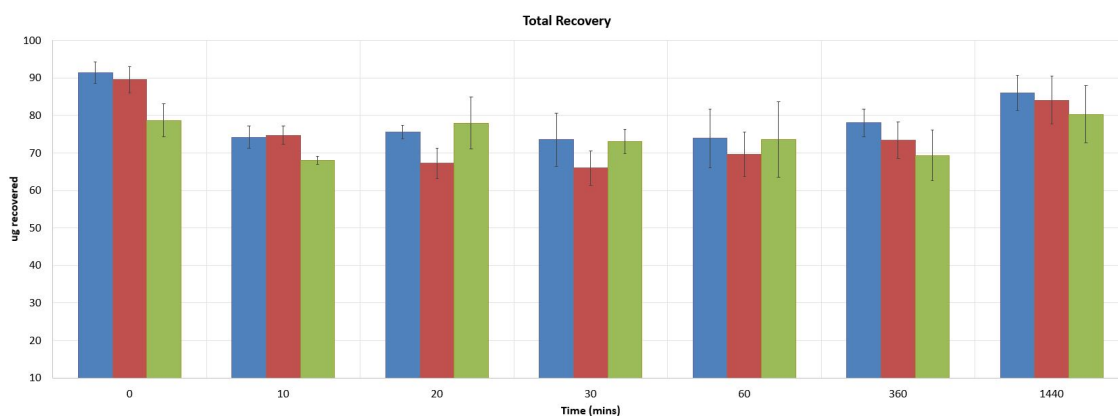


Figure 4.5: The sum of the percentages recovered from three treatments of agrochemical solution onto cabbage leaf after water washing, extraction process, and the hexane washes of the cuticle wax. AZ (blue), AZ with Tween 20 (red) and AZ with Finsolv TN (green)

Figure 4.5 shows the total percentage of material recovered over the course of the experiment. We estimated a full equivalence (100% material of material recovered) of 4 µg of compound per treatment, which the figure shows to be unachieved in this experiment, with the largest percentage of recovered material around 95%. The percentage of applied material can show expected

variation. This is contributed to human errors, be it droplet size or concentration variations from pipetting or stock solution. With droplet sizes fixed to 0.4 ug, and the hydrophobicity of the leaf surface, the solution provided difficulties upon leaving the needle. This was a particular challenge on the varying cabbage surfaces (darker or lighter green areas).

4.6 Summary

Here, LCMS has been used to separate analytes from components of AZ, and measure the percentage of recovered material from both cabbage leaf sections. Hexane partitioning allows us to show if the component is in the cuticle wax, or has passed through and is inside the leaf itself. What can be concluded with this experiment is neither Finsolv TN or Tween 20 have a significant effect on the diffusivity of AZ over the full 24-hour period. The results raise many questions about the earlier time points, with some dramatic gradient variations seen particularly in AZ with Finsolv TN. In these early time points (t=0-30) we see little difference between the percentages recovered. However, after this point, AZ with Finsolv TN shows that it diffuses irregularly when compared to AZ alone or AZ with Tween 20, which appear far more linear in uptake, before plateauing. This varying result for AZ with Finsolv TN could provide argument that Finsolv TN manipulates or deforms the cuticle wax surface in a way that Tween 20, nor AZ alone, can.

LCMS is a sensitive technique, and one can gather accurate quantitative data. However, as discussed in Chapter 2, LCMS provides no spatial resolution and cannot perform in real-time, with an incredibly lengthy sample preparation time, and showing far lesser accuracy and repeatability than other techniques we will explore in the following chapters. Furthermore, with results showing a lack of

discrepancy or any real quantitative difference between that of the AI alone against identical experiments with aided with an adjuvant, there is a huge opportunity for a technique that can give insight particularly into the early time points in this type of experiment. With an ideal technique being rapid, this is a real limitation of the technique, along with its destructive and invasive nature and high cost. Hereafter, we aim to show results derived in real-time, with improved detection limits, and spatial resolution, whilst maintaining the chemical specificity and quantitative nature of the technique. This would improve efficiency of uptake measurements dramatically in industry, and allow us to understand more about the mechanisms of diffusion that take place in the early time points. All without compromising on any of the properties LCMS possesses.

Chapter 5: Development of an Analytical Model System for Cuticle Wax

5.1 Introduction

This chapter explores spontaneous and coherent Raman measurements of extracted cuticle wax from various plants, as well as a suitable model system for cuticle wax, for high throughput, rapid imaging and data analysis – paraffin wax.

The cuticle is a protective covering that coats the epidermis of leaves that consists of a cutin matrix (ester-linked long-chain hydrocarbon polymers (C₂₀-C₄₀), often with additional hydroxyl, carboxylic, epoxy and oxy groups in secondary mostly mid-chain positions) with cuticular waxes embedded on the surface.⁶⁸ This plant-specific barrier limits the effectiveness of agrochemicals, to penetrate beyond the leaf surface. For initial experiments in the agrochemical industry, a material assumed as a uniform, infinite diffusion sink, would have to provide highly accurate and repeatable results. Whereas extracted leaf waxes contain varying amounts of alkanols in their hydrocarbon chains, waxes such as paraffin are up to 100% absent of alkanol groups (Figure 5.5), contaminants and differences from external forces during growth such as light, temperature and pollutants, making them an attractive model for high-throughput screening. Using paraffin wax may also prove beneficial to industry as it removes the requirement for hexane washing to remove wax from a leaf's surface. This method is the current standard and takes long periods of time, with a low yield of wax. Melting paraffin wax into cuboid molds on a slide is a far more rapid and solution, yielding identical wax blocks.

5.2 Raman on wax

Raman scattering is necessary prior to CRS to identify peaks of interest for which to tune to. Strong and non-overlapping peaks are required for simultaneously imaging wax and agrochemical agent. Here, spontaneous Raman spectra of a number of waxes were obtained using the Renishaw RM1000 Raman Microscope (Renishaw PLC, UK) discussed in Chapter 4. Here we have reviewed the differences in paraffin wax, which has been used as a model system, against two extracted waxes (*sedum morganianum* and grape).

5.2.1 Cuticle wax

Various cuticle waxes have also been used herein to show the current standard for wax extraction. These, however, have to be extracted, before melting the wax and forming it in molds. There are several reported methods used to remove cuticles and/or cuticle wax from the surface of a plant using hexane, acetone or alcohol,⁶⁹ with that cuticular wax could be removed using four 10 second rinses.⁷⁰ As cutin is not soluble in chloroform and hexane, 'short-term' washes only remove the epicuticular waxes. Chapter 5 alike, we have used hexane, and once the hexane wash has been performed, the cuticle wax, identically to the paraffin wax, was melted and allowed to set in identically sized cuboid molds.

5.2.1.1 *Sedum Morganianum*

Sedum is a genus of almost 300 species in the northern hemisphere, with around 100 of those reported to be in Mexico alone.⁷¹ *Sedum Morganianum* is considered the most widespread in cultivation, with 90-100 cm long stems and

thick waxy leaves up to 8 mm thick. Although not a plant we will focus on for the future of food security, these leaves have a large amount of wax and yield highly per extraction, and so are ideal for this application. As stated in the previous section, the leaves were hexane-washed using four 10 second hexane rinses to obtain wax, before setting it in a cuboid mold for spontaneous Raman.

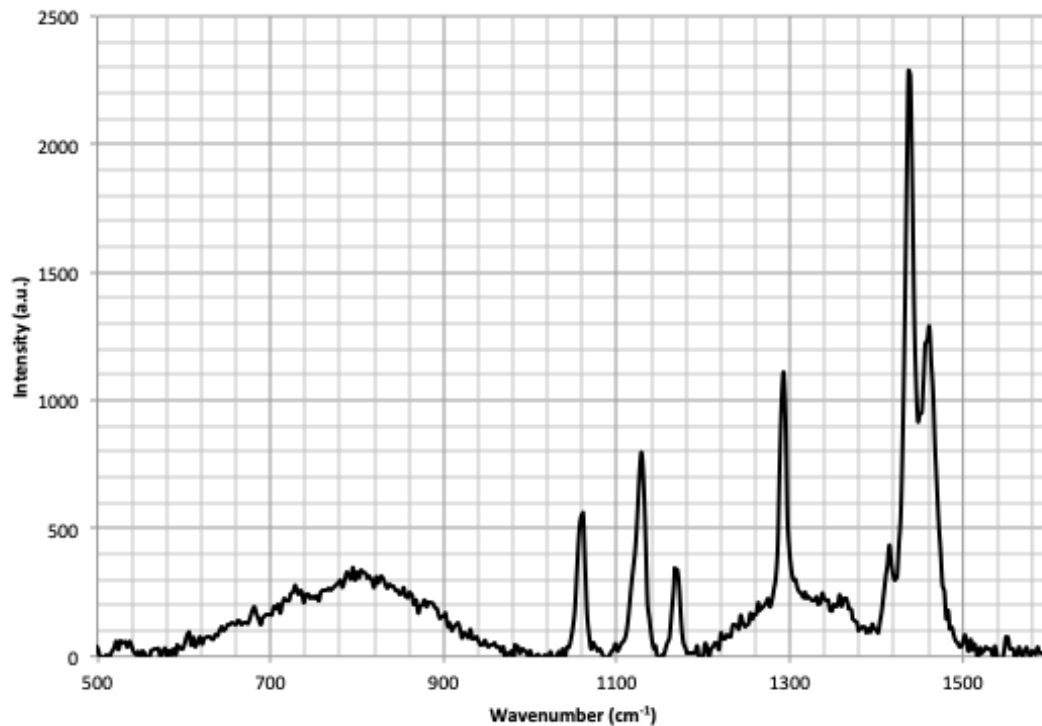


Figure 5.1: Mean Raman spectrum of wax extracted from *Sedum Morganianum*, in the fingerprint region. The spectrum was measured using the 785 nm laser with 300 l/mm grating.

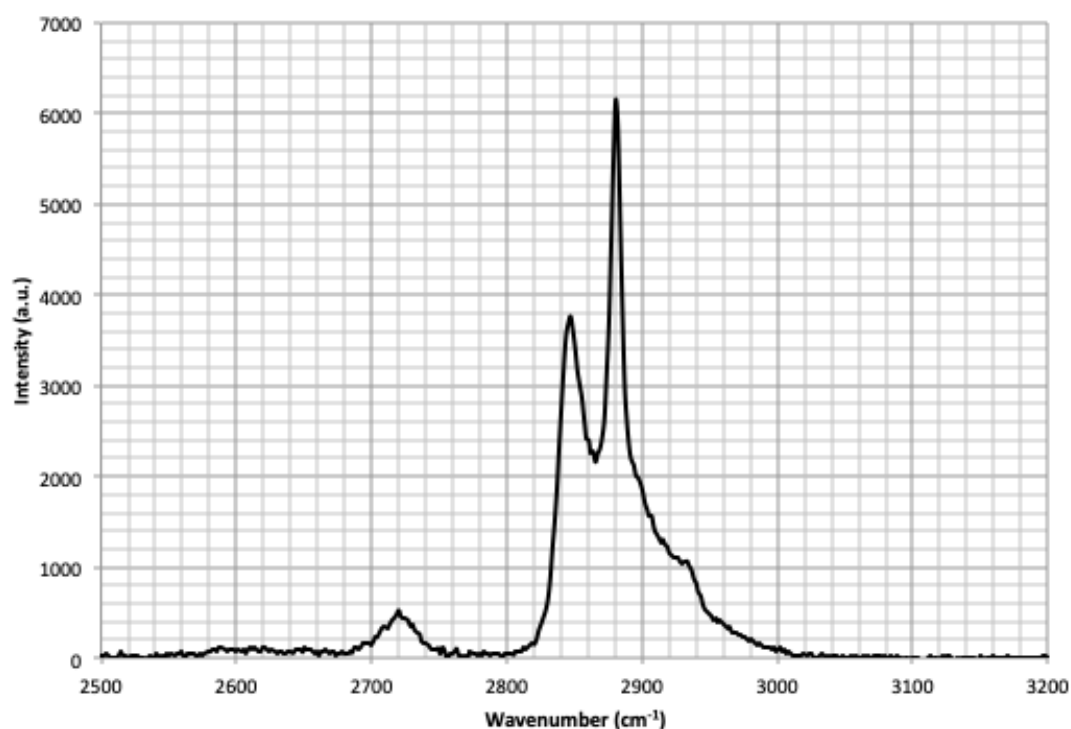


Figure 5.2: Mean Raman spectrum of wax extracted from *Sedum Morganianum*, in the high wavenumber region. The spectrum was measured using the 785 nm laser with 300 l/mm grating.

The peaks that appear in the high wave number region, shown in Figure 5.2, are again associated with CH₂ asymmetric and symmetric stretching, whilst the fingerprint region, Figure 5.1, shows various peaks associated with C-C stretching (1130 cm⁻¹), C-H in-plane bending (1290 cm⁻¹) and CH₂ bending (1420 cm⁻¹ and 1440 cm⁻¹).

5.2.1.2 *Vitis Vinifera* (common grape)

Grape wax was chosen for this study, due to its documented history with FDL, one of our AIs. FDL is a fungicidal AI that has shown to reduce bacterial numbers on the surface of grapes, and it's effectiveness in controlling infections such as *B. cinerea*.⁷² As stated in the previous section, the leaves were hexane-washed using four 10 second hexane rinses to obtain wax, before setting it in a cuboid mold for spontaneous Raman.

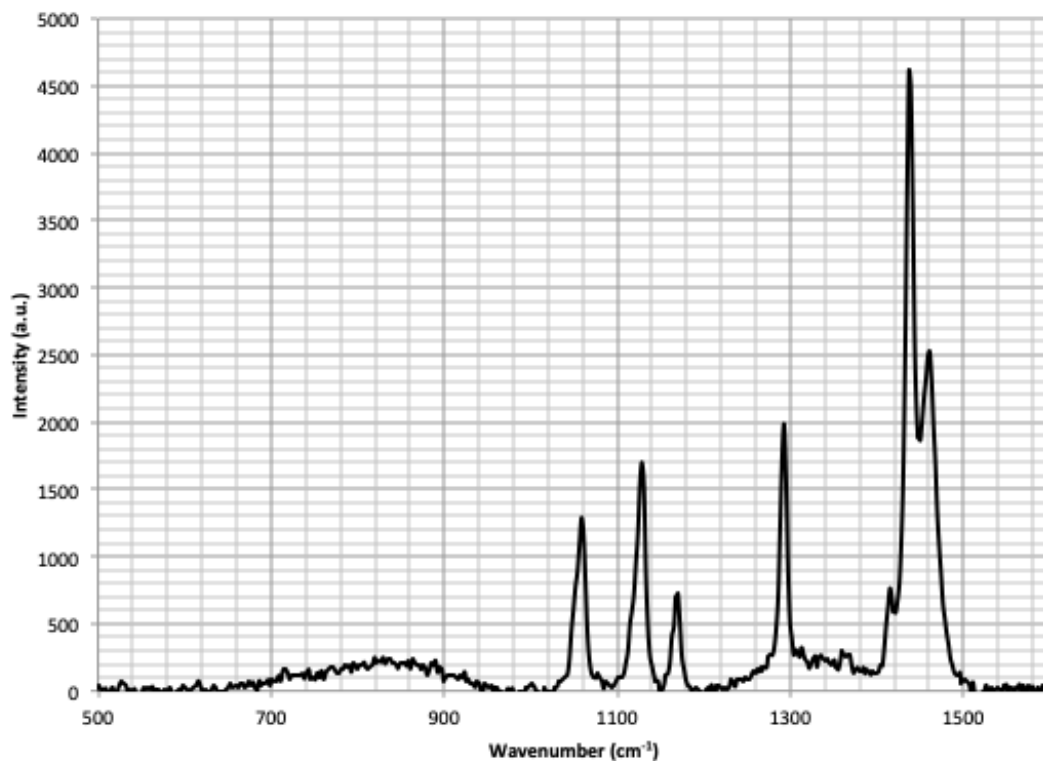


Figure 5.3: Mean Raman spectrum of wax extracted from *vitis vinifera*, in the fingerprint region. The spectrum was measured using the 785 nm laser with 300 l/mm grating.

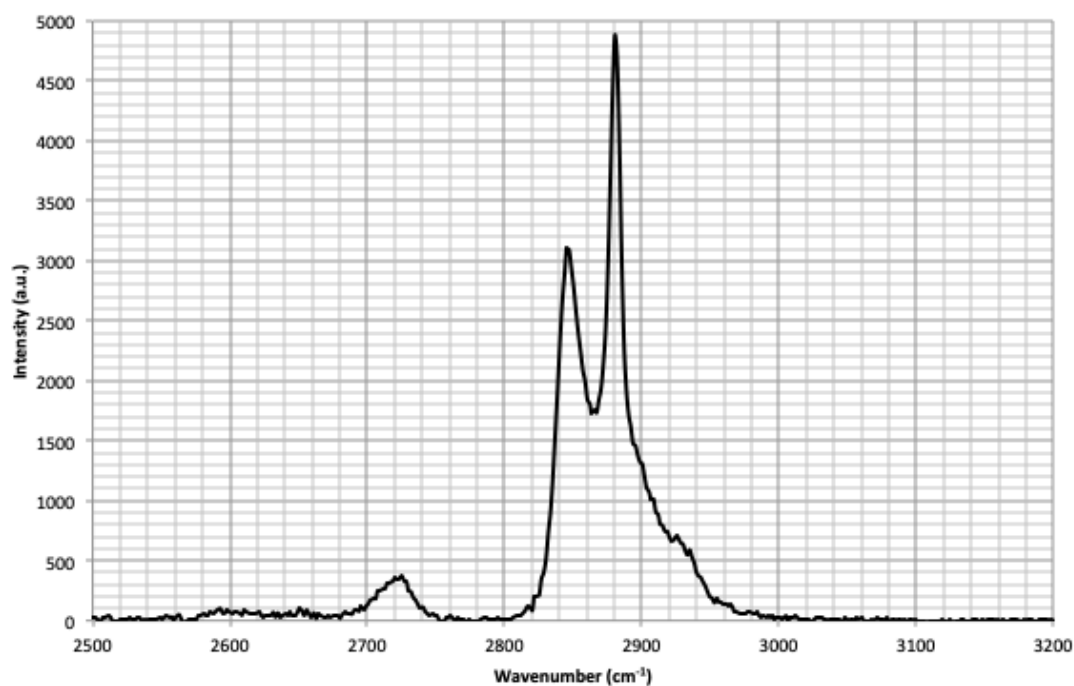


Figure 5.4: Mean Raman spectrum of wax extracted from *vitis vinifera*, in the high wavenumber region. The spectrum was measured using the 785 nm laser with 300 l/mm grating.

Figure 5.4 shows peaks in the high wave number region that are associated with CH₂ asymmetric and symmetric stretching. What we see in the fingerprint region spectra, Figure 5.3, are various peaks associated with C-C stretching (1130 cm⁻¹), C-H in-plane bending (1290 cm⁻¹) and CH₂ bending (1420 cm⁻¹ and 1440 cm⁻¹).

5.5.3 Paraffin wax

Paraffin wax (Sigma Aldrich), with structure shown in Figure 5.5, has been used as a cuticle wax in this study due to its similar physicochemical properties and structure. Paraffin wax is melted and allowed to set in identically sized cuboid molds.

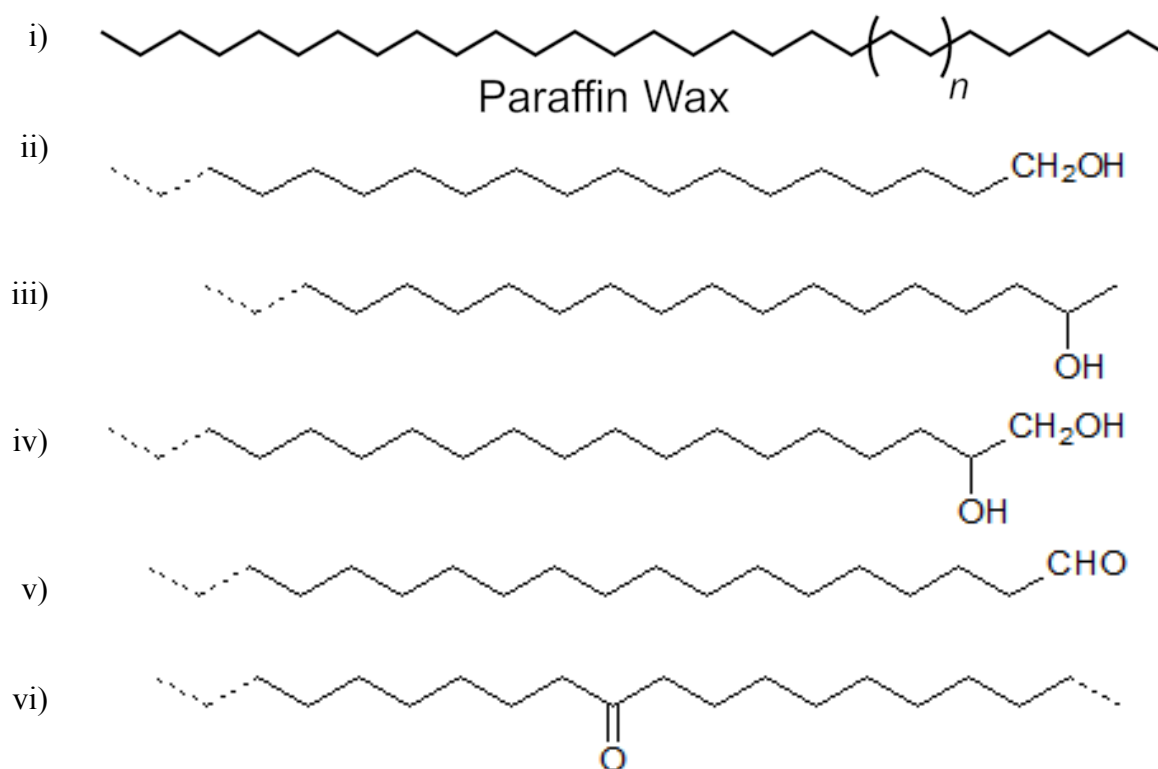


Figure 5.5: i) Generalised structure of Paraffin Wax, with some common plant wax constituents; ii), iii) and iv) showing different position or amounts of alkanol groups, with v) aldehyde and vi) ketone groups

A spontaneous Raman spectrum of a block of paraffin wax in the fingerprint region is shown in Figure 5.6, and for the high wave number region in Figure 5.7, with the most prominent peaks assigned in Table 3.

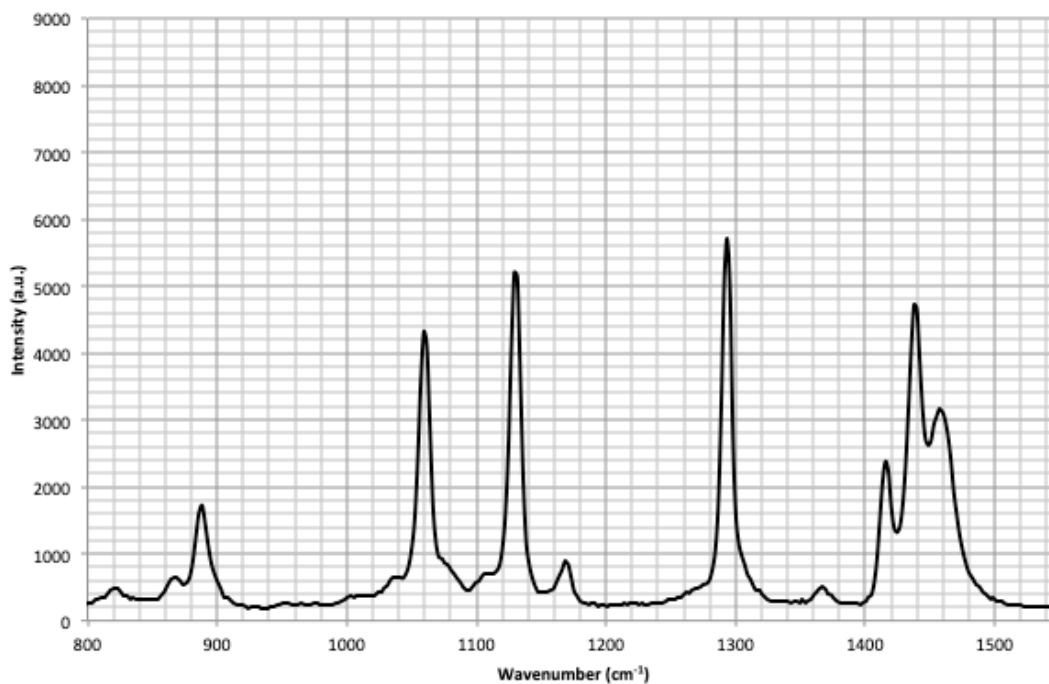


Figure 5.6: Mean Raman spectrum of paraffin wax, in the fingerprint region. The spectrum was measured using the 785 nm laser with 300 l/mm grating.

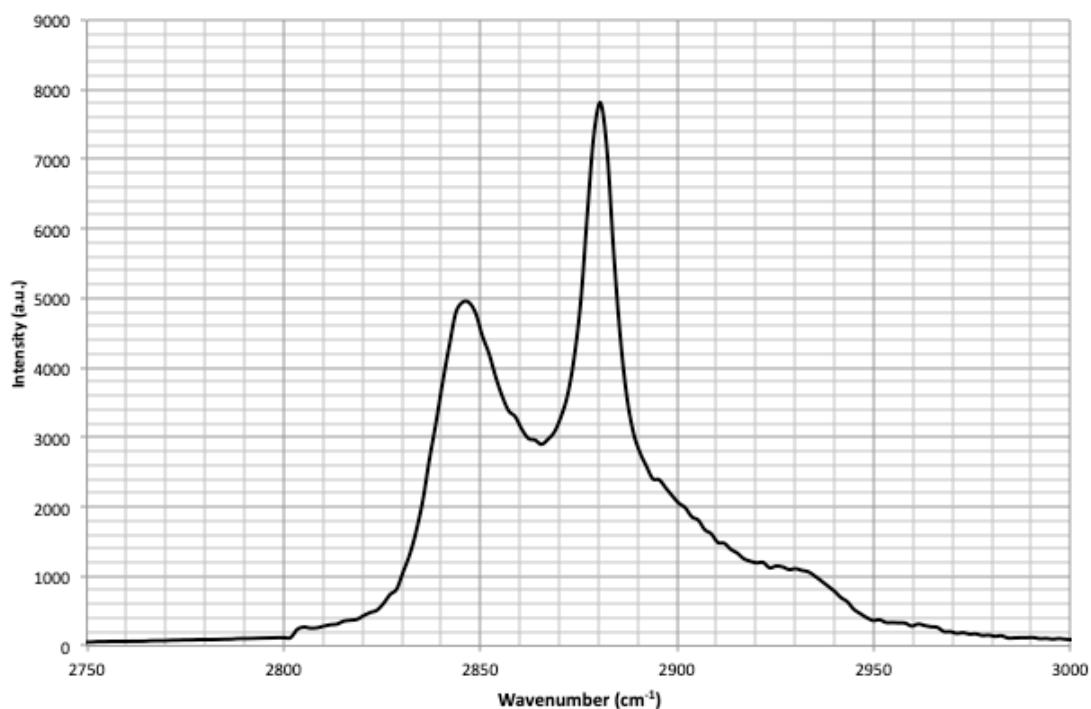


Figure 5.7: Mean Raman spectrum of paraffin wax, in the high wavenumber region. The spectrum was measured using the 785 nm laser with 300 l/mm grating.

Peak Position (cm ⁻¹)	Vibrational Mode
1130	C-C Stretching
1290	C-H in-plane bending
1420	CH ₂ bending
1440	CH ₂ bending
2845	CH ₂ symmetric stretch
2880	CH ₂ asymmetric stretch

Table 3: Peak assignments of the most prominent peaks in the Raman spectrum for Paraffin wax in both fingerprint and high wave number regions.

The intense peaks that appear in the high wave number region, Figure 5.7 are associated with CH₂ asymmetric and symmetric stretching, whilst the fingerprint region, Figure 5.6, shows various peaks associated with C-C stretching (1130 cm⁻¹), C-H in-plane bending (1290 cm⁻¹) and CH₂ bending (1420 cm⁻¹ and 1440 cm⁻¹).

5.3 Paraffin vs. Cuticle wax

To show the similarities between paraffin and cuticle wax, Figures 5.8 and 5.9 show grape and *sedum morganianum* waxes plotted against paraffin for their high wavenumber region and fingerprint region respectively, with their peaks labelled.

5.3.1 Raman Spectroscopy

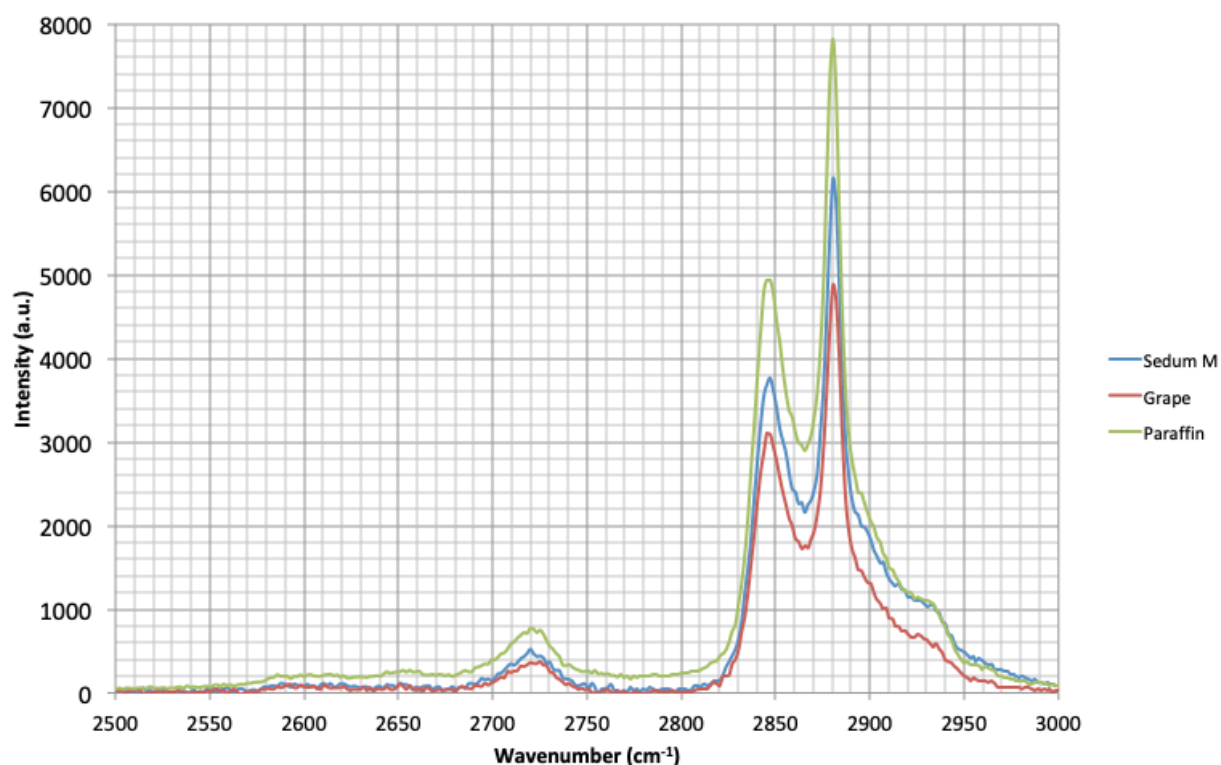


Figure 5.8: Mean Raman spectra comparing the wax extracted from *vitis vinifera* (red), *sedum morganianum* (blue) and paraffin wax (green) in the high wave number region.

When comparing the high wave number region spectra of all three waxes, it is clear they collapse into a near-identical shape. The main peaks at 2845 cm^{-1} and 2880 cm^{-1} represent the symmetric and asymmetric stretches of CH_2 respectively.

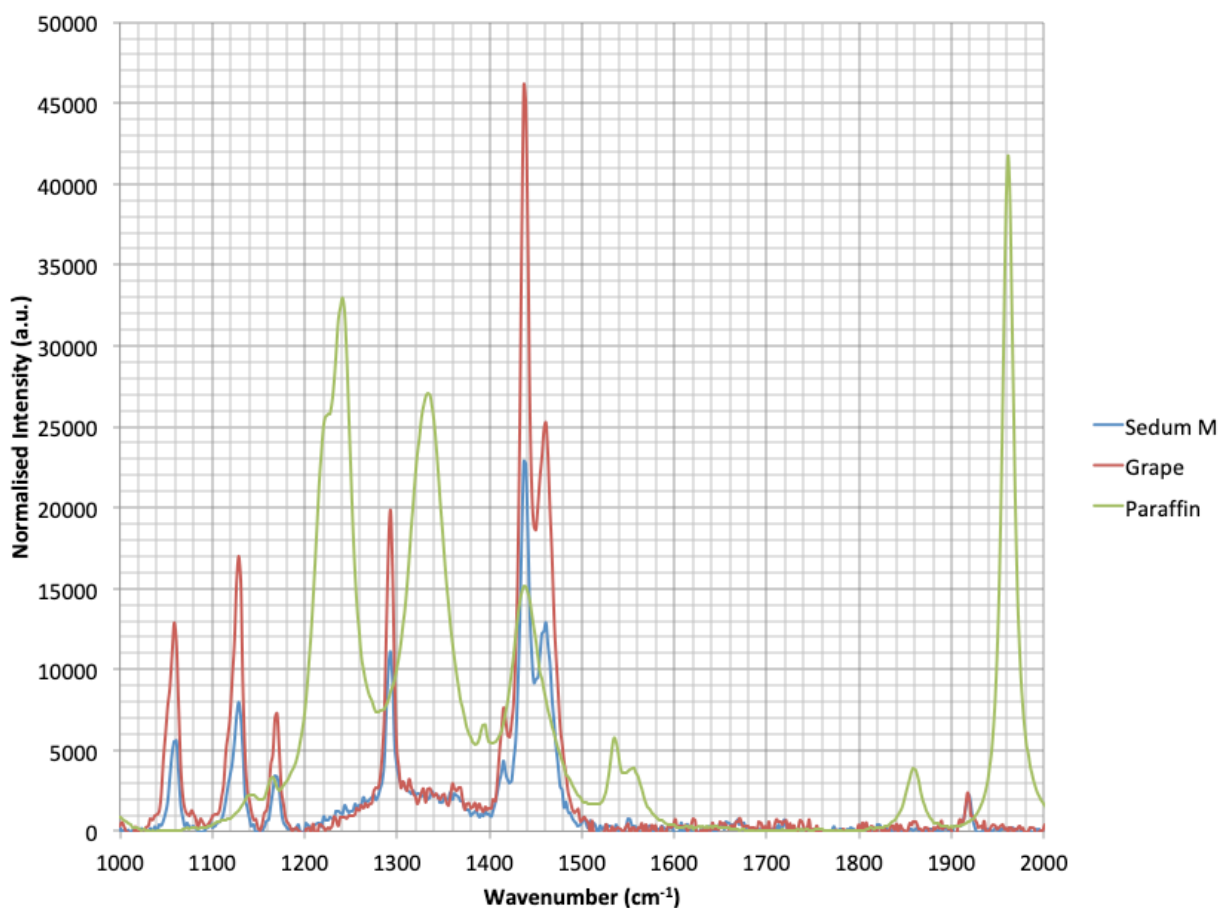


Figure 5.9: Mean Raman spectra comparing the wax extracted from *vitis vinifera* (red), *sedum morganianum* (blue) and paraffin wax (green) in the fingerprint region.

Where the high wavenumber region showed the similarities between the spectra, the fingerprint region depicts the differences between the two. As shown in Figure 5.5, plant waxes can consist of varying amounts of alkanols, aldehydes and ketones, which show unique peaks that appear in both grape and *sedum morganianum*, but do not appear in the paraffin spectrum. A table of peak assignments from the extracted wax spectra is shown overleaf in Table 4.

Peak Position (cm ⁻¹)	Vibrational Mode
1060	Primary alcohol CC-O
1130	Secondary alcohol C-O
1170	Tertiary alcohol CC-O
1293	C-C aliphatic chain vibrations
1919	C=C

Table 4: Peak assignments, from Socrates (2004), of the most prominent peaks in the Raman spectra for extracted waxes in fingerprint region.⁷³

The peaks that only appear in the *sedum morganianum* and grape spectra, at 1060 cm⁻¹, 1130 cm⁻¹ and 1170 cm⁻¹, represent the alkanols we expected to see in plant waxes that would not appear in paraffin wax. However, we do not see any major peaks that would suggest the presence of ketones or aldehydes, which would appear between 1700-1800 cm⁻¹.

We can summarise from these results that, although not identical, paraffin wax is an acceptable proxy for experimentation. The lack of plant-specific concentrations of alkanols is a limitation, however, paraffin wax will allow us to make consistent wax blocks for the measurement of agrochemical diffusion, with results not being affected by different crystalline structures within. Diffusion, therefore, will only be affected by the different agrochemicals we use in this thesis.

5.3.2 CRS

As previously mentioned in Chapter 2, far stronger Raman signals can be obtained using coherent Raman scattering due to the signal strength depending nonlinearly on the illumination intensity. It has been shown to be unaffected by

autofluorescence, combining structural imaging with *in situ* chemical analysis of plant materials in real time, providing sub-cellular spatial resolution⁶⁴ and soon after was shown to provide in-vivo 3-D images of plant cuticles. In this section we explore the differences between both paraffin and plant waxes using this technique with 2- and 3-D surface reconstructions and time lapse images on the same position to both monitor the effect of the laser on the morphology of the wax over time, and measure the uptake of the various agrochemical compounds.

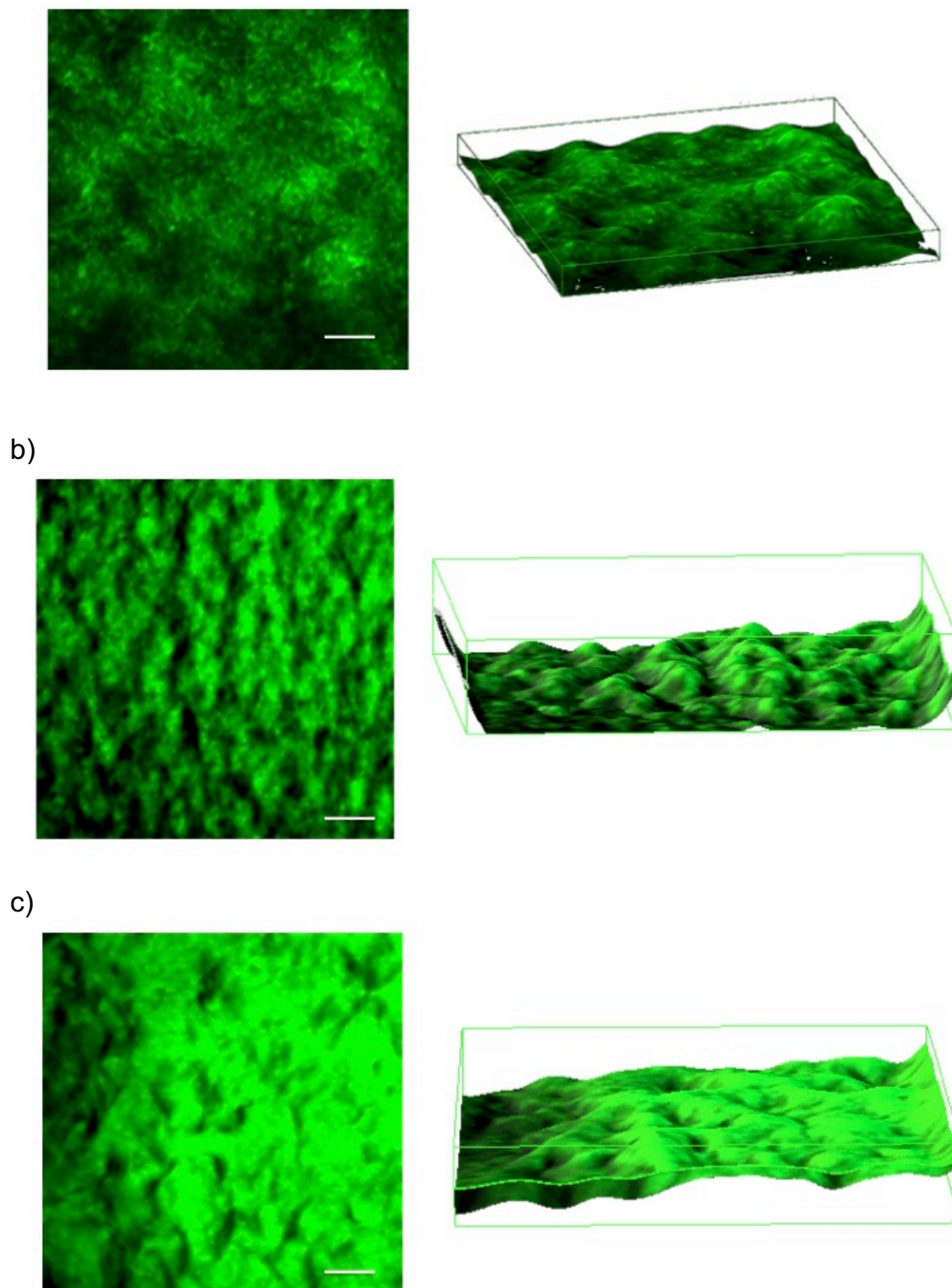


Figure 5.10: CARS image and 3D representation of a) Paraffin wax block b) extracted *sedum morganianum* wax block and c) extracted grape wax block at the CH₂ peak (2845 cm⁻¹). Scale bar represents 10 μm

As seen both in Figure 5.10 and the previously shown spontaneous Raman spectra, paraffin wax does vary in signature when compared to extracted plant

waxes. Here we have utilised their overlapping intense peaks, at 2845 cm^{-1} , which is associated with CH_2 vibration. The images in Figure 5.10 display these differences by comparing the different surface morphology of the waxes in CARS. However, the differences we see here could be due to a crystallinity change, brought on by the extraction process. Due to the varying amount of wax yielded from each extraction, the differing ratio between hexane and wax could provide the answer as to why these images do not appear uniform in morphology. This reasoning is also a strong reason paraffin wax can be considered a good proxy, as its uniformity is not limited by this extraction process.

It is also important to see if the laser influences the morphology of the wax, namely whether the heat caused changes the surface or crystallinity. To test this, an experiment was designed to rapidly image, with laser average power at 180 mW (pump at 76 mW and Stokes at 104 mW) and visualise the effect of this on the deformity of the wax at its edge, so the images can be normalized against the background. The system was set to 2 ps pulses and an 80MHz repetition rate, set to image the wax's CH_2 vibration at 797.8nm. Figure 5.11 compares the x-y wax image from the 1st to the 80th and shows any non-identical pixels that appear, as colours coordinating to a colour map, where orange/yellow is pseudocolour-assigned to the early images, all the way through to pink and reds showing the changes in the latter stages of this experiment.

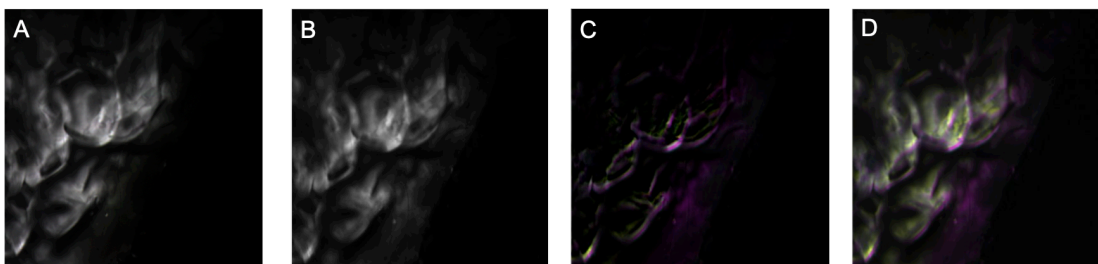


Figure 5.11: SRS images to investigate laser damage on a paraffin wax sample using 180mW average power. (A) First scan, (B) Last (80th) scan with (C) Difference between (A) and (B) highlighted in pink. (D) composite image.

Tightly focused beams readily can cause photodamage at high powers to biological tissues, however no evidence has been provided for their effects on waxes. Figure 5.11 shows the preliminary experiments performed to assess the average laser power used throughout this thesis, and to test the coherent Raman set-up could be used on wax without causing photodamage or morphological change. The sample area was scanned 80 times to replicate the amount of exposure from a time-lapse series of data, measuring uptake. Here we do not see any significant damage caused to the wax by using this power. Any regions of change have been pseudocoloured in pink due to them only appearing in the latter scans, and are circled in Figure 5.11 (B) and (D). These correspond to intense pixels that may fluctuate very slightly due to focusing errors, but are minimal and therefore can conclude the wax morphology will not be altered by the laser power.

5.4 Paraffin wax: A cuticle wax model diffusion system

As discussed in the previous chapter, using cuticle wax as a standard proves difficult for three reasons: 1. The extraction process. Mostly done using hexane or chloroform washes of a leaf, this strips the wax off by dissolving it, before reforming after the solvent has evaporated off. This process is lengthy, and low

yielding, whilst also possibly having a destructive effect on the wax, and thus changing its overall crystalline structure. 2. Non-uniformity. Every plant is different and varying amounts of alkanol bonds can be found on these long chain hydrocarbons, meaning there is a high likelihood of vastly varying results, based on impurities in these waxes. Utilising the uniformity of paraffin wax, we can create identical structures to measure this uptake through and with no low-yielding time-consuming extraction process; this method saves a lot of time for a user. And 3. High-throughput. The needs of industry are for easily reproducible data, and varying amounts of alkanol functional groups in different species of plant could provide wildly different results between experiments. The wax from plants grown in the field can also vary dramatically from those grown in different conditions in both thickness and functional group concentration. Removing this, and utilizing paraffin wax not only removes these variations in condition, but also removes the need to monitor a plants age, as this also can affect aspects of cuticle wax growth and development.

There is likely to be variation in actual result between an extracted wax and paraffin wax, and this section probes this by comparing the uptake into paraffin wax, seen in the previous sections, to that of waxes extracted from *Sedum Morganianum* (SM), a waxy species of flowering plant from the *Crassulaceae* family, and common grape (*Vitis vinifera*). Previously, in Figure 5.8 and 5.9, we have shown the spontaneous Raman spectra for these three waxes, and in the next chapter, for the first time to our knowledge; we explore and compare their differences using CRS.

5.5 Summary

These results show there is a difference between paraffin wax and extracted waxes. This was to be expected due to the lack of plant- and species-specific alkanol bonds present in paraffin wax, as well as other impurities perhaps extracted from the plant with the cuticle wax. Whilst the high wave number region remains almost identical, intense peak differences can be seen in the fingerprint region, which can also be owed to dissimilar CH₃ deformations.

We have also successfully investigated laser power against wax and proven the lack of morphological changes over 80 scans. We have shown comparative data between these various waxes and have provided argument that paraffin wax is a useable model system, avoiding the need for time-consuming and low-yielding extraction process. Paraffin shows near identical diffusion coefficient changes, however the position of this curves is skewed higher than both extracted waxes, this will most likely be due to the randomly allocated alkanol functional groups present in the extracted plant waxes which are not present in paraffin wax, but could also be due to structural changes caused by the hexane washes to remove this wax from the leaf surface.

This method of sample preparation also proved rapid and would provide industry with a uniform sample set for high-throughput data. The following chapter will explore this further as a method of high-throughput diffusion studies.

Chapter 6: Development of a Diffusion Protocol for Agrochemical agents.

Elements of this chapter were compiled into a paper entitled Agrochemical Diffusion in wax measured by stimulated Raman scattering microscopy, currently in progress.

This chapter explores the diffusion kinetics of various agrochemical agents, into the cuticle wax model discussed in the previous chapter. The compounds used in this thesis can be categorised into AIs and adjuvants. AIs provide the plant with the required material to aid its growth, or fight against pests. An adjuvants job is to aid the penetration of an agrochemical AI into a leaf. This penetration relates to the physicochemical properties of its AI, with the uptake rate being directly correlated with an AIs' molecular size and lipophilicity.²¹ Adjuvants are used to aid the diffusivity of agrochemicals, having being used to aid the increase in foliar uptake, and limit the amount of losses from spray drift and poor penetration.⁷⁴ They work due to their effect on factors such as droplet size, distribution, adhesion and molecular weight.⁷⁴ The properties of the adjuvants used in this thesis allow increased penetration into the leaf. However, quantifying the effects of an adjuvant on the AI has been a challenge that current industry methods fail to meet all the demands.

Due to the extraction of wax from a leaf surface being a lengthy procedure, with a minute yield per plant, here we utilise paraffin wax in part to mimic the activity of the wax due to structural and physicochemical similarities, and can be easily manipulated into identical sized wax blocks, for imaging outlined below in Figure

6.1. Compared to this are the diffusion rates acquired for *sedum morganianum* and grape to prove the accuracy of paraffin as a cuticle wax model system.

Results discussed in this chapter compare the calculated diffusion rates of our active ingredients AZ and FDL into wax, with the diffusion rates of these AIs aided with adjuvants, Tween 20 and Finsolv TN. Diffusion rates, wax boundaries and visualization of the agrochemical diffusion were all done using an internally written piece of MATLAB code, outlined in full in Appendix A. The data, and written algorithm, also allows us to characterise the diffusion kinetics involved in the uptake of agrochemicals into wax.

Currently the majority of agrochemical research utilises chromatography techniques⁴⁶, which are both destructive and provide no spatial resolution. The ability to provide a high spatial resolution, in real-time, whilst remaining non-destructive and highly sensitive are all attributes for a viable solution, which are not matched by any singular instrumentation in the agrochemical industry, as summarised in Table 2. CRS could offer a solution to this challenge, having all the attributes required, as well as being a label-free imaging technique. Having already been applied to a range of studies in both biomedical and pharmaceutical areas including, visualizing living cells, mapping diffusion processes of drugs into human nail⁶³, mammalian skin⁶² and through seed coatings⁷⁵, SRS is shown to be a viable option for the future of the agrochemical industry. To begin this chapter, the two chosen AIs were measured using Spontaneous Raman scattering, to isolate in the silent region, which would not overlap with anything found in the wax spectra discussed in the previous chapter. Following this, there is a comparison of the signals visible

from the selected adjuvants, Finsolv TN and Tween 20, to show any peaks they contain that also do not overlap with wax or the Als. After, we show the Als uptakes into paraffin wax and plant waxes, showing both the diffusivity of these Als and also the effect changing the type of wax has on uptake kinetics. Furthermore, we explore the adjuvant uptake kinetics, and how these aid Als' diffusion, and comment on the noticeable differences between the Als and the effectiveness of adjuvant addition.

6.1 Diffusion Cell

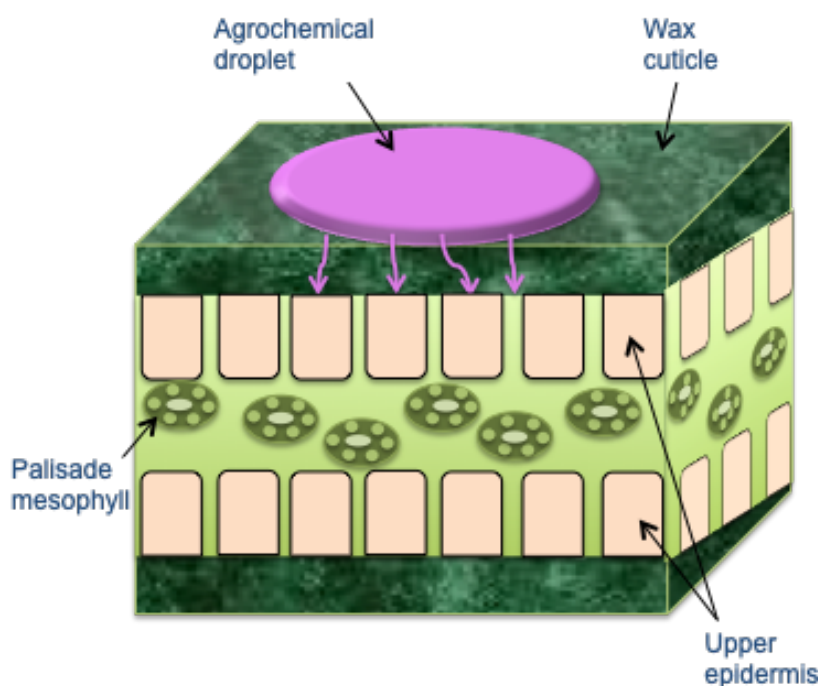


Figure 6.1: Internal structure of a typical leaf. The surface of a leaf contains waxy cuticle, epidermal cells as cover for the upper and lower surface, and palisade mesophyll to aid the absorption of light.

Figure 6.1 shows the internal structure of a typical leaf, which one must mimic in order to create a suitable model system. As mentioned previously, the leaf's

first barrier is the cuticle wax (shown in marble green), through which an agrochemical (shown in magenta) can diffuse. Hereafter we have focused on developing a diffusion cell to measure the rate through this first layer, separately from the rest of the leaf.

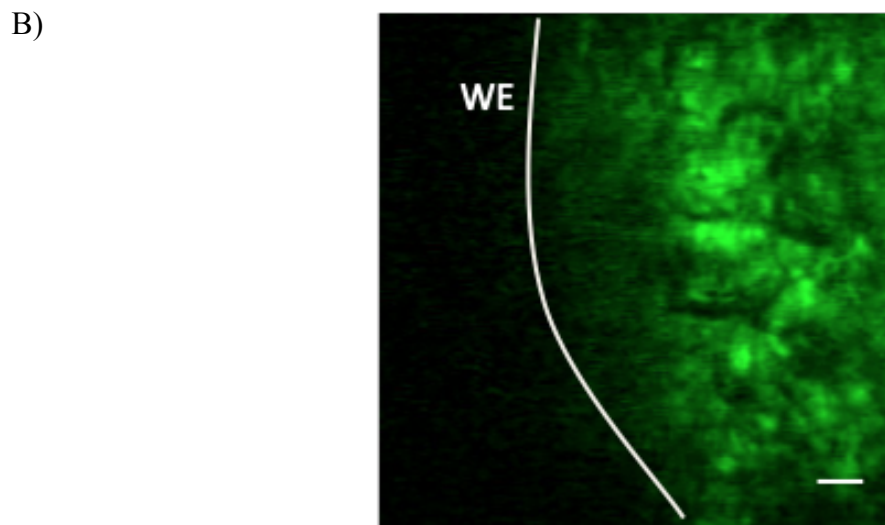
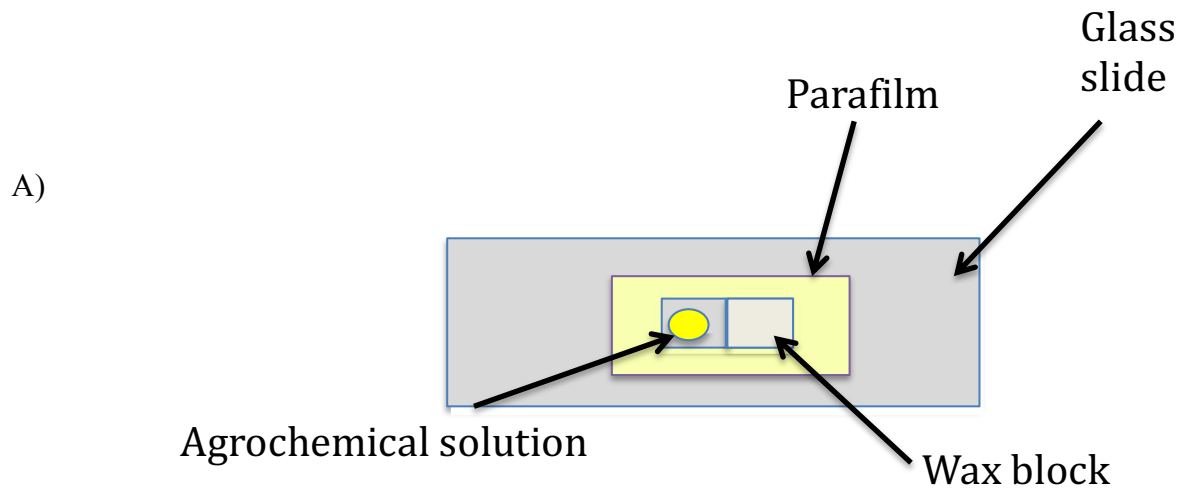


Figure 6.2: (A) Schematic of diffusion cell, made 130 μm height. (B). WE showing the edge of the wax which can be found and plotted using MATLAB code outlined in Appendix A. Background shown in black. Scale bar represents 2 μm .

Figure 6.2 (A) shows a schematic for the diffusion cell developed for this study. Applying the wax to half of the slide, and a droplet of the mixture of AI or

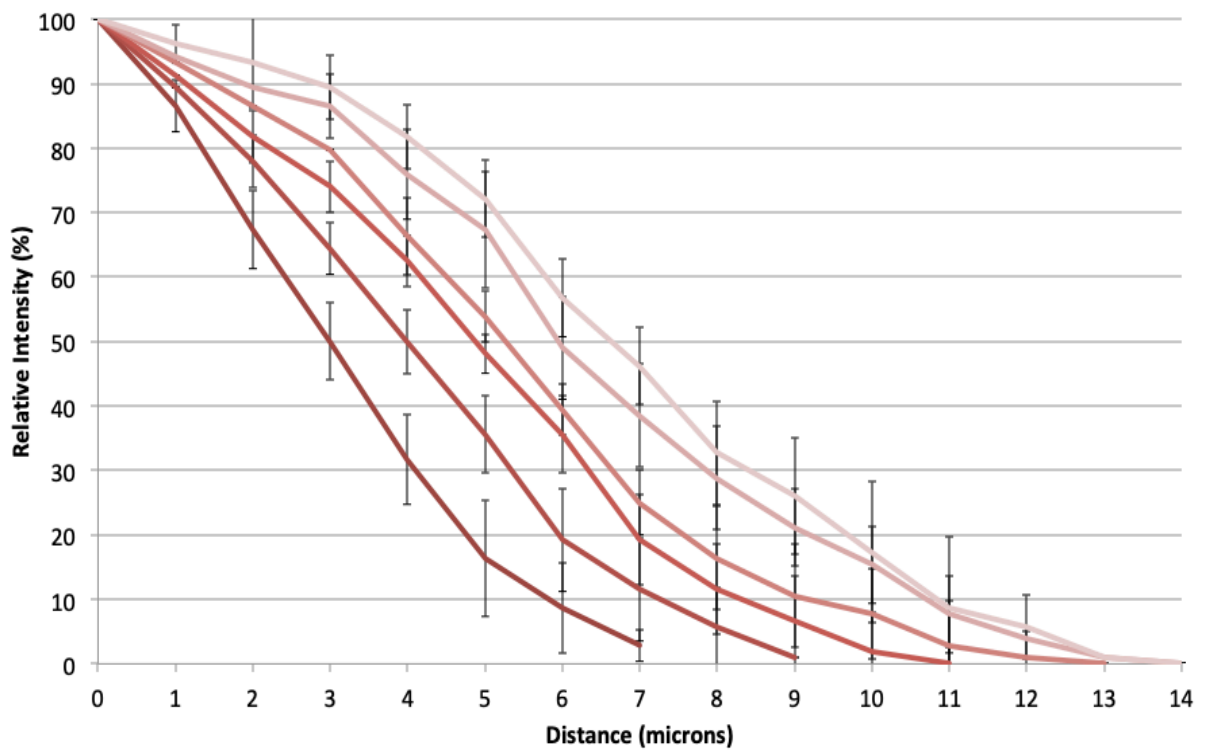
adjuvant dissolved in water, at their individual solubility limits, to the other side of the slide once the edge of the wax has been identified and focused upon, shown in Figure 6.2 (B). An image is then looped in real time until the droplet reaches the exposed wax edge, at which point a high-resolution image is taken every 60 seconds to measure both the distance travelled through the wax and the concentration of adjuvant throughout the sample.

By arranging the materials this way, one can avoid using the z direction. In 3D imaging work, continuously imaging different planes in the z direction is a time-consuming process, therefore, by eliminating the z direction we can image the same area more rapidly and further probe agrochemical movement during the moments after first contact with the wax edge. This will provide us with vital information about the initial interaction between agrochemical agent and wax, and any morphological changes in the wax. The diffusion rate and boundary detection MATLAB codes, outlined in Appendix B, provide essential insights into the varying position of the wax boundary, and help to calculate both the position of the wax boundary, and calculate the pixel per second value. And thus, allows us to gain deeper knowledge of the diffusion rates, plotted in the many of the following figures.

6.2 Paraffin vs Cuticle waxes Diffusion

This experiment measured the uptake of unaided AZ, one of our model AIs used earlier in this section, to measure the differences in uptake between the extracted waxes from grape and SM against paraffin wax's uptake of AZ.

(A)



(B)

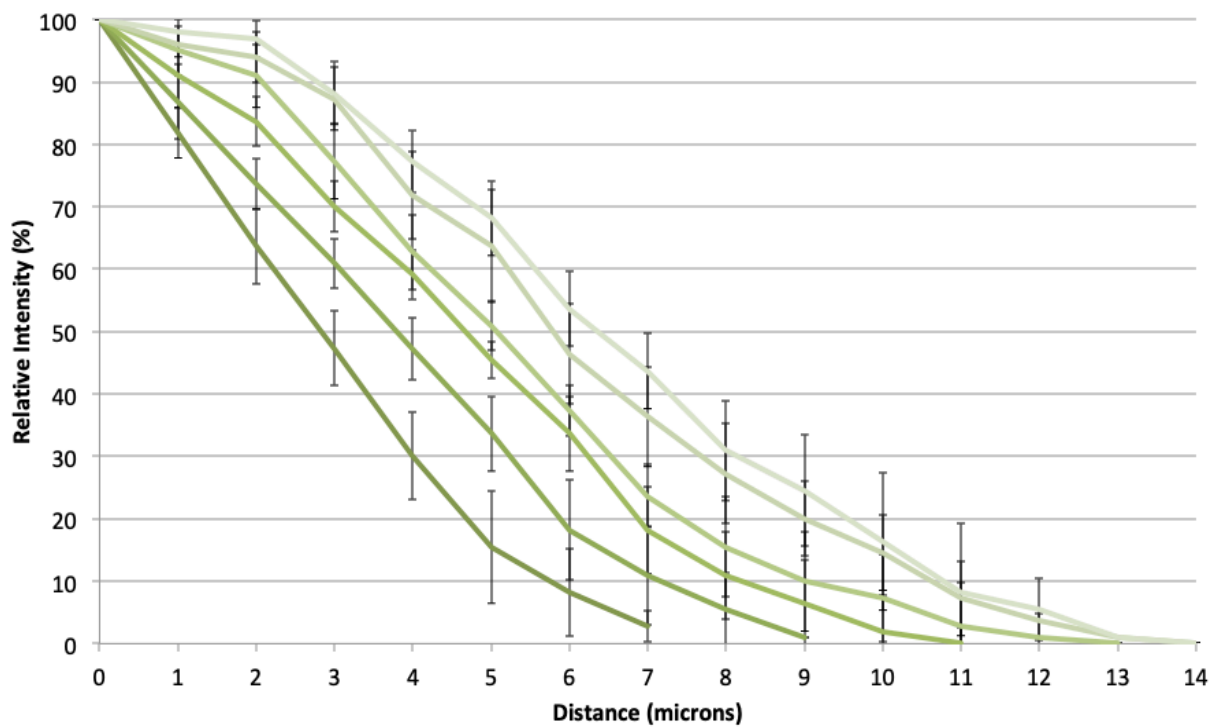


Figure 6.3: The diffusion curves for uptake of AZ into (A) Grape and (B) SM

In Figure 6.3, we see the uptake of AZ into both of these extracted waxes. These values are near identical to each other, however drastically differ from those of paraffin, which becomes clear in Figure 6.4.

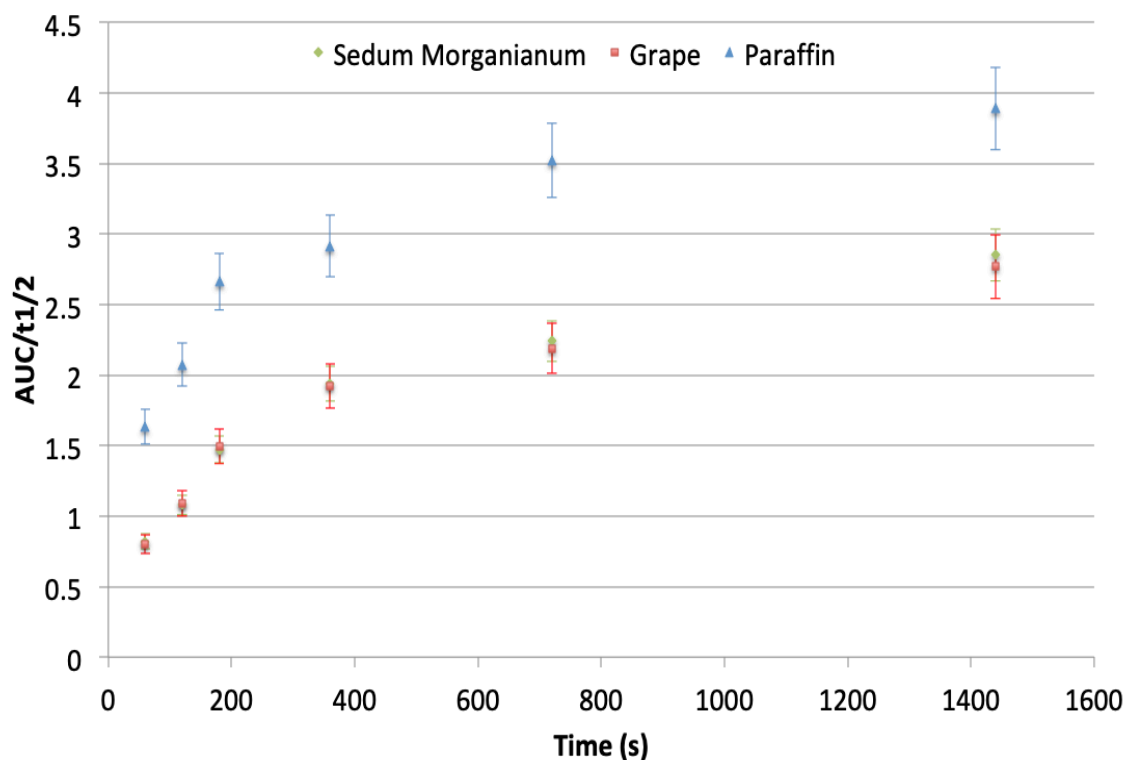


Figure 6.4: Diffusion coefficients for the uptake of AZ into SM (green), Grape (red) and paraffin (blue)

Figure 6.4, we show the diffusion coefficients for the uptake of AZ into wax, pulled from the extracted waxes diffusion curves. These are plotted alongside its paraffin counterpart.

Figure 6.4 shows the limited difference between the uptake of AZ into grape wax and SM wax, with the two sets of diffusion coefficients collapsing near-perfectly onto the same curve. What we also see, however, is the large difference in diffusion coefficient between these extracted waxes and paraffin, and therefore a large difference in uptake into the wax. However, it is clear that

the curve shapes are near identical, and thus we can conclude that our measurements in paraffin can simply apply a scalar difference to that of extracted waxes. These differences have been outlined below in Table 5.

Wax	t-60	Scale difference compared with Paraffin	t-180	Scale difference compared with Paraffin	t-720	Scale difference compared with Paraffin
	Diffusion Coefficient		Diffusion Coefficient		Diffusion Coefficient	
Paraffin	1.60	N/A	2.66	N/A	3.52	N/A
Sedum M.	0.80	2x	1.47	1.81x	2.24	1.57x
Grape	0.82	1.95x	1.50	1.77x	2.19	1.60x

Table 5: Scalable differences between the extracted wax samples, and our model system of Paraffin wax.

Table 5 shows the average diffusion coefficient at three chosen time points of 60 seconds, 180 seconds and 720 seconds, comparing the differences between their uptake pattern. From these numbers, we can scale our information to match a different wax. In this case, we can see paraffin shows around double diffusivity to the same compound uptake in *sedum morganianum* and grape.

6.3 Active Ingredients

The AIs used in this thesis, FDL and AZ, were also supplied by our partner, Syngenta, and are widely used in the industry. Here we have measured both AIs in order catalogue their different functional groups, and show they are acceptable compounds for the purpose of this thesis. As this thesis will explore the uptake of agrochemical agents into wax, we simultaneously require contrasting wax and agrochemical signatures. Thus, the key criteria for a suitable AI for this study are peak(s) that appear within the areas in paraffin wax's spontaneous Raman spectra without features, namely between 1550-1900 cm^{-1} and 2100-2800 cm^{-1} .

6.3.1 Azoxystrobin

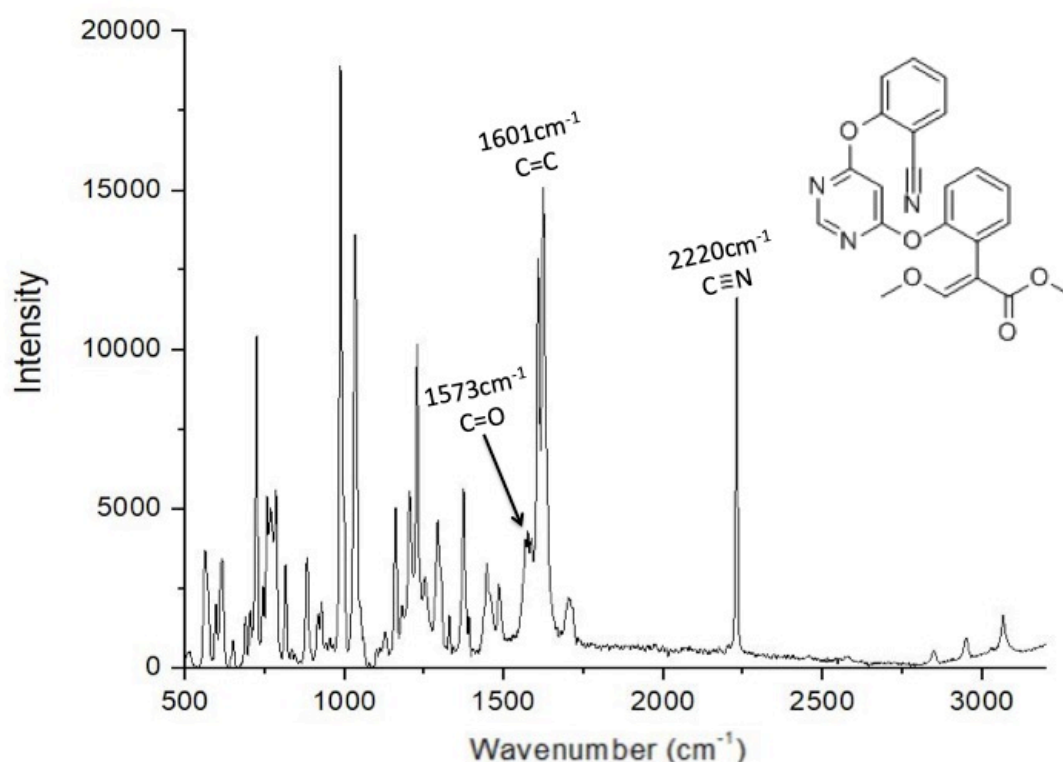


Figure 6.5: Mean Raman spectra for AI Azoxystrobin, with chemical structure and tentatively assigned peak of interest, which appears in paraffin wax's silent region.

Azoxystrobin is a methoxyacrylate compound, with structure shown in Figure 6.5, used as a preventive and curative systemic fungicide, which aids the activity against several diseases such as rusts, downy or powdery mildew, late blight and Septoria on many edible crops.

From its Raman spectra, we can see various C-O, C-C, N-H, C=N and vibrations associated with C-H bonds, all of which will fall outside our region of interest. We do, however, have a C=O and C=C stretch which do appear prominently as a branched peak in the Raman spectra, at 1573 cm^{-1} and 1601 cm^{-1} respectively. We also see a strong, well-defined peak at 2220 cm^{-1} , which we can attribute to the presence of a nitrile bond, $\text{C}\equiv\text{N}$.

6.3.2 Fludioxonil

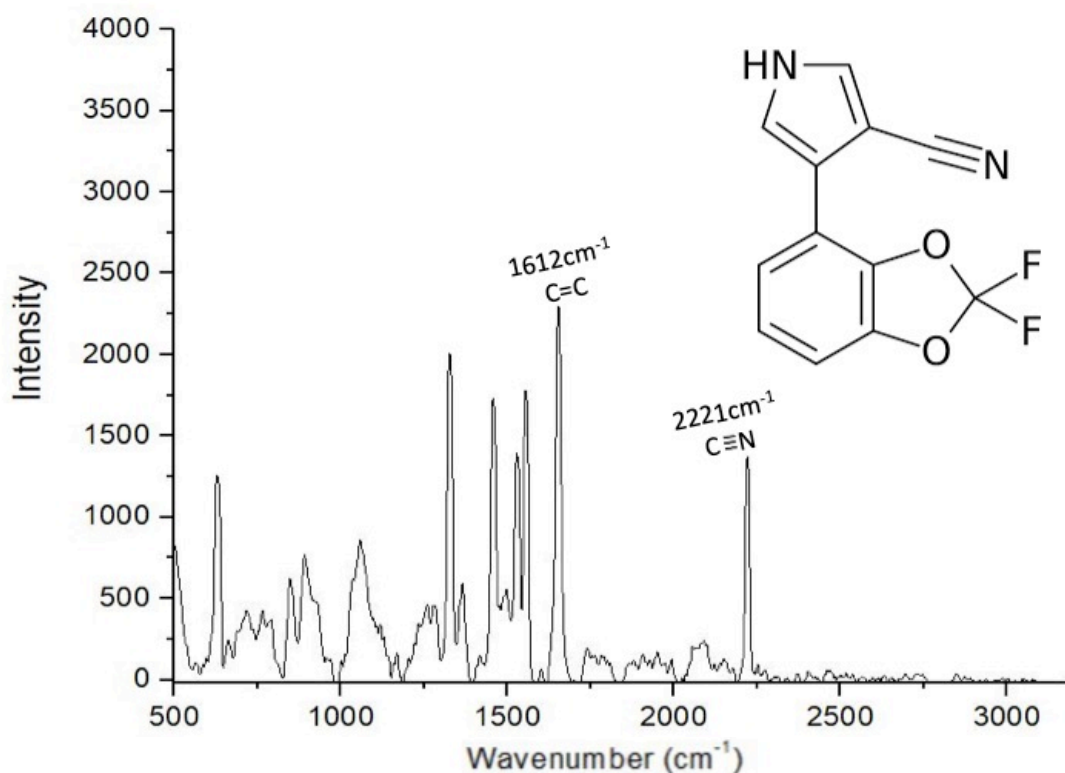


Figure 6.6: Mean Raman spectra for AI Fludioxonil, with chemical structure and tentatively assigned peak of interest, which appears in paraffin wax's silent region.

Fludioxonil, a phenylpyrrole, with structure shown in Figure 6.6, inhibits the growth of pathogens by hindering the protein kinase in the biosynthesis of glycerol and is a non-systemic fungicide, used mainly in the treatment of cereals, fruits and vegetables.

From its Raman spectra, we can see various C-O, C-C, N-H, C-N and vibrations associated with C-H and C-F bonds, all of which will fall outside our region of interest. Again, we see the presence of the aromatic C=C which do appear prominently as a peak in the Raman spectra, 1601 cm^{-1} . We also see another strong, well-defined peak at 2221 cm^{-1} , which we can attribute to the presence of a nitrile bond, $\text{C}\equiv\text{N}$.

6.3.3 Comparison and Discussion

The appearance of these strong nitrile bonds in both Azoxystrobin and Fludioxonil at 2220 cm^{-1} and 2221 cm^{-1} respectively, allows us not only to simultaneously measure the uptake of these AIs into wax using SRS, but we can also now measure the effects the adjuvants have on the AIs, and *visa versa*, by comparing the uptake at both the nitrile and carboxyl signals.

6.4 Adjuvants

Here we survey a group of common adjuvants to identify peaks of interest that do not overlap with either cuticle wax, our model system of paraffin wax, or the AIs selected in the section prior to this. The adjuvants used in this thesis were

all supplied by our partner, Syngenta, and are widely used in the industry. Each will have information about its uses in industry and its key functionalities such as retention, enhanced uptake, humectancy, wetting and spreading properties. Here we have measured various adjuvants in order catalogue their different functional groups, and find acceptable compounds for the purpose of this thesis. As this thesis will explore the uptake of agrochemical agents into wax, we simultaneously require contrasting wax and agrochemical signatures. Thus, the key criteria for a suitable adjuvant for this study are peak(s) that do not overlap with paraffin wax's spontaneous Raman spectra, namely between $1550\text{-}1900\text{ cm}^{-1}$ and $2100\text{-}2800\text{ cm}^{-1}$.

6.4.1 Acetophenone

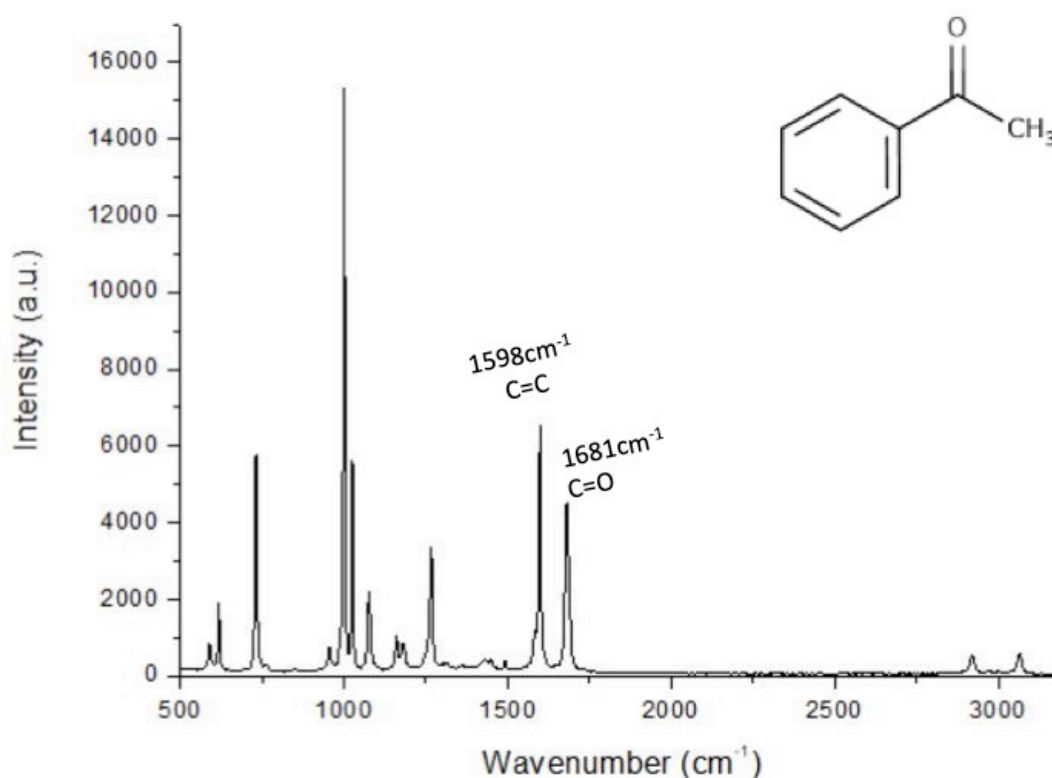


Figure 6.7: Mean Raman spectra for adjuvant Acetophenone, with chemical structure and tentatively assigned peaks of interest, which appear in paraffin wax's silent region.

Acetophenone is the simplest aromatic ketone, with structure shown in Figure 6.7. It is used in the agrochemical industry as a sensitising adjuvant known for its ability to improve photolysis of herbicides⁷⁶ and can also contribute to the sweet taste and smell of various fruits when applied.

Acetophenone's Raman spectrum gives us two peaks of interest. Both the peak at 1598 cm^{-1} and 1681 cm^{-1} fall inside the paraffin wax silent region and can be assigned to the C=C bonds in the phenyl group, and the C=O from the ketone group respectively.

6.4.2 Aerosol OT-B

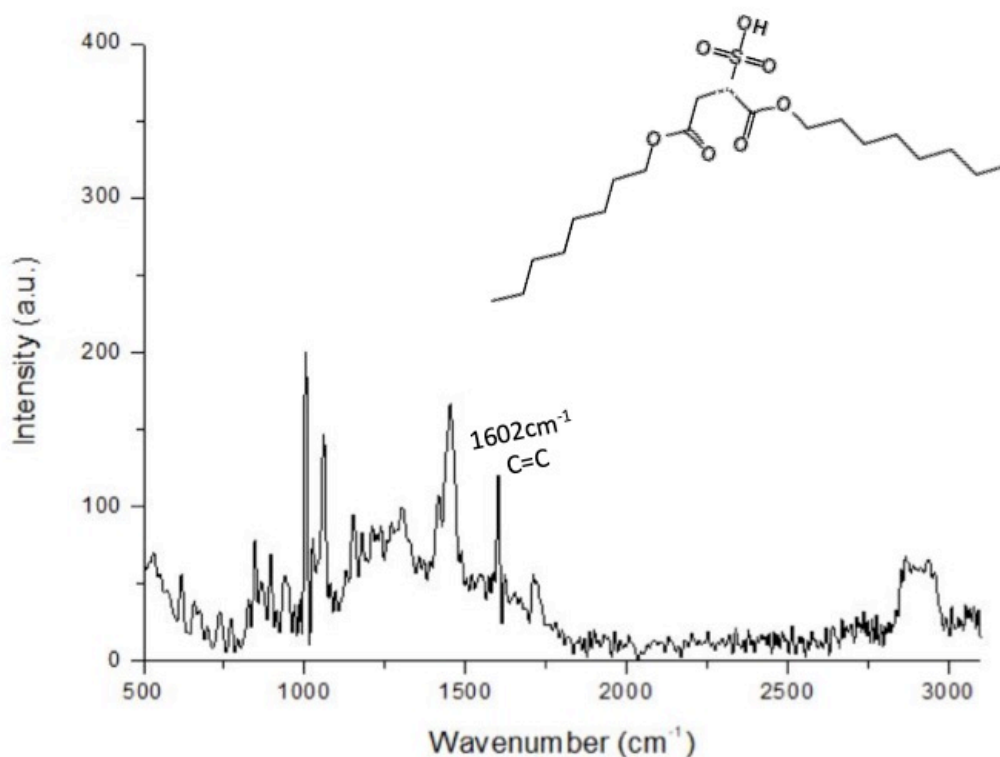


Figure 6.8: Mean Raman spectra for adjuvant Aerosol OT-B, with chemical structure and tentatively assigned peak of interest, which appears in paraffin wax's silent region.

Aerosol OT-B is used in the agrochemical industry as a wetting agent, softener and emulsifier which can provide surface modifying properties to an agrochemical, allowing increased absorbency and penetration into a leaf.

Its Raman spectra provides us with only one rather weak peak of interest at 1602cm^{-1} which can be assigned to the C=O vibration.

6.4.3 Brij O10

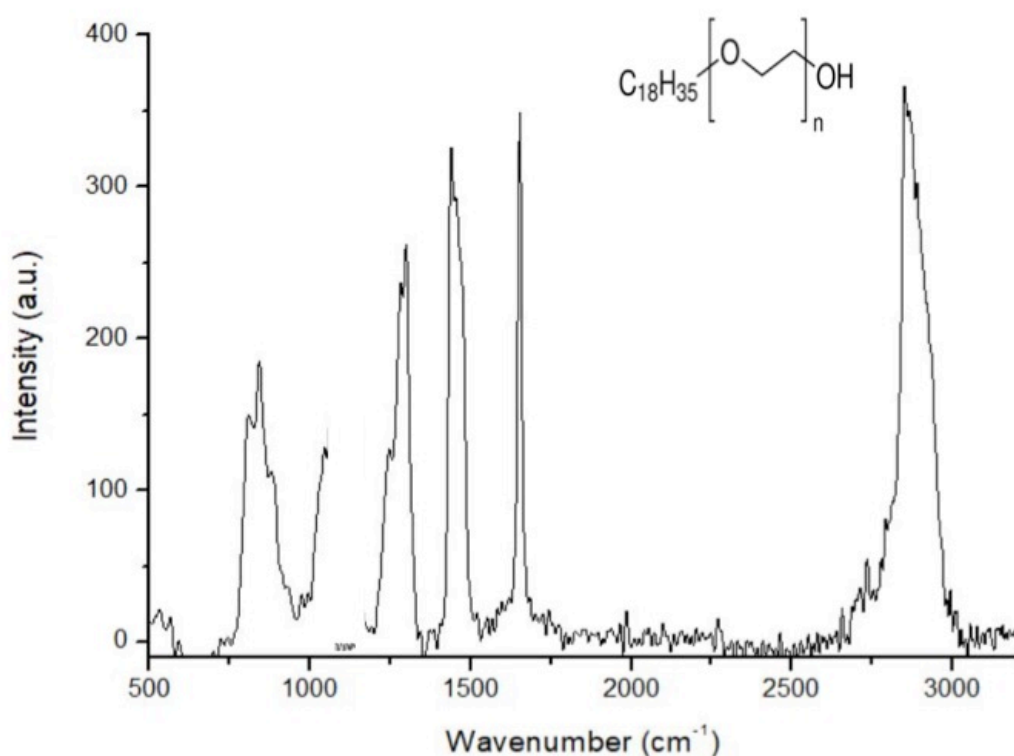


Figure 6.9: Mean Raman spectra for adjuvant Brij O10, with chemical structure and no tentatively assigned peaks of interest, as no recognised unique vibrations appear in paraffin wax's silent region.

Brij O10 is derived from alcohol ethoxylate, which is used in the agrochemical industry as non-ionic surfactant, in the emulsification or dispersion of a two-phase system.

Figure 6.9 shows the mean Raman spectra for this compound, in this case we do not see any prominent peaks in paraffin wax's silent region. The majority of these peaks, C-O, O-H and ones associated with various C-H vibrations, appear in the fingerprint region, which would not contrast against the peaks from paraffin.

6.4.4 Emulsogen EL360

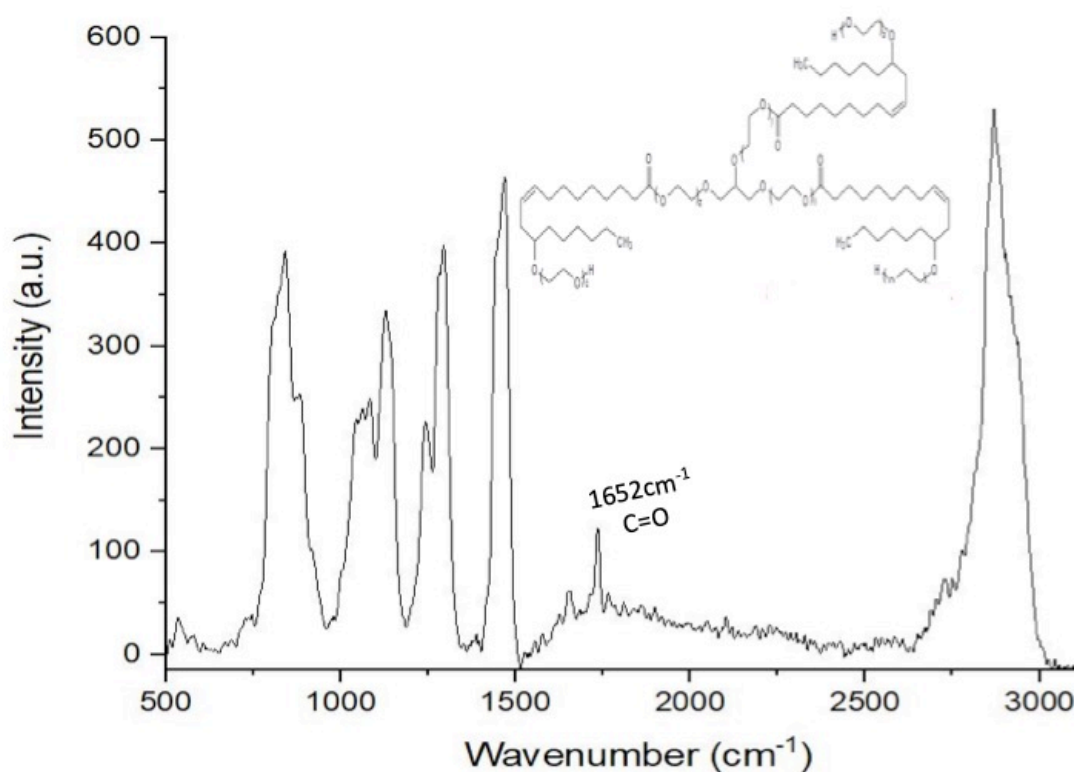


Figure 6.10: Mean Raman spectra for adjuvant Emulsogen, with chemical structure and tentatively assigned peak of interest, which appears in paraffin wax's silent region.

Emulsogen EL360 has uses as an emulsifier, particularly useful in the emulsification of biocides. Emulsogen EL360 is seen as a more economical adjuvant due to its combinations proving more adaptable than any individual emulsifier.

Its structure, shown above in Figure 6.10, shows a long-branched compound, with C=O peaks, which can be seen in the Raman spectra at 1652 cm^{-1} , all other vibrations appear outside the scope of interest, i.e. before 1550 cm^{-1} or after 1900 cm^{-1} .

6.4.5 Finsolv TN

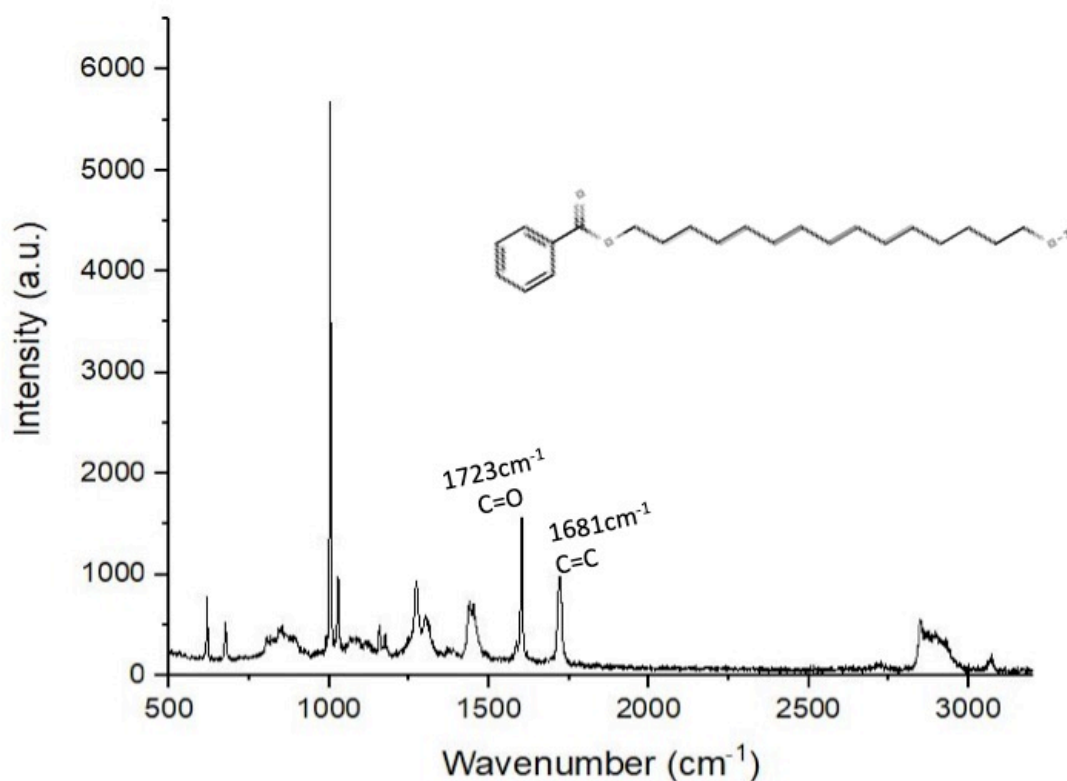


Figure 6.11: Mean Raman spectra for adjuvant Finsolv TN, with chemical structure and tentatively assigned peaks of interest, which appear in paraffin wax's silent region.

Finsolv TN is an aromatic ester, with structure shown above in Figure 6.11, which is utilised in the agrochemical industry due to its multiple functions as a non-toxic water-insoluble emollient. Aromatic esters were, until relatively recently considered only as solvents, however, their lipophilic nature hands themselves perfectly to the penetration of cuticular wax.

Above, we see the Raman spectra for Finsolv TN with two prominent peaks of interest for the C=O vibration, appearing at 1723 cm^{-1} , and a peak associated with C=C, at 1681 cm^{-1} .

6.4.6 Genagen (DMLA)

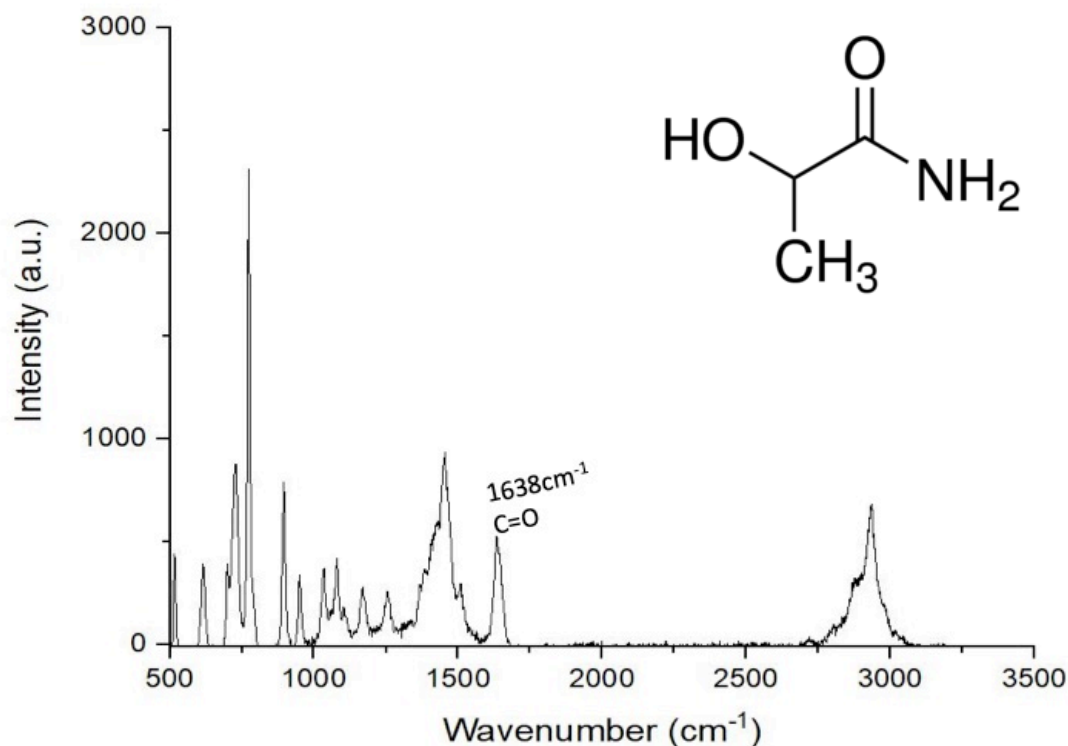


Figure 6.12 Mean Raman spectra for adjuvant Gengagen DMLA, with chemical structure and tentatively assigned peak of interest, which appears in paraffin wax's silent region.

Gengagen DMLA is a simple lactamide, with structure shown in Figure 6.12. It finds use in the agrochemical industry for its versatility as a non-water miscible solvent, used primarily in triazole fungicides, preventing crystallisation and supports emulsion stabilization.

In its Raman spectra, we see a peak of interest at 1638 cm^{-1} that coincides with the C=O vibration.

6.4.7 Hexamoll Dinch

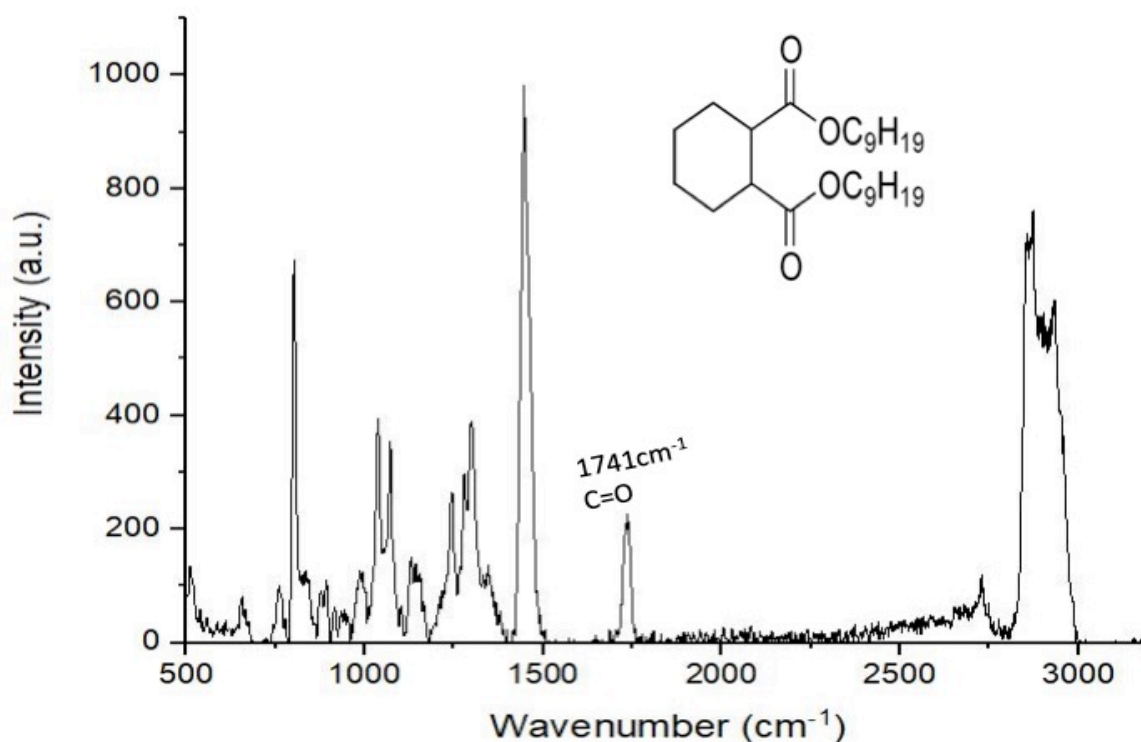


Figure 6.13: Mean Raman spectra for adjuvant Hexamoll Dinch, with chemical structure and tentatively assigned peak of interest, which appears in paraffin wax's silent region.

Hexamoll Dinch is an ester, used in the agrochemical industry as a plasticiser and impact modifier, changing the viscosity of a material or altering their physical properties.

The structure of this compound, shown in Figure 6.13, tells us we have multiple C=O peaks, which we do see appear at 1741 cm⁻¹. Its other signatures, such as C-O and C-H peaks, would appear outside the scope of interest, 1550-1900 cm⁻¹.

1.

6.4.8 Methyl Oleate

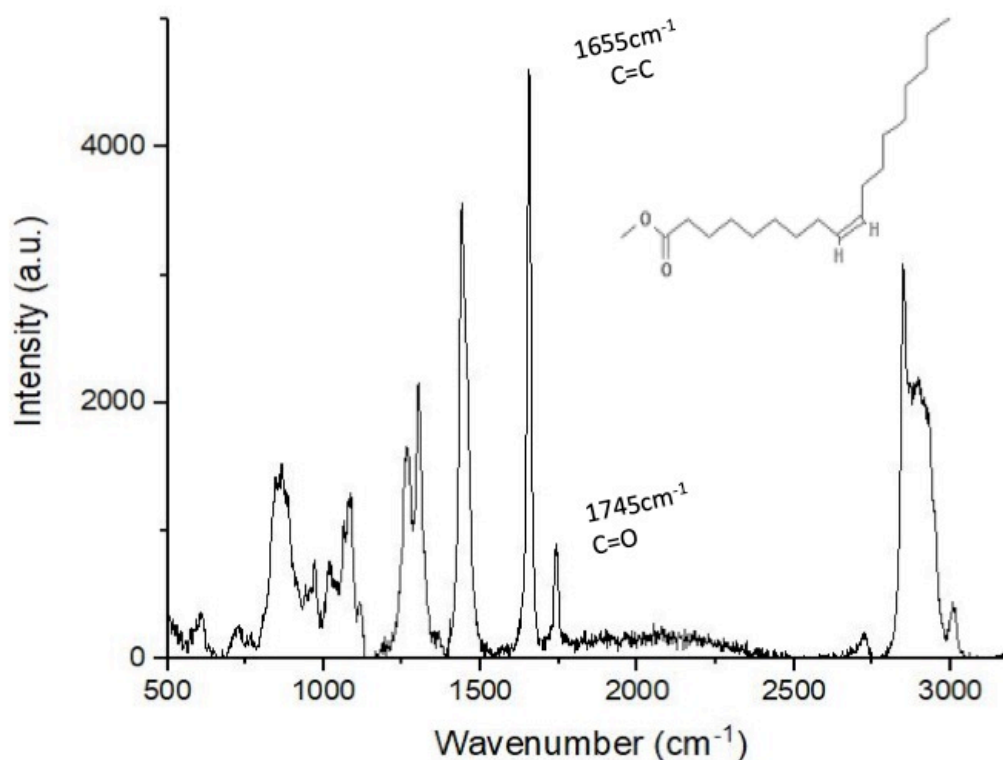


Figure 6.14: Mean Raman spectra for adjuvant Methyl Oleate, with chemical structure and tentatively assigned peaks of interest, which appear in paraffin wax's silent region.

Methyl Oleate is another ester, however differs in function to Hexamoll Dinch as it is used as an emulsifier or solvent. As a solvent, it has various traits that aid the uptake of an active ingredient, such as improving absorbability and wettability whilst reducing the adhesion coefficient.

The structure of Methyl Oleate, shown above in Figure 6.14, shows two peaks we know appear in our silent region, those associated with C=C and C=O, which appear at 1655 cm⁻¹ and 1745 cm⁻¹ respectively.

6.4.9 Nansa EVM

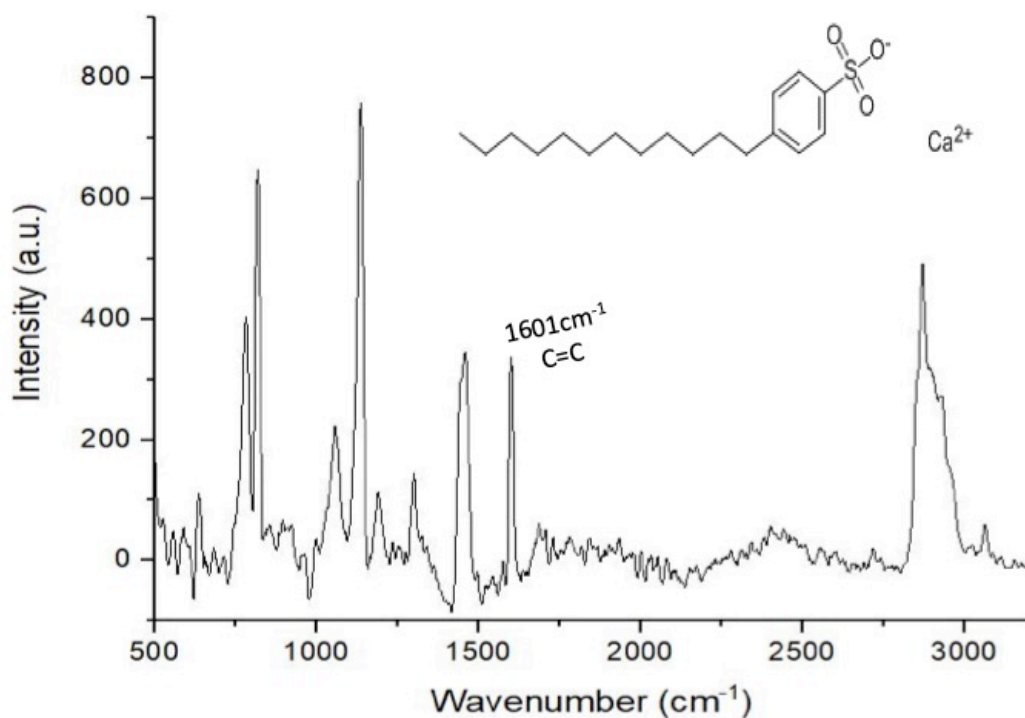


Figure 6.15: Mean Raman spectra for adjuvant Nansa EVM, with chemical structure and tentatively assigned peak of interest, which appears in paraffin wax's silent region.

Nansa EVM is a non-ionic surfactant amine salt. As its calcium salt, it has a low hydrophile-lipophile balance, meaning it's less water-soluble. Therefore, it has found uses as an emulsifier and wetting agent in dry and liquid formulations in the agrochemical industry.

Its structure, shown in Figure 6.15, shows the presence of aromatic C=C bonds, which can be seen in the mean Raman spectra, appearing at 1601 cm⁻¹.

6.4.10 Pluronic PE 10400

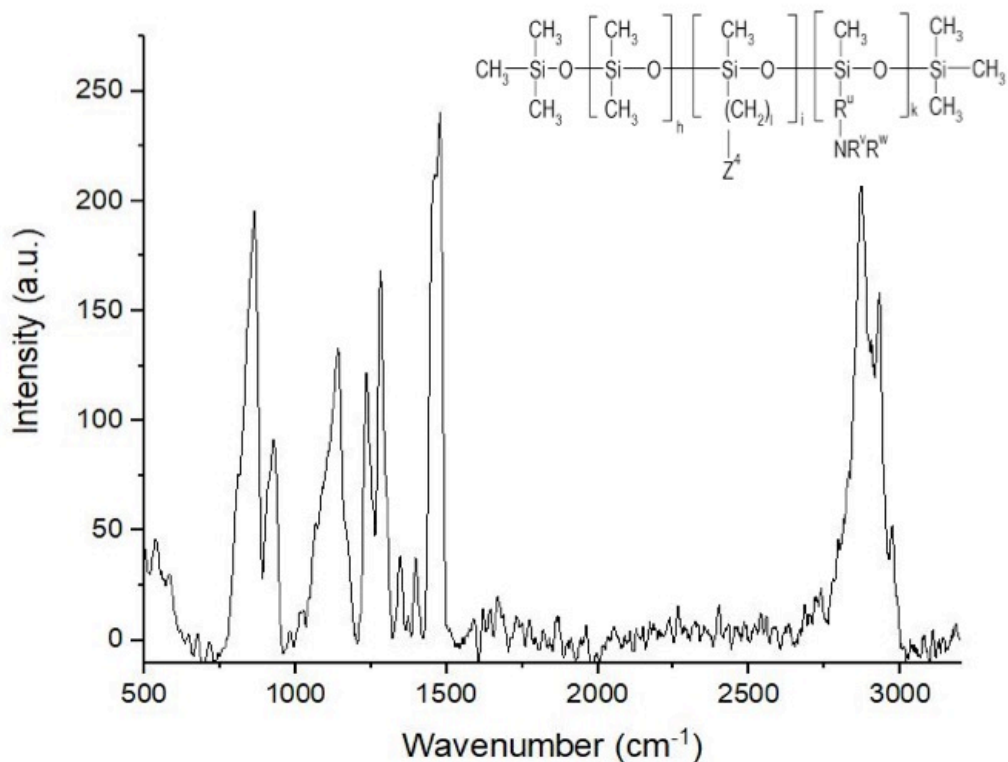


Figure 6.16: Mean Raman spectra for adjuvant Pluronic PE10400, with chemical structure and no tentatively assigned peaks of interest, as no recognised unique vibrations appear in paraffin wax's silent region.

Pluronic products are used in the agrochemical industry as low-foaming, non-ionic dispersants and emulsifiers, with an unlimited controlled hydrophile-lipophile balance. The Pluronic PE types conform to a structural formula however are designated a four or five-digit number to classify. The start digit(s) signify a scale for molecular weight between 850 and 3250 g/mol, whereas the last three show the percentage of polyethylene glycol in the molecule, divided by 10. With this, we can say our molar mass is 3250 g/mol, with percentage of polyethylene glycol at 40%.

The structure, therefore, can be derived from this, and we can see the lack of vibrations in our area of interest in the mean Raman spectra, shown in Figure 6.16.

6.4.11 Silwet L77

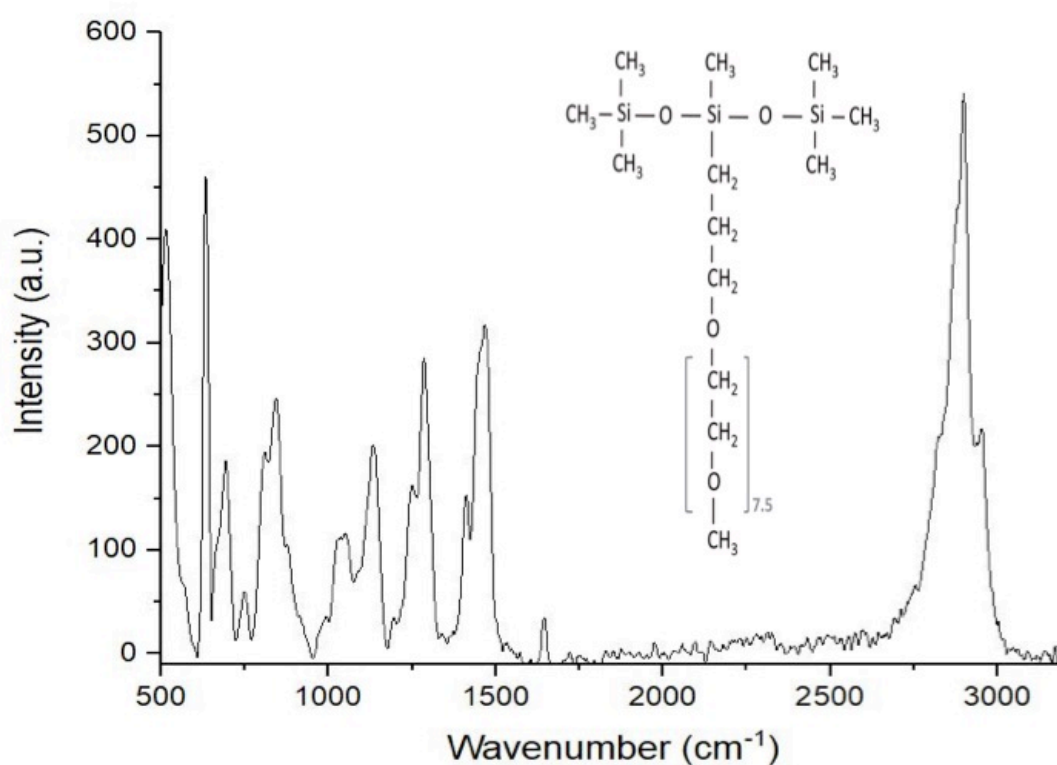


Figure 6.17: Mean Raman spectra for adjuvant Silwet L77, with chemical structure and no tentatively assigned peaks of interest, as no recognised unique vibrations appear in paraffin wax's silent region.

Silwet L77 has a similar structure to that of Pluronic PE 10400, and has a similar function, although is specifically designed as a spreading aid, as it reduces surface tension.

With similarities to Pluronic PE10400, however, it does not have any prominent peaks within our silent region that can be used for this thesis.

6.4.12 Soprophor BSU

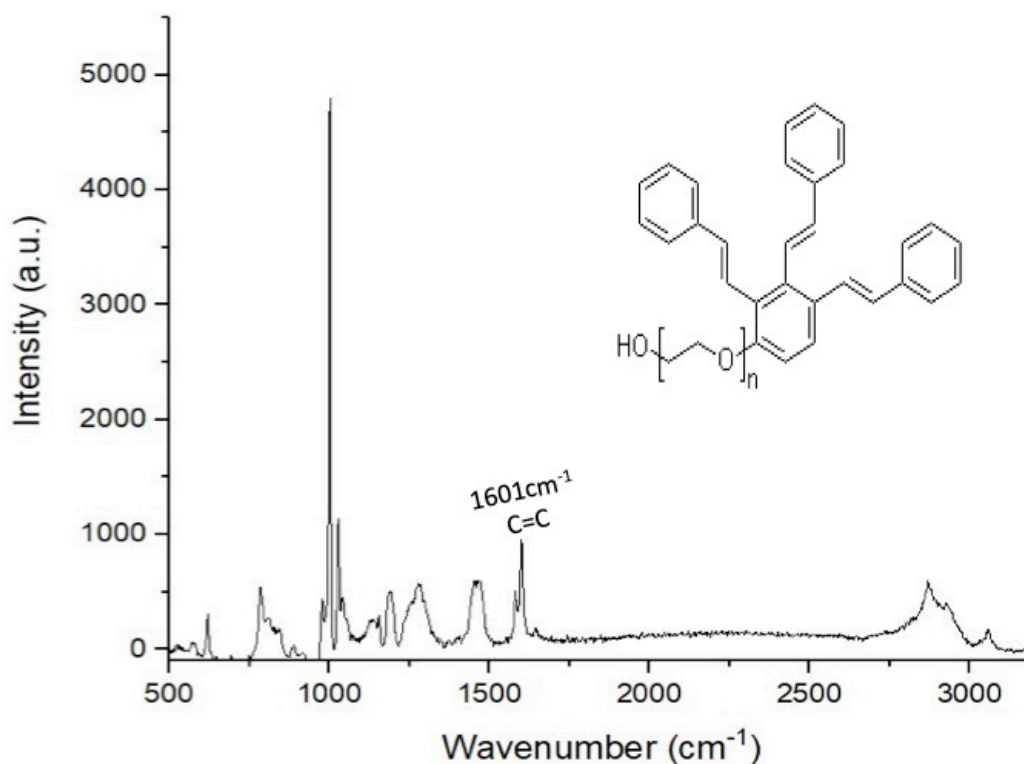


Figure 6.18: Mean Raman spectra for adjuvant Soprophor BSU, with chemical structure and tentatively assigned peak of interest, which appears in paraffin wax's silent region.

Soprophor BSU is an ethoxylate that is used in the agrochemical industry as a non-ionic emulsifier, dispersant and suspending agent, with structure shown above in Figure 6.18. This structure shows the presence of multiple aromatic and aliphatic C=C vibrations, which appear as a branched peak at 1601cm⁻¹.

6.4.13 Tween 20

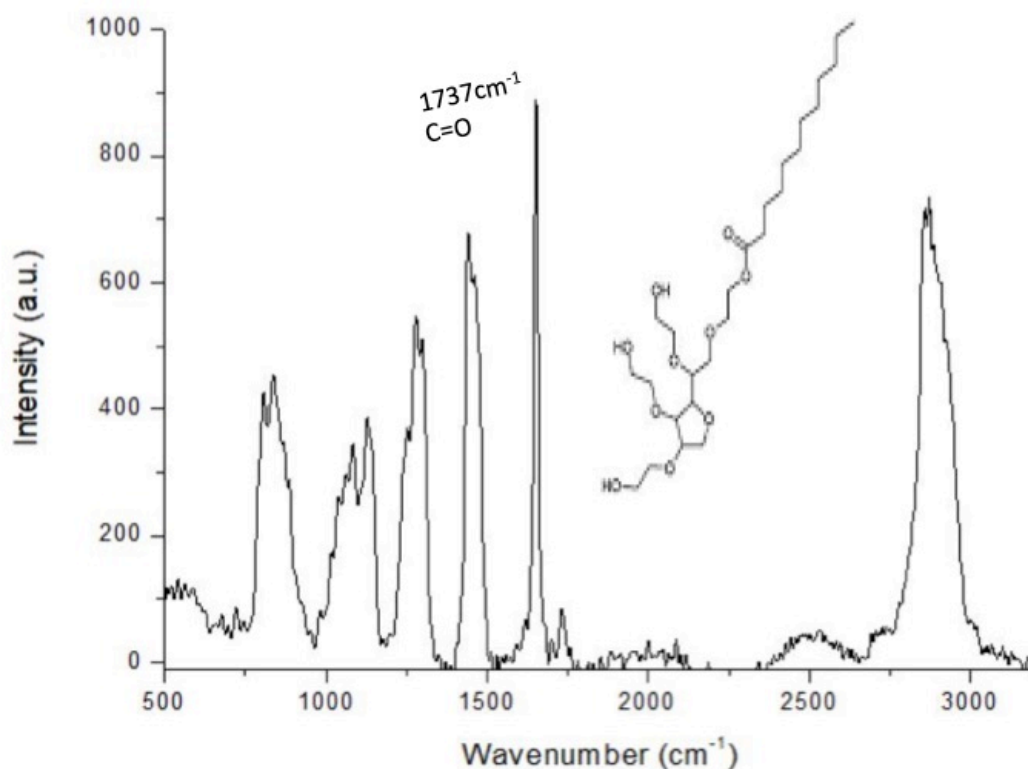


Figure 6.19: Mean Raman spectra for adjuvant Tween 20, with chemical structure and tentatively assigned peak of interest, which appears in paraffin wax's silent region.

Tween 20 is a polysorbate, which are known for delivering multiple key functionalities such as retention, enhanced uptake, humectancy, wetting and aiding the spreading of agrochemicals.

From its structure, shown in Figure 6.19, we can see various C-O, O-H, C-C and C-H bonds, all of which will fall outside our region of interest. We do, however, have a C=O stretch which does appear prominently in the Raman spectra, at 1737cm⁻¹.

6.5 Comparison and Discussion

From these mean Raman spectra, we can firstly discount Brij O10, Pluronic PE10400 and Silwet L77 from this study, due to the lack of peaks in our area of interest. For the study of these compounds, we would most likely have to utilise fluorescent labeling or autoradiography techniques, which were discussed in Chapter 2. For the simultaneously imaging of wax and an adjuvant, it is essential to have contrasting peaks. However, here we have 10 adjuvants that contain peaks that appear within our region of interest, namely Acetophenone, Aerosol OT-B, Emulsogen EL360, Finsolv TN, Gengagen DMLA, Hexamoll Dinch, Methyl Oleate, Nansa, EVM, Soprophor BSU and Tween 20. Out of these, however, only Finsolv TN, Tween 20, Methyl Oleate and Acetophenone show very strong or defined peaks in this region.

From these, Tween 20 and Finsolv TN were identified as adjuvants that would be of interest to take further in this thesis, summarised in Table 6 alongside the chosen AIs. In the following sections we explore the differences between the uptake of the two chosen adjuvants and the effects they have on the uptake of the AIs in paraffin wax.

	Active Ingredient		Adjuvant	
	AZ	FDL	Tween 20	Finsolv TN
Molecular Formula	$C_{22}H_{17}N_3O_5$	$C_{12}H_6F_2N_2O_2$	$C_{38}H_{114}O_{26}$	$C_{22}H_{36}O_3$
Molecular Weight (g/mol)	403.39	248.19	1227.51	348.53
Solubility Limit (mg/L)	6.7	1.8	6	1.1
Density (g/cm ³)	1.25	1.54	1.1	0.928
pH	6.4	8.6	6.1	6.2
Melting/Boiling Point (°C)	115	199.8	100	300
Surface Tension (Dynes/cm)	66.6	62.3	33	31.5

Table 6: Active Ingredient and adjuvant chemical properties.

6.6 Agrochemical Formulation Solutions into Paraffin Wax

We utilise the same method of sample preparation shown in Figure 6.1, applying the wax to half of the slide, and now applying a droplet of the AI dissolved in water, at its individual solubility limit, to the other side of the slide once the edge of the wax has been identified and focused upon. An image is then looped in real time until the droplet reaches the exposed wax edge, at which point a high-resolution image is taken every 60 seconds to measure both the distance travelled through the wax and the concentration of adjuvant throughout the sample.

6.6.1 Azoxystrobin

As discussed in section 6.3.1, Azoxystrobin is a methoxyacrylate compound, which showed the presence of both C=O and C=C stretch which do appear prominently as a branched peak in the Raman spectra, at 1573 cm⁻¹ and 1601

cm^{-1} respectively. However, we saw a very intense and well-defined peak at 2220 cm^{-1} , which we attributed to the presence of a nitrile bond, $\text{C}\equiv\text{N}$. Using the CARS equation shown in Chapter 2 to get tune our pump beam to 839.6 nm , whilst our Stokes beam remains fixed at 1032 nm , we can image this vibration, shown in Figure 6.20. A droplet of AZ, dissolved in water at concentration 6.7 mg/L , is imaged in (B), showing the intense signal given at this wavenumber. Alongside in (A), an off-resonance image showing the complete lack of signal when tuned away from this peak, found after a hyperspectral of the wavenumber range was performed.

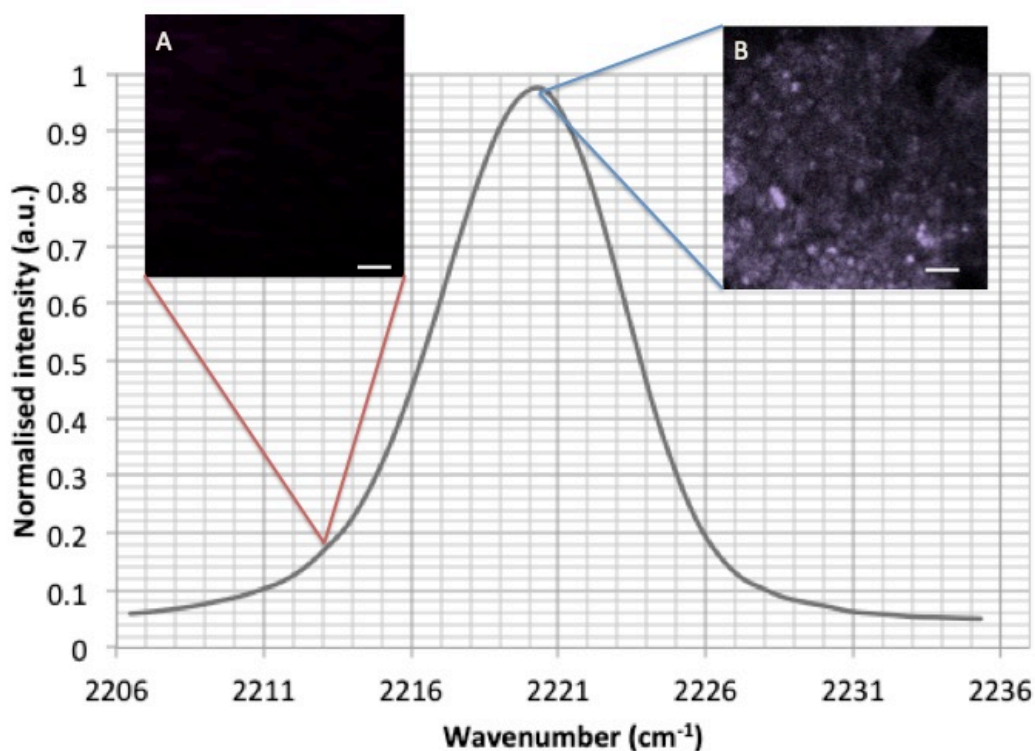


Figure 6.20: Hyperspectral data for a droplet of AZ in water imaged by SRS at its signal at the spontaneous Raman peak at 2220 cm^{-1} , corresponding with the $\text{C}\equiv\text{N}$ vibration. (A) Shows the off-resonance image with (B) showing intense resonance from the peak.

Figure 6.20 (A), a superimposed pseudo-coloured map, displays the depth penetration signal at each scan for the different AIs over the time period of 720 seconds. These signals, recorded at 6 different time-points between 0 and 12 minutes, are represented each by a separate colour on the visible spectrum scale shown in Figure 6.21 (A) with; blue corresponding to the measurement at $t = 0$ seconds, cyan to that at $t = 60$ seconds and so on. This was prepared using ImageJ's transparent zero function to generate an uptake image for AZ into paraffin wax. Columns 1-3 represent repeats to confirm accuracy. Figure 6.21 (B) shows AZ (pseudo-colour: magenta) at different time-points during the 12 minutes, diffusing into the wax (pseudo-colour: green).

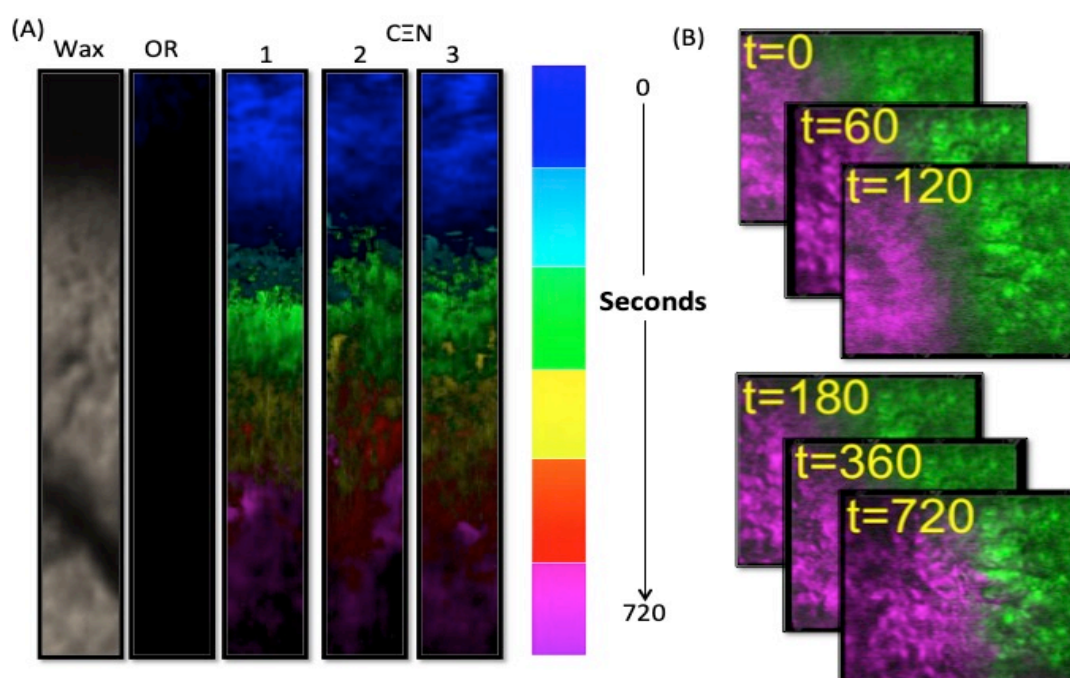


Figure 6.21: (A) SRS x-y images of the penetration depth into three wax samples as a function of time. The spectrum indicates the signal from CEN recorded every 60 seconds for a total of 720 seconds, from the initial contact. The colour spectra labelled 1-3 show various repeats. The untreated wax is shown on the far left (labelled wax) and the off resonance is to its immediate right (labelled OR). Scale bar, 2 μm . (B) Shows the diffusion of AZ into wax,

over 720 seconds, imaged with Coherent Raman scattering images of paraffin wax's CH₂ (CARS, green) and AZ's chemically specific C≡N (SRS, magenta). Field of view 129.3 μm².

Using the pseudo-coloured x-y planar images again, one can produce diffusion curves for both concentration, relative to signal intensity, and distance travelled, over time, shown in Figure 6.22.

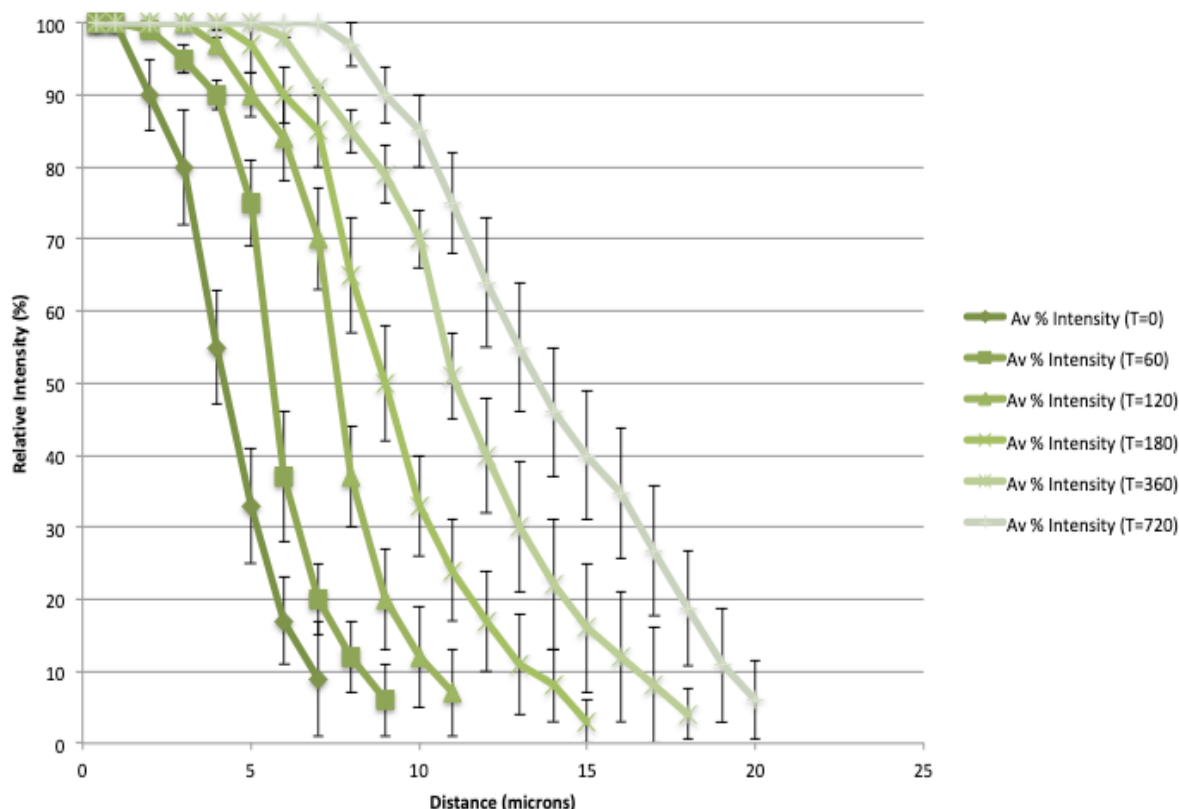


Figure 6.22: Diffusion depth profile for AZ, as a function of time, into paraffin wax.

These profiles allow us to compare the unaided AIs and adjuvants, and calculate their unique diffusion coefficients, shown in Figure 6.23.

Initial contact (t=0) is shown as the darkest green line, and then the lightness of the line corresponds to a longer time-point. We can see the progression of the

AI penetrate through the wax, however, it is clear the diffusion flux is far lower than that of the adjuvants.

This experiment was repeated and averaged to give a margin of error for these profiles, which we then use to compare the unaided AIs and adjuvants, and calculate their unique diffusion coefficients, which for AZ is shown in Figure 6.23.

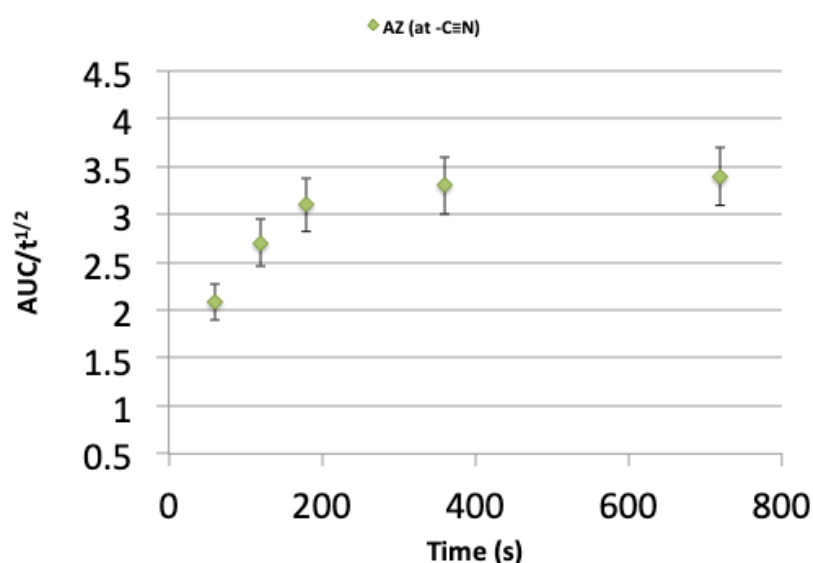


Figure 6.23: The area under the curve divided by the square root of time provides us with diffusion coefficients over time, for AZ into paraffin wax

Once more, by using these diffusion coefficients, we can fit the data with diffusion theory to obtain quantitative diffusion characteristics of cuticle wax-active ingredient interactions. Predicted evolution of the SRS signal following the same assumptions mentioned for Finsolv TN, would allow us to predict the evolution of the SRS signal as the diffusion proceeds. However experimentally, as time increases, again, so does the diffusion coefficient, meaning a substantial deviation from this law, which would show a constant diffusion coefficient independent from time. This provides argument for non-Fickian

diffusion, as spoken about in Chapter 2, with a diffusion coefficient that appears time dependent.

6.6.2 Fludioxonil

In section 6.1.2 we discussed Fludioxonil, a phenylpyrrole, which showed various C-O, C-C, N-H, C-N and vibrations associated with C-H and C-F bonds, all of which will fall outside our region of interest. However, again we saw the presence of a nitrile bond, which appeared as a strong, well-defined peak at 2221 cm^{-1} . Tuning our pump beam to 839.6 nm , whilst our Stokes beam remains fixed at 1032 nm , we can image this vibration, shown in Figure 6.24. A droplet of FDL, dissolved in water at concentration 1.8 mg/L , is imaged in (B), showing the intense signal given at this wavenumber. Alongside in (A), an off-resonance image showing the complete lack of signal when tuned away from this peak, found after a hyperspectral of the wavenumber range was performed.

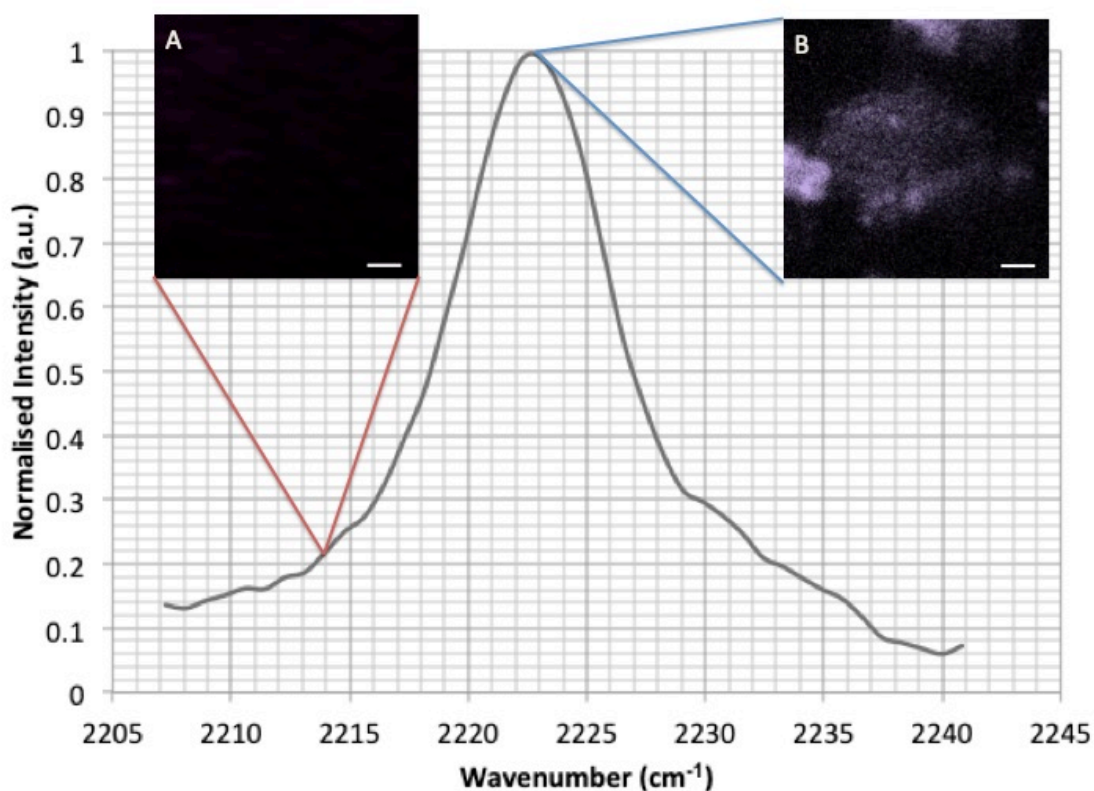


Figure 6.24: Hyperspectral data for a droplet of FDL in water imaged by SRS at its signal at the spontaneous Raman peak at 2221 cm^{-1} , corresponding with the $\text{C}\equiv\text{N}$ vibration. (A) Shows the off-resonance image with (B) showing intense resonance from the peak.

Figure 6.24 represents a superimposed pseudo-coloured map, displays the depth penetration signal at each scan for the different AIs over the time period of 720 seconds. These signals, recorded at 6 different time-points between 0 and 12 minutes, are represented each by a separate colour on the visible spectrum scale shown in Figure 6.25 with; blue corresponding to the measurement at $t = 0$ seconds, cyan to that at $t = 60$ seconds and so on. This was prepared using ImageJ's transparent zero function to generate an uptake image for AZ into paraffin wax. The three coloured columns represent repeats to confirm accuracy.

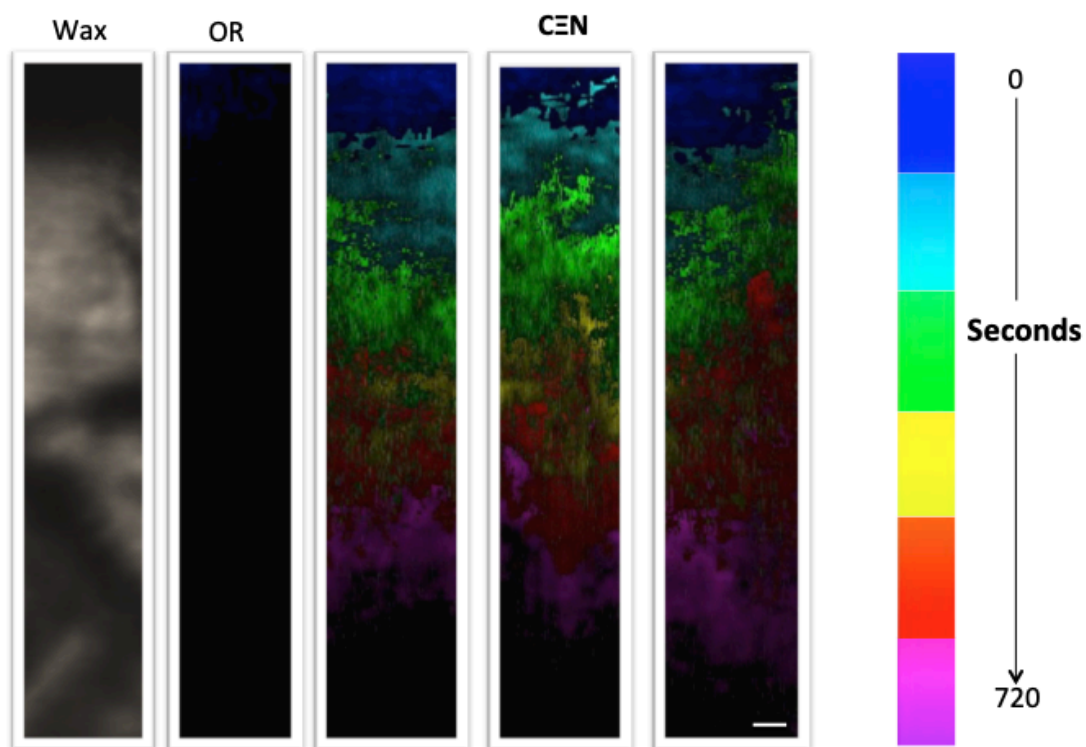


Figure 6.25: SRS x-y images of the penetration depth of FDL into three wax samples as a function of time. The spectrum indicates the signal from CEN recorded every 60 seconds for a total of 720 seconds, from the initial contact. The three colour spectra show repeats. The untreated wax is shown on the far left (labelled wax) and the off resonance is to its immediate right (labelled OR). Scale bar, 2 μ m.

Using the pseudo-coloured x-y planar map, one can produce diffusion curves for both concentration, relative to signal intensity, and distance travelled, over time, shown in Figure 6.26.

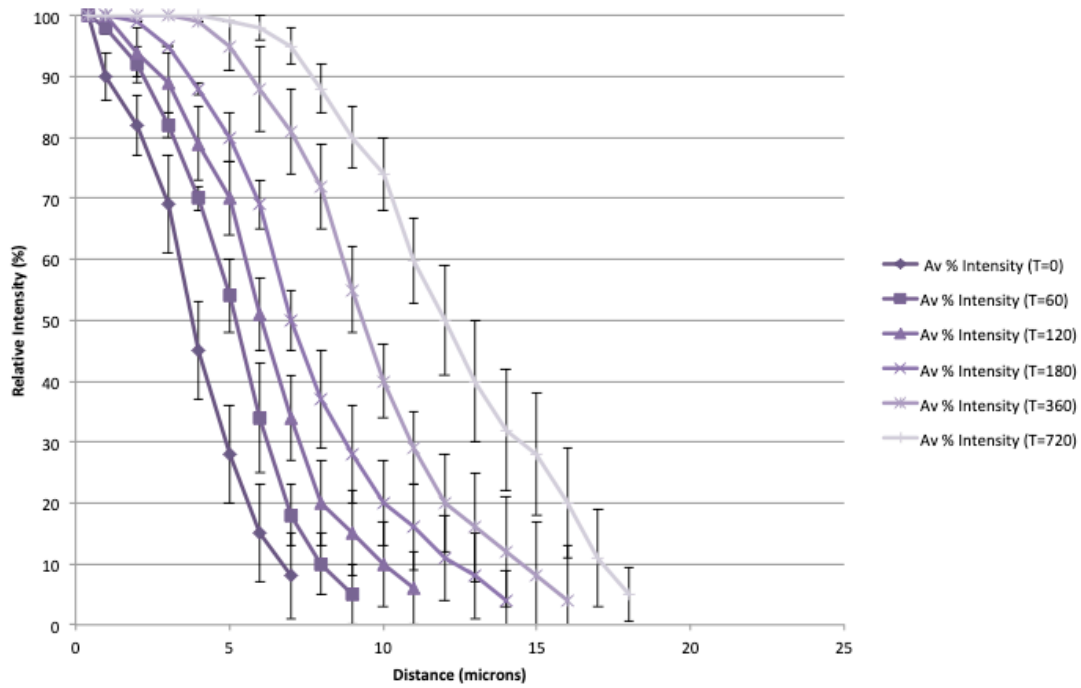


Figure 6.26: Diffusion depth profile for FDL, as a function of time, into paraffin wax.

These profiles allow us to compare the unaided AIs and adjuvants, and calculate their unique diffusion coefficients, shown in Figure 6.27.

Initial time ($t=0$) is shown as the darkest purple line, and then the lightness of the line corresponds to a longer time-point. We can see the progression of the AI penetrate through the wax, however, it is clear the diffusion flux is far lower than that of the adjuvants.

This experiment was repeated and averaged to give a margin of error for these profiles, which we then use to compare the unaided AIs and adjuvants, and calculate their unique diffusion coefficients, which for FDL is shown in Figure 6.27.

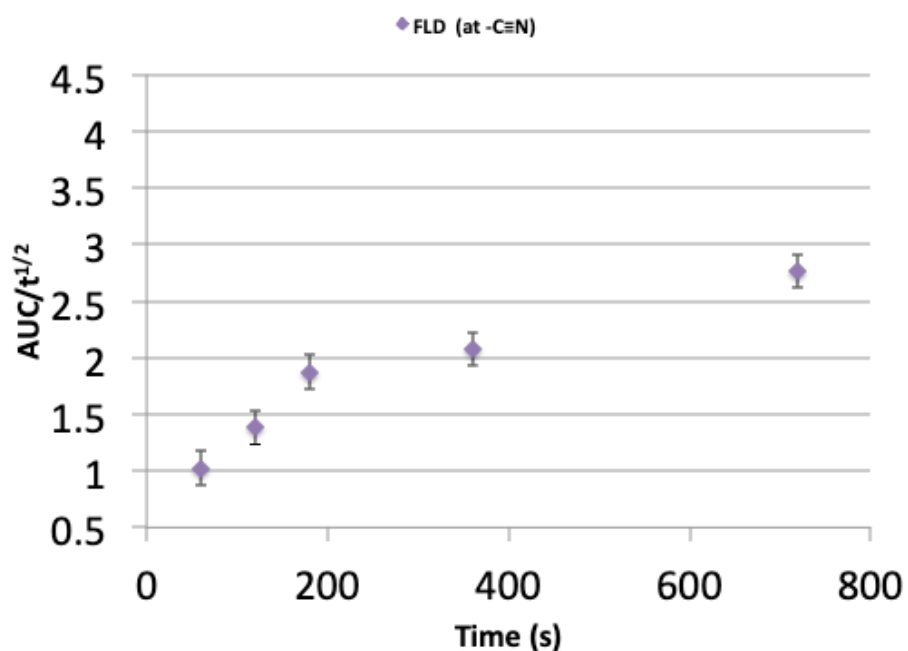


Figure 6.27: The area under the curve divided by the square root of time provides us with diffusion coefficients over time, for FDL into paraffin wax

Once more, by using these diffusion coefficients, we can fit the data with diffusion theory to obtain quantitative diffusion characteristics of cuticle wax-active ingredient interactions. Predicted evolution of the SRS signal following the same assumptions mentioned for Finsolv TN, would allow us to predict the evolution of the SRS signal as the diffusion proceeds. However experimentally, as time increases, again, so does the diffusion coefficient, meaning a substantial deviation from this law, which would show a constant diffusion coefficient independent from time. This provides argument for a non-Fickian diffusion pathway. Like the theory outlined in Chapter 2, a time dependent diffusion coefficient highlights this.

6.6.3 Finsolv TN

As stated in section 6.4.5, Finsolv TN is an aromatic ester, with two prominent peaks of interest for the C=O vibration, appearing at 1723cm⁻¹, and a peak

associated with C=C, at 1681cm^{-1} . Out of these we measure the C=O peak, and convert using the CARS equation shown in Chapter 3 to get tune our pump beam to 876.2nm , whilst our Stokes beam remains fixed at 1032nm .

A droplet of Finsolv TN, dissolved in water at concentration 1.1mg/L , is imaged in Figure 6.28 (B), showing the intense signal given at this wavelength. Alongside in (A), an off-resonance image showing the complete lack of signal when tuned away from this peak, found after a hyperspectral of the wavenumber range was performed.

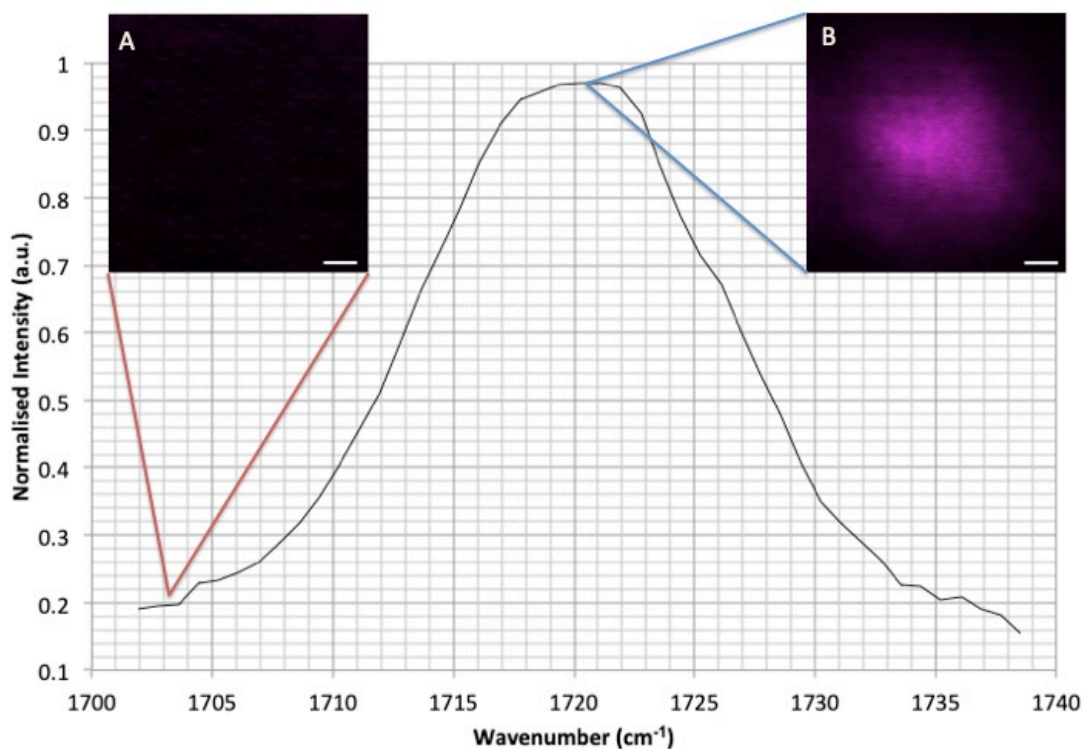


Figure 6.28: Hyperspectral data for a droplet of Finsolv TN in water imaged by SRS at its signal at the spontaneous Raman peak between $1702\text{-}1735\text{cm}^{-1}$ showing the peak at 1723cm^{-1} , corresponding with the C=O vibration. (A) Shows the off-resonance image with (B) showing intense resonance from the intense peak.

Then, using the experimental setup shown in Figure 6.1, 1.1mg/L of Finsolv TN solution can be pipetted alongside the paraffin wax, which had already been focussed on with ScanImage software, using the SRS setup described in Figure 4.2. The same FOV can simultaneously image the paraffin wax and the flow and diffusion of the Finsolv TN, summarised as a series of time-lapse images in Figure 6.29.

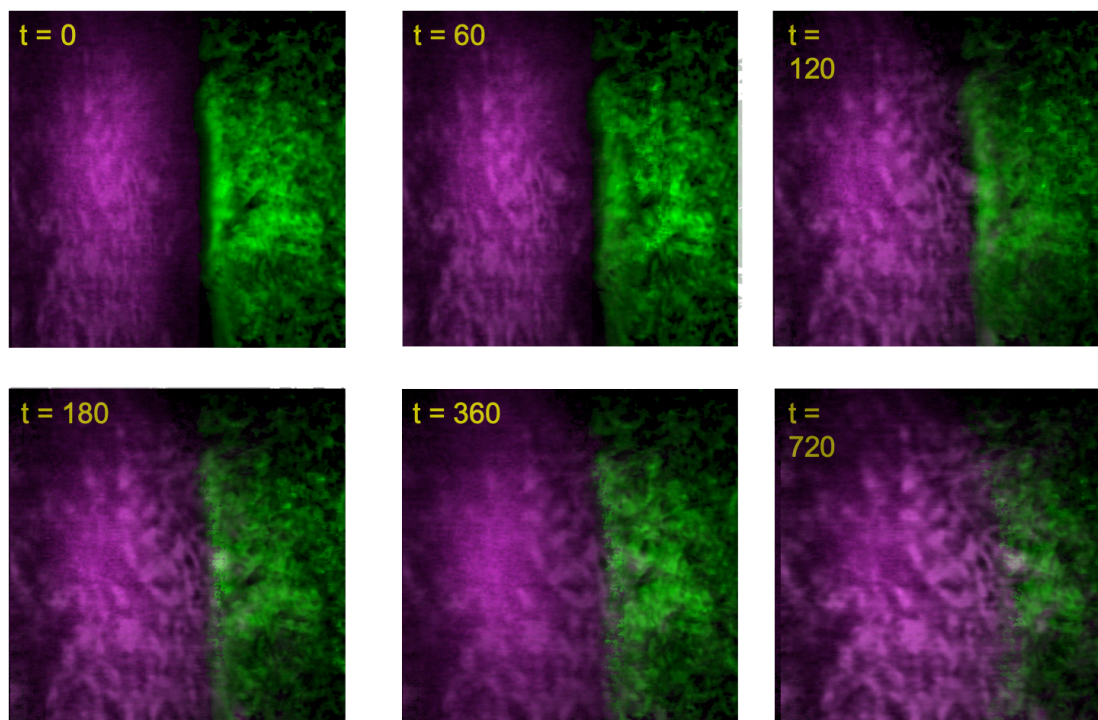


Figure 6.29: Finsolv TN uptake into paraffin wax, shown as a pseudo-coloured time series, with magenta representing Finsolv TN and green representing the paraffin wax. Images were acquired every minute for 30 minutes, with 6 of these time-points compiled here between initial contact at $t=0$ seconds, and 720 seconds. Scale bar = 10 microns

In this time-lapse series, we can see the progression of the adjuvant penetration through the surface of the wax, and with these pseudo-coloured x-y planar images we can produce diffusion curves for both concentration, relative to signal intensity, and distance travelled, over time, shown in Figure 6.30, using code written on Matlab.

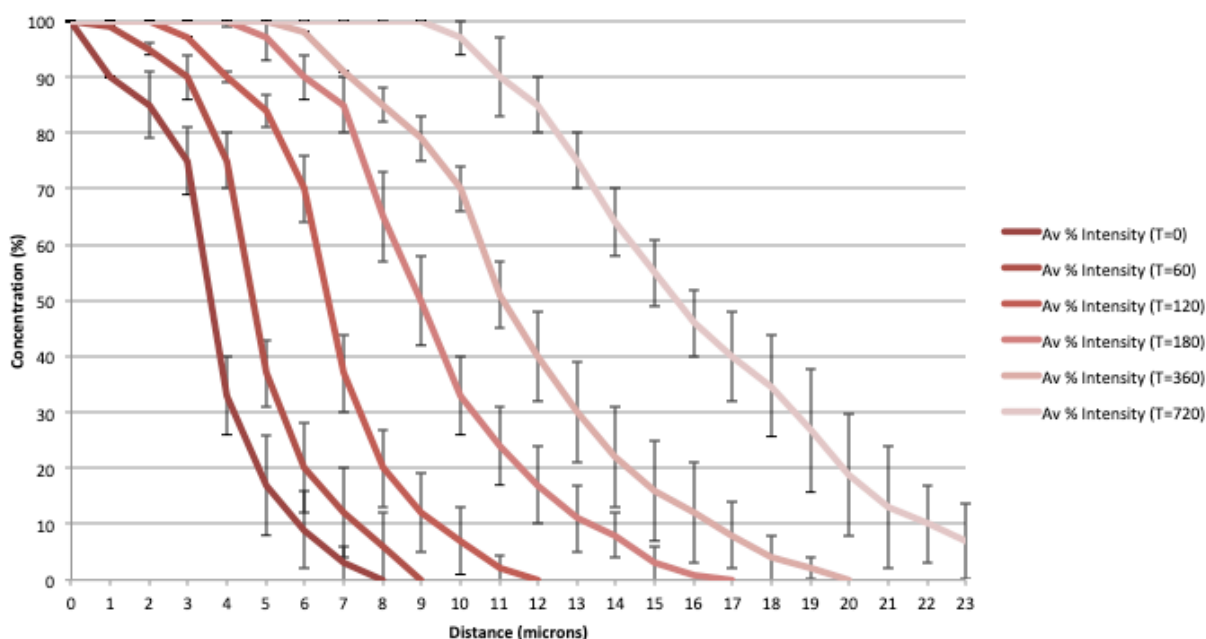


Figure 6.30 Diffusion depth profile for Finsolv TN, as a function of time, into paraffin wax.

These curves show the penetration of the adjuvant into paraffin wax, over the course of 720 seconds, which each curve being a different time-point. Initial contact (t=0) is shown as the darkest red line, and then the lightness of the line corresponds to a longer time-point. Again, here we can see the progression of the adjuvant penetration through the wax.

This experiment was repeated and averaged to give a margin of error for these profiles, which we then use to compare the unaided AIs and adjuvants, and

calculate their unique diffusion coefficients, which for Finsolv TN is shown in Figure 6.31.

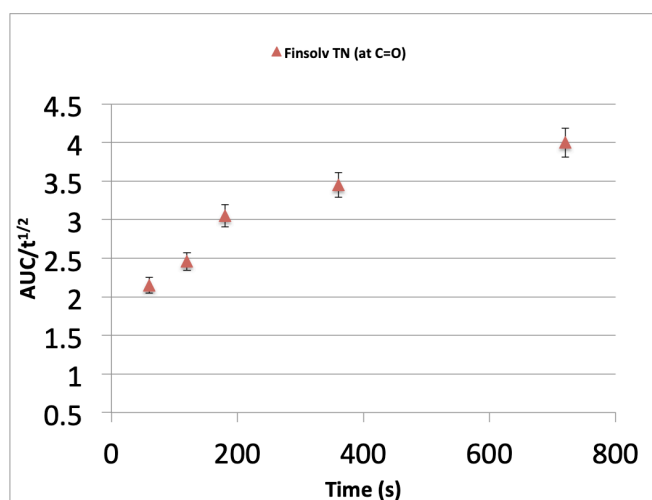


Figure 6.31: The area under the curve divided by the square root of time provides us with diffusion coefficients over time, for Finsolv TN into paraffin wax.

Moreover, using these diffusion coefficients, we can fit the data with diffusion theory to obtain quantitative diffusion characteristics of cuticle wax-active ingredient interactions. Predicted evolution of the SRS signal, based on Fick's second law, shown in Chapter 2, alongside the assumptions outlined, would say nonsteady-state diffusion into an infinite source, assuming that paraffin wax is a homogenous plane sheet with constant diffusivity, D_i , with the boundary conditions: (a) Agrochemical agent signal ($S/S_z = 0$) on the surface wax ($z = 0$) equals 1 at all times, $t \geq 0$, (b) at $t = 0$, $S/S_z = 0 = 0$ at $z > 0$, and (c) at $t \geq 0$, $S/S_z = 0 = 0$ at $z = \infty$. So, firstly, there is always a constant source of agrochemical at the surface of the wax. Secondly, at the initial time point, there is no agrochemical inside the wax. And, lastly, the wax's thickness can be considered infinite during the observed period.

Using Fick's second Law, we can predict the evolution of the SRS signal as the diffusion proceeds. However experimentally, as time increases, so does the diffusion coefficient, meaning a substantial deviation from this law, which would show a constant diffusion coefficient independent from time. This provides argument for non-Fickian diffusion, with a time dependent diffusion coefficient.

6.6.4 Tween 20

As stated in section 6.4.13, Tween 20 is a polysorbate, where the C=O stretch which does appear prominently in the Raman spectra, at 1737cm^{-1} . Using the CARS equation shown in Chapter 2 to get tune our pump beam to 875.1nm, whilst our Stokes beam remains fixed at 1032nm.

A droplet of Tween 20, dissolved in water at concentration 6mg/L, is imaged in Figure 6.32 (B), showing the intense signal given at this wavenumber. Alongside in (A), an off-resonance image showing a very small amount of signal, pseudocoloured pink, when tuned away from this peak, found after a hyperspectral of the wavenumber range was performed.

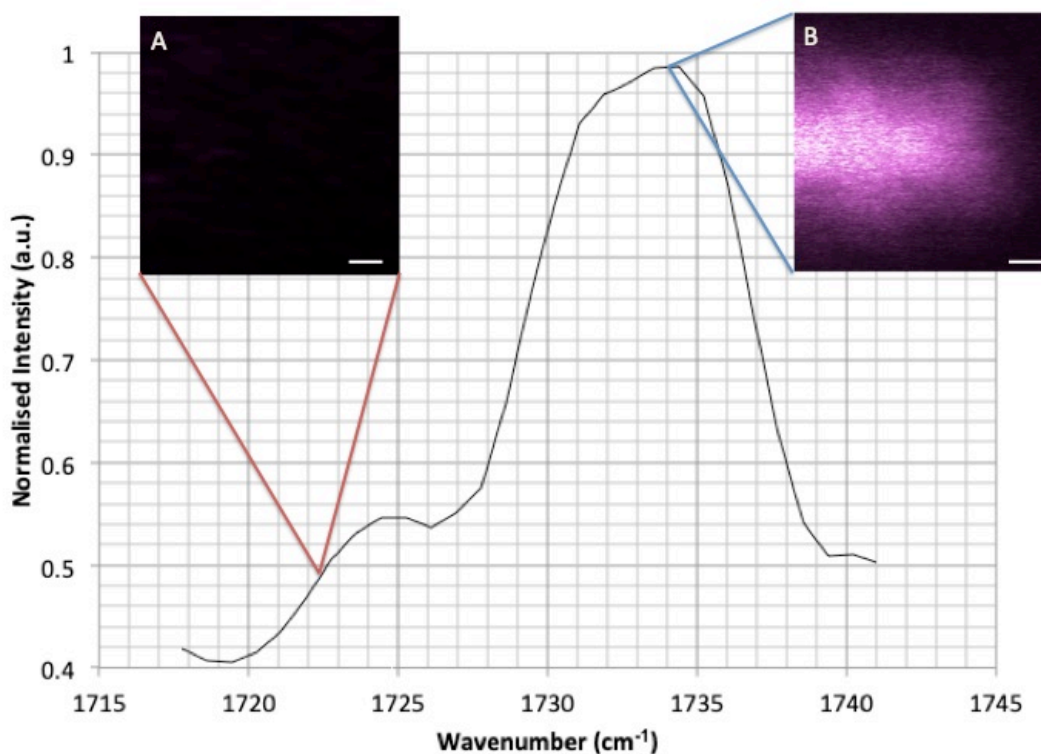


Figure 6.32: Hyperspectral data for a droplet of Tween 20 in water imaged by SRS at its signal at the spontaneous Raman peak at 1737cm^{-1} , corresponding with the C=O vibration. (A) Shows the off-resonance image with (B) showing intense resonance from the peak.

Then, using the experimental setup shown in Figure 6.1, 6mg/L of Tween 20 solution can be pipetted alongside the paraffin wax, which had already been focussed on with ScanImage software, using the SRS setup described in Figure 4.2. The same FOV can simultaneously image the paraffin wax and the flow and diffusion of the Finsolv TN, summarised as a series of time-lapse images in Figure 6.33.

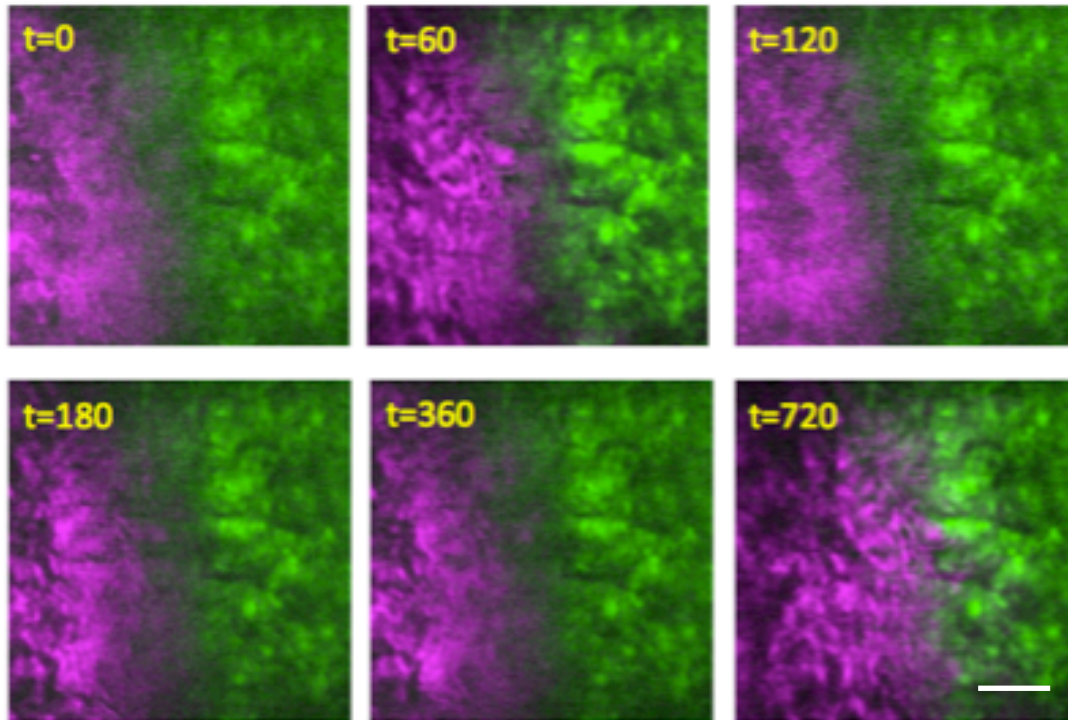


Figure 6.33: Tween 20 uptake into paraffin wax, shown as a pseudo-coloured time series, with magenta representing Tween 20 and green representing the paraffin wax. Images were acquired every minute for 30 minutes, with 6 of these time-points compiled here between initial contact at $t=0$ seconds, and 720 seconds. Scale bar = 10 microns

These pseudo-coloured x-y planar images again, can be used to produce diffusion curves for both concentration, relative to signal intensity, and distance travelled, over time, shown in Figure 6.34.

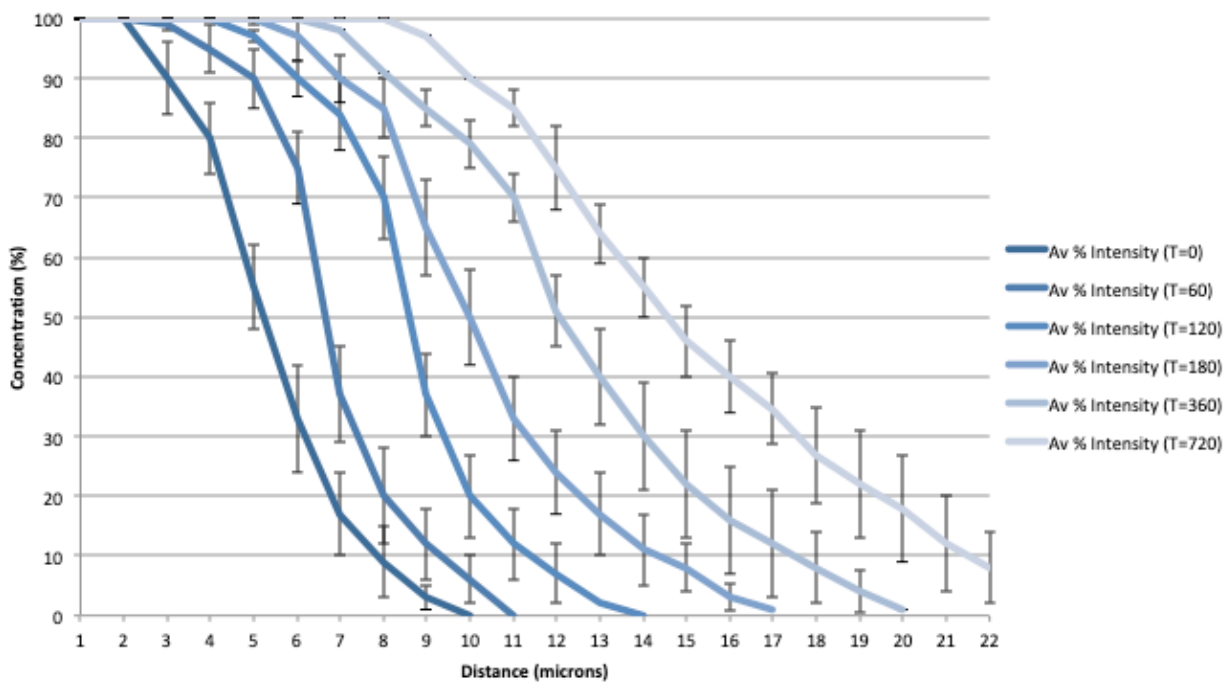


Figure 6.34: Diffusion depth profile for Tween 20, as a function of time, into paraffin wax.

These profiles allow us to compare the unaided AIs and adjuvants, and calculate their unique diffusion coefficients, shown in Figure 6.35.

Initial contact ($t=0$) is shown as the darkest blue line, and then the lightness of the line corresponds to a longer time-point. The graph clearly shows the progression of the adjuvant penetration through the wax.

This experiment was repeated and averaged to give a margin of error for these profiles, which we then use to compare the unaided AIs and adjuvants, and calculate their unique diffusion coefficients, which for Tween 20, is shown in Figure 6.35.

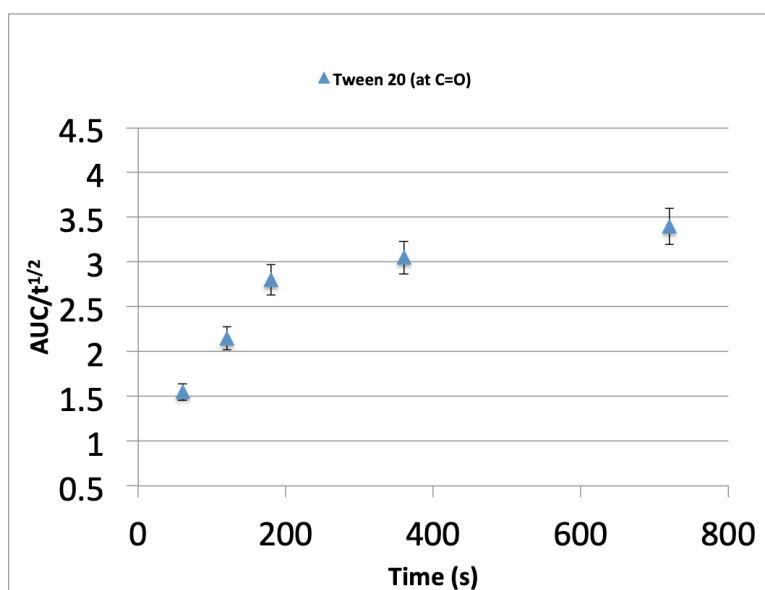


Figure 6.35: The area under the curve divided by the square root of time provides us with diffusion coefficients over time, for Tween 20 into paraffin wax

Again, using these diffusion coefficients, we can fit the data with diffusion theory to obtain quantitative diffusion characteristics of cuticle wax-active ingredient interactions. Predicted evolution of the SRS signal following the same assumptions mentioned for Finsolv TN, would allow us to predict the evolution of the SRS signal as the diffusion proceeds. However experimentally, as time increases, again, so does the diffusion coefficient, meaning a substantial deviation from this law, which would show a constant diffusion coefficient independent from time. This provides argument for non-Fickian diffusion, with an ever-changing diffusion coefficient.

6.7 Comparison and Discussion

As shown when comparing Figures 6.31 and 6.35, plotted together to produce Figure 6.36, one can see Finsolv TN's higher diffusivity than Tween 20, with a higher concentration of the adjuvant reaching deeper into the wax, in the allotted time.

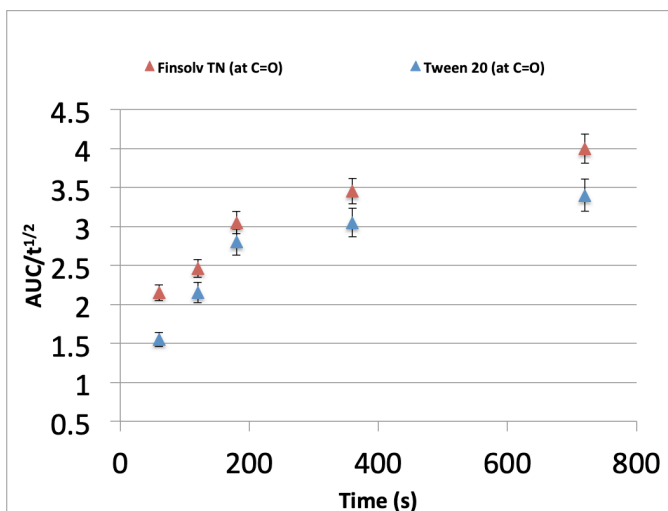


Figure 6.36: Diffusion coefficients for Finsolv TN and Tween 20, from 6.31 and 6.35 respectively, plotted on the same axis to reveal Finsolv TN's increased diffusivity over 720 seconds.

This was to be expected, due to Tween 20 being used as an emulsifier rather than a lipophilic emollient, like Finsolv TN, which allows further penetration by deforming and softening the wax. Both adjuvants do penetrate deeper in the allotted time than both the active ingredients, which again was expected. AZ and FDL alone do not penetrate well into paraffin wax, and therefore require the addition of these adjuvants to increase diffusivity in order to be effective. The next section will show the effects of adjuvants on the diffusivity of the AIs, and visa versa, to show a protocol for next-generation adjuvant effectiveness experiments.

6.8 Active Ingredients with Adjuvants into Paraffin Wax

6.8.1 AZ with adjuvants

To measure the uptake of AZ with adjuvants into paraffin wax, we utilise the sample preparation outlined in Figure 6.1, and mixed the compounds in water at their individual solubility limits, set in Table 3, before applying to the same experimental setup shown in Figure 3.2, using SRS to probe the C≡N vibration

from the AZ. Shown in Figure 6.37, we can see the AZ uptake shown as a pseudo-coloured time series against identical time series with the addition of one of the adjuvants.

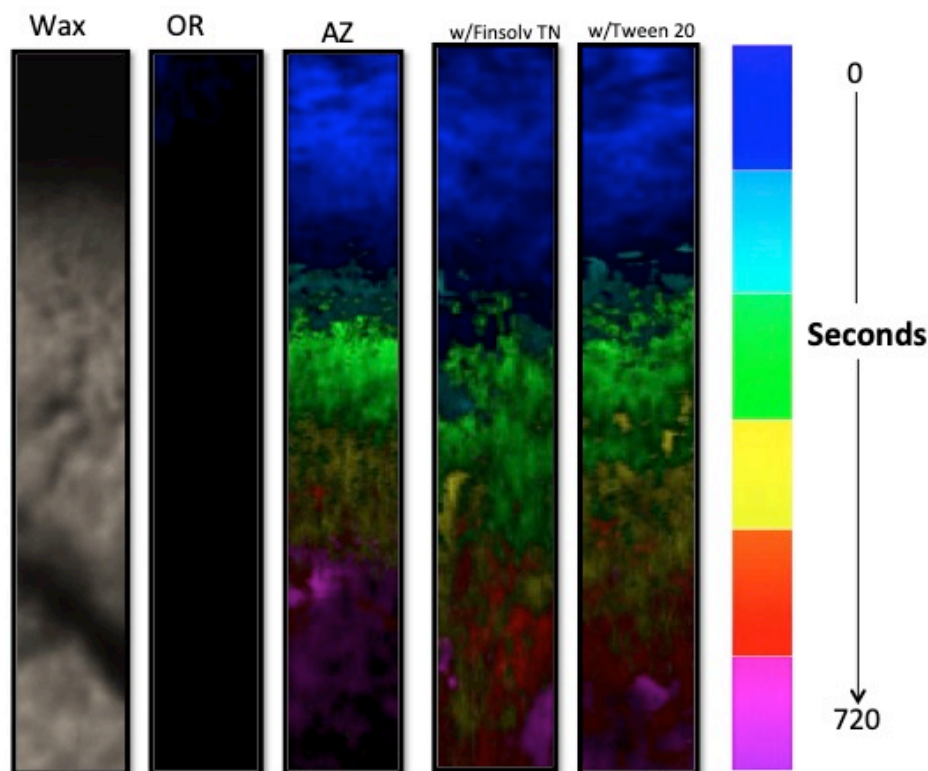


Figure 6.37: SRS x-y images of the penetration depth of AZ into three paraffin wax samples as a function of time. The spectrum indicates the signal from C \equiv N recorded every 60 seconds for a total of 720 seconds, from the initial contact. The three colour spectra show AZ, AZ with Finsolv TN and AZ with Tween 20 respectively. The untreated wax is shown on the far left (labelled wax) and the off resonance is to its immediate right (labelled OR).

Figure 6.37 shows AZ's uptake, also shown in the previous chapter, alongside that of AZ with Finsolv TN and Tween 20 respectively. The colour-map shows the progression of the agrochemical solution, imaged at AZ's C \equiv N peak at 2220cm $^{-1}$, in each of the six chosen time points, at 0, 60, 120, 180, 360 and finally 720 seconds. What becomes obvious from this map is that Finsolv TN

adjuvant visibly improves the diffusion of the AI through the wax, thus improving its uptake through the cuticle wax model system. This can be confirmed when comparing the graphically plotted diffusion curves, shown in Figure 6.38 by plotting AI against AI with each adjuvant, at separated time-points, to compare the concentration and depth reached with the addition of adjuvants.

—■ AZ w/ Finsolv TN
 —■ AZ
 —■ AZ w/ Tween 20

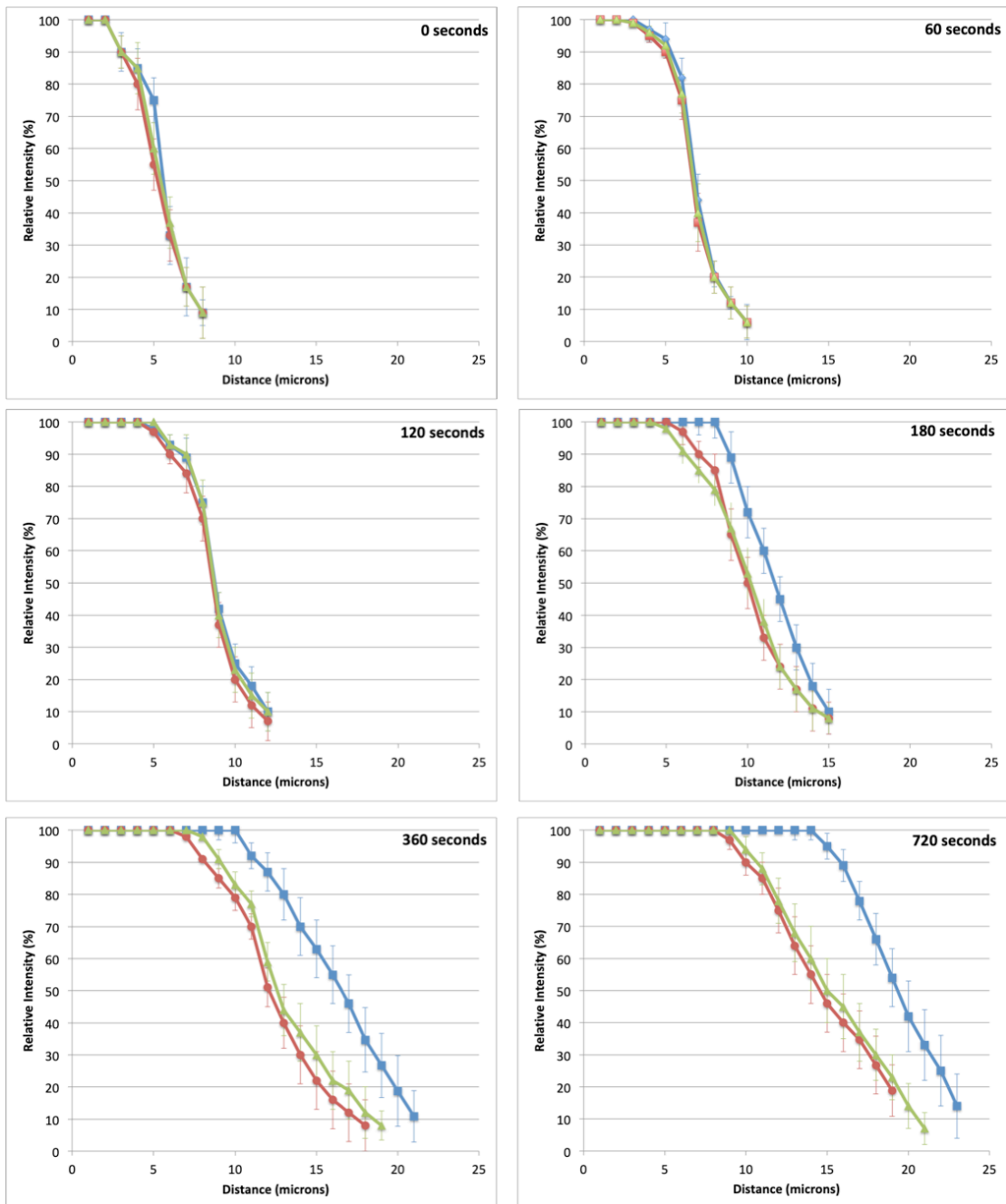
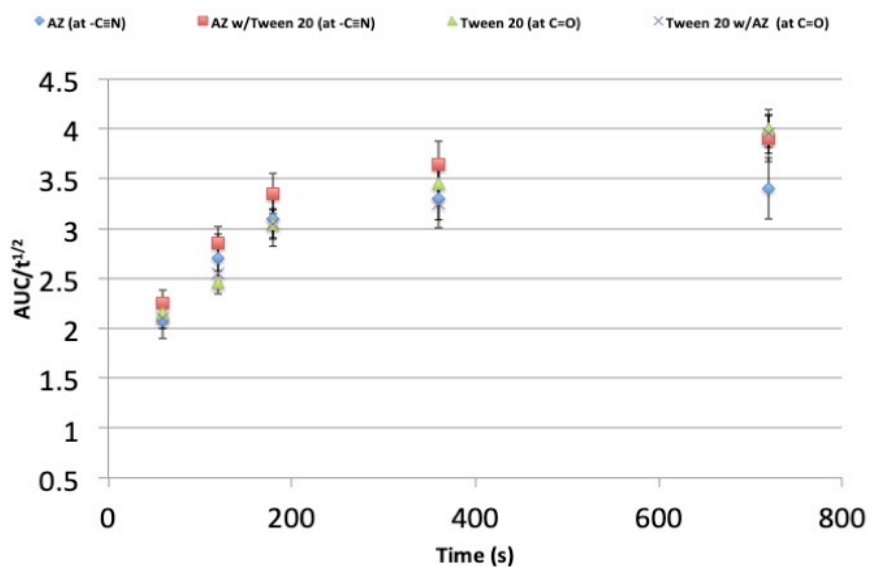


Figure 6.38: Six different time-points, showing the uptake of AZ into wax, with and without the addition of adjuvants Tween 20 (green) and Finsolv TN (blue). AZ unaided is shown in red. Time points 0-720 showing AI with and without adjuvant.

These separated time-points, shown in Figure 6.38, unequivocally show the improvement in uptake with the addition of Finsolv TN. After as little as 180 seconds, the diffusion curves show an uptake improvement of 10%. In the following time-points, this margin widens further and clearly shows a far improved uptake of the AI.

Again, we can use these curves to produce diffusion coefficients for both the AIs and adjuvants separately, and when mixed. These are shown overleaf in Figure 6.39.

(A)



(B)

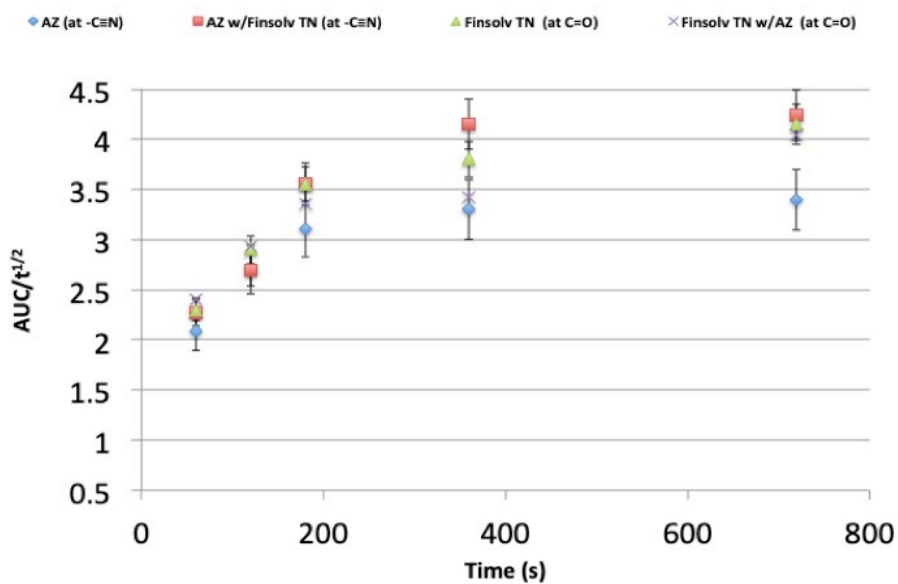


Figure 6.39: Diffusion coefficients of (A) AZ with Tween 20 and (B) AZ with Finsolv TN.

Figure 6.39 compares the diffusion coefficients of both adjuvants with AZ. The area under these experimental curve profiles (AUC), are normalized by the $t^{1/2}$ as a function of time. (A) Shows AZ and Tween 20 diffusion coefficients, both singularly and their diffusion coefficient changes when both in solution. (B) AZ

and Finsolv TN diffusion coefficients, both singularly and their diffusion coefficient changes when both in solution.

From the diffusion coefficients shown in Figure 6.39 (A), what becomes increasingly clear is the effect, however limited, Tween 20 has on the diffusivity of AZ, and *visa versa*. We can see the small increase from AZ (blue diamonds) to the aided diffusivity with Tween 20 (red squares), which are still within error margins of each other at all time-points. However, on average, the 'AZ with Tween 20' diffusion coefficients are higher than that of AZ and Tween 20, singularly. This, therefore, provides argument that the mixture of compounds acts on the wax differently than the individual components.

6.6.2 FDL with adjuvants

To measure the uptake of FDL with adjuvants into paraffin wax, we mixed the compounds in water at their individual solubility limits, set in Table 3, before applying to the same experimental setup shown in Figure 6.1, using SRS to probe the C≡N vibration from the FDL. Shown in Figure 6.40, we can see the FDL uptake shown as a pseudo-coloured time series against identical time series with the addition of one of the adjuvants.

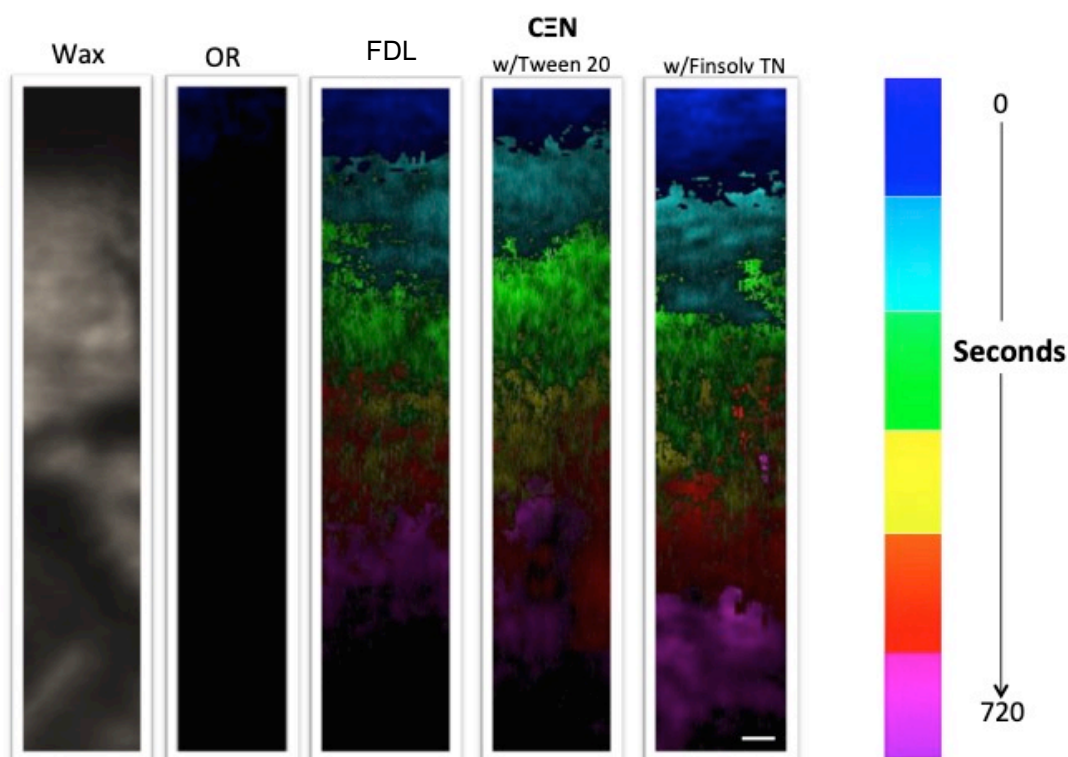


Figure 6.40: SRS x-y images of the penetration depth of FDL into three wax samples as a function of time. The spectrum indicates the signal from CEN recorded every 60 seconds for a total of 720 seconds, from the initial contact. The three colour spectra show FDL, FDL with Tween 20 and FDL with Finsolv TN respectively. The untreated wax is shown on the far left (labelled wax) and the off resonance is to its immediate right (labelled OR). Scale bar, 2 μm .

Figure 6.41 shows FDL's uptake, also shown in the previous chapter, alongside that of FDL with Finsolv TN and Tween 20 respectively. The colour-map shows the progression of the agrochemical solution, imaged at FDL's CEN peak at 2221cm^{-1} , in each of the six chosen time points, at 0, 60, 120, 180, 360 and finally 720 seconds. What again becomes obvious from this map, although not quite as prominent as for AZ, is both adjuvants visibly improve the diffusion of the AI through the wax, thus improving its uptake through the cuticle wax model system. Again, we can confirm this when comparing the graphically plotted

diffusion curves, shown in Figure 6.41 by plotting AI against AI with each adjuvant, at separated time-points, to compare the concentration and depth reached with the addition of adjuvants.

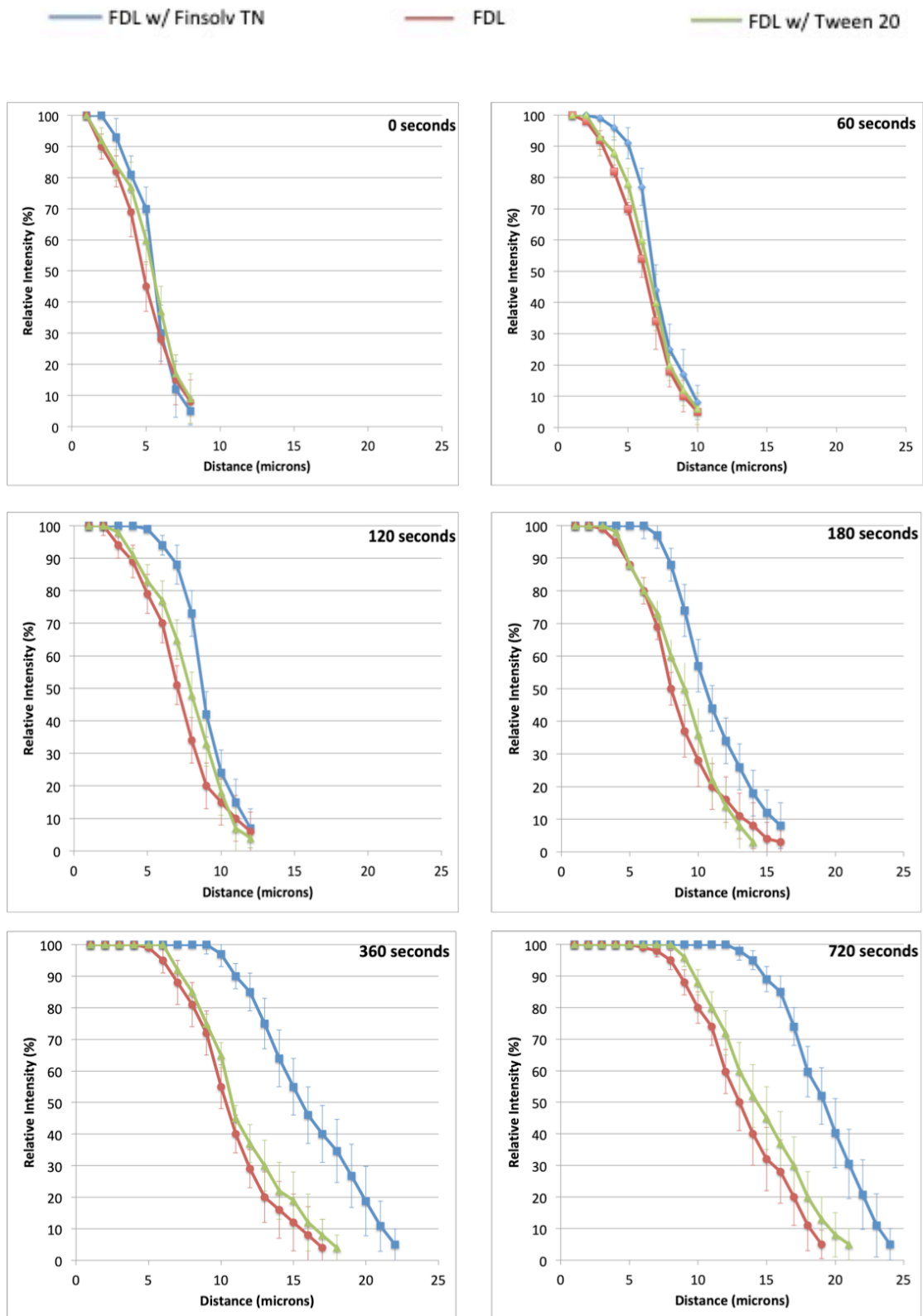


Figure 6.41: Six different time-points, showing the uptake of FDL into wax, with and without the addition of adjuvants Tween 20 (green) and Finsolv TN (blue). AZ unaided is shown in red. Time points 0-720 showing AI with and without adjuvant.

These separated time-points, shown in Figure 6.41, again show the improvement in uptake with the addition of Finsolv TN. After as little as 180 seconds, the diffusion curves show an uptake improvement of 10%. In the following time-points, this margin widens further and clearly shows a far improved uptake of the AI.

Once more, we can use these curves to produce diffusion coefficients for both the AIs and adjuvants separately, and when mixed. These are shown overleaf in Figure 6.42.

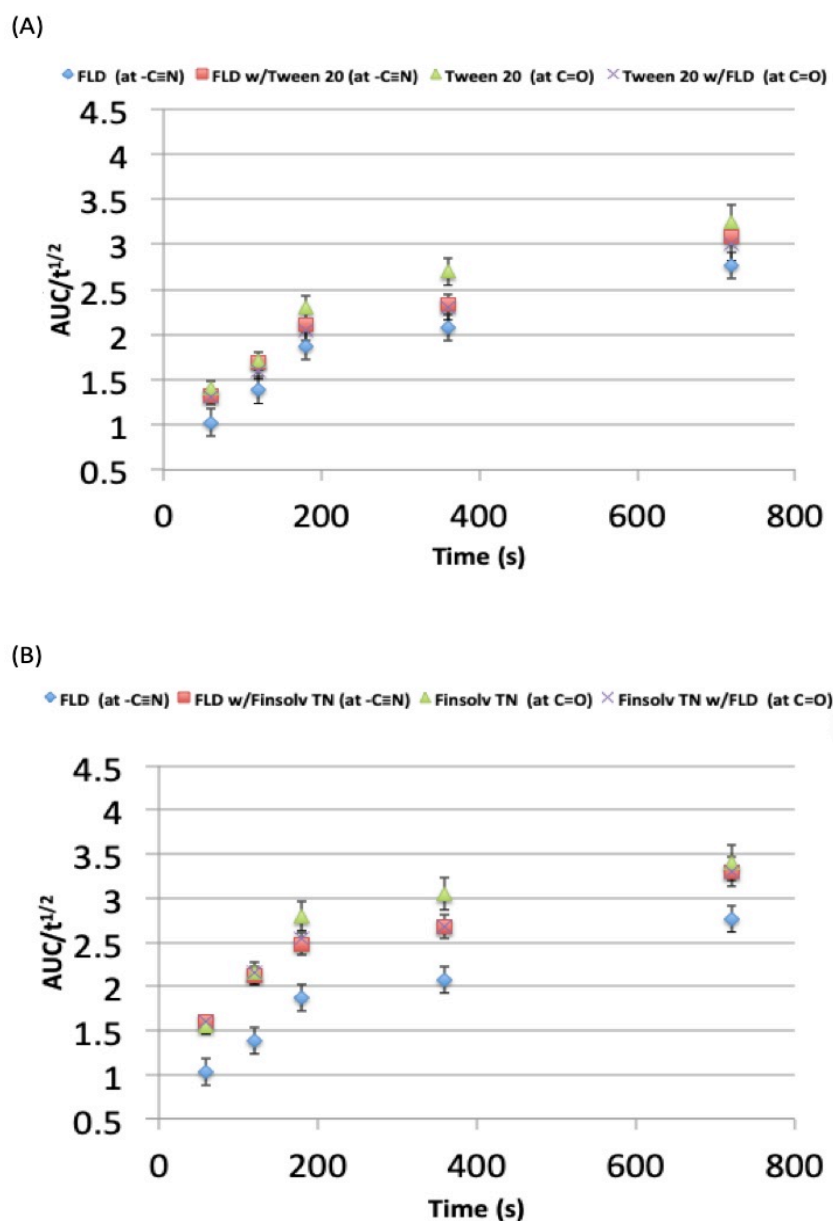


Figure 6.42: Diffusion coefficients of (A) FDL with Tween 20 and (B) FDL with Finsolv TN.

Figure 6.42 compares the diffusion coefficients of both adjuvants with FDL. The area under these experimental curve profiles (AUC), are normalized by the $t^{1/2}$ as a function of time. (A) Shows FDL and Tween 20 diffusion coefficients, both singularly and their diffusion coefficient changes when both in solution. (B) FDL and Finsolv TN diffusion coefficients, both singularly and their diffusion coefficient changes when both in solution.

From the diffusion coefficients shown in Figure 6.42 (A), what becomes increasingly clear is the effect is limited; Tween 20 has on the diffusivity of FDL, and *visa versa*. We can see an insignificant change when comparing the data from FDL (blue diamonds) to the aided diffusivity with Tween 20 (red squares), which are still within error margins of each other at all time-points. However, on average, the 'FDL with Tween 20' diffusion coefficients are lower than that of Tween 20 singularly, and higher than that of the AI separately. This, therefore, provides argument that the mixture of compounds acts on the wax differently than the individual components, negatively affecting the diffusivity of the adjuvant, whilst positively affecting that of the AI.

Comparatively, the diffusion coefficients shown in Figure 6.42 (B) show the effect Finsolv TN has on FDL. This is the largest diffusivity change measured, with the curve being roughly 1 unit greater at every time-point when comparing FDL unaided to FDL with Finsolv TN. Interestingly, the diffusion coefficient curve for Finsolv TN singularly (green triangles) lies on top of the curve for that of FDL with Finsolv TN (red squares) for 3 of the time-points (60, 120 and 720 seconds), however, the shift seen in time-points 180 seconds and 360 seconds, could reveal an argument that the mixture of compounds acts on the wax differently than the individual components.

6.7 Comparison and Discussion

In this section, we can compare the diffusivity changes the adjuvants have on the model AIs, but we are not limited to that. We can also map these changes the other way around, meaning the effect of AI on adjuvant uptake. To the best

of our knowledge, this is the first instance of AI and adjuvant diffusion coefficient comparison using CRS. This method of experimentation can unequivocally show adjuvant effects on AI uptake, and also the interactions between AI and adjuvant throughout this process. This protocol allows the probing of the initial contact between compound and wax, which will prove invaluable when there is a need to see the early stages of agrochemical diffusion.

What becomes obvious from this section, is the positive affect the adjuvants, in particular Finsolv TN, have on the uptake of both AIs. This method could therefore be used in industry, measuring the uptake of new agrochemical agents and developing new adjuvants that can show larger uptake differences to the AI. What will cement this as a key method for measuring agrochemical uptake is proving paraffin wax is a useable model system, which will be discussed in the next section.

6.8 Summary

This section has shown CRS has the ability to not only measure the uptake of agrochemical agents into a variety of waxes, but also can show the changes in diffusivity caused by individual components in these solutions. In this chapter, I have successfully catalogued the effects of Tween 20 and Finsolv TN on two different AIs, showing Finsolv TN's dominance when it comes to improving diffusivity of these AIs. Finsolv TN shows a higher diffusivity than Tween 20, with a higher concentration of the adjuvant reaching deeper into the wax, in the allotted time. Both adjuvants do penetrate deeper in the allotted time than both the active ingredients, which again was to be expected. The diffusion rate and

boundary mapping code has shown AZ and FDL alone do not penetrate well into paraffin wax, and therefore require the addition of these adjuvants to increase diffusivity in order to be effective. The next section will show the effects of adjuvants on the diffusivity of the AIs, and visa versa, to show a protocol for next-generation adjuvant effectiveness experiments.

Using Fick's second Law, we can predict and compare the evolution of the SRS signal as the diffusion proceeds. However experimentally, as time increases, so does the diffusion coefficient, meaning a substantial deviation from this law, which would show a constant diffusion coefficient independent from time. This provides argument for non-Fickian diffusion, with an ever-changing diffusion coefficient.

We have also raised questions as to the before unseen effects the AIs have on the adjuvants, with the adjuvants' diffusivities being reduced in some cases, improved in others, and sometimes showing no effect on the adjuvant. These effects, for now, will remain a future direction for this research.

We have confirmed this method as a protocol for a high throughput of samples, which would be ideal for the needs of industry, particularly with initial measurements for new agrochemicals.

The next stage, however, is to work on leaf sections, to fully compare the technique to that of LCMS, discussed in Chapter 4. The following chapter explores these measurements.

Chapter 7: Exploration of agrochemical diffusion *in planta*

7.1 Introduction

Using conventional methods in Chapter 4, we have been able to see the shortcomings of currently used industry techniques, and in Chapters 5 and 6, we applied CRS to this problem, making protocols to measure the uptake of agrochemical agents into a cuticle wax model system, and have then compared them to extracted wax samples to confirm they are viable results, and that our model system is reliable. The next step, therefore, was to scale up to plant systems, starting with sections of a fresh leaf. *In planta* measurements would be the ideal for industry to get accurate results on a particular species of plant for a targeting AI. This chapter will explore the uptake of our one of our model AIs, FDL, into these leaf systems and again, compare to the results from previous chapters. For this work, we chose cabbage and ivy leaves to work on. Cabbage is a common crop, which will potentially have FDL used on in the field⁷⁷, whereas plants like ivy will be a target for an agrochemical that specialises in weed killing.

7.2 Cabbage

Cabbage leaves were sectioned and the surface imaged, shown in Figure 7.1, using the experimental setup shown in Figure 3.2. As can be seen, in this Figure, there is only the visible presence of cuticle wax structures on the surface, and a lack of the appearance of any cells. This can probably be explained by variation in leaf thickness and water content.

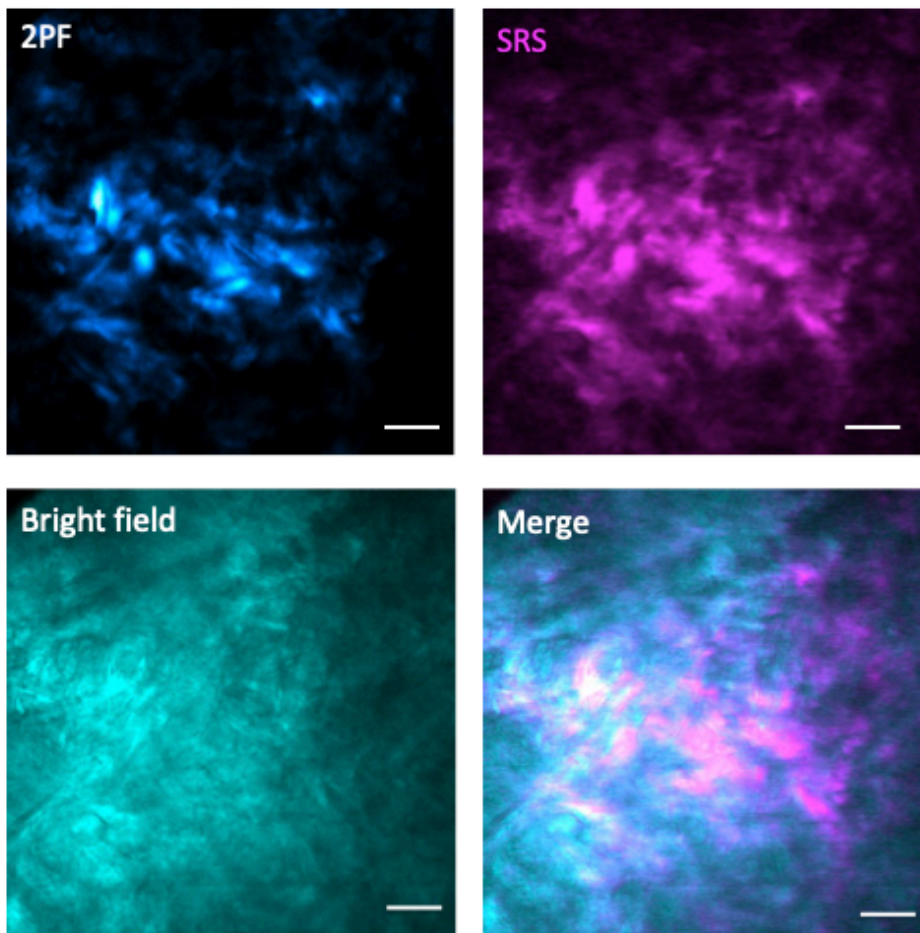


Figure 7.1: CRS image of wax surface on a cabbage leaf. 2 photon-fluorescence (2PF) and SRS, as well as the Brightfield image, can be simultaneously gathered, and merged. Pump beam, set to 838.6nm had average power of 80mW, with Stokes beam, also averaging 80mW, is fixed at 1032nm. Scale bar = 10um

Cabbage leaves were sectioned and mounted between slides, utilising the protocol outlined in Figure 5.2, only differing by fixing the cabbage sectioned leaf on its side, to mimic the same x-y images achieved with the wax.

Figure 7.2 shows this x-y image of the cabbage leaf section, with tentatively assigned cuticle wax boundaries (shown as a red line). Alongside, a colour-map showing the uptake of FDL, with and without the addition of Finsolv TN. The column titled 'OR' represents the off-resonance image, showing limited signal.

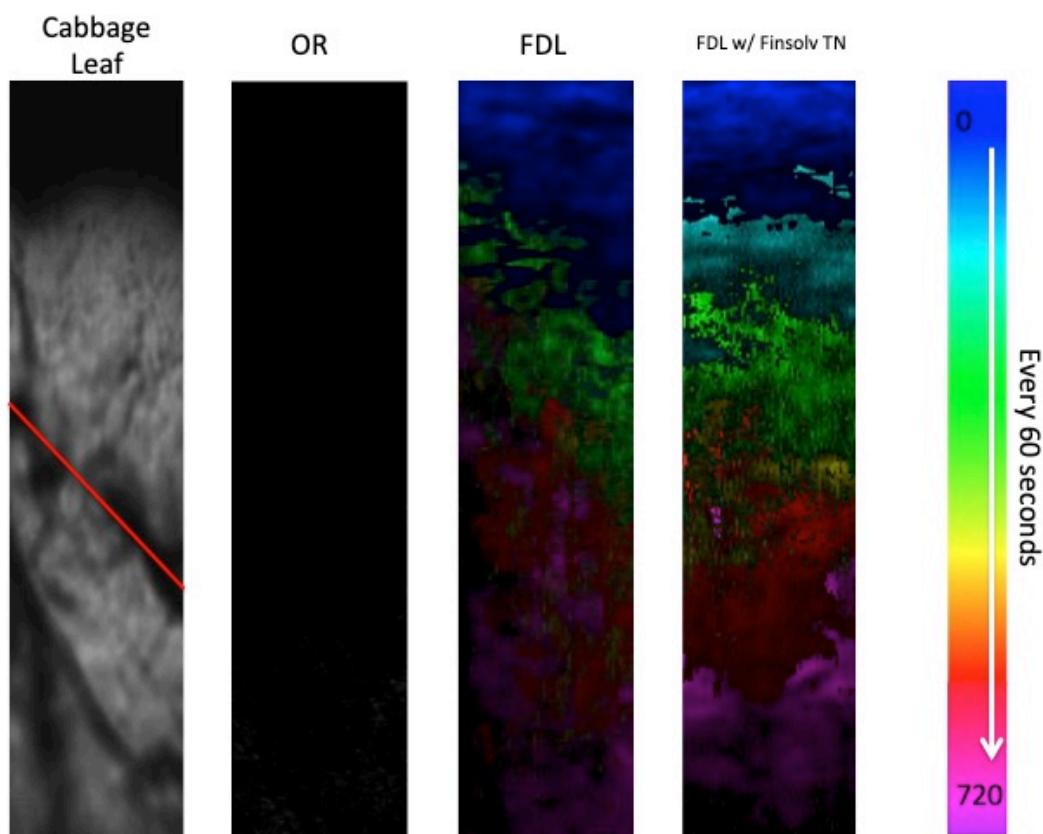


Figure 7.2: SRS x-y images of the penetration depth of FDL into cabbage leaf section samples as a function of time. The spectrum indicates the signal from CEN recorded every 60 seconds for a total of 720 seconds, from the initial contact. The two-colour spectra show FDL and FDL with Finsolv TN respectively. The untreated leaf is shown on the far left (labelled Cabbage Leaf) and the off resonance is to its immediate right (labelled OR).

This colour-map reveals several pieces of vital, interesting information. Firstly, the red line that tentatively defines the cuticle wax boundary has a large

gradient to it, and this gradient is almost matched by the uptake pattern in the column titled FDL, possibly revealing this smaller amount of cuticle wax hinders the uptake. Compare this to FDL w/Finsolv TN and the uptake pattern is far straighter, similar to that seen in the previous sections, showing uptake into a more uniform wax, paraffin. It is also obvious in this time frame, whereas in the previous chapter Finsolv TN visibly positively affected the uptake of FDL, here it is less clear. Only the t=60s time-point (shown as a cyan colour) shows any particular change in the rate of uptake. These experiments were repeated 5 times, and measuring 512x512 pixel images, we can average over around 3500 lines of pixels to monitor the uptake. These results, shown in Figure 7.3, show a much higher rate of error between experiments and even nearby areas on the same leaf section. This, again, could be argued to be affected by the thickness and crystal structures in the cuticle wax, as well as the presence of alkanol functional groups within the wax. We could also consider the layers underneath the cuticle wax may show a drastically different uptake rate.

The changes in uptake rate can be seen in Figure 7.3, showing the diffusion curves, taken from the uptake data in the previous Figure. What becomes obvious are the changes to this uptake occurring between the 1- and 5-micron point, which would match well with the range of thicknesses expected in plant waxes.

Along with this, what also becomes obvious is the rate of uptake is improved by adjuvant Finsolv TN through the early time-points. After 180s, the effects of the adjuvant are far more limited, until t=720s where they are insignificant. Although originally designed for personal care, Finsolv TN distorts the wax and allows

increased movement through that, so we can theorise that it's effects after the wax, which here ends between 5 and 10 microns, are minimal.

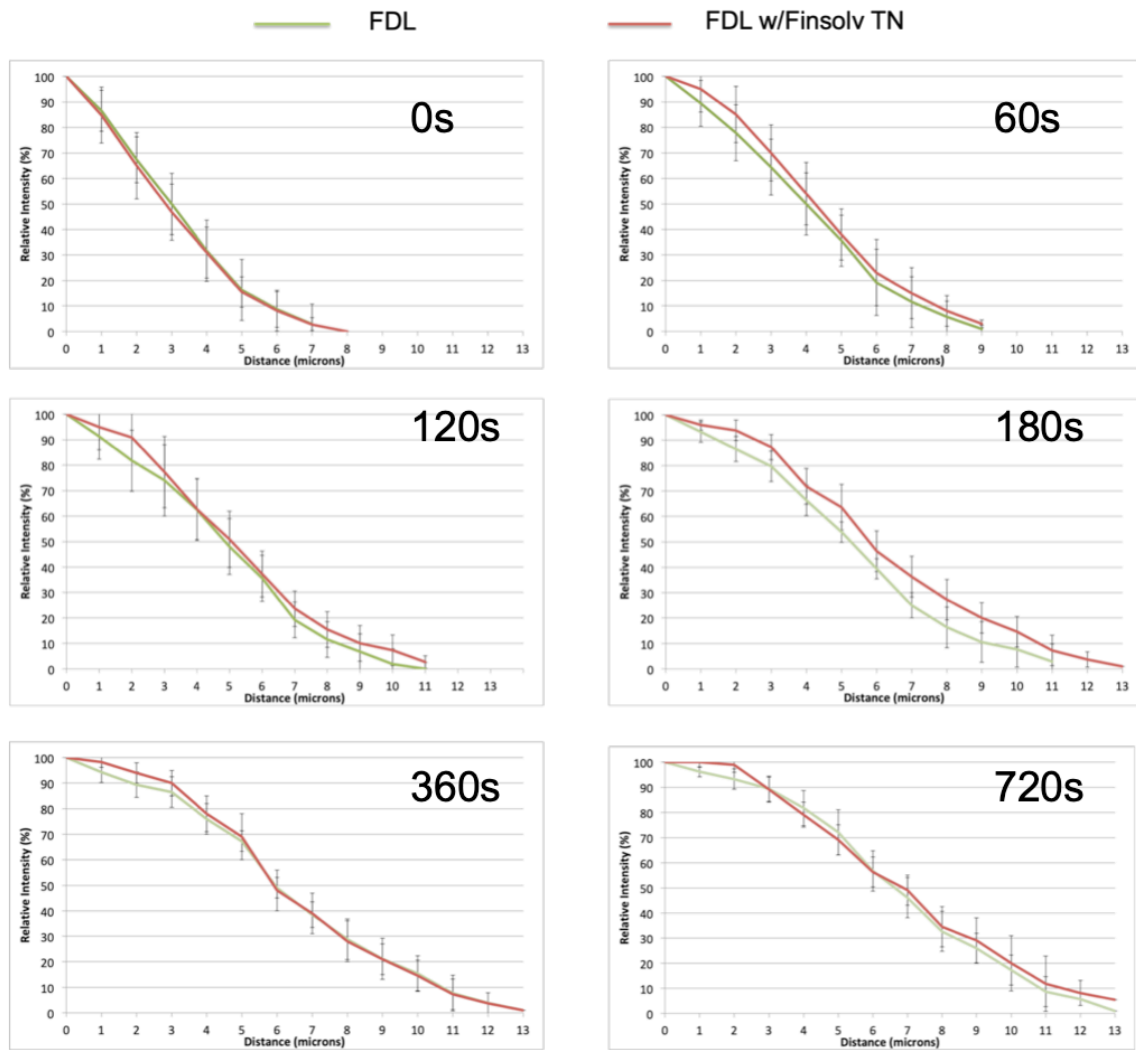


Figure 7.3: Diffusion depth profile for FDL, as a function of time, into a cabbage leaf section

Once more we can use these diffusion curves to calculate the diffusivity of the compound, with and without the adjuvant. These diffusivities are shown in Figure 7.4, with FDL alone in colour, and FDL with the aid of adjuvant Finsolv TN in colour.

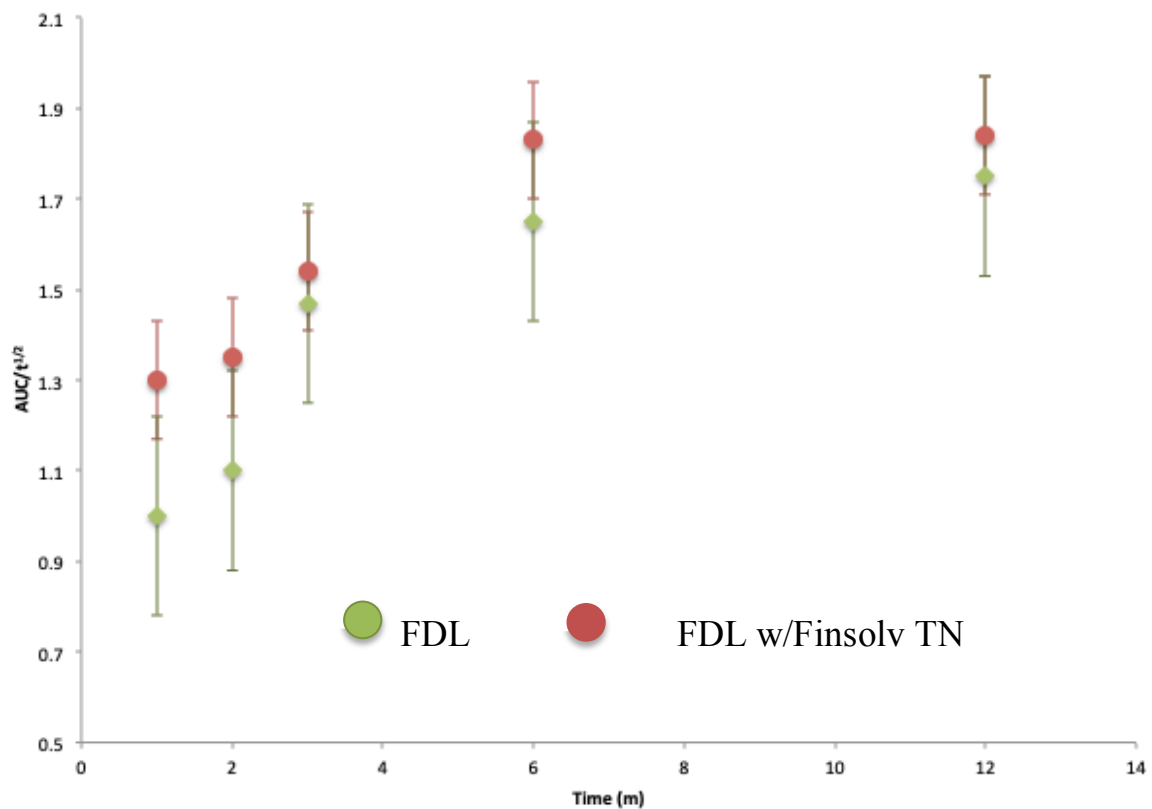


Figure 7.4: Diffusion coefficients calculated from Figure 7.3 for FDL with and without Finsolv TN, into a cabbage leaf section. The data set coloured green shows FDL alone, whereas FDL with Finsolv TN is shown in red.

Figure 7.4 shows the diffusion coefficients for FDL into cabbage, both through its cuticle wax, and other regions near the leaf surface. Here we can see a jump around the 3-minute mark, before rising steadily again until 6 minutes, beginning to plateau out as we reach the experiment end point - 12 minutes.

These rises in both sets of diffusion coefficient could again be due to the change in structure inside the leaf, having passed the cuticle wax and diffusing more easily through other plant material.

Figure 7.4 also shows us the difference in Al uptake with the addition of Finsolv TN. Both curves are sigmoidal in shape, with Finsolv TN-aided diffusion allowing an increase in the overall diffusivity of the droplet.

7.3 Ivy

Ivy leaves were sectioned and the surface imaged, shown in Figure 7.5, using the experimental setup shown in Figure 3.2. As can be seen, in this Figure, there is only the visible presence of cuticle wax structures on the surface, and a lack of the appearance of any cells. This can probably be explained by variation in leaf thickness and water content.

Ivy leaves were sectioned and mounted between slides, utilising the identical protocol outlined in the previous section with cabbage (altered slightly from Figure 5.2), by fixing the sectioned leaf on its side, to mimic the same x-y images achieved with the wax.

What is obvious from this Figure is the amount of structure visible in both 2PF and SRS. This can be due to the elements both in the cuticle and under, in the epidermis or palisade mesophyll, which are labelled in Figure 1.1.

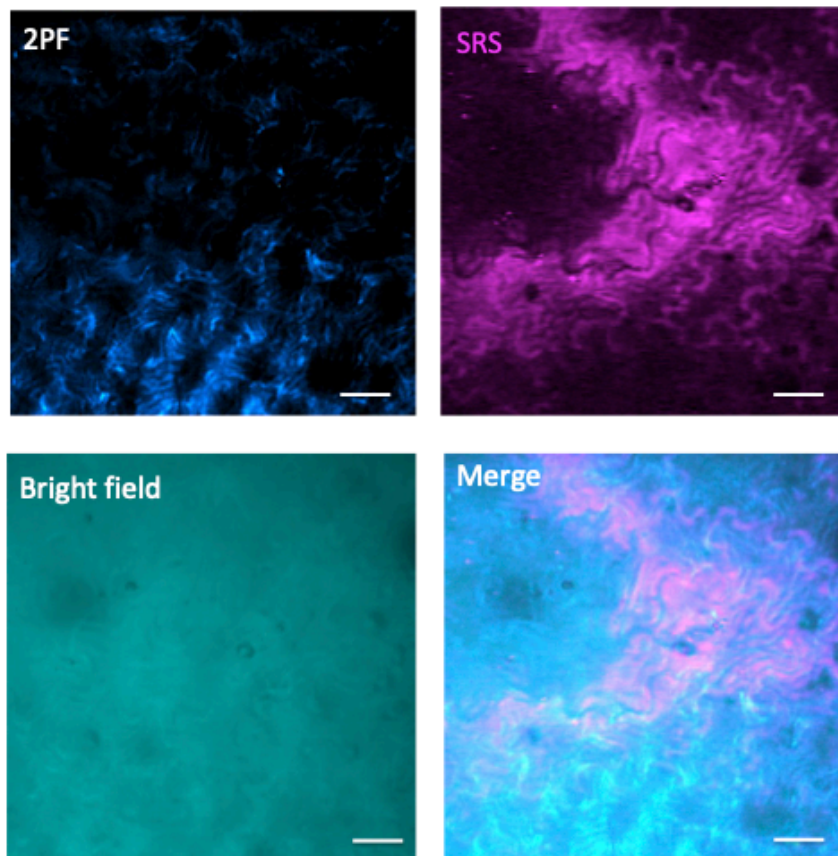


Figure 7.5: CRS image of wax surface on an ivy leaf. 2 photon-fluorescence (2PF) and SRS, as well as the Brightfield image, can be simultaneously gathered, and merged. Pump beam, set to 838.6nm had average power of 80mW, with Stokes beam, also averaging 80mW, is fixed at 1032nm. Scale bar = 10um

Ivy leaves were sectioned and mounted between slides, utilising the protocol outlined in Figure 5.2, only differing by fixing the cabbage sectioned leaf on its side, to mimic the same x-y images achieved with the wax.

Figure 7.6 shows this x-y image of the cabbage leaf section, with tentatively assigned cuticle wax boundaries (shown as a red line). Alongside, a colour-map showing the uptake of FDL, with and without the addition of Finsolv TN. The column titled 'OR' represents the off-resonance image, showing limited signal.

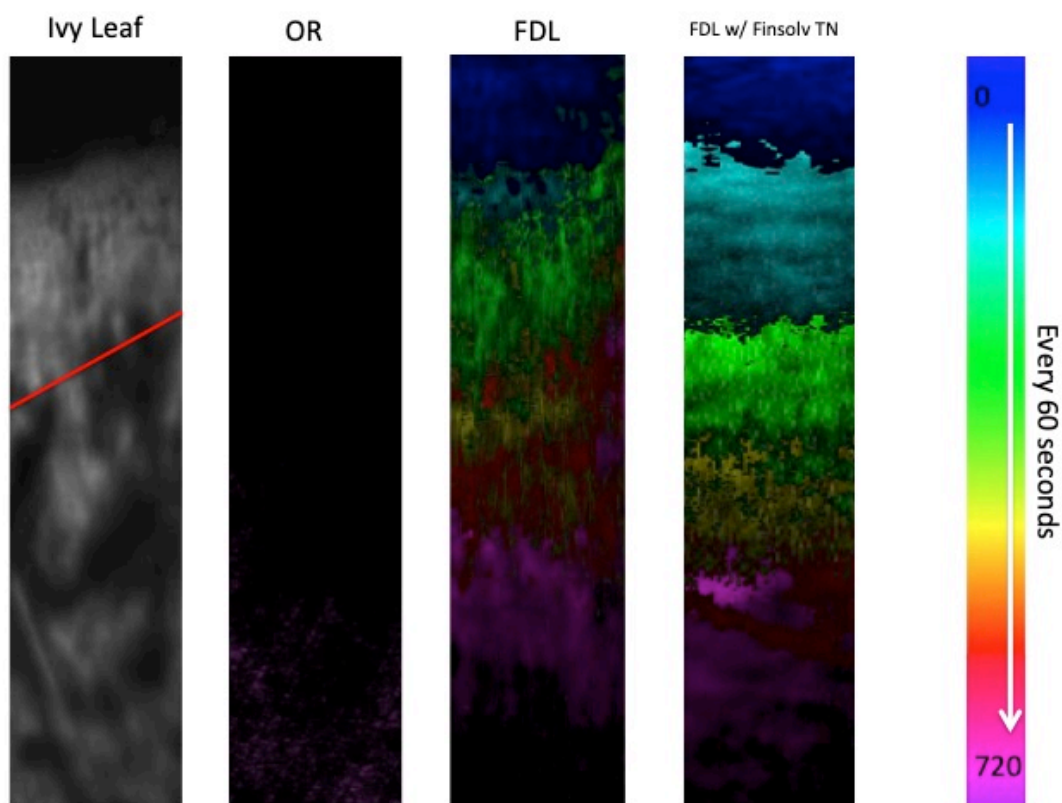


Figure 7.6: SRS x-y images of the penetration depth of FDL into ivy leaf section samples as a function of time. The spectrum indicates the signal from CEN recorded every 60 seconds for a total of 720 seconds, from the initial contact. The two-colour spectra show FDL and FDL with Finsolv TN respectively. The untreated leaf is shown on the far left (labelled Ivy Leaf) and the off resonance is to its immediate right (labelled OR).

This colour-map does reveal similar information to Figure 7.2. Firstly, the red line that tentatively defines the cuticle wax boundary has a large gradient to it, and this gradient is almost matched by the uptake pattern in the column titled FDL, most significantly at $t=180$ (shown in green), possibly revealing this smaller amount of cuticle wax hinders the uptake. Compare this to FDL w/Finsolv TN and the uptake pattern is, again, far straighter, similar to that seen

in Chapter 5, which showed the uptake into paraffin wax. Differently to Figure 7.2, however, it is obvious in this time frame Finsolv TN positively affect the uptake of FDL, allowing a higher concentration penetrate further over the same time allowance. This is shown far more clearly than in previous experiments with cabbage leaves.

These results, shown graphically in Figure 7.7, show a much higher error margin between experiments and even nearby areas on the same leaf section, which, arguably can be caused by changes to the thickness and crystal structures in the cuticle wax, as well as the presence of alkanol functional groups within the wax. And again, we can also see the layers underneath the cuticle wax show different uptake rates compared to one another.

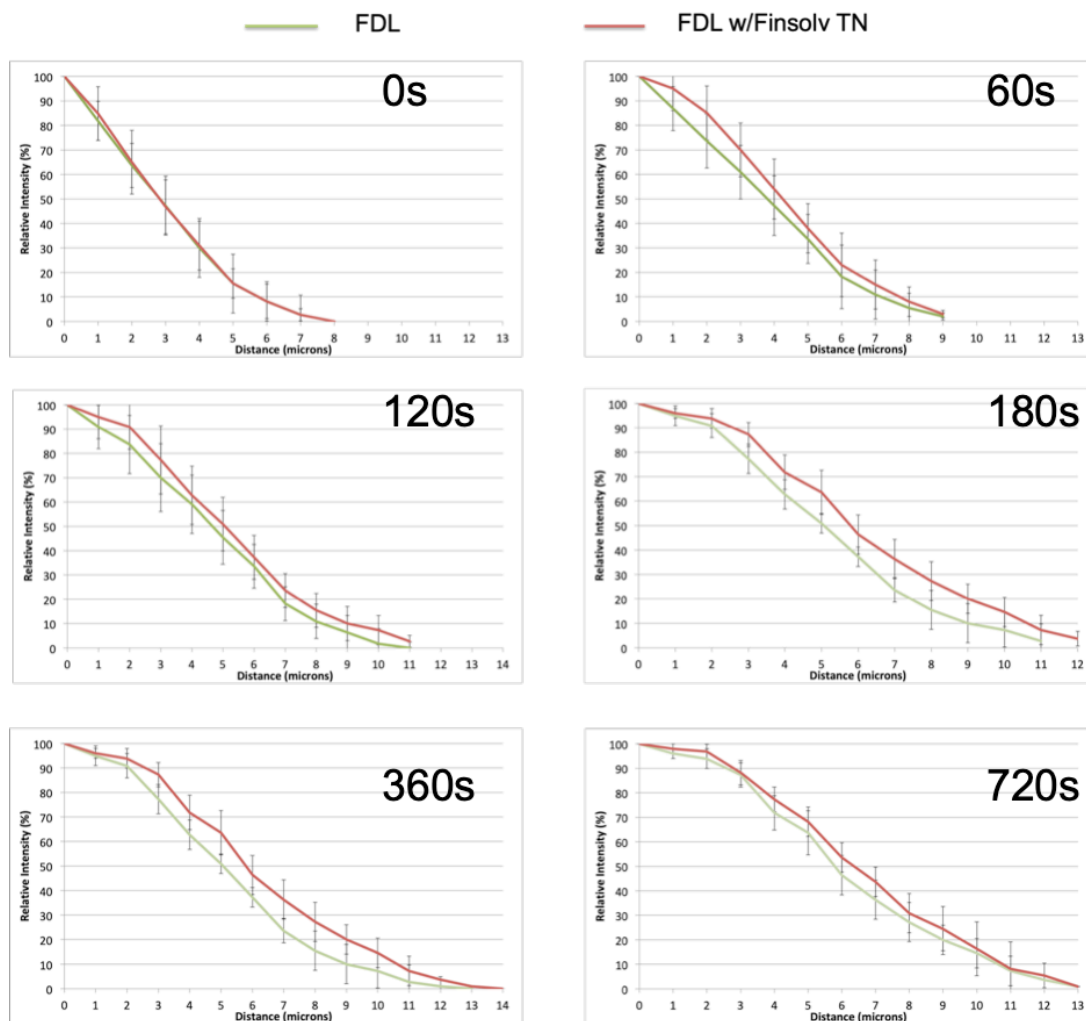


Figure 7.7: Diffusion depth profile for FDL, as a function of time, into a ivy leaf section, with the green line representing FDL unaided, and the red showing the uptake improvement, with aid from adjuvant Finsolv TN.

The uptake rate differences can be seen in Figure 7.7, which plots the diffusion curves over time, taken from the uptake data in the previous Figure. Again we can see changes to this uptake occur between the 1- and 10-micron point, which would match well with the range of thicknesses expected in plant waxes.⁷⁸

Alongside, what one can also see is the improvement of the rate by adjuvant Finsolv TN throughout the entire time frame, but most predominantly through

the first subsequent time-points after initial contact ($t=0$). After this point in time and space, the effects of the adjuvant are more limited, and the final time-point, at $t=720s$, shown in pink, the differences border on insignificant. These results can again provide argument for Finsolv TN's ability to distort the wax and allow increased movement through, and after the wax.

Once more we can use these diffusion curves to calculate the diffusivity of the compound, with and without the adjuvant. These diffusivities are shown in Figure 7.8, with FDL alone in colour, and FDL with the aid of adjuvant Finsolv TN in colour.

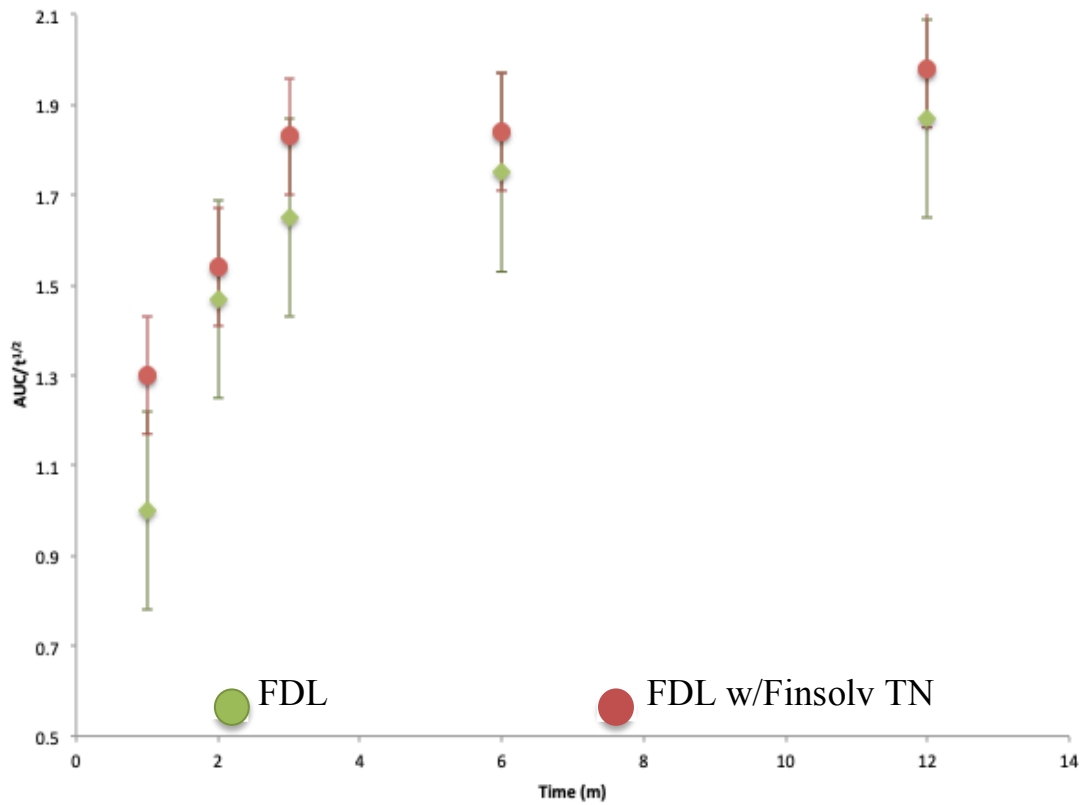


Figure 7.8: Diffusion coefficients calculated from Figure 7.3 for FDL with and without Finsolv TN, into a cabbage leaf section. The data set coloured green shows FDL alone, whereas FDL with Finsolv TN is shown in red.

Figure 7.8 shows the uptake of FDL into cabbage, both through its cuticle wax, and other regions near the leaf surface. Here we can see earlier jump around the 2-minute mark, before rising steadily again until 3 minutes, where this curves gradient begins to lesser towards the experiment end point - 12 minutes.

Again, here we see this initial jump, with this time occurring at an earlier time point. We see this pattern in both the aided and non-aided by Finsolv TN, and it could be due to the change in structure inside the leaf, having passed the smaller cuticle wax section and diffusing more easily through other plant material.

Figure 7.8 also shows us the difference in AI uptake with the addition of Finsolv TN. Both curves are of a similar in shape, with Finsolv TN-aided diffusion allowing an increase in the overall diffusivity of the droplet, having a larger effect during the first contact with the cuticle wax.

7.4 Summary

This chapter has shown CRS has the ability to not only measure the uptake of agrochemical agents into a variety of leaf sections, but also can show the changes in diffusivity caused by individual components inside them. In this chapter, we have successfully catalogued the effects of Finsolv TN on the AI, FDL, again showing Finsolv TN's dominance when it comes to improving diffusivity of these AIs.

We have shown comparative data between both leaves, and provided insight into the differing diffusion kinetics when it comes to different areas of the leaf section. Within this, we have provided argument that paraffin wax is a more reliable model system, with far smaller error margins than leaf sections.

This chapter also provides us with the ability to compare very similar experiments between this chapter and Chapter 4, on LCMS. The two sets of results complement one another, showing, in both sets, the ability to measure Finsolv TN's ability to change the diffusivity of a compound. However, using CRS, one has the ability to see results in real-time, over the course of the first 24 minutes. Maintaining the positives LCMS possesses whilst providing high spatial resolution, and quantitative data, 75x quicker. Drastically reducing preparation and experimentation time from 30 hours to under 30 minutes. CRS

can also detect far lower concentrations than LCMS. In Chapter 5 all solutions were diluted to 1000 ppm, whereas using CRS, the solubility limits listed in Table 6 limit our agrochemical agent-water solutions, therefore the concentrations can be as low as 1 ppm.

Chapter 8: Discussion and Conclusions

8.1 Discussion

The aim of this work was to assess coherent Raman techniques as a method to measure the uptake of agrochemical agents into cuticle wax. As coherent Raman probes inherent molecular vibrations, this technique is particularly suited to these applications. CRS is a relatively new technique, but has already excelled in various applications in pharmaceuticals and biomedical science, including measuring uptake of drugs into human nail.⁶³ However, this is the first instance using CRS to measure agrochemical uptake.

For this to be considered as a potential industry tool, it is important to consider the requirements of the user. With this technique the user can acquire label-free, non-invasive images, whilst providing an enhancement on the inherently weak Raman signal. The criteria for a new industry standard technique, shown in Table 2, also requires a high spatial resolution, with high chemical specificity and the ability to quantify data, a checklist that currently only coherent Raman scattering completes. Coherent Raman is able to provide spatial information based on chemical contrasts in a sample, in a matter of seconds, however, performing a hyperspectral stack to gain spectral information dramatically increases these measurement times. Compared to spontaneous Raman, these spectral times are lengthy, with spontaneous providing a spectrum in less than a minute. The combination of these two techniques may provide the answer for both rapid spatial and spectral information. This method has been applied here,

to find significant peaks utilising spontaneous Raman's spectral speed, before using CRS for its spatial resolution.

8.2 Conclusion

The purpose of this research is to explore CRS as a potential next-generation tool for the agrochemical industry, providing more rapid label-free spatial information, in comparison to current conventional techniques. Thus, aiding the agrochemical industry and the future of food security. Whilst biomedical research is constantly supplied with the latest technologies, plant biology is done with much more basic microscopy. The aim of this thesis is to utilise laser imaging techniques such as CARS and SRS as novel analytical techniques that will give the agrochemical industry the tools for *in situ* analysis of agrochemicals in living plant tissues at a cellular level. Throughout this work, CARS and SRS have been shown to be both rapid and capable of detecting a concentration of agrochemical far lower than that achievable in techniques like LCMS.

This rapid imaging technique allowed visualisation of agrochemical products without the use of labels, revealing interactions between the materials of the product and with the model leaf surface in real time, for the first time in our knowledge, and will enable changes in the agrochemical design process, increasing their efficacy and environmental impact. SRS has been used to challenge a current diffusion model, as well as characterise and visualise the kinetics involved in AI uptake, showing it varies with the chemistry of the AI, at a sub-micron level, and shown that these agrochemical adjuvants can alter the diffusion coefficients on AIs.

CRS has the ability to not only measure the uptake of agrochemical agents into a variety of waxes, but also can show the changes in diffusivity caused by individual components in these solutions. SRS has successfully catalogued the effects of Tween 20 and Finsolv TN on two different AIs, showing Finsolv TN improves diffusivity more so than Tween 20.

We have also shown comparative data between these various waxes and have provided argument that paraffin wax is a suitable model system, due to its ease of use, and avoiding the need for time-consuming and low-yielding extraction process. Paraffin shows near identical diffusion coefficient changes, however the position of this curves is skewed higher than both extracted waxes, which was most likely we due to the varying allocation of alkanol functional groups present in the extracted plant waxes which are not present in paraffin wax, but could also be due to structural changes caused by the hexane washes to remove this wax from the leaf surface.

The agrochemical industry would benefit from a non-destructive, real-time characterisation technique with high chemical selectivity and high spatial resolution. Although many techniques meet some of these requirements, currently only CRS enables all to be met by a single measurement. The use of CRS techniques such as CARS and SRS enables the monitoring and imaging of active ingredients *in planta*, at video-rate speed without the use of potentially interfering labels and could help guide the development of improved agrochemical formulations.

8.3 Future Directions

The diffusion results presented in this thesis represent a small initial study to assess the viability of this technique in this area. Should this technique be considered as the next step for the agrochemical industry, future work should involve the measuring the uptake of hundred more adjuvants and active ingredients, forming a catalogue of diffusion coefficients to shape the development of next-generation agrochemical agents.

Earlier, we had also raised questions as to the before unseen effects the AIs have on the adjuvants, with the adjuvants' diffusivities being reduced in some cases. These effects, for now, will remain a possible future route for this research, to probe deeper into these interactions and fit these diffusion pathways at a higher level of accuracy.

Future work in this area should also investigate the utility of SRS with fiber laser excitation as a tool for label free, real-time diffusion measurements *in planta*. Due to time constraints within this study, only images of leaf sections were achieved. Further work would have involved measuring the uptake through a living leaf, then mapping the AI uptake throughout the rest of the plant. Preliminary work was performed on corn cells, further probing AI interactions by visualizing deuterated agrochemical agents' penetration into corn cells, and whether the compound freely moves in and out of the cell or if it then remains in the cell until cell death.

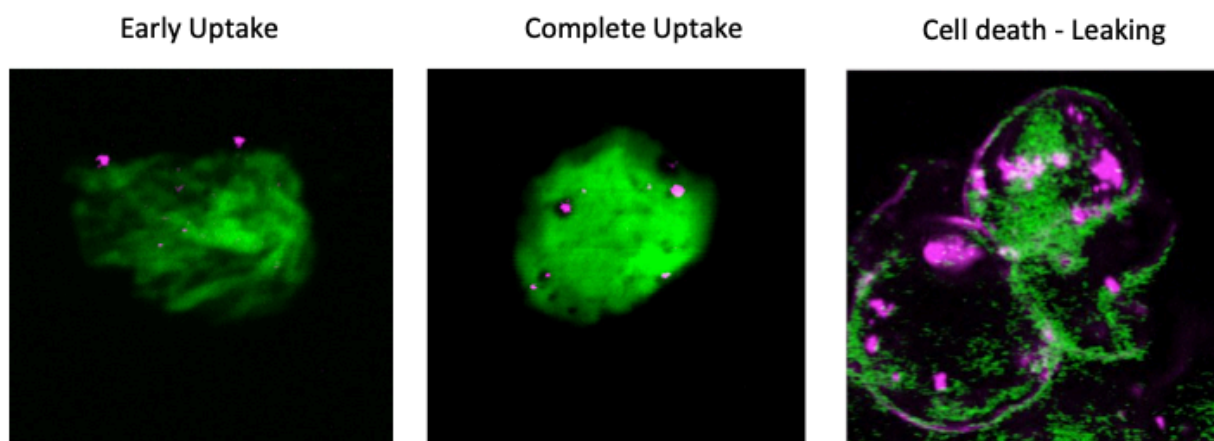


Figure 8.1: Three stages showing the uptake of agrochemical agent Dicamba-d₃ in corn cells.

Figure 8.1 shows corn cells at various stages of the uptake of Dicamba-d₃. The magenta false-colour signal arises from the deuterated Dicamba (Dicamba-d₃), which can be seen clearly in the cell walls and aggregating in different areas of the plant cells. The green false-colour is applied to the cell, shown by probing 2235 cm⁻¹, which represents the CH₂ vibration. Early stage uptake we can see the Dicamba-d attaching to the outside of the cell, and then we witness complete uptake of the agrochemical inside the cell. Cells that are experiencing cell death, can be seen to spill the Dicamba-d₃, whereas the living cells show no sign of releasing the compound, with it aggregating inside the cell.

References

1. Mohanty, S. P., Hughes, D. P. & Salathé, M. Using Deep Learning for Image-Based Plant Disease Detection. *Front. Plant Sci.* **7**, 1–10 (2016).
2. Sands, H. S. *et al.* Development of a combined confocal and scanning near-field Raman microscope for deep UV laser excitation. *J. Raman Spectrosc.* **33**, 730–739 (2002).
3. Mahmood, I., Imadi, S. R., Shazadi, K. & Gul, A. in *Plant, Soil and Microbes* **1**, 10.1007/978-3-319-27455-3_13. (2015).
4. United Nations. *World Population by 2300*. (2004).
5. Sonnenfeld, D. A. Mexico's 'Green Revolution,' 1940-1980: Towards an Environmental History. *Environ. Hist. Rev.* **16**, 29–52 (1992).
6. Tenenbaum, D. Food Fuel: Diversion of Crops could cause more Hunger. *Environ. Health Perspect.* **116**, 254–257 (2008).
7. Napoli, M., Muro, P. P. De & Mazziotta, P. M. Towards a Food Insecurity Multidimensional Index (FIMI). (2011).
8. Syngenta. *The Good Growth Plan*. (2014). at [https://www.syngenta.com/global/corporate/en/goodgrowthplan/Documents/pdf/The Good Growth Plan_ 16pp brochure ENG.pdf](https://www.syngenta.com/global/corporate/en/goodgrowthplan/Documents/pdf/The%20Good%20Growth%20Plan_16pp%20brochure%20ENG.pdf)
9. Oerke, E. C. Crop losses to pests. *Agric. Sci.* **144**, 31–43 (2006).
10. Oerke, E. & Dehne, H. Safeguarding production — losses in major crops and the role of crop protection. *Crop Prot.* **23**, 275–285 (2004).
11. Thompson, P. B. The Agricultural Ethics of Biofuels: The Food. *Agriculture* **2**, 339–358 (2012).
12. Brown, L. R. in *The Great Transition* 1–2 (2008).
13. Jie, C., Jing-zhang, C., Man-zhi, T. A. N. & Zi-tong, G. Soil degradation : a global problem endangering sustainable development. *J. Geogr. Sci.* **2**, 243–252 (2002).
14. Rattner, B. A. History of wildlife toxicology. *Ecotoxicology* **18**, 773–783 (2009).
15. Carvalho, F. P. Pesticides, environment, and food safety. *Food Energy Secur.* **6**, 48–60 (2017).
16. Huang, Y. *et al.* Microbial Degradation of Pesticide Residues and an Emphasis on the Degradation of Cypermethrin and Benzoic Acid: A Review. *Molecules* **23**, 1–23 (2018).

17. Alavanja, M. C. R. Pesticides Use and Exposure Extensive Worldwide. *Rev Env. Heal.* **24**, 303–309 (2009).
18. History of Pesticide use. <http://www2.mcdaniel.edu/Biology/eh01/pesticides/historyofpesticidesuse.html> (1998).
19. Delaplane, K. *Pesticide Usage in the United States : History, Benefits, Risks, and Trends.* (1996).
20. Jabbar, A. & Mallick, S. *Pesticides and environment situation in Pakistan.* (1994).
21. Wang, C. J. & Liu, Z. Q. Foliar uptake of pesticides — Present status and future challenge. *Pestic. Biochem. Physiol.* **87**, 1–8 (2007).
22. Burghardt, M., Schreiber, L. & Riederer, M. Enhancement of the Diffusion of Active Ingredients in Barley Leaf Cuticular Wax by Monodisperse Alcohol Ethoxylates. *J. Agric. Food Chem.* **8561**, (1998).
23. Zabkiewicz, J. A. Adjuvants and herbicidal efficacy: present status and future prospects. *Weed Res.* **40**, 139–149 (2000).
24. Logan, A. N. *Behavior of Pesticides in Plants.* (1974).
25. Felsot, A. S. *et al.* Agrochemical spray drift ; assessment and mitigation — A review. *Environ. Sci. Heal.* **46**, 1–23 (2011).
26. ISF. Seed Treatment: A Tool for Sustainable Agriculture. *WorldSeed.org* 1–2 (2007). at http://www.worldseed.org/cms/medias/file/TradeIssues/SeedTreatment/A_Tool_Sustainable_Agriculture_EN.pdf.
27. Rothrock, C. S., Winters, S. A., Miller, P. K., Verhalen, L. M. & Greenhagen, B. E. Importance of Fungicide Seed Treatment and Environment on Seedling Diseases of Cotton. *Plant Dis.* **96**, 1805–1817 (2012).
28. Diffen. Angiosperms vs. Gymnosperms. *Diffen: Compare Anything* 1 (2015). at http://www.diffen.com/difference/Angiosperms_vs_Gymnosperms
29. Dudzik, M. Seed Plants: Gymnosperms and Angiosperms. *OpenStax* 1 (2015). at <http://cnx.org/contents/74c90184-cfcd-4362-aebd-4850f12ea41d@1/Seed-Plants-Gymnosperms-and-An>
30. Goduti, D. *Seed Plants: Angiosperms. Concepts of Biology* (2013).
31. Rokne, J. G. A Simplified Model for Light Interaction with Plant Tissue.

- (1998).
32. Fiedor, L., Kania, A., My, B. & Orze, Ł. Understanding Chlorophylls: Central magnesium ion and phytol as structural determinants. *Biochim. Biophys. Acta* **1777**, 1491–1500 (2008).
 33. Pavia, D. L., Lampman, G. M., Kriz, G. S. & Engel, R. G. *Introduction to Organic Laboratory Techniques: A Microscale Approach*. (1999).
 34. Dominguez, E., Heredia-Guerrero, J. A. & Heredia, A. The biophysical design of plant cuticles: An overview. *New Phytol.* **189**, 938–949 (2011).
 35. Yeats, T. H. & Rose, J. K. C. Topical Review on Cuticle Synthesis and Function The Formation and Function of Plant Cuticles 1. *Plant Physiol.* **163**, 5–20 (2013).
 36. Dean, R. *et al.* The Top 10 fungal pathogens in molecular plant pathology. *Mol. Plant Pathol.* **13**, 414–430 (2012).
 37. Deising, H. B., Werner, S. & Wernitz, M. The role of fungal appressoria in plant infection. *Microbes Infect.* **2**, 1631–1641 (2000).
 38. Longhi, S. & Cambillau, C. Structure-activity of Cutinase, a small lipolytic enzyme. *Biochim Biophys Acta* **1441**, 185–196 (1999).
 39. Boller, T. & Felix, G. A renaissance of elicitors: perception of microbe-associated molecular patterns and danger signals by pattern-recognition receptors. *Annu Rev Plant Biol* **60**, 379–406 (2009).
 40. Carvalho, F. P. Agriculture, pesticides, food security and food safety. *Environ. Sci. Policy* **9**, 685–692 (2006).
 41. Grusak, M. A. & Dellapenna, D. Improving The Nutrient Composition of Plants to Enhance Human Nutrition and Health¹. *Annu. Rev. Plant Physiol. Plant Mol. Biol.* **1**, 133–161 (1999).
 42. Ausveg. Fungal Diseases. (2015). at <http://ausveg.com.au/intranet/technical-insights/cropprotection/fungal-diseases.htm>
 43. Pernezny, K., Elliott, M., Palmateer, A. & Havranek, N. *Guidelines for Identification and Management of Plant Disease Problems : Part II . Diagnosing Plant Diseases Caused by Fungi , Bacteria and Viruses 1. IFAS Extention* (2014).
 44. Ausveg. Bacterial Diseases. (2015). at <http://ausveg.com.au/intranet/technical-insights/cropprotection/bacterial-diseases.htm>

45. Gaunt, N. P., Thomson, N., Padia, F., Seymour, M. & Moger, J. Advances in Analytical Capability to Power Agrochemical Product Design. *Outlooks Pest Manag.* **29**, 104–110 (2018).
46. Codex Committee for Pesticide Residues. *The List of Methods for Pesticide Residue Analysis, including Methods of Determination for Dithiocarbamates.* (2001). at <<http://www-naweb.iaea.org/nafa/fep/Methods-Main.pdf>>
47. Alder, L., Greulich, K., Kempe, G. & Vieth, B. Residue analysis of 500 high priority pesticides: Better by GC–MS or LC–MS/MS? *Mass Spectrosc. Rev.* **25**, 838–865 (2006).
48. Benninghoven, A. Analysis of Submonolayers on Silver by Negative Secondary Ion Emission. *Phys. status solidi* **34**, K169–K171 (1969).
49. Spengler, B., Hubert, M. & Kaufmann, R. MALDI Ion Imaging and Biological Ion Imaging with a new Scanning UV-Laser Microprobe. in *42nd ASMS Conference on Mass Spectrometry* 1041–1044 (1994).
50. Buchholz, A. & Nauen, R. Translocation and translaminar bioavailability of two neonicotinoid insecticides after foliar application to cabbage and cotton. *Pest Manag. Sci.* **16**, 10–16 (2002).
51. Létondor, C., Pascal-lorber, S. & Laurent, F. Uptake and distribution of chlordecone in radish: Different contamination routes in edible roots. *Chemosphere* **118**, 20–28 (2015).
52. Grossmann, K., Hutzler, J., Caspar, G., Kwiatkowski, J. & Brommer, C. L. Saflufenacil (Kixor™): Biokinetic Properties and Mechanism of Selectivity of a New Protoporphyrinogen IX Oxidase Inhibiting Herbicide. *Weed Sci.* **59**, 290–298 (2011).
53. Krause, C. R. Foliar penetration of a fungicide as detected by scanning electron microscopy and energy dispersive x-ray analysis. *Scan. Electron Microsc.* **2**, 811–815 (1985).
54. Liu, Z. Confocal laser scanning microscopy – an attractive tool for studying the uptake of xenobiotics into plant foliage. *J. Microsc.* **213**, 87–93 (2004).
55. Liu, Y. & Liu, T. in *Computer and Computing Technologies in Agriculture IV: 4th IFIP TC 12 Conference, CCTA 2010, Nanchang, China, October 22-25, 2010, Selected Papers, Part IV* (eds. Li, D., Liu, Y. & Chen, Y.) 427–434 (Springer Berlin Heidelberg, 2011). doi:10.1007/978-3-642-

56. Zhang, P. X., Zhou, X., Cheng, A. Y. S. & Fang, Y. Raman Spectra from Pesticides on the Surface of Fruits Raman Spectra from Pesticides on the Surface of Fruits. *J. Phys. Conf. Ser.* **28**, 7–11 (2006).
57. Clauson, S. L., Sylvia, J. M., Arcury, T. A., Summers, P. & Spencer, K. M. Detection of Pesticides and Metabolites Using Surface-Enhanced Raman Spectroscopy (SERS): Acephate. *Appl. Spectrosc.* **69**, 785–793 (2015).
58. Yu, Y., Sohma, Y., Takimoto, S., Miyauchi, T. & Yasui, M. Direct visualization and quantitative analysis of water diffusion in complex biological tissues using CARS microscopy. *Sci. Rep.* **3**, 1–11 (2013).
59. Min, W., Freudiger, C. W., Lu, S. & Xie, X. S. Coherent Nonlinear Optical Imaging: Beyond Fluorescence Microscopy. *Annu. Rev. Phys. Chem.* **62**, 507–530 (2011).
60. Freudiger, C. W. *et al.* Label-Free Biomedical Imaging with High Sensitivity by Stimulated Raman Scattering Microscopy. *Science (80-.).* **322**, 1857–1861 (2008).
61. Lee, M. *et al.* In vivo imaging of the tumor and its associated microenvironment using combined CARS / 2- photon microscopy In vivo imaging of the tumor and its associated microenvironment using combined CARS / 2-photon microscopy. *IntraVital* **4**, 1–8 (2015).
62. Drutis, D. M. *et al.* Three-dimensional chemical imaging of skin using stimulated Raman scattering microscopy. *J. Biomed. Opt.* **19**, 111604 (2014).
63. Sin, W., Belsey, N. A., Garrett, N. L., Moger, J. & Delgado-charro, M. B. Molecular diffusion in the human nail measured by stimulated Raman scattering microscopy. *PNAS* **112**, 6–11 (2015).
64. Mansfield, J. C. *et al.* Label-free Chemically Specific Imaging *in planta* with Stimulated Raman Scattering Microscopy. *Anal. Chem.* **85**, 5055–5063 (2013).
65. Littlejohn, G. R. *et al.* In Vivo Chemical and Structural Analysis of Plant Cuticular Waxes Using Stimulated Raman Scattering Microscopy 1 [OPEN]. *Plant Physiol.* **168**, 18–28 (2015).
66. Tolles, W. M., States, U. & Nibler, J. W. A Review of the Theory and Application of Coherent Anti-Stokes Raman Spectroscopy (CARS). *J. Appl. Spectrosc.* **31**, 253–271 (1977).

67. Maker, P. & Terhune, R. Study of Optical Effects Due to an Induced Polarization Third Order in the Electric Field Strength. *Phys. Rev.* **137**, 801–818 (1965).
68. Schreiber, L. & Riederer, M. Determination of diffusion coefficients of octadecanoic acid in isolated cuticular waxes and their relationship to cuticular water permeabilities. *Plant, Cell Environ.* **19**, 1075–1082 (1986).
69. Bewick, T. A., Shilling, D. G. & Querns, R. Evaluation of Epicuticular Wax Removal from Whole Leaves with Chloroform Author (s): Te Evaluation of Epicuticular Wax Removal from Whole Leaves with Chloroform. *Weed Technol.* **7**, 706–716 (1993).
70. Martin, J. Determination of the components of plant cuticles. *J. Sci. Food Agric.* **11**, 635–640 (1960).
71. Stephenson, R. *Sedum, cultivated stonecrops*. (1994).
72. Rogiers, S. Y. A., Greer, L. A. A., White, R. G. A. & Steel, C. C. A. Effects of spray adjuvants on grape (*Vitis vinifera*) berry microflora , epicuticular wax and susceptibility to infection by *Botrytis cinerea*. *Australas. Plant Pathol.* **34**, 221–228 (2005).
73. Socrates, G. *Infrared and Raman Characteristic Group Frequencies Contents*. (2004).
74. Baur, P. Mechanistic aspects of foliar penetration of agrochemicals and the effect of adjuvants. *Recent Res. Dev. Agric. Food Chem.* **2**, 809–837 (1998).
75. Wang, C. *et al.* *In situ* chemically specific mapping of agrochemical seed coatings using stimulated Raman scattering microscopy. *J. Biophotonics* **11**, 1–7 (2018).
76. Harrison, S. K. & Wax, L. M. The Effect of Adjuvants and Oil Carriers on Photodecomposition of 2,4-D, Bentazon, and Haloxyfop. *Weed Sci.* **34**, 81–87 (1986).
77. FAO & WHO. *Pesticide residues in food – 2004*. (2004).
78. Schreiber, L. & Riederer, M. Ecophysiology of cuticular transpiration : comparative investigation of cuticular water permeability of plant species from different habitats. *Oecologia* **107**, 426–432 (1996).

Appendix A

The follow pages outline the code created for this work. All code herein was written internally, by myself or with help from the Moger group. The code has also been heavily annotated (with red boxes and bold black text) to better explain the different segments, and their functions.

The code, printed below, has been split into 5 steps, which all provide essential functions towards a successful boundary plot and diffusion rate calculation. Step one simply allows for optimised initial steps, data loading and conversion into an array, whereas steps 2-4 are vital for boundary detection, monitoring, and overall rate calculation. Step 5 is an additional tool, which was created to act as a “zoom-in” function, and noise reduction step. The following two-page annotated algorithm schematic goes into further detail about the codes’ function and outputs.

```
#####
%% 1) Initialisation %%
#####
clc;
tic; %% Start tracking the execution time.
number_of_images = 1;
image_length = 512; %% We assume the images are 512 x 512.
image = zeros(number_of_images, image_length, image_length);
for i_index = 1:number_of_images
    %% Case I: Stack of images
    if number_of_images > 1
        image_raw = imread('Stack2.tif', i_index);
        image(i_index, :, :) = im2double(image_raw);
    %% Case II: A single image
    else
        image_raw = imread('test.jpg');
        image_raw = image_raw(1:image_length, 1:image_length, :);
        image(i_index, :, :) = im2double(image_raw(:, :, 2));
    end
end
clear i_index
#####
%% 2) Create Boundary %%
#####
boundary_array = zeros(number_of_images, image_length);
for a_index = 1:number_of_images
    for b_index = 1:image_length
        s_index = 0;
        image_start = 1;
        image_stop = image_length;
        image_midpoint = image_length/2;
        middle = median([max(image(a_index, b_index, :)) ...
min(image(a_index, b_index, :))]);
        while (s_index ~= 1) % Locate the slice's transition
            point.
                mean_left = mean(image(a_index, b_index, image_start...
                    : (image_start+(image_stop+1-
                        image_start)/2)));
                mean_right =
                    mean(image(a_index, b_index, ((image_start+...
                        (image_stop+1-
                            image_start)/2)+1):image_stop));
                if (abs(middle-mean_left) < abs(middle-mean_right))
                    image_stop = image_stop-2;
                else
                    image_start = image_start+2;
                end
                if image_stop-image_start == 1
                    s_index = 1;
                    boundary_array(a_index, b_index) = image_start;
                end
            end
        end
    end
    toc; %% Display the current timestamp.
end
clear a_index b_index s_index
#####
%% 3) Calculate diffusion rates %%
#####

#####
displacement = zeros(number_of_images, image_length);
mean_displacement = squeeze(zeros(1, number_of_images-1));
for d_index = 1:(number_of_images-1)
    displacement(d_index, :) = boundary_array(d_index+1, :)-...
        boundary_array(d_index, :);
    mean_displacement(d_index) = mean(displacement(d_index, :));
end
time_stamp = [0 60 120 180 360 720 1440];
diffusion_rate = displacement./time_stamp(2);
#####
%% 4) Plot boundaries and displacements %%
#####
for p_index = 1:number_of_images
    figure(1)
    subplot(2,4,plot_index)
    surf(squeeze(image(p_index, :, :)), 'edgecolor', 'none');
    hold on;
    plot3(boundary_array(p_index, :), 1:image_length, ...
        linspace(1,1, image_length), 'r');
    view([0 0 90]);
    if p_index ~= number_of_images
        figure(2)
        subplot(2,3,p_index)
        plot(displacement(p_index, :))
        title(['Mean Displacement = ' ...
            num2str(mean_displacement(p_index))])
    end
end
#####
%% 5) Error and noise reduction tool %%
#####
s1_index = 1;
cut_off_point = min(boundary_array(slice_index, 101:end));
shift_array = boundary_array(slice_index, 101:end)-cut_off_point;
max_shift = max(shift_array);
cut_image = zeros(image_length-100, image_length-max_shift);
for c_index = 1:(image_length-100)
    cut_image(c_index, :) = image(s1_index, c_index+100, ...
        (shift_array(c_index)+1):(end-(max_shift-
            shift_array(c_index))));
end
figure(3)
subplot(1,2,1)
surf(squeeze(image(s1_index, 101:end, :)), 'edgecolor', 'none');
hold on;
plot3(boundary_array(s1_index, 101:end), 1:image_length-...
    100, linspace(1,1, image_length-100), 'r');
view([0 0 90]);
subplot(1,2,2)
surf(cut_image, 'edgecolor', 'none');
hold on;
plot3(linspace(cut_off_point, cut_off_point, image_length-100), ...
    1:image_length-100, linspace(1,1, image_length-
    100), 'r', 'LineWidth', 4);
view([0 0 90]);
```

```

%% 1) Initialisation %%
clc;
tic; %% Start tracking the execution time.
number_of_images = 1;
image_length = 512; %% We assume the images are 512 x 512.
image = zeros(number_of_images,image_length,image_length);
for i_index = 1:number_of_images
    %% Case I: Stack of images
    if number_of_images > 1
        image_raw = imread('Stack2.tif',i_index);
        image(i_index, :, :) = im2double(image_raw);
    %% Case II: A single image
    else
        image_raw = imread('test.jpg');
        image_raw = image_raw(1:image_length,
1:image_length, :);
        image(i_index, :, :) = im2double(image_raw(:, :, 2));
    end
end
clear i_index
%% 2) Create Boundary %%
boundary_array = zeros(number_of_images,image_length);
for a_index = 1:number_of_images
    for b_index = 1:image_length
        s_index = 0;
        image_start = 1;
        image_stop = image_length;
        image_midpoint = image_length/2;
        middle = median([max(image(a_index,b_index, :) ...

min(image(a_index,b_index, :))]);
        while (s_index ~= 1) % Locate the slice's transition
point.
            mean_left = mean(image(a_index,b_index,image_start...
:(image_start+(image_stop+1-
image_start)/2));
            mean_right = mean(image(a_index,b_index,
((image_start+...
                (image_stop+1-image_start)/
2)+1):image_stop));
            if(abs(middle-mean_left) < abs(middle-
mean_right))
                image_stop = image_stop-2;
            else
                image_start = image_start+2;
            end
            if image_stop-image_start == 1
                s_index = 1;
                boundary_array(a_index,b_index) =
image_start;
            end
        end
    end
end
toc; %% Display the current timestamp.
clear a_index b_index s_index

```

The initialisation step below, tackles the initial data loading step and enables easy-to-read data manipulation by taking the image and making it into an array.

"Zeroing" the data creates a canvas array, under the assumption that all images are 512 x 512 pixels.

Here we have two separate cases. Case I represents a part of the code that scans through each frame of the .tif stack. Whereas Case II is a less complex version for a single image, simply used to map the boundary of one pre-selected image.

The follow piece of code detail the detection, assumption and creation of a boundary boundary line. Slice by slice, this segment scans in two indexes. Every row of data has a transitional point, where there was an intensity spike between background and imaged material.

a_index scans through A Index scans through the number of images in the boundary array.

b_index identifies the wax boundary by scanning the rows – honing in on the boundary itself by searching for a larger than "normal" intensity difference.

Note: "tic" and "toc" are simple coding tools used to detect timing inefficiencies, or areas in which the algorithm has become stuck. Used at various stages throughout the creation of this code.

Here, the code has detected the boundary, and exits its "while loop" and begins the same process on the next row. This is repeated until the full image has been fully detected.

Appendix B

Posters and Presentations

‘Econos’ 2-5th April 2017 – Jena, Germany.

Coherent Raman Scattering for Agrochemical Research & Development

Nicholas P Gaunt^a, Niall Thomson^b, Faheem Padia^b, Julian Moger^a

^a *Biomedical Physics, School of Physics & Astronomy, University of Exeter, Exeter, UK*

^b *Syngenta, Jealott's Hill, Bracknell, Berkshire, UK*

With the global population continually rising ever closer to 10 billion, so does the pressure on the agricultural industry to meet the demands of food supply in a sustainable manner. Whilst there is no plausible way to stop the population growth, we can invest in fundamental plant and agrochemical research and in the development of improved analytical tools to support research in these areas. Imaging techniques such as coherent anti-Stokes Raman Scattering (CARS) and stimulated Raman Scattering (SRS) provide a label-free image contrast, which is not susceptible to fluorescence from pigments in the plants, like other current techniques. We have applied coherent Raman Scattering (CRS) as a novel analytical technique that allows *in situ* analysis of agrochemical active ingredients (AIs) and adjuvants through a plants first defence, its wax. The ability to visualise these AIs and adjuvants through wax to reveal the diffusion properties of separate products will enable a step change in agrochemical design, through determination of the spatial distribution of the materials and their roles within the applied products.

Coherent Raman Scattering for Agrochemical Research & Development

Nicholas P Gaunt^a, Niall Thomson^b, Faheem Padia^b, Julian Moger^a

^a Biomedical Physics, School of Physics & Astronomy, University of Exeter, Exeter, UK

^b Syngenta, Jealott's Hill, Bracknell, Berkshire, UK



NG314@exeter.ac.uk

Introduction

With global food security, climate change and the decreasing amount of arable land becoming more problematic, it has become of paramount importance to increase our plant yields. [1] Research suggests that, without agrochemicals, we would have 40% less than we currently have, showing how much we rely on the continued improvement of agrochemicals. [2]

An agrochemical's first obstacle is the cuticle. Composed of wax, it works as a barrier against water loss, as well as halting the ingress of toxins and pathogens into the plant. In the investigation, we image wax at submicron resolution, using Coherent Raman Spectroscopy.

Coherent Raman Spectroscopy

CRS provides a label-free image contrast, which is not susceptible to fluorescence from pigments like current techniques. By applying this technology we have suggested a novel analytical technique that allows in-situ analysis of agrochemical AIs in wax.

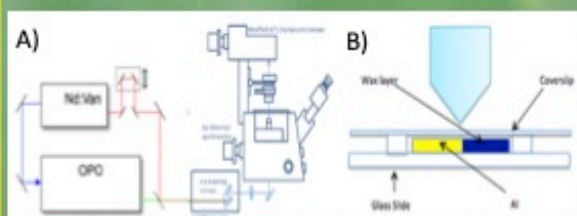


Fig 1 a) CRS set up b) 2D diagram of imaging method in XY plane, using an oil Immersion lens.

CRS was performed with the setup in figure 1, using bands in the silent region, shown in the Raman Spectra shown in figure 2. Both Alkyl Benzoate and Tween 20, two active ingredients used by heavily by the agrochemical industry contain several bonds not found in cuticle wax, such as the C=O stretch found at $\sim 1740\text{cm}^{-1}$. When measured in conjunction with CH_2 (Lipid) stretch, which is the dominating bond type in cuticle wax, we can create video-speed contrasted images to map and analyse the diffusion of these specific agrochemical ingredients.

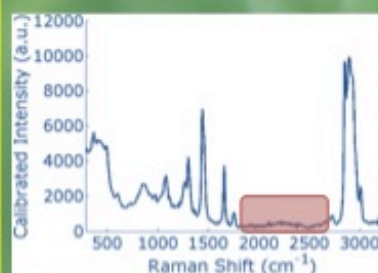


Fig 2 Raman Spectra for Paraffin Wax. Red highlight between $1600\text{-}2800\text{cm}^{-1}$ showing a region with no peaks, which can be used to help identify the diffused species, with high specificity.

Conclusion

The chemical composition and structure of the cuticle in plants are crucial elements for survival, physiology, and development. We have shown that SRS microscopy can be used to acquire images of wax with a variety of AIs, enabling simultaneous analysis of diffusion. In contrast to CARS microscopy, which is more common, SRS images of plant tissues would contain very low auto-fluorescence from chloroplasts or cell walls and are therefore easier to interpret. We can now use the protocol for a multitude of AIs, in combination. With this in mind, we can be a part of a step-wise change to introduce next generation agrochemicals.

Diffusion

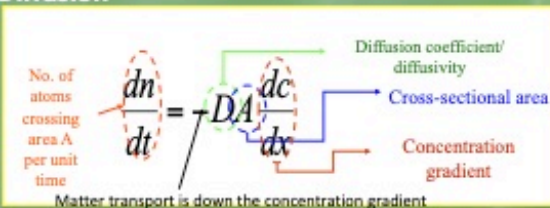


Fig 3 Annotated Fick's First Law of Diffusion. The diffusion flux along direction x is proportional to the concentration gradient

By measuring the concentration of diffusion of these compounds over time, we are able to determine the spatial distribution of the materials and their roles within an applied product. Here, we have shown the measurable difference in diffusion between an Alkyl Benzoate and Tween 20, two AIs.

Results

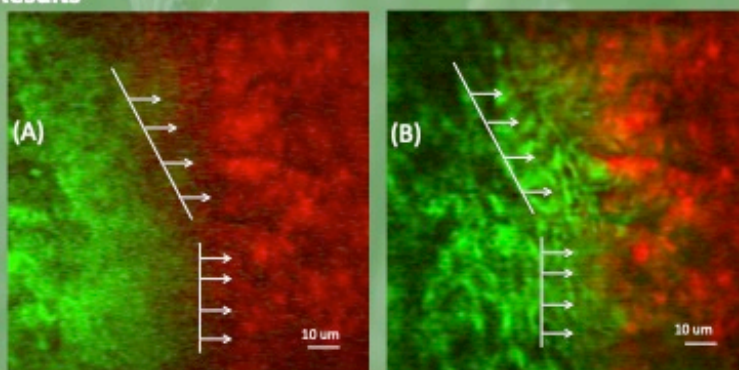


Fig 4 A time series of SRS x-y planar image of the penetration of Alkyl Benzoate (Green) into Paraffin Wax (Red). C=O of Alkyl Benzoate at 1737cm^{-1} at $t=0$ with CH_2 of wax at 2845cm^{-1} . A) shows $t=0$, B) showing the same position at $t=1440\text{s}$

Images show the diffusion process at 2 time points (0s and 1440s) diffusing in the x-y direction. Using MATLAB to plot the wax boundary, we are able to define pixel intensity and plot, not only distance diffused, but the percentage concentration to give us Fig 5 and the ability to gather data on the diffusivity, relating to Fig 3

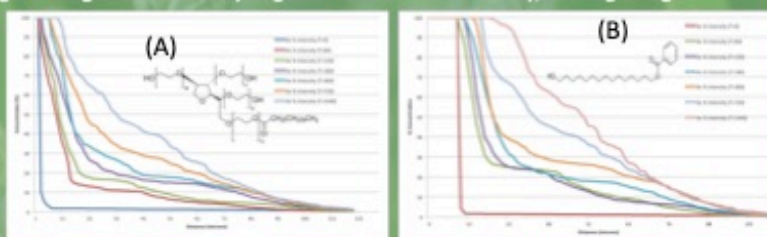


Fig 5 Experimentally measured, SRS signal versus diffusion depth profiles for (A) Tween 20 and (B) Alkyl Benzoate.

Experimentally measured at 7 time points over 1440 second, SRS signal versus diffusion depth profiles for Alkyl Benzoate and Tween 20. Analysis of the SRS profiles revealed Alkyl Benzoate's much faster diffusion, compared to Tween 20, showing a faster uptake into the wax, seeing 4x higher concentrations of Alkyl Benzoate in regions after 1440 seconds. The shape of (A) shows it is obeying Fick's 1st Law, however (B) suggests a two-step diffusion process with a changing co-efficient.

Acknowledgements

I would like to thank Syngenta and all members of the Moger group, and EPSRC for funding the project

References

- [1] Food and Agricultural Organization of the United Nations
- [2] United Nations Environment Programme

**SPIE Photonics West 27th-1st February 2018 –
San Francisco, USA.**

PROCEEDINGS OF SPIE

[SPIDigitalLibrary.org/conference-proceedings-of-spie](https://spiedigitallibrary.org/conference-proceedings-of-spie)

Monitoring agrochemical diffusion through cuticle wax with coherent Raman scattering

Nicholas P. Gaunt, Niall Thomson, Faheem Padia, Julian
Moger

Nicholas P. Gaunt, Niall Thomson, Faheem Padia, Julian Moger, "Monitoring agrochemical diffusion through cuticle wax with coherent Raman scattering," Proc. SPIE 10498, Multiphoton Microscopy in the Biomedical Sciences XVIII, 1049836 (23 February 2018); doi: 10.1117/12.2289746

SPIE.

Event: SPIE BiOS, 2018, San Francisco, California, United States

Downloaded From: <https://www.spiedigitallibrary.org/conference-proceedings-of-spie> on 31 May 2019 Terms of Use: <https://www.spiedigitallibrary.org/terms-of-use>

Monitoring Agrochemical Diffusion Through Cuticle Wax with Coherent Raman Scattering

Nicholas P Gaunt ^a, Niall Thomson ^b, Faheem Padia ^b, Julian Moger ^{a*}

^a School of Physics, University of Exeter, Exeter. EX4 4QL, UK;

^b Syngenta, Jealott's Hill Research Station, Bracknell, Berkshire UK

*To whom correspondence should be addressed.

Email: J.Moger@exeter.ac.uk

ABSTRACT

The world's population is increasing rapidly and higher calorific diets are becoming more common; as a consequence the demand for grain is predicted to increase by more than 50% by 2050 without a significant increase in the available agricultural land. Maximising the productivity of the existing agricultural land is key to maintaining food security and agrochemicals continue to be a key enabler for the efficiency gains required. However, agrochemicals can be susceptible to significant losses and thus often require further chemical to be applied to compensate. Sources of such losses include spray drift, poor spray retention/capture by the target and poor penetration through the plant cuticle. Adjuvants can be used to help mitigate such losses but characterising how they alter the movement of the active ingredients (AIs) can be challenging. In this contribution we demonstrate the use of coherent Raman Scattering (CRS) as a tool to enable in-situ, real-time, label free characterisation of agrochemical AI as they move through wax.

Keywords: stimulated Raman scattering, microscopy, cuticle wax, plant, seed, diffusion, agrochemical, active ingredient

1. INTRODUCTION

The world's population could rise as high as 15.8 billion by the end of the century¹ and the demand for high calorie diets is increasing. Coupled with climate change, land erosion and the increased use of arable land for biofuel production, reducing the availability of agricultural land; maintaining global food security will be a significant challenge. Agrochemicals are a key factor in crop yields and without them currently 40% of the world's food would not exist.² However, agrochemicals can be susceptible to significant losses due to spray drift and poor spray retention, as well as poor penetration into the plant cuticle. Adjuvants are commonly used to reduce these losses and improve uptake of AIs into the epicuticular wax but there is currently no technique to reveal the real-time, label free location of the AI. CRS has been shown previously to provide information on uptake of nail treatment drugs into human nail³ and enable chemically specific *in planta* imaging⁴. Thanks to its ability to produce image-format data rapidly CRS could provide a fantastic insight into the way AIs interact with epicuticular wax.

In this study, we use stimulated Raman scattering (SRS) microscopy with a fiber laser source to analyse the diffusion of active ingredients (AIs) into wax. Paraffin wax has been used in this investigation due to its chemical similarity to epicuticular wax, its ready availability and its signature will not interfere with C≡N stretch (2220 cm⁻¹). The AIs can be

Multiphoton Microscopy in the Biomedical Sciences XVIII, edited by Ammasi Periasamy,
Peter T. C. So, Karsten König, Xiaoliang S. Xie, Proc. of SPIE Vol. 10498, 1049836
© 2018 SPIE · CCC code: 1605-7422/18/\$18 · doi: 10.1117/12.2289746

Proc. of SPIE Vol. 10498 1049836-1

Downloaded From: <https://www.spiedigitallibrary.org/conference-proceedings-of-spie> on 31 May 2019
Terms of Use: <https://www.spiedigitallibrary.org/terms-of-use>

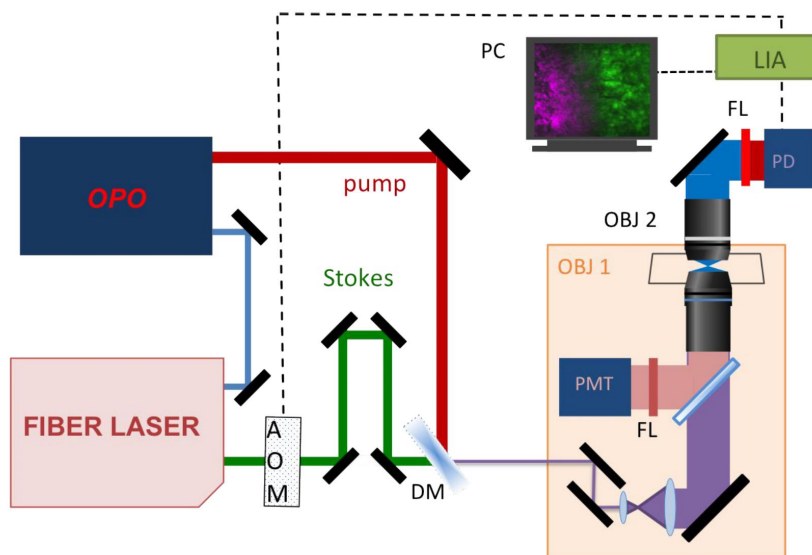


Figure 1: The optical setup of fiber laser-based stimulated Raman scattering for AIs and wax. AOM: acousto-optic modulator, DM: dichroic mirror, OBJ: objective, FL: filter, PMT: photomultiplier tube, PD: photodiode, LIA: lock-in amplifier.

Spontaneous Raman spectroscopy

Spontaneous Raman spectra of waxes and agrochemical components were obtained using a Renishaw RM1000 Raman Microscope (Renishaw PLC, UK). This contained a 785 nm diode continuous wave laser with a maximum power at the sample of 300 mW and a spectral grating with 1200 lines/mm, which gave a spectral resolution of 1 cm^{-1} . The system was calibrated prior to every spectral acquisition using the Raman band of a silicon wafer at 521 cm^{-1} . Spectral data were acquired using Renishaw v.1.2 WiRE software.

Sample preparation

Paraffin wax was obtained from Sigma-Aldrich Company Ltd. The wax was melted and sealed between two cover slips. The AIs; Fludioxonil and Azoxystrobin (Syngenta) were dissolved in distilled water at 1.8mg/L and 6mg/L, respectively, before injection between the slips.

3. RESULTS

Figure 2 shows the CARS (pseudo color: green) and SRS (pseudo color: magenta) images of wax and Azoxystrobin (AZ), respectively.

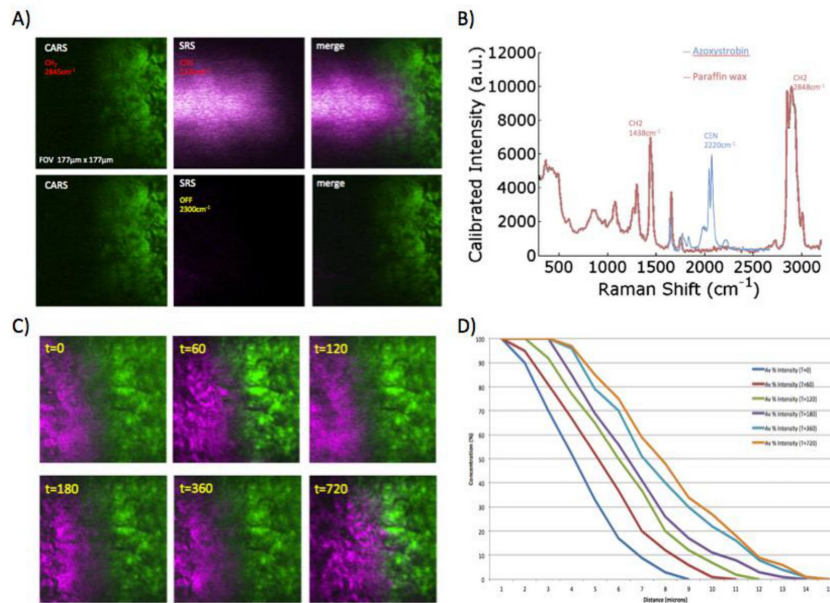


Figure 2: A) Coherent Raman scattering images of paraffin wax's CH₂ and AZ's chemically specific C≡N. (B) shows the spontaneous Raman spectra of AZ (C≡N) over paraffin wax's Raman signature. The diffusion of AZ into wax can be imaged and analyzed as shown in (C) and (D). Field of view of (A) and (C): 177 μm x 177 μm.

Moreover, we can fit the data with diffusion theory to obtain quantitative diffusion characteristics of cuticle wax-active ingredient interactions.³ **Figure 3 (A) and (B)** show the average pixel intensity data extracted from the SRS images, presented graphically as a function of time and depth of two AIs, (A) AZ and (B) Fludioxonil. (C) and (D) show the predicted evolution of the SRS signal as the experiment proceeds based on the analytical solution to Fick's second law expressed in **Equation 1**. This model has been used as experiments performed follow nonsteady-state diffusion into an infinite source, assuming that paraffin wax is a homogenous plane sheet with constant diffusivity, D_i . During the course of the experiment we make the assumption that is a constant source of AI to the wax boundary and the wax is infinite in thickness.

$$\frac{S}{S_{z=0}} = 1 - \operatorname{erf}\left(\frac{z}{2\sqrt{D_i t}}\right)$$

Equation 1 Analytical solution for Ficks' second law with; normalised signal ($S/S_{z=0}$), depth into nail (z), diffusion coefficient (D_i), time (t) and error function (erf)

Figure 3 (A) and (B) highlight the experimental difference in diffusivity between AZ and Fludioxonil into paraffin wax over the course of 24 minutes. These plots show AZ's diffusivity is greater than that of Fludioxonil. The predictions shown in **Figure 3 (C) and (D)** demonstrate how the experimental results deviate from classical modeling as the time of diffusion increases. As the shape of the concentration profiles (at different time points) differs from the calculated model, it is safe to assume variation in D_i . This behaviour is characteristic of a time- and concentration-dependent diffusion coefficient. This evolution is shown in **Figure 3 (E)**, illustrated by plotting, as a function of time, the areas under the srs signal profiles, normalized by the square root of time. The shaded areas on this graph represent the ranges that would be anticipated if the AI diffusivity were constant. However, because these values change considerably more than the given range predicted (by mean plus or minus standard deviation), the results would imply a progressive uptake of these AIs with a varying diffusion co-efficient.

4. CONCLUSION

SRS microscopy has been successfully used to visualise and characterise AI uptake kinetics and how that varies with the chemistry of the AI. Furthermore, SRS has been used as a tool to determine diffusion model. Future work will investigate the utility of SRS with fiber laser excitation as a tool for label free, real-time diffusion measurements *in planta*.

ACKNOWLEDGMENTS

We thank the Industrial Cooperative Awards in Science and Technology (iCASE) and Syngenta for funding this work.

REFERENCES

1. United Nations. *World Population by 2300*. (2004).
2. Oerke, E. C. Crop losses to pests. *Agric. Sci.* **144**, 31–43 (2006).
3. Sin, W., Belsey, N. A., Garrett, N. L., Moger, J. & Delgado-charro, M. B. Molecular diffusion in the human nail measured by stimulated Raman scattering microscopy. *PNAS* **112**, 6–11 (2015).
4. Mansfield, J. C. *et al.* Label-free Chemically Specific Imaging in Planta with Stimulated Raman Scattering Microscopy. *Anal. Chem.* **85**, 5055–5063 (2013).

INTRODUCTION

The plant cuticle is a composite membrane which forms the outer surface of a plant, controlling the exchange of matter between the leaf and its environment. It provides the first line of defense against pathogens, and is the first barrier an applied agrochemical must pass. The ability to characterise and tune the uptake of agrochemicals into plants in real time, may enable a lower environmental dose to be applied and be advantageous for the development of new agrochemical products

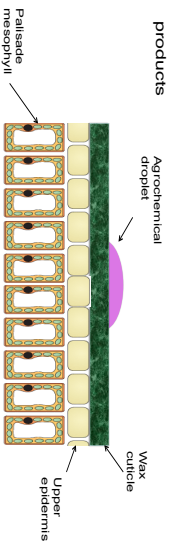


Figure 1: Internal structure of a typical leaf. The surface of a leaf contains wax cuticle, epidermal cells as cover for the upper and lower surface, and palisade mesophyll to aid the absorption of light.

Here, we use stimulated Raman scattering (SRS) microscopy to analyse the diffusion of active ingredients (AIs) into a cuticle proxy, paraffin wax. The AIs, Azoxystrobin (AZ) and Fludioxonil (FDL), can be identified by imaging chemically distinct bonds such as C≡N stretch (2220 cm⁻¹). By characterising the movement of the agrochemical AIs through the cuticle barrier and harnessing the characterisation power of the SRS, we will enable increased understanding of the interaction of AIs and support further innovation.

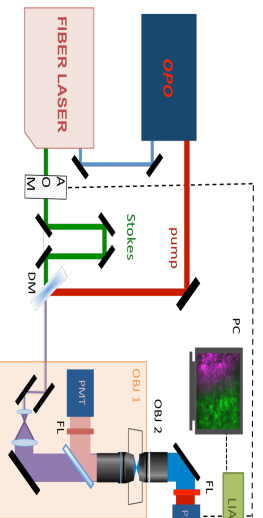


Figure 2: The optical setup of fiber laser-based stimulated Raman scattering for AIs and wax. AOM: acousto-optic modulator, DM: dichroic mirror, OBI: objective, FL: filter, PMT: photomultiplier tube, PD: photodiode, LIA: lock-in amplifier.

SRS OF ACTIVE INGREDIENTS

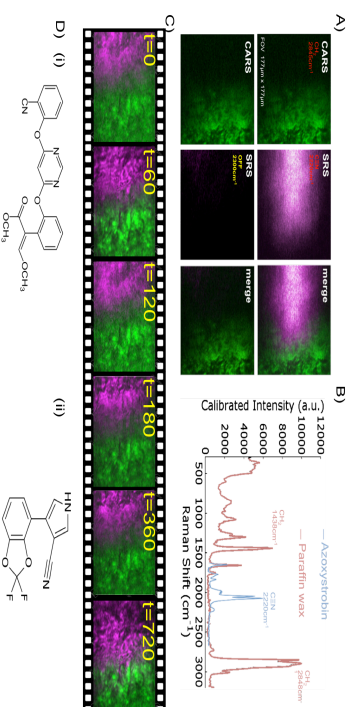


Figure 3: (A) Coherent Raman scattering images of paraffin wax's CH₂ (CARS, green) and AZ's chemically specific C≡N (SRS, magenta). (B) shows the spontaneous Raman spectra of AZ (C≡N) over paraffin wax's Raman signature. The diffusion of AZ into wax can be imaged and analyzed as shown in (C). Field of view of (A) and (C): 1771μm x 1771μm. (D) Structures of (i) AZ and (ii) Fludioxonil

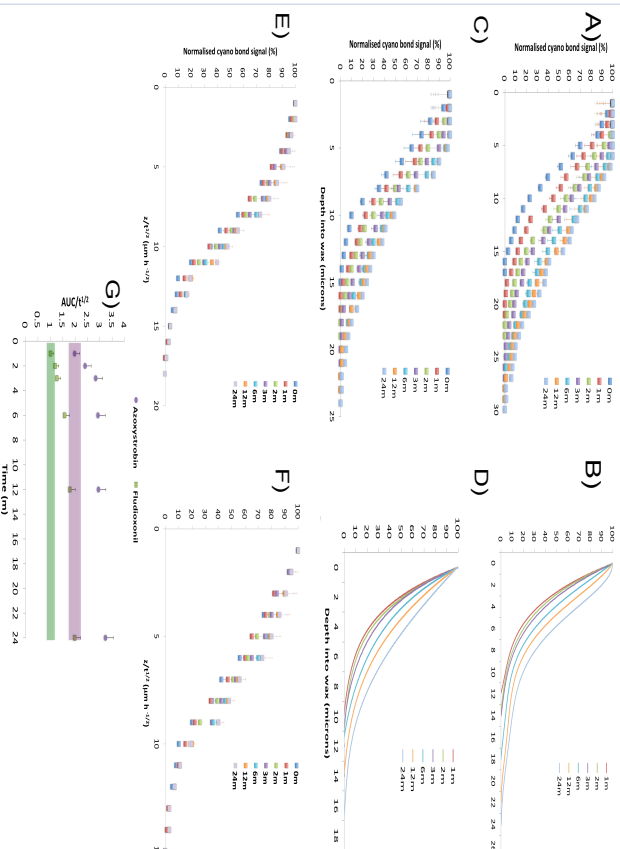


Figure 4: Comparison of depth profiles for (A) AZ, (B) FDL as a function of time, compared with the corresponding predicted profiles calculated by Eq. 1, assuming a constant source of AI. (C) AZ (D) FDL. Normalised SRS signal of (E) AZ and (F) FDL, as a function of $z_{1/2}$. (G) The area under these experimental curve profiles (AUC), normalised by the $1/2$ as a function of time. The shaded area (AZ purple, Fludioxonil green) represent the range predicted (mean \pm standard deviation) for constant diffusion co-efficient values.

UPTAKE KINETICS

We fit the data with diffusion theory to obtain quantitative diffusion characteristics of cuticle wax-AI interaction. We fit the data to Fick's second law, as experiments follow non-steady-state diffusion into an infinite source.

$$\frac{S}{S_z = 0} = 1 - \operatorname{erf} \left(\frac{z}{2\sqrt{Dit}} \right)$$

Equation 1 Analytical solution for Fick's second law with: normalised signal ($S/S_{z=0}$), depth into wax (z), diffusion coefficient (D), time (t) and error function (erf)

Figures 4 (A) and (B) highlight the experimental difference in diffusivity between AZ and FDL into paraffin wax over the course of 24 minutes. These plots show that the diffusivity of AZ is greater than that of FDL. The predictions shown in Figures 4 (C) and (D) demonstrate how the experimental results deviate from classical modelling as the time of diffusion increases. As the shape of the concentration profiles (at different time points) differs from the calculated model, it is conclusive of variation in D.

If D is constant, plotting $t^{1/2}$, as shown in Figure 4 (E) and (F), would show the data points collapse into one single curve. This behaviour is not seen, and is therefore characteristic of a time- and concentration-dependent diffusion coefficient. This evolution, plotted as the normalised area under the SRS signal as a function of time is shown in Figure 4 (G). The shaded areas on this graph represent the ranges that would be anticipated if the AI diffusivity were constant. However, because these values change considerably more than the given range predicted (by mean plus or minus standard deviation), the results would imply a progressive uptake of these AIs with a varying diffusion coefficient.

CONCLUSIONS

SRS microscopy has been successfully used to visualise AI uptake kinetics and characterise how that varies with the chemistry of the AI. Furthermore, SRS has been used as a tool to determine the diffusion model. Future work will investigate the utility of SRS with fiber laser excitation as a tool for label free, real-time diffusion measurements *in planta*.

ACKNOWLEDGEMENTS

We thank the Industrial Cooperative Awards in Science and Technology (ICAST) and Syngenta for funding this work.

‘Econos’ 8-11th April 2018 – Milan, Italy.

Visualising Agrochemical Uptake Kinetics Through Wax with Stimulated Raman Scattering

Nicholas Philip Gaunt

Biomedical Physics, School of Physics & Astronomy, University of Exeter, Exeter

Niall Thomson², Faheem Padia², Julian Moger¹

1. Biomedical Physics, School of Physics & Astronomy, University of Exeter, Exeter

2. Syngenta, Jealott’s Hill, Bracknell, UK

Increasing population, land erosion and use of land for biofuel production mean sustainably feeding the world is increasingly a challenge.⁴⁰ Agrochemicals already play an essential role in meeting these demands, with 40% of the world’s food being attributed to their use,¹⁵ but further performance gains in agrochemical products need to be found in order to maintain global food security. One area of active research is in improving penetration of the agrochemical active into the plant through the cuticle, as this can be a significant source of loss. A plant’s cuticle is a composite membrane, covering the outer surface of a plant and controlling the exchange of matter between the leaf and the environment and thus presents the first barrier an applied agrochemical must pass.³⁴ The ability to control the uptake of agrochemicals into plants, may enable a lower dose to be applied and be advantageous for the development of new agrochemical products. Imaging techniques such as coherent anti-Stokes Raman Scattering (CARS) and stimulated Raman Scattering (SRS) can help by providing a label-free image contrast, which is not susceptible to fluorescence from pigments in the plants, like other current techniques in order to characterise uptake kinetics. We have applied coherent Raman Scattering (CRS) as a novel analytical technique that allows *in situ* analysis of agrochemical active ingredients (AIs) and adjuvants through wax. The ability to visualise AIs, like Azoxystrobin, through wax reveals the uptake kinetics and allows a determination of the diffusion model. This could enable a step change in agrochemical design, through determination of the spatial distribution of the materials and their roles within the applied products.

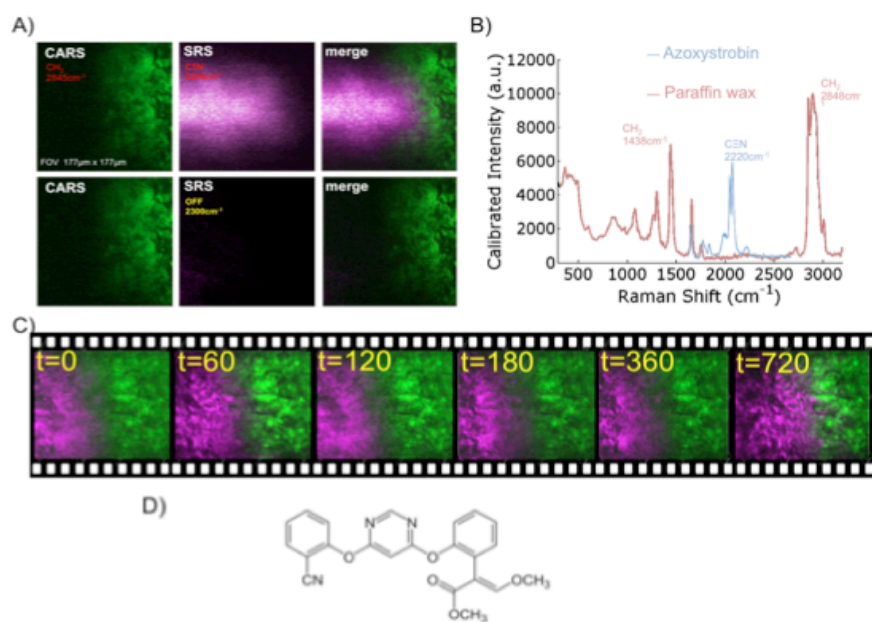




Fig. 1 A) Coherent Raman scattering images of paraffin wax's CH_2 (CARS, green) and Azoxystrobin's (AZ) chemically specific $\text{C}\equiv\text{N}$ (SRS, magenta). (B) shows the spontaneous Raman spectra of AZ ($\text{C}\equiv\text{N}$) over paraffin wax's Raman signature. The diffusion of AZ into wax can be imaged and analyzed as shown in (C). Field of view of (A) and (C): $177\mu\text{m} \times 177\mu\text{m}$. (D) Structure of AZ

Chemistry Collaborative Research Conference (Syngenta) 13th September – Bracknell, UK.




Visualising Agrochemical Kinetics Through Cuticle Wax with Stimulated Raman Scattering



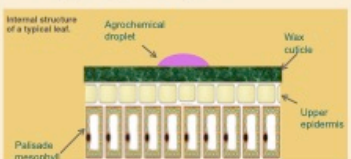
Nicholas P Gaunt^a, Niall Thomson^b, Faheem Padia^b, Julian Moger^{a*}

^aBiomedical Physics, School of Physics & Astronomy, University of Exeter, Exeter, UK; ^bSyngenta, Jealott's Hill, Bracknell, Berkshire, UK *Email: J.Moger@exeter.ac.uk



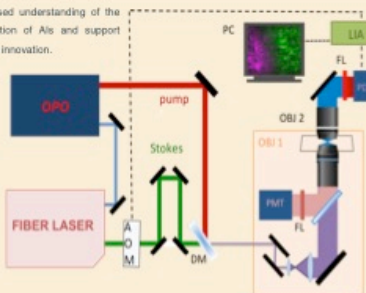
INTRODUCTION

The plant cuticle is a composite membrane which forms the outer surface of a plant, controlling the exchange of matter between the leaf and its environment. It provides the first line of defense against pathogens, and is the first barrier an applied agrochemical must pass. The ability to characterise and tune the uptake of agrochemicals into plants in real time, may enable a lower environmental dose to be applied and be advantageous for the development of new agrochemical products



OPTICAL SETUP

Here, we use stimulated Raman scattering (SRS) microscopy to analyse the diffusion of active ingredients (AIs) into a cuticle proxy, paraffin wax. The AIs, Azoxystrobin (AZ) and Fludioxonil (FDL), can be identified by imaging chemically distinct bonds such as C≡N stretch (2220 cm⁻¹). By characterising the movement of the agrochemical AIs through the cuticle barrier and harnessing the characterisation power of SRS, we will enable increased understanding of the interaction of AIs and support further innovation.



The optical setup of fiber laser-based stimulated Raman scattering for AIs and wax. AOM: acousto-optic modulator, DM: dichroic mirror, OBI: objective, FL: filter, PMT: photomultiplier tube, PD: photodiode, LIA: lock-in amplifier.

KINETICS

We fit the data with diffusion theory to obtain quantitative diffusion characteristics of cuticle wax-AI interaction. We fit the data to **Fick's second law**, as experiments follow non-steady-state diffusion into an infinite source.

$$\frac{S}{S_{z=0}} = 1 - \text{erf}\left(\frac{z}{2\sqrt{Dt}}\right)$$

Figures 2 (A) and (B) highlight the experimental difference in diffusivity between AZ and FDL into paraffin wax over the course of 24 minutes. These plots show that the diffusivity of AZ is greater than that of FDL. The predictions shown in Figures 2 (C) and (D) demonstrate how the experimental results deviate from classical modeling as the time of diffusion increases. As the shape of the concentration profiles (at different time points) differs from the calculated model, it is conclusive of variation in D.

If D is constant, plotting t^{1/2}, as shown in Figure 2 (E) and (F), would show the data points collapse into one single curve. This behaviour is not seen, and is therefore characteristic of a time- and concentration-dependent diffusion coefficient. This evolution, plotted as the normalised area under the SRS signal as a function of time is shown in Figure 2 (G). The shaded areas on this graph represent the ranges that would be anticipated if the AI diffusivity were constant. However, because these values change considerably more than the given range predicted (by mean plus or minus standard deviation), the results would imply a progressive uptake of these AIs with a varying diffusion coefficient.

CONCLUSION

SRS microscopy has been successfully used to visualise AI uptake kinetics and characterise how that varies with the chemistry of the AI. Furthermore, SRS has been used as a tool to determine the diffusion model. Future work will investigate the utility of SRS with fiber laser excitation as a tool for label free, real-time diffusion measurements in plants.

SRS OF ACTIVE INGREDIENTS

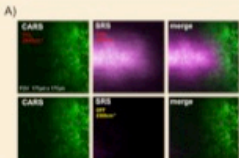
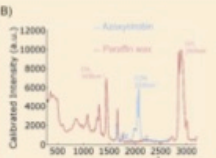
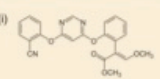
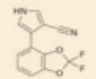


Figure 1: A) Coherent Raman scattering images of paraffin wax's CH₂ (CARS, green) and AZ's chemically specific C≡N (SRS, magenta). (B) shows the spontaneous Raman spectra of AZ (C≡N) over paraffin wax's Raman signature. The diffusion of AZ into wax can be imaged and analyzed as shown in (C). Field of view of (A) and (C): 177µm x 177µm. (D) Structures of (i) AZ and (ii) Fludioxonil





(i)

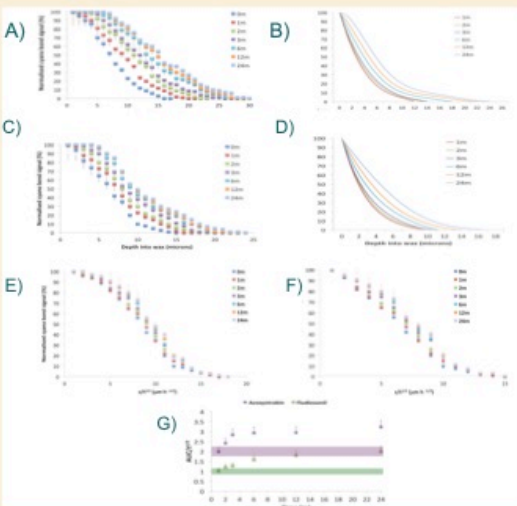


(ii)

ACKNOWLEDGEMENTS

We thank the Industrial Cooperative Awards in Science and Technology (ICAST) and Syngenta for funding this work.

Figure 2: Comparison of depth profiles for (A) AZ, (B) FDL as a function of time, compared with the corresponding predicted profiles calculated by Eq. 1, assuming a constant source of AI, (C) AZ (D) FDL. Normalised SRS signal of (E) AZ and (F) FDL, as a function of z/ t^{1/2}. (G) The area under these experimental curve profiles (AUC), normalised by the t^{1/2} as a function of time. The shaded area (AZ purple, Fludioxonil green) represent the range predicted (mean ± standard deviation) for constant diffusion coefficient values.



Papers

Outlooks on Pest Management – April 2018

ADVANCES IN ANALYTICAL CAPABILITY TO POWER AGROCHEMICAL PRODUCT DESIGN

Nicholas P. Gaunt¹, Niall Thomson², Faheem Padia², Mark Seymour² and Julian Moger¹; ¹Biomedical Physics, School of Physics and Astronomy, University of Exeter, Exeter, UK, ²Syngenta, Jealott's Hill Research Station, Bracknell, Berkshire UK

Keywords: stimulated Raman scattering, agrochemical, crop, spectroscopy



Nicholas Gaunt

Niall Thomson

Faheem Padia



Mark Seymour

Julian Moger

Agrochemicals and the industry

The rapid growth in global population exerts mounting pressure on farmers to grow more food. Agrochemicals, such as herbicides, fungicides and insecticides, are a key factor in improving crop yields and without them around 35% (Oerke & Dehne, 2004) of the world's food could not be produced. The widespread use of newer and more effective products since the middle of the last century has increased food security and improved standards of living around the world. To enable further improvements and meet demand, the ability to monitor the movement of active ingredients and their interactions with co-formulants *in planta* would be hugely advantageous.

Usually, agrochemicals are applied to a plant via an aqueous spray. When optimised, the spray can contain a complex mixture of components, such as surfactants and oils, which can improve the retention of the spray droplets to the leaf,

the spreading of the droplets on the leaf surface and enhance uptake into the plant. Currently the effectiveness of these components is measured via time-consuming offline processes or by monitoring biological performance. A key enabler for developing improved agrochemical activity is the ability to track the spatial-temporal distribution of agrochemical compounds in living plant tissues (i.e. *in planta*). This report outlines the current state of the art, summarised in Table 1, and reviews the techniques that show the potential to meet the growing requirements of the agrochemical industry. The ideal technique would be non-destructive, provide real time video and quantification of active ingredients *in planta* without the need for fluorescent labelling which can perturb the biokinetics. Table 1 compares the available characterisation techniques and the following text discusses the pros and cons.

Multiple techniques are already used in the agrochemical industry to monitor the interactions of agrochemicals with crops, however, none of the current techniques alone can meet the demands of sensitive, non-destructive, high spatial resolution imaging in real time. Results gathered from many countries by the Codex Committee on Pesticide Residues (CCPR, 2001) showed the majority of the methods referred to pesticides amenable to gas chromatography (GC) or liquid chromatography (LC). These methods cover approximately 75% of the compounds in the Codex system and do not satisfy the *in planta* characterisation needs. Other techniques include Time-of-Flight Secondary Ion Mass Spectroscopy (ToF-SIMS), Matrix-assisted laser desorption/ionisation (MALDI) and autoradiography, plus emerging methods such as spontaneous and coherent Raman scattering. The following sections review the suitability of spectrometry, autoradiography, electron and microscopy to meet the *in planta* characterisation needs of the agrochemical industry.

Mass Spectrometry (MS)

Mass spectrometry (MS) in combination with chromatography is the most widely used analytical technique for pesticide residue analysis. MS in combination with chromatography separates all of the components in a sample and provides a compound-specific output and can provide quantitative high chemical specificity, without the use of labels, when measuring agrochemical uptake. However, MS provides only very limited spatio-temporal information, and cannot be used *in planta*. Alder *et al* (2006) reported a comparative study on the capabilities of mass spectrometry in combination with chromatography for the determination of a multitude of

ADVANCES IN ANALYTICAL CAPABILITY

Table 1. Comparative table of the advantages and disadvantages of *in planta* characterisation techniques used in the agrochemical industry.

Technique	Non-invasive/ Non-destructive (in planta)	Spatial Resolution	Chemical Label Free	Chemical Specificity	Low Detection Limit	Cost of Use	Real-time	Quantitative
GCMS	✗	Low	✓	High	✓	Moderate	✗	✓
LCMS	✗	Low	✓	High	✓	High	✗	✓
SEM (EDX)	✗	Very high	✓	Low	✓	High	✗	✓
Fluorescent Microscopy	✓	High	✗*	High [§]	✓	Low	✓	✓
Imaging Mass Spectrometry	✗	Moderate	✓	High	✓	High	✓	✓
Autoradiography	✓	Low	✓	High [§]	✓	Moderate	✓	✓
Spontaneous Raman microscopy	✗**	High	✓	High	✗	Low	✗	N/A
Coherent Raman Spectroscopy	✓	High	✓	High	✓	High	✓	✓

*Bar specialised cases

**Due to fluorescence of chlorophyll

§ If labeled

pesticides. GCMS with electron impact (EI) ionization and the combination of LC with tandem mass spectrometers (LCMS/MS) using electrospray ionization (ESI) are identified as the techniques most often applied in multi-residue methods for pesticides at present with LCMS currently being the most common technique. However, its inability to provide spatial resolution or the ability to monitor compounds *in planta* in a non-destructive manner are major limitations.

ToF-SIMS and MALDI-MS both suffer from similar disadvantages to MS techniques, being destructive and with very limited spatio-temporal information achievable. ToF-SIMS has been used to analyse polymers and biological materials since the late 1960s (Benninghoven, 1969), whereas MALDI was first reported in 1994 (Spengler *et al.*, 1994). The predominant method used since then has been MALDI-ToF MS, which has been applied to visualise proteins and peptides, allowing identification of compounds directly on tissue surfaces (Stahl *et al.*, 1997) and distinguishing between low molecular weight proteins in plant matter (Grusak & Dellapenna, 1999). The technique proved to be a rapid, accurate and cost effective method of microbial characterisation and identification. With its generated characteristic mass spectral fingerprints it was ideal for strain typing and identification. The conventional technique of MALDI-ToF MS requires the destruction of the specimen under study. However, with many advancements made to MALDI-ToF, the specimen may be partially preserved for further studies. In cases with small mass differences, say different nucleotides, the technique may not be able to determine the mass accurately. MALDI-ToF is

also mostly limited to two dimensions, which is a major limitation for *in planta* imaging.

Autoradiography

Autoradiography is widely used by the agrochemical industry to visualise the *in planta* distributions of radioisotopically-labelled substances. The technique utilises radioactive nuclei, such as tritium, radioactive phosphorus and carbon, to map the movement of molecules. This allows the systemic distribution of labelled organic molecules such as carbohydrates and proteins to be visualised *in planta*. For example, it has been used to monitor the spreading of the bacterium *Bacillus thuringiensis* within cotton plants, systemically map the translocation and translaminar bioavailability of neonicotinoid insecticides in cabbages (Buchholz & Nauen, 2002) and visualise the uptake and distribution of insecticides, through radish roots (Létondor *et al.*, 2015) and black nightshade (Grossmann *et al.*, 2011) shown in Figure 1.

Although autoradiographic imaging of radiolabelled compounds can provide non-destructive information about their systemic distribution, it lacks sufficient spatial resolution to determine their localisation at the cellular scale.

Scanning Electron Microscopy (SEM)

Scanning electron microscopy (SEM), with Energy dispersive X-ray microanalysis (EDX), is a well-known technique in the agrochemical industry. Commonly coupled together, the

2 Outlooks on Pest Management – April 2018

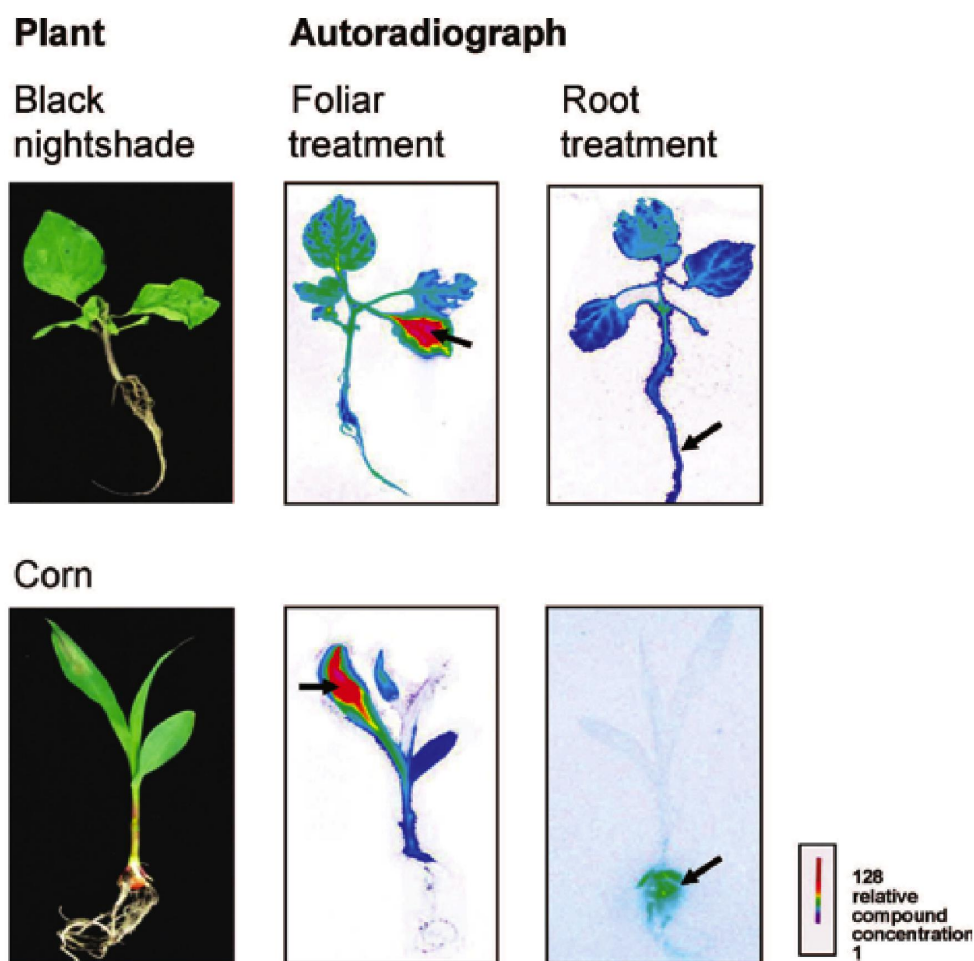


Figure 1. Autoradiographs of corn and black nightshade (*Solanum nigrum*) plants, which were foliar and root treated. Reprinted from Grossmann *et al.* 2011.

techniques can provide simultaneously both topography and elemental composition of a sample with submicron spatial resolution. This technique has been used to detect specific elements in soils and plants and has been used to characterise the distribution pattern of active ingredients on plant surfaces (Krause, 1985). Whilst being one of the most cost-effective methods, SEM-EDX provides low chemical specificity and usually requires a sample to be coated with gold and held under vacuum, meaning real-time *in planta* measurements are impossible, as are measurements of materials remaining on the surface. Another significant limitation is that the spatial localisation and quantification of molecules is only possible when the molecule has at least one distinctive element that does not occur naturally in or on the untreated sample.

Optical Microscopy

Optical techniques are preferable as they provide non-invasive imaging with a diffraction limited spatial resolution. However, the major challenge in optical imaging is deriving chemically specific contrast from the molecular species of interest. The following sections discuss the various optical techniques that

can be used to provide optical contrast of agrochemical active ingredients (AIs).

Fluorescence microscopy

Fluorescence microscopy has become ubiquitous within modern biology and with the advent of immunolabelling and genetically encoded fluorophores it can be used to provide the spatio-temporal distribution of biomolecules at the cellular scale with a high degree of chemical specificity. Today, fluorescence microscopy has become an essential tool in biology. The application of a diverse range of fluorophores has made it possible to identify cells and sub-microscopic cellular components with a high degree of specificity amid non-fluorescing material. Through the use of a multiple fluorescent label, different probes can identify several target molecules simultaneously. For example, in 2004 Liu *et al* showed the transcuticular diffusion of three dyes and the effects of surfactants on the diffusion of these compounds (Figure 2).

Despite having several advantages over non-optical techniques, confocal has several limitations such as depth-of-field and a reliance on fluorescent species. Unless a compound

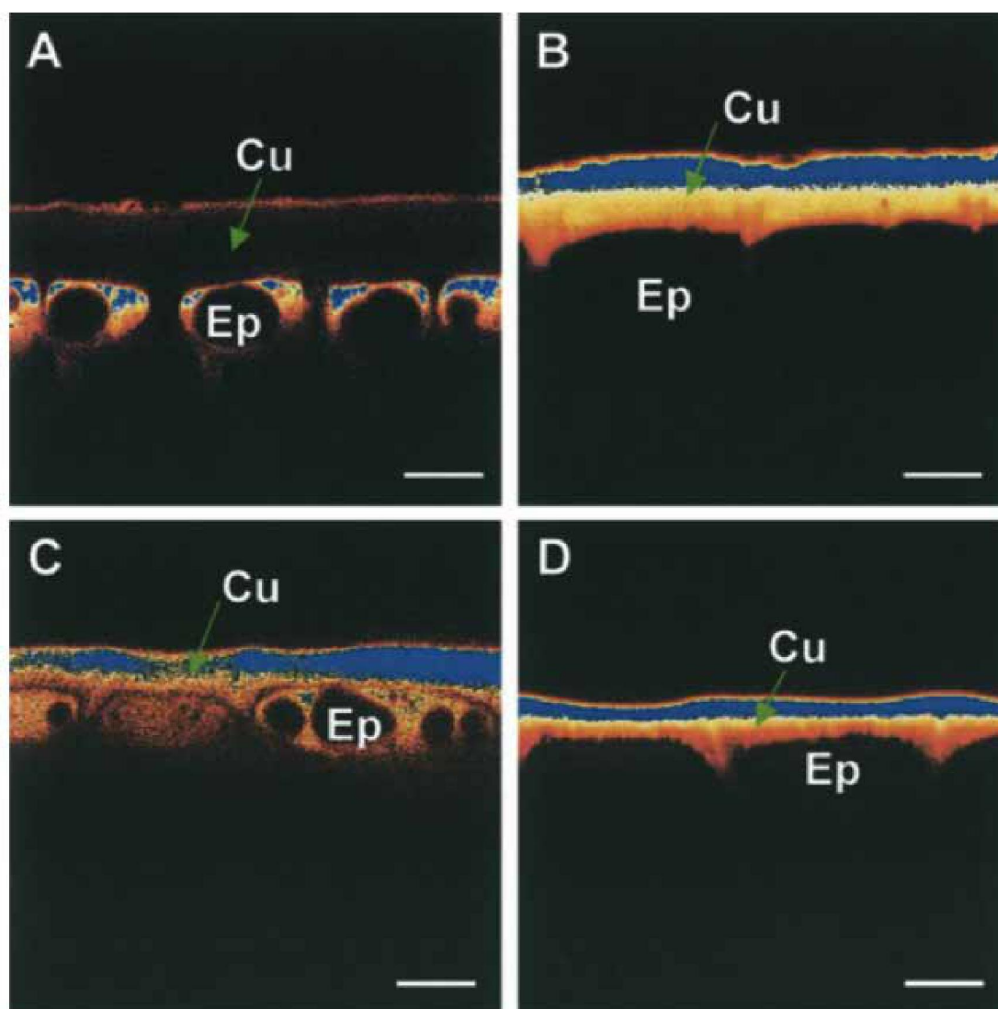


Figure 2. Localisation of dyes in apples and peppers. Cu, cuticle; Ep, epidermal cells. Scale bars = 20 μ m. Reprinted from Liu *et al.*, 2004.

exhibits intrinsic fluorescence, it must be labelled with a fluorophore in order to provide contrast. The addition of fluorophores to macromolecules such as proteins causes very little perturbation, as their molecular weights are typically 10–100 fold greater than that of fluorophores, which are usually of the order of a few hundred Da. However, these fluorophores are in most cases comparable in size of agrochemical AIs and hence drastically alter their transport kinetics. Moreover, the use of these large labels can perturb biological function and may be phytotoxic, which complicates their use for studying long-term biological dynamics.

Raman spectroscopy

Optical techniques based on vibrational spectroscopy provide *in situ* chemical analysis derived from the vibrational frequencies of molecular bonds within a sample. However, due to water absorption and the intrinsically low spatial resolution associated with the long infrared wavelengths required to excite molecular vibrations directly, infrared absorption techniques have limited value for bio-imaging. However, Raman

scattering, provides analysis of IR vibrational frequencies by examining the inelastic scattering of visible (or near IR) light. The Raman scattered light is frequency-shifted with respect to the incident light by discrete amounts which correspond to molecular vibrational frequencies. The spectrum of Raman scattered light excited by a single incident wavelength consists of a series of peaks that correspond to the molecular vibrational frequencies. This can be regarded as a chemical fingerprint of a sample and holds a wealth of information regarding chemical composition and conformation.

Modern Raman spectroscopy techniques are rapidly becoming recognised as valuable analytical tools for agrochemical R&D, being utilised to determine and identify various pesticides in crops. For example, Liu and Liu (2011) and Zhang *et al* (2006) demonstrated the characteristic peaks of standard pesticide spectra could be identified on the surface of fruits and vegetables. In addition, enhanced systems, such as Surface-Enhanced Raman spectroscopy (SERS) are even more sensitive and thus can be used to produce protocols for environmental particulates analysis with the goal to monitor exposure to organic pollutants

4 Outlooks on Pest Management – April 2018

and identify health risks and environmental contaminants quickly (Clauson *et al.*, 2015).

Unfortunately, Raman scattering is an extremely weak effect and typical photon conversion efficiencies in biological materials are of the order of 1 in 10 (Yu *et al.*, 2013). This severely limits the application of Raman for studying living systems since long acquisition times (100 ms to 1 s per pixel) at relatively high excitation powers (several hundred mW) are required to image most biomolecules with sufficient sensitivity. This lack of sensitivity is compounded by its susceptibility to interference from autofluorescence. The Stokes-shifted Raman scattered light is overwhelmed by fluorescent emissions, which virtually prohibits its application in all but a few applications in living plant tissues.

Coherent Raman Spectroscopy (CRS)

Fortunately, far stronger Raman signals can be obtained using an emerging Raman based imaging technique known as coherent Raman scattering (CRS) (Min *et al.*, 2011). CRS achieves signal enhancement by focusing the excitation energy onto a specific Raman mode of the biomolecules of interest. A pump and Stokes beam, with frequencies ω_p and ω_s respectively, are incident upon the sample with the frequency difference $\omega_p - \omega_s$ chosen to match the molecular vibrational frequency of interest. Under this resonant condition, bonds are coherently driven by the excitation fields and a strong nonlinear coherent Raman signal is produced. Due to the nonlinear dependence of the signal on excitation intensity, further enhancement can be achieved by excitation with ultra-short light pulses, which deliver extremely high peak intensities with modest average powers that are comparable with those routinely used in confocal microscopy. Optimal conditions for CRS require pulses of a few picoseconds in duration that have sufficient intensity to excite CRS without having bandwidths that extend beyond the line width of typical Raman bands.

When applied in microscopy format, CRS benefits from the nonlinear nature of the process which confines the signal to a sub-micron focus that can be scanned in space, allowing three-dimensional mapping of biomolecules with sub-micron resolution. CRS microscopy has particular advantages for bio-imaging: chemically specific contrast is derived from the vibrational signature of endogenous biomolecules within the sample, negating the need for extraneous labels/stains; low energy near-IR excitation wavelengths can be employed which reduce photodamage and increase depth penetration into scattering tissues; and since the CRS process does not leave sample molecules in an excited state it does not suffer from photobleaching and can be used for long term time series studies.

Coherent Raman scattering microscopy may be achieved by detecting either coherent anti-Stokes Raman scattering (CARS) or stimulated Raman scattering (SRS). CARS uses the anti-Stokes signal generated at frequency $\omega_{as} = 2\omega_p - \omega_s$, which, by using filters, is spectrally isolated from the pump and Stokes beams, and its intensity used to map the location of biomolecules of interest. The anti-Stokes (blue) shift of the emission with respect to the excitation wavelengths makes CARS more resistant to interference from sample autofluorescence than

spontaneous Raman. However, for highly fluorescent samples such as plant tissues, the usually weak two-photon fluorescence (also blue-shifted with respect to the excitation wavelengths) overlaps and overwhelms the CARS signal. SRS relies on detecting subtle changes in the intensities of the excitation fields that occur by virtue of stimulated excitation (Freudiger *et al.*, 2008). When the difference frequency, $\omega_p - \omega_s$ matches a molecular vibrational frequency the intensity of the Stokes beam, I_s , experiences a gain, ΔI_s , while the intensity of the pump beam, I_p , experiences a loss, ΔI_p . The intensity transfer from the pump to the Stokes beam only occurs when both beams are incident upon the sample and can be detected with high sensitivity using modulation transfer detection. Modulating the intensity of the Stokes beam modulates the SRS process and hence transfers an intensity modulation onto the pump beam. The amplitude of the transferred intensity modulation is directly proportional to the concentration of target molecules and by modulating at frequencies above laser noise (>1 MHz) can be detected with a lock-in amplifier with great sensitivity (1 in 10^6 photons).

CRS's high spatio-temporal resolution has had a huge impact in biomedical research and has already been demonstrated to have adequate sensitivity to allow the visualisation of various tissues like skin (Yu *et al.*, 2013) and made significant advances in the field of cancer diagnosis (Lee *et al.*, 2015). In addition, CRS has been used to image the diffusion of low molecular weight drug molecules into human skin and nails (Drutis *et al.*, 2014; Sin *et al.*, 2015). These measurements have similarities to that of an AI diffusing across a cuticle boundary and hence indicate that CRS has potential to overcome the limitations of fluorescence. However, strong two-photon absorption in heavily pigmented leaves have prevented *in planta* applications of CRS.

Recently, Mansfield *et al.* (2013) developed an SRS detection technique that overcomes the effect of two-photon absorption, combining structural imaging with *in situ* chemical analysis of plant materials, providing real-time subcellular spatial resolution *in planta*, shown in Figure 3. Following this, Littlejohn *et al.*, (2015) showed that SRS can be used to acquire *in-vivo*, 3D images of cuticles, thanks to SRS's low autofluorescence compared to CARS. CRS shows a lot of promise in the agrochemical area, enabling real-time high spatial resolution imaging techniques with high chemical specificity. CRS has been shown to provide quantitative information, whilst remain non-destructive *in planta*. These advances could lead to CRS being more heavily utilised as next generation techniques for agrochemical development and research.

Summary

The agrochemical industry would benefit from a non-destructive, real-time characterisation technique with high chemical selectivity and high spatial resolution. Although many techniques meet some of these requirements, currently only CRS enables all to be met by a single measurement. The use of CRS techniques such as CARS and SRS enables the monitoring and imaging of active ingredients *in planta*, at video-rate speed without the use of potentially interfering labels and could help guide the development of improved agrochemical formulations.

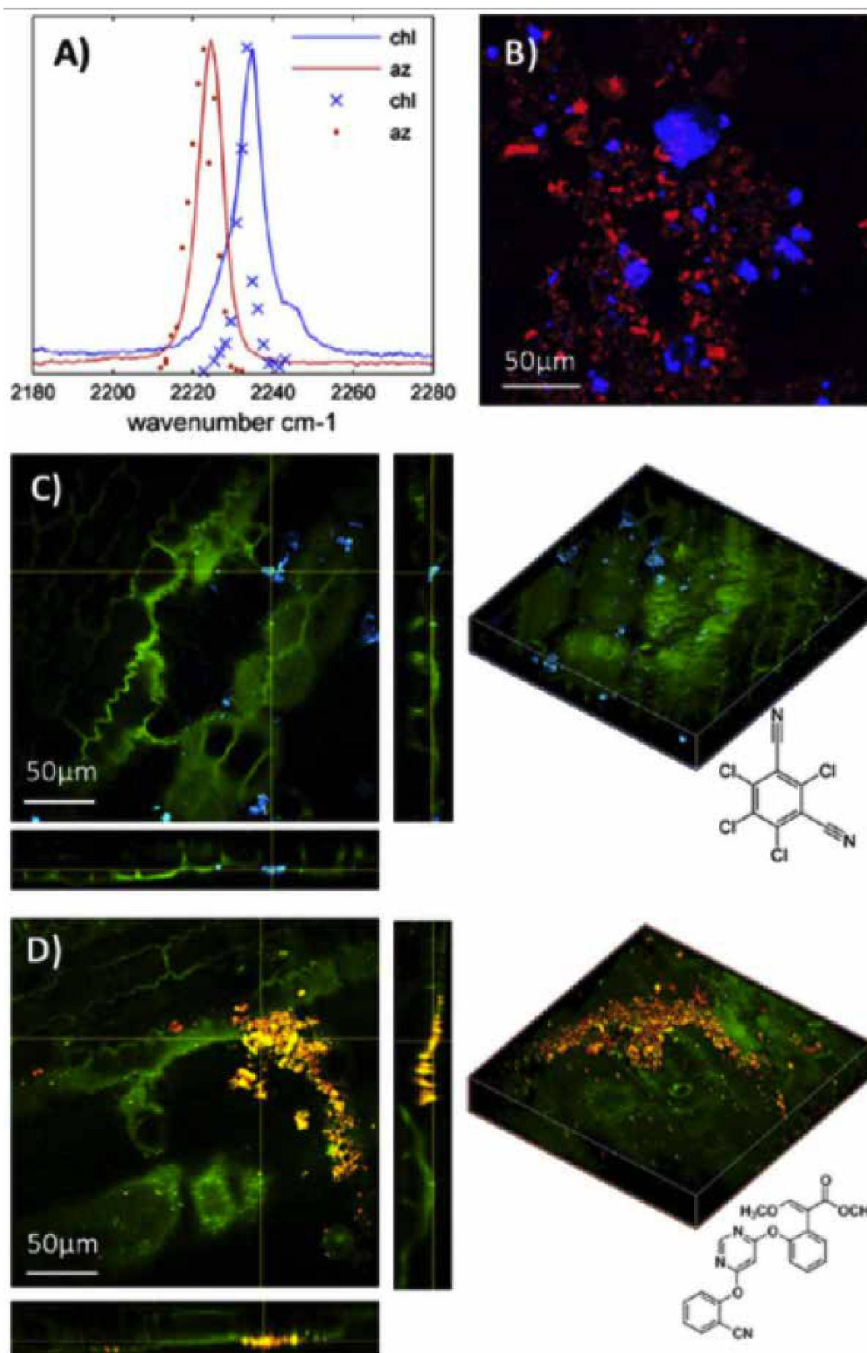


Figure 3. Two fungicides azoxystrobin (az) and chlorothalonil (chl) imaged on maize leaves. (A) SRL and spontaneous Raman at C≡N bond (B) SRL image of a mixture of az and chl (C) chl distribution on maize (D) az distribution on maize leaf. Reprinted from Mansfield *et al.* (2013).

References

Alder, L., Greulich, K., Kempe, G. & Vieth, B. (2006) Residue analysis of 500 high priority pesticides: Better by GC-MS or LC-MS/MS? *Mass Spectrosc. Rev.* 25, 838–865.
 Benninghoven, A. (1969) Analysis of Submonolayers on Silver by Negative Secondary Ion Emission. *Phys. status solidi* 34, K169–K171.

Buchholz, A. & Nauen, R. (2002) Translocation and translaminar bioavailability of two neonicotinoid insecticides after foliar application to cabbage and cotton. *Pest Manag. Sci.* 16, 10–16.
 Clauson, S. L., Sylvania, J. M., Arcury, T. A., Summers, P. & Spencer, K. M. (2015) Detection of Pesticides and Metabolites Using Surface-Enhanced Raman Spectroscopy (SERS): Acephate. *Appl. Spectrosc.* 69, 785–793.

6 Outlooks on Pest Management – April 2018

© 2018 Research Information Ltd. All rights reserved. www.pestoutlook.com

- Codex Committee for Pesticide Residues. *The List of Methods for Pesticide Residue Analysis, including Methods of Determination for Dithiocarbamates*. (2001). at <http://www.naweb.iaea.org/nafa/fep/Methods-Main.pdf>
- Drutis, D. M. *et al.* (2014) Three-dimensional chemical imaging of skin using stimulated Raman scattering microscopy. *J. Biomed. Opt.* **19**, 111604.
- Freudiger, C. W. *et al.* (2008) Label-Free Biomedical Imaging with High Sensitivity by Stimulated Raman Scattering Microscopy. *Science*. **322**, 1857–1861.
- Grossmann, K., Hutzler, J., Caspar, G., Kwiatkowski, J. & Brommer, C. L. (2011) Saflufenacil (Kixor™): Biokinetic Properties and Mechanism of Selectivity of a New Protoporphyrinogen IX Oxidase Inhibiting Herbicide. *Weed Sci.* **59**, 290–298.
- Grusak, M. A. & Dellapenna, D. (1999) Improving The Nutrient Composition of Plants to Enhance Human Nutrition and Health. *Annu. Rev. Plant Physiol. Plant Mol. Biol.* **1**, 133–161.
- Krause, C. R. (1985) Foliar penetration of a fungicide as detected by scanning electron microscopy and energy dispersive x-ray analysis. *Scan. Electron Microsc.* **2**, 811–815.
- Lee, M. *et al.* (2015) *In vivo* imaging of the tumor and its associated microenvironment using combined CARS / 2-photon microscopy *In vivo* imaging of the tumor and its associated microenvironment using combined CARS / 2-photon microscopy. *IntraVital* **4**, 1–8.
- Létondor, C., Pascal-lorber, S. & Laurent, F. (2015) Uptake and distribution of chlordecone in radish: Different contamination routes in edible roots. *Chemosphere* **118**, 20–28.
- Liu, Z. (2004) Confocal laser scanning microscopy – an attractive tool for studying the uptake of xenobiotics into plant foliage. *J. Microsc.* **213**, 87–93.
- Liu, Y. & Liu, T. (2011) in *Computer and Computing Technologies in Agriculture IV: 4th IFIP TC 12 Conference, CCTA 2010, Nanchang, China, October 22–25, 2010, Selected Papers, Part IV* (eds. Li, D., Liu, Y. & Chen, Y.) 427–434 (Springer Berlin Heidelberg, Germany 2011). doi:10.1007/978-3-642-18369-0_50
- Littlejohn, G. R. *et al.* (2015) *In Vivo* Chemical and Structural Analysis of Plant Cuticular Waxes Using Stimulated Raman Scattering Microscopy 1 [OPEN]. *Plant Physiol.* **168**, 18–28.
- Mansfield, J. C. *et al.* (2013) Label-free Chemically Specific Imaging *in planta* with Stimulated Raman Scattering Microscopy. *Anal. Chem.* **85**, 5055–5063.
- Min, W., Freudiger, C. W., Lu, S. & Xie, X. S. (2011) Coherent Nonlinear Optical Imaging: Beyond Fluorescence Microscopy. *Annu. Rev. Phys. Chem.* **62**, 507–530.
- Oerke, E. & Dehne, H. (2004) Safeguarding production – losses in major crops and the role of crop protection. *Crop Prot.* **23**, 275–285.
- Sin, W., Belsey, N. A., Garrett, N. L., Moger, J. & Delgado-charro, M. B. (2015) Molecular diffusion in the human nail measured by stimulated Raman scattering microscopy. *PNAS* **112**, 6–11.
- Spengler, B., Hubert, M. & Kaufmann, R. (1994) MALDI Ion Imaging and Biological Ion Imaging with a new Scanning UV-Laser Microprobe. in *42nd ASMS Conference on Mass Spectrometry* 1041–1044.
- Stahl, B., Linos, A., Karas, M., Hillenkamp, F. & Steup, M. (1997) Analysis of Fructans from Higher Plants by Matrix- Assisted Laser Desorption/Ionization Mass Spectrometry. *Anal. Biochem.* **204**, 195–204.
- Yu, Y., Sohma, Y., Takimoto, S., Miyachi, T. & Yasui, M. (2013) Direct visualization and quantitative analysis of water diffusion in complex biological tissues using CARS microscopy. *Sci. Rep.* **3**, 1–11.
- Zhang, P. X., Zhou, X., Cheng, A. Y. S. & Fang, Y. (2006) Raman Spectra from Pesticides on the Surface of Fruits. *J. Phys. Conf. Ser.* **28**, 7–11.

Nicholas P. Gaunt is a PhD candidate in Biophysics, Living Systems Institute, University of Exeter. Since 2015, his research focuses on monitoring the uptake of agrochemical active ingredients into plants, using CRS techniques.

Niall Rae Thomson is a Team Leader in Formulation Development at Syngenta's Jealott's Hill International Research Centre with a principle research interest in the interaction of spray droplets with the leaf surface.

Faheem Padia is a Technical Specialist in the Formulation Technology Group at Syngenta's Jealott's Hill International Research Centre. His research currently focuses on the physical processes governing delivery of agrochemical formulation to plants.

Mark Seymour is a Science and Technology Fellow at Syngenta's Jealott's Hill International Research Centre in Berkshire. His interests include optical spectroscopies and how these can be applied to address measurement challenges relevant to the agriscience sector.

Julian Moger is an Associate Professor at the University of Exeter. His research is in the field of Biophotonics – the interface between Biology and Photonics that deals with the interaction between light and biological systems. His research currently focuses on the development and application of cutting-edge optical technologies to tackle healthcare and global sustainability research challenges.

Similar articles that appeared in *Outlooks on Pest Management* include –